
founded by H.K.V. Lotsch

Editor-in-Chief: W. T. Rhodes, Atlanta

Editorial Board: A. Adibi, Atlanta
T. Asakura, Sapporo
T. W. Hänsch, Garching
T. Kamiya, Tokyo
F. Krausz, Garching
B. Monemar, Linköping
H. Venghaus, Berlin
H. Weber, Berlin
H. Weinfurter, München

Springer Series in OPTICAL SCIENCES

The Springer Series in Optical Sciences, under the leadership of Editor-in-Chief *William T. Rhodes*, Georgia Institute of Technology, USA, provides an expanding selection of research monographs in all major areas of optics: lasers and quantum optics, ultrafast phenomena, optical spectroscopy techniques, optoelectronics, quantum information, information optics, applied laser technology, industrial applications, and other topics of contemporary interest.

With this broad coverage of topics, the series is of use to all research scientists and engineers who need up-to-date reference books.

The editors encourage prospective authors to correspond with them in advance of submitting a manuscript. Submission of manuscripts should be made to the Editor-in-Chief or one of the Editors. See also www.springer.com/series/624

Editor-in-Chief

William T. Rhodes

Georgia Institute of Technology
School of Electrical and Computer Engineering
Atlanta, GA 30332-0250, USA
E-mail: bill.rhodes@ece.gatech.edu

Editorial Board

Ali Adibi

Georgia Institute of Technology
School of Electrical and Computer Engineering
Atlanta, GA 30332-0250, USA
E-mail: adibi@ee.gatech.edu

Toshimitsu Asakura

Hokkai-Gakuen University
Faculty of Engineering
1-1, Minami-26, Nishi 11, Chuo-ku
Sapporo, Hokkaido 064-0926, Japan
E-mail: asakura@eli.hokkai-s-u.ac.jp

Theodor W. Hänsch

Max-Planck-Institut für Quantenoptik
Hans-Kopfermann-Straße 1
85748 Garching, Germany
E-mail: t.w.haensch@physik.uni-muenchen.de

Takeshi Kamiya

Ministry of Education, Culture, Sports
Science and Technology
National Institution for Academic Degrees
3-29-1 Otsuka, Bunkyo-ku
Tokyo 112-0012, Japan
E-mail: kamiyatk@niad.ac.jp

Ferenc Krausz

Ludwig-Maximilians-Universität München
Lehrstuhl für Experimentelle Physik
Am Coulombwall 1
85748 Garching, Germany
and
Max-Planck-Institut für Quantenoptik
Hans-Kopfermann-Straße 1
85748 Garching, Germany
E-mail: ferenc.krausz@mpq.mpg.de

Bo Monemar

Department of Physics
and Measurement Technology
Materials Science Division
Linköping University
58183 Linköping, Sweden
E-mail: bom@ifm.liu.se

Herbert Venghaus

Fraunhofer Institut für Nachrichtentechnik
Heinrich-Hertz-Institut
Einsteinufer 37
10587 Berlin, Germany
E-mail: venghaus@hhi.de

Horst Weber

Technische Universität Berlin
Optisches Institut
Straße des 17. Juni 135
10623 Berlin, Germany
E-mail: weber@physik.tu-berlin.de

Harald Weinfurter

Ludwig-Maximilians-Universität München
Sektion Physik
Schellingstraße 4/III
80799 München, Germany
E-mail: harald.weinfurter@physik.uni-muenchen.de

Igor A. Sukhoivanov

Igor V. Guryev

Photonic Crystals

Physics and Practical Modeling

With 109 Figures



Springer

Dr. Igor A. Sukhoivanov

Guanajuato University, Dept. of Electronics Engineering, FIMEE
Comm. Palo Blanco, 36885 Salamanca, GTo, Mexico
E-mail: i.sukhoivanov@ieee.org

Igor V. Guryev

National University of Radio Electronics, Lab. Photonics
Lenin av., 14 Kharkov 61166, Ukraine
E-mail: iguru@list.ru

Springer Series in Optical Sciences ISSN 0342-4111 e-ISSN 1556-1534

ISBN 978-3-642-02645-4 e-ISBN 978-3-642-02646-1

DOI 10.1007/978-3-642-02646-1

Springer Heidelberg Dordrecht London New York

Library of Congress Control Number: 2009929176

© Springer-Verlag Berlin Heidelberg 2009

This work is subject to copyright. All rights are reserved, whether the whole or part of the material is concerned, specifically the rights of translation, reprinting, reuse of illustrations, recitation, broadcasting, reproduction on microfilm or in any other way, and storage in data banks. Duplication of this publication or parts thereof is permitted only under the provisions of the German Copyright Law of September 9, 1965, in its current version, and permission for use must always be obtained from Springer. Violations are liable to prosecution under the German Copyright Law.

The use of general descriptive names, registered names, trademarks, etc. in this publication does not imply, even in the absence of a specific statement, that such names are exempt from the relevant protective laws and regulations and therefore free for general use.

Cover design: SPi Publisher Services

Printed on acid-free paper

Springer is part of Springer Science+Business Media (www.springer.com)

Preface

The great interest in photonic crystals and their applications in the last 15 years is being expressed in the publishing of a large number of monographs, collections, textbooks and tutorials, where existing knowledge concerning operation principles of photonic crystal devices and microstructured fibers, their mathematical description, well-known and novel applications of such technologies in photonics and optical communications are presented. They challenge authors of new books to cover the gaps still existing in the literature and highlight and popularize of already known material in a new and original manner.

Authors of this book believe that the next step towards wide application of photonic crystals is the solution of many practical problems of design and computation of the specific photonic crystal-based devices aimed at the specific technical application. In order to make this step, it is necessary to increase the number of practitioners who can solve such problems independently. The aim of this book is to extend the group of researchers, developers and students, who could practically use the knowledge on the physics of photonic crystals together with the knowledge and skills of independent calculation of basic characteristics of photonic crystals and modeling of various elements of integrated circuits and optical communication systems created on the basis of photonic crystals.

The book is intended for qualified readers, specialists in the field of optics and photonics, students of higher courses, master degree students and PhD students. As an introduction to the snopest, the book contains the basics of wave optics and radiation propagation in simple guiding media such as planar waveguides and step-index fibers.

Relying on fundamental laws and models, we give descriptions of physical principles of light propagation inside 1D, 2D and 3D photonic crystals and microstructured fibers. Detailed explanations of the basic terms used in photonic crystal physics, such as reciprocal lattice vectors, Brilluoin zone, matrix eigen-vectors and eigen-states, basis functions, etc. are given.

The following chapters describe methods of the eigen-problems solution for 1D, 2D and 3D photonic crystals as well as methods for computation of field distribution inside nonuniform media. Solutions to several specific problems, such as field distribution and eigen-states of microstructured fibers and photonic crystal waveguides are given. In the last chapter, an example of the design of the photonic crystal-based wavelength division demultiplexer is considered.

For each case, models which allow to obtain fundamental characteristics of a photonic crystal are considered. Detailed descriptions of problems such as computation of the band structure and field distribution inside photonic crystal devices are given. Main attention is given to numerical implementation of the considered models. Algorithms and computation procedures for the plane wave expansion method and finite-difference time-domain method are given.

The important feature of this book is the combination of theoretical material and description of algorithms and program printouts based on the authors' experiences.

Each chapter of the book, except the first two, contains examples of a problem which includes computation techniques, algorithm description, and peculiarities of its implementation, as well as computed results reflecting all of intermediate and final stages of the computation, with a detailed analysis. Thus, after studying the theoretical material, the reader can use the programs provided for solving the examples recommended for knowledge consolidation as well as original problems.

Besides commonly considered problems on computation of photonic band structure and field distribution inside photonic crystals, the design method of wideband photonic crystal filters which can be used for WDM demultiplexing is given in the final chapter as an example of complex photonic crystal-based device synthesis. Such an example consolidate the knowledge and skills acquired the previous chapters together with described photonic band gap maps, photonic density of states maps and computed spectral characteristics.

We try teaching the reader to make a purposeful choice of a method and to understand its implementation algorithms. So we have provided convenient tools for unassisted solution of the problems described in a separate chapter. Program printouts can be directly used for modeling. Thus, we consider our book as an effective practical addition to the well known, widely distributed books.

Authors wish to express our thanks and appreciation to all colleagues, who contributed to development of this book. We thank our colleagues O. Ibarra-Manzano, J.A. Andrade Lucio, E. Alvarado Mendez from FIMEE, University of Guanajuato (Mexico) who have organized visits of one of the authors (Igor Guryev) to the University of Guanajuato and who stimulated work on this book. We express our great thanks to our colleagues and friends, especially,

Dr. O. Shulika from Kharkov National University of Radio Electronics for numerous helpful discussions, and reading and editing the final text. We would also like to thank our Pierian spring, Mrs Alla Kublyk for her friendly support and assistance.

Salamanca, Mexico and Kharkov, Ukraine,
June 2009

Igor Sukhoivanov
Igor Guryev

Contents

| | | |
|----------|---|----|
| 1 | Introduction to Photonic Crystals | 1 |
| 1.1 | Introduction: What are Photonic Crystals? | 1 |
| 1.2 | Photonic Crystal Lattice | 3 |
| 1.3 | Basic Terminology | 5 |
| 1.4 | Historical Notes | 6 |
| 1.5 | Problems and Questions | 12 |
| 2 | Fundamentals of Wave Optics | 13 |
| 2.1 | What is an Optical Medium? – Theoretical Models | 13 |
| 2.1.1 | Wave Optics | 14 |
| 2.1.2 | Geometric Optics | 15 |
| 2.2 | Wave Propagation: Maxwell’s Equations | 15 |
| 2.3 | Wave Equation in Vacuum | 18 |
| 2.4 | Waves in Dielectric Media | 20 |
| 2.4.1 | Refractive Index of Dielectric Medium | 21 |
| 2.4.2 | Lossy Dielectric Medium | 21 |
| 2.5 | Group Velocity | 23 |
| 2.6 | Summary | 24 |
| 2.7 | Problems and Questions | 25 |
| 3 | Fundamentals of Computation of Photonic Crystal Characteristics | 27 |
| 3.1 | Computation of the Field Distribution in One-Dimensional (1D) Photonic Crystal | 27 |
| 3.2 | Applications of the Field Distribution Computation | 32 |
| 3.3 | Summary | 35 |
| 3.4 | MATLAB Program Reflectance Spectrum Computation of 1D PhC | 35 |
| 3.5 | Problems and Questions | 39 |

| | | |
|----------|---|-----|
| 4 | Band Structure Computation of 1D Photonic Crystals | 41 |
| 4.1 | Problem Definition | 41 |
| 4.2 | Unit Cell | 44 |
| 4.3 | Lattice Vectors | 45 |
| 4.4 | Reciprocal Lattice | 46 |
| 4.5 | Reciprocal Lattice Vectors and Brillouin Zone | 48 |
| 4.6 | Band Structure Computation | 50 |
| 4.7 | Eigen-Values and Eigen-Vectors of a Matrix | 53 |
| 4.8 | Computation Results | 54 |
| 4.9 | Fourier Expansion of the Dielectric Function | 55 |
| 4.10 | The Eigen-Value Problem for Electric Field | 57 |
| 4.11 | Algorithm of PWE Method | 58 |
| 4.12 | Off-Axis Band Structure of 1D PhC | 58 |
| 4.13 | Summary | 61 |
| 4.14 | MATLAB Program for 1D PhC Band Structure Computation by Means of PWE Method | 61 |
| 4.15 | Problems and Questions | 65 |
| 5 | Band Structure Computation of 2D and 3D Photonic Crystals | 67 |
| 5.1 | Problem Definition for 3D Photonic Crystal | 67 |
| 5.2 | Problem Definition for 2D Photonic Crystal | 70 |
| 5.3 | Fourier Expansion of the Dielectric Function | 72 |
| 5.3.1 | Dielectric Spheres | 72 |
| 5.3.2 | Dielectric Rods | 73 |
| 5.3.3 | Fourier Expansion Coefficient of an Arbitrary Dielectric Function | 74 |
| 5.3.4 | Validation of the Fourier Expansion | 76 |
| 5.4 | Wave Vectors Set | 78 |
| 5.5 | Reciprocal Lattice Vectors Set | 79 |
| 5.6 | Results of the Band Structure Computation | 80 |
| 5.7 | Analysis of the Band Structure | 81 |
| 5.8 | Photonic Band Gap Maps | 82 |
| 5.9 | Photonic Density of States | 84 |
| 5.10 | Off-Plane Band Structure for 2D Photonic Crystal | 85 |
| 5.11 | Band Structure Computation of the PhC with Defect | 88 |
| 5.12 | Experimental Verification of the PWE Method | 90 |
| 5.13 | Advantages and Disadvantages of the Plane Wave Expansion Method | 93 |
| 5.14 | Summary | 94 |
| 5.15 | MATLAB Program for Band Structure Computation of 2D PhC by Means of PWE Method | 94 |
| 5.16 | Problems and Questions | 100 |

| | | |
|----------|---|-----|
| 6 | Finite-Difference Time-Domain Method for PhC Devices Modeling | 103 |
| 6.1 | Problem Formulation for the Field Distribution Computation: Finite-Difference Time-Domain Method | 103 |
| 6.2 | Maxwell's Equations Discretization | 104 |
| 6.3 | Definition of the Dielectric Function | 108 |
| 6.4 | Definition of Initial and Boundary Conditions | 109 |
| 6.4.1 | Initial Conditions | 109 |
| 6.4.2 | Conditions at the Boundaries of Computation Region | 109 |
| 6.5 | FDTD Method Stability | 113 |
| 6.6 | FDTD Method Application for Experimentally Obtained PhC with Hexagonal Lattice Structure | 113 |
| 6.7 | Summary | 117 |
| 6.8 | Problem Solution Example | 117 |
| 6.9 | MATLAB Program for Computation of Field Distribution in Nonuniform Optical Medium | 121 |
| 6.10 | Problems and Questions | 125 |
| 7 | Photonic Crystal Optical Fibers | 127 |
| 7.1 | Photonic Crystal Fibers: New Class of Optical Waveguides | 127 |
| 7.2 | Modes in Conventional Optical Fibers | 129 |
| 7.3 | Solution of Helmholtz Equation in Axial-Symmetric System | 130 |
| 7.4 | Hybrid Modes in Fibers and Mode Parameters | 133 |
| 7.4.1 | Fundamental Mode Distribution in Weakly Guiding Fibers | 135 |
| 7.4.2 | Effective Mode Index and Cutoff Conditions | 135 |
| 7.4.3 | bV Diagram | 136 |
| 7.5 | Single-Mode Fibers | 138 |
| 7.5.1 | Single-Mode Condition | 138 |
| 7.6 | Microstructured Fibers | 139 |
| 7.6.1 | Computation of Eigen-States of Microstructured Fibers | 140 |
| 7.6.2 | Computation of the Mode Field Distribution in Microstructured Fibers | 142 |
| 7.7 | Index-Guided Microstructured Fibers | 144 |
| 7.7.1 | Effective Refractive Index of the PhC-Fiber | 146 |
| 7.7.2 | Step-Index Fiber Model of the Index-Guided PhC Fibers | 146 |
| 7.7.3 | Numerical Aperture of the PhC Fiber | 147 |
| 7.7.4 | Macro-Bending Losses | 148 |
| 7.8 | Photonic Band Gap Fibers | 150 |

| | | |
|-----------|--|------------|
| 7.9 | Band Gap Diagram of the PBG Fiber | 152 |
| 7.9.1 | Coupling Losses of the PhC Fiber | 153 |
| 7.10 | Summary | 154 |
| 7.11 | MATLAB Program for Computation of the Fundamental Mode Distribution in Microstructured Fiber by Means of Plane Wave Expansion Method | 155 |
| 7.12 | Problems and Questions | 161 |
| 8 | FDTD Method for Band Structure Computation | 163 |
| 8.1 | Problem Definition | 163 |
| 8.2 | Computation Region Definition | 164 |
| 8.3 | Boundary Conditions Definition | 165 |
| 8.4 | Initial Conditions | 166 |
| 8.5 | Structure Response Analysis | 167 |
| 8.6 | Summary | 169 |
| 8.7 | MATLAB Program for Band Structure Computation of 1D PhC by Means of FDTD Method | 170 |
| 8.8 | Problems and Questions | 175 |
| 9 | Photonic Crystal Waveguides | 177 |
| 9.1 | Conventional Planar Waveguides | 177 |
| 9.1.1 | Guided Modes in a Slab | 178 |
| 9.1.2 | Characteristic Equations | 181 |
| 9.2 | Weakly Guiding Slabs | 182 |
| 9.2.1 | Graphical Solution of Characteristic Equation | 182 |
| 9.2.2 | bV Diagram: Modal Field Distribution in a Slab Waveguide | 183 |
| 9.3 | Kinds of PhC Waveguides | 185 |
| 9.4 | PWE Method for PhC Waveguides | 186 |
| 9.5 | Analysis of the Dispersion Diagram | 191 |
| 9.6 | FDTD Modeling of the PhC Waveguides | 194 |
| 9.7 | Summary | 196 |
| 9.8 | MATLAB Program for Computation of Dispersion Diagrams of 2D PhC Waveguide | 197 |
| 9.9 | Problems and Questions | 203 |
| 10 | Application for Design and Simulation of Optical WDM Demultiplexer | 205 |
| 10.1 | Problem Formulation | 205 |
| 10.2 | Band Structure Analysis | 206 |
| 10.2.1 | Waveguide Design | 207 |
| 10.2.2 | PBG Maps Design | 208 |
| 10.2.3 | Photonic DOS Maps Design | 211 |
| 10.3 | Temporal Response of DEMUX | 214 |
| 10.4 | Summary | 215 |

| | |
|--|-----|
| 10.5 MATLAB Program for the Computation of the PBG Map of PhC by Means of PWE Method..... | 216 |
| 10.6 Problems and Questions..... | 224 |
| References | 225 |
| Index | 239 |

Acronyms

| | |
|------------|---|
| 1D | One-Dimensional |
| 2D | Two-Dimensional |
| 3D | Three-Dimensional |
| BZ | Brillouin Zone |
| CGS | Centimetre Gram Second system of units |
| CW | Continuous Wave |
| DEMUX | DEMultipleXer |
| DFB | Distributed FeedBack |
| EM | ElectroMagnetic |
| FBG | Fiber Bragg Grating |
| FCC | Face-Centered Cubic |
| FDTD | Finite-Difference Time-Domain |
| GLAD | GLanced Angle Deposition |
| KKR | Korringa-Kohn-Rostoker |
| LP | Linearly Polarized |
| PBG | Photonic Band Gap |
| PCF | Potonic Crystal Fiber |
| PhC | Photonic Crystal |
| PhDOS | Photonic Density Of States |
| PWE | Plane Wave Expansion |
| PML | Perfectly Matched Layer |
| SI | le Système International d'unités (international system of units) |
| TE or H | Transversal Electric |
| TIR | Total Internal Reflection |
| TM or E | Transversal Magnetic Mode |
| VCSEL | Vertical-Cavity Surface-Emitting Laser |
| WDM | Wavelength-Division Multiplexing |
| a, b, c | Linear dimensions of unit cell along X, Y, Z axes respectively |
| a_+, a_- | Amplitudes of forward and backward waves |

| | |
|--|---|
| a_{WG} | Period of the PhC waveguide along the waveguide direction |
| A | Amplitude of the forward wave |
| A_j | Amplitude of the forward wave inside j th layer of the layered structure |
| $\mathbf{a}_1, \mathbf{a}_2, \mathbf{a}_3$ | Primitive lattice vectors |
| \mathbf{B} | Magnetic induction |
| b | Normalized propagation constant |
| B | Amplitude of the backward wave |
| B_j | Amplitude of the backward wave inside j th layer of the layered structure |
| $\mathbf{b}_1, \mathbf{b}_2, \mathbf{b}_3$ | Primitive reciprocal lattice vectors |
| c | Light velocity in vacuum |
| $d_1, d_2, \dots d_{N-1}$ | Widths of layers of the layered structure |
| \mathbf{D} | Electric displacement field |
| D_x | x -component of the electric displacement |
| D_y | y -component of the electric displacement |
| D_z | z -component of the electric displacement |
| \mathbf{E} | Electric field vector |
| E | Electric field |
| E_0 | Electric field amplitude |
| E_x | x -component of the electric field |
| E_y | y -component of the electric field |
| E_j | Electric field inside j -th layer of the layered structure |
| E_ρ | Radial component of the electric field in polar coordinate system |
| \tilde{E} | Fourier transform of \mathbf{E} |
| $\mathbf{E}_{\mathbf{k}n}(\mathbf{G})$ | Eigen-vector of electric field |
| $\mathbf{E}_+, \mathbf{E}_-$ | Forward and backward waves |
| E_ϕ | Azimuthal component of the electric field in polar coordinate system |
| F, F_1, F_2 | Real numbers |
| $g(\mathbf{k})$ | Dielectric function in wave vector representation |
| G_0 | Primitive reciprocal lattice vector length in 1D reciprocal space |
| $\mathbf{G}, \mathbf{G}', \mathbf{G}''$ | Reciprocal lattice vectors |
| $\mathbf{G}_{ }$ | 2D in-plan reciprocal lattice vector |
| H | Magnetic strength |
| \mathbf{H} | Magnetic field vector |
| H_m | Hankel function |
| $\mathbf{H}_{\mathbf{k}n}(\mathbf{G})$ | Eigen-vector of magnetic field |
| H_ρ | Radial component of the magnetic field in polar coordinate system |
| H_ϕ | Azimuthal component of the magnetic field in polar coordinate system |

| | |
|------------------------------|--|
| HE_{ml}, EH_{ml} | Hybrid fiber mode |
| I_m | Modified Bessel function |
| j | Imaginary unit |
| J | Current density |
| J_m | Bessel function of the m -th order |
| J_0, J_1 | Bessel function of the order 0 and 1 |
| k | Wave vector |
| k_0 | Free space wave number |
| $\mathbf{k}_1, \mathbf{k}_2$ | Wave vector inside medium 1 and 2 |
| K_m | Modified Hankel function |
| k_x, k_y, k_z | Wave vector components |
| $\mathbf{k}_{ }$ | In-plane wave vector |
| l, m, n | Integer number determining length and direction of the lattice vector |
| l', m', n' | Integer number determining length and direction of the reciprocal lattice vector |
| LP_{lm} | Linearly polarized fiber mode |
| M | Number of modes |
| M | Magnetic polarization |
| n | Refractive index |
| n_1, n_2, \dots, n_{N-1} | Refractive indices of layers of the layered structure |
| n_0 | Refractive index of the medium before the layered structure |
| n_N | Refractive index of the medium after the layered structure |
| n_j | Refractive index of j -th layer of the layered structure |
| N | Number of layers of the layered structure |
| \bar{n} | Mode index; effective index; effective refractive index |
| n_{eff} | Effective refractive index |
| N_m | Neumann function |
| N_x, N_y, N_z | Number of mesh nodes along x -, y - and z direction correspondingly |
| P | Electric polarization |
| S | Poynting vector |
| r | Coordinate vector |
| r_a | Radius of the spherical or cylindrical element |
| $\mathbf{r}_{ }$ | In-plane coordinate vector |
| r_H, t_H | Reflectance and transmittance coefficients for TM wave |
| r_E, t_E | Reflectance and transmittance coefficients for TE wave |
| R | Lattice vector |
| $S(\mathbf{r})$ | Step function |
| t | Time |
| V_0 | Volume of the unit cell of PhC |
| v_g | Group velocity |
| V | Normalized frequency |

XVIII Acronyms

| | |
|--------------------------------------|--|
| u, v, w | Transversal phase and attenuation constants inside the slab, substrate and the space above the slab respectively |
| w | Mode radius of the step-index fiber |
| W_1, W_2, W_n | Designations of the waveguides formed by missing 1, 2 or n rows of the PhC elements |
| x, y, z | Cartesian coordinates |
| $\mathbf{x}, \mathbf{y}, \mathbf{z}$ | Unit vectors in Cartesian coordinate system |
| x_j | Coordinate of the interface between 1-st and j -th layer |
| Δx | Linear dimension of computation cell in x -direction |
| Δy | Linear dimension of computation cell in y -direction |
| Δz | Linear dimension of computation cell in z -direction |
| α | Absorption coefficient |
| α_x | Attenuation coefficient in direction transversal to the propagation one |
| β | Propagation constant |
| β_{ml} | Solution of the eigen-value equation for the step-index fiber |
| $\bar{\beta}$ | Mean propagation constant |
| β_1, β_2 | Propagation constant inside medium 1 and 2 |
| $\Delta\beta$ | Propagation constant difference |
| Γ, X, M, K, U, L, W | High symmetry points |
| $\delta_{i,j}$ | Kronecker delta |
| Δ | Laplacian, second order differential operator |
| ε | Dielectric constant, permittivity |
| ε_0 | Electric constant |
| ε_r | Relative permittivity |
| θ | Angle |
| θ_{2c} | Critical angle |
| $\hat{\theta}$ | Differential operator in matrix form |
| $\hat{\theta}_{G,G'}$ | Matrix element of $\hat{\theta}$ |
| θ_B | Brewster angle |
| $\hat{\Theta}$ | Differential operator |
| λ | Wavelength |
| λ_0 | Vacuum wavelength |
| λ_g | Wavelength inside a waveguide |
| λ_C | Cutoff wavelength |
| λ_{br} | Bragg wavelength |
| μ | Permeability |
| μ_0 | Magnetic constant |
| ρ | Charge density, radius in polar coordinate system |
| σ | Conductivity |
| σ_x | Electric conductivity within x -direction |
| σ_y | Electric conductivity within y -direction |
| σ_z | Electric conductivity within z -direction |
| σ_x^* | Magnetic conductivity within x -direction |

| | |
|------------------------------------|--|
| σ_y^* | Magnetic conductivity within y -direction |
| σ_z^* | Magnetic conductivity within z -direction |
| σ_g | Dispersion of the group velocity |
| τ | Period of harmonic function |
| χ | Electric susceptibility |
| $\tilde{\chi}$ | Fourier transform of χ |
| ϕ | Angle in polar coordinate system |
| Φ_{01}, Φ_{12} | Phase shift after the first and the second reflections from the boundaries of the slab waveguide |
| Φ_E, Φ_M | Phase shift of the electric and magnetic component after the reflection |
| $\chi(\mathbf{G})$ | Fourier expansion coefficients of the inverted permittivity distribution function |
| ψ | Wave function |
| ψ_p | Basis function |
| ω_0 | Center frequency of the photonic band gap |
| ω_1, ω_2 | Angular frequency |
| $\omega_{\mathbf{k}n}^{(E)}$ | Eigen-frequency for electric field |
| $\omega_{\mathbf{k}n}^{(H)}$ | Eigen-frequency for magnetic field |
| $\omega_{\mathbf{k}_{ },n}^{(E)}$ | Eigen-frequency for TM polarization |
| $\omega_{\mathbf{k}_{ },n}^{(H)}$ | Eigen-frequency for TE polarization |
| ω | Angular frequency |
| $\bar{\omega}$ | Mean frequency |
| $\Delta\omega$ | Half-width of PBG, frequency difference |
| ω_r | Relative frequency |
| ∇ | Nabla, first-order differential operator |

Introduction to Photonic Crystals

Summary. Chapter 1 gives a brief introduction into the basics of photonic crystals which are a special class of optical media with periodic modulation of permittivity. We give a general idea of what photonic crystals are and then describe different kinds of photonic crystal lattices and introduce and discuss the basic terminology. Main attention is paid to the band structure, eigen states and photonic band gaps. Finally, some historical notes are given, where the first computed band structures of three dimensional photonic crystal with face-centered cubic and diamond lattices are presented as well as the band structure of inverted opal. At the end of the chapter different areas of photonic crystal applications in optical communications and lasers are given, such as waveguides, optical insulators, splitters, microresonators for spontaneous emission management, etc.

1.1 Introduction: What are Photonic Crystals?

Photonic crystals (PhCs) are novel class of optical media represented by natural or artificial structures with periodic modulation of the refractive index. Such optical media have some peculiar properties which gives an opportunity for a number of applications to be implemented on their basis. Depending on geometry of the structure, PhCs can be divided into three broad categories, namely one-dimensional (1D), two-dimensional (2D) and three-dimensional (3D) structures. Examples are shown in Fig. 1.1.

In 1D PhCs, the periodic modulation of the permittivity occurs in one direction only, while in two other directions structure is uniform. As an example of such a PhC it can be given the Bragg grating which is widely used as a distributed reflector in vertical cavity surface emitting lasers. Besides, such structures are widely used as antireflecting coatings which allow to decrease dramatically the reflectance from the surface and are used to improve the quality of lenses, prisms and other optical components.

2D PhC can have comparatively large variety of configurations, because it possesses periodicity of the permittivity along two directions, while in the third direction the medium is uniform. A good example of the 2D PhC is

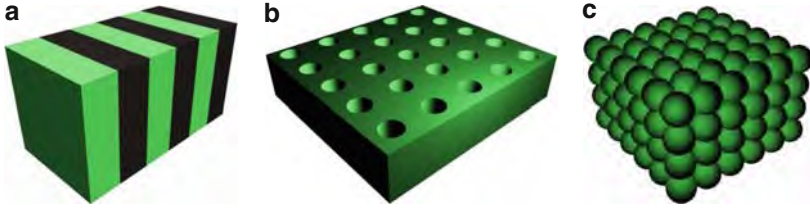


Fig. 1.1. Examples of 1D, 2D and 3D photonic crystals (a) 1D PhC, (b) 2D PhC, (c) 3D PhC

porous silicon with periodically arranged pores, which is represented by the silicon substrate with etched holes. Another example of 2D PhC is a periodically arranged system of dielectric rods in air. 2D PhC can also be found in nature. For instance, the pattern on the butterfly's wing and its rainbow play is caused by the light reflection from the microstructure on the wing.

3D PhC has permittivity modulation along all three directions. At that, the number of possible PhC configurations is much larger than in case of 1D or 2D PhC. Many works are dedicated to the design of new geometric configuration of 3D PhC, which discover new possibilities of their application. The most known naturally formed 3D PhC is valuable stone opal. This stone is known by its unique optical properties. When turned around, it plays different colors. Because of such a behavior, ancient people believed that opal possesses some magic powers. However, now we know that all these peculiarities are caused by the microstructure of opal. It consists of a number of microspheres placed at nodes of face-centered cubic (FCC) lattice. Reflectance of such a structure strongly depends on the radiation incident angle. So when one turns it around, it starts to reflect the radiation with different wavelengths. Thus, optical properties of PhCs are determined by the existence of the periodic modulation of the permittivity or the refractive index of the medium. At that, observed effects have strong analogy to the solid state, i.e., the periodically arranged structure of atoms in crystal lattice. Such a similarity between the physics of PhCs and solid-state physics gives the possibility to draw the analogy between some properties and computation methods applied to solid-state and PhCs physics.

The most important similarities between PhC and solid-state physics are as follows: Periodic modulation of the refractive index in a PhC forms a lattice similar to atomic lattice of solid-state; behavior of photons in a PhC is similar to electron and hole behavior in an atomic lattice; due to the lattice periodicity both PhC and solid-state provide band gap, the range of energies which particle cannot have inside the structure. From theoretical viewpoint, determination of the eigenfunctions in a PhC is very similar to calculation of the particle wave functions in the solid-state. This similarity is used to obtain photonic band structure.

However, along with strong similarity, there exist some essential differences. One of the main differences is the particle energy distribution. Electrons obey the Fermi–Dirac distribution while photons obey Bose–Einstein distribution. Besides, electrons are affected by intracrystalline field which leads to the necessity of taking it into account (it is necessary to note that the shape of intracrystalline field is unknown, and investigators have to use approximate methods such as k - p method). Photons are not affected by intracrystalline field. Therefore, computation of the optical field distribution or the photonic band structure is essentially simplified.

The most important property which determines practical significance of the PhC is the presence of the photonic band gap. The photonic band gap (PBG) refers to the energy or frequency range where the light propagation is prohibited inside the PhC. When the radiation with frequency inside the PBG incidents the structure, it appears to be completely reflected. However, if one introduces the defect to the strictly periodic structure, the effect of such a defect is the same as the defect introduction to the crystalline structure of a semiconductor. This means that new eigen-state appears inside the PBG with energy corresponding to the eigen-frequency of the defect. Thus, the radiation within the defect frequency will propagate inside the structure or, in case of multiple defects radiation will be guided like in waveguide.

Thus, there exist quite strong analogy between PhC physics and solid-state physics both from the physical and mathematical points of view.

1.2 Photonic Crystal Lattice

Previously it was shown that PhCs possess different geometric conformations. These conformations correspond to types of crystal lattice of solid-state crystals. This fact gives the possibility to use the term “lattice” to indicate the geometric conformation of the PhC.

1D PhC have very low number of possible periodic structure variations because it is represented by the layered structure, so only the refractive index, layer’s thickness and the number of layers within the period can be varied. Thus, we start consideration of kinds of PhC lattices from 2D case. It is obvious to assume that variation of the elements shape and their placement gives an infinite number of lattice types. However, for technological reasons, there are two commonly used types of the 2D PhC lattice, namely, square and hexagonal. The unit cell of the PhC with square lattice has the shape of square. Elements of such a PhC type must be similar to each other, i.e., they all can have round, square, hexagonal or some other shape. The unit cell of hexagonal lattice have the form of regular hexagon and the elements, like for the square lattice, must be similar. Examples of such PhC types are shown in Fig. 1.2.

3D PhCs geometry can be varied in very different manners so they can have a great number of lattice types. Because 3D PhCs are the most similar to solid-state crystals, many lattice types of such PhCs have similar conformation and

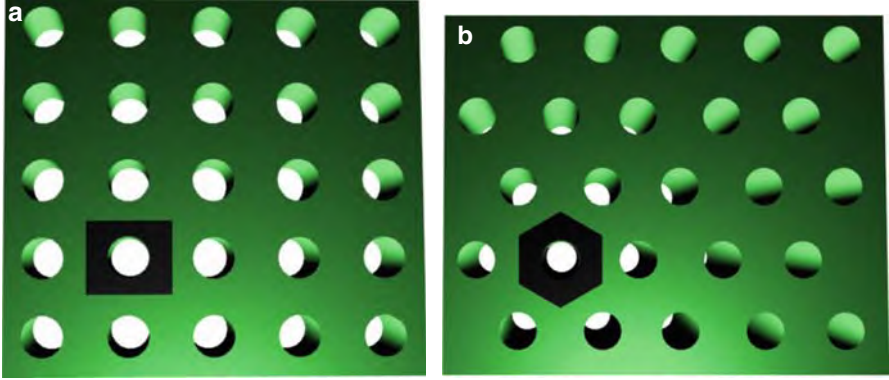


Fig. 1.2. Examples of 2D PhC lattice types. (a) 2D PhC with square lattice and round elements shape, (b) 2D PhC with hexagonal lattice and round elements shape

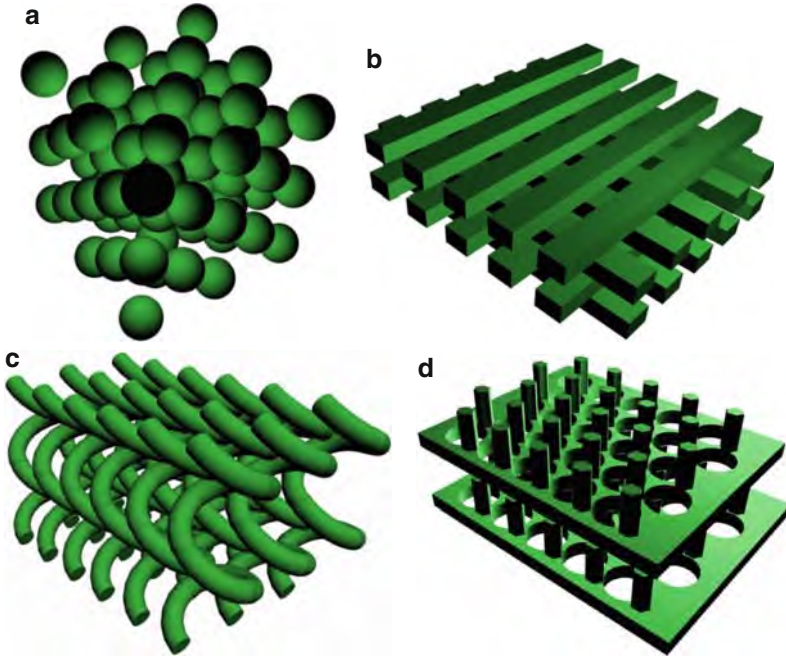


Fig. 1.3. Examples of 3D PhC lattices types. (a) FCC (face-centered cubic), (b) woodpile, (c) spiral lattice (GLAD GLancing Angle Deposition), (d) quasi-diamond lattice

similar names. Moreover, depending on the method of the PhC production, it can possess conformation which cannot be obtained in solid-state crystals. Some examples of the 3D PhC crystal lattices are shown in Fig. 1.3. Between

them the FCC and diamond lattices have the solid-state analogs while the woodpile and spiral (or GLAD) lattices are unique and can be obtained in PhCs only.

Thus, PhCs have a number of possible lattice types which determines a wide range of their fundamental properties such as the band structure, transmittance and reflectance spectra.

1.3 Basic Terminology

Before we start to discuss the characteristics and computation methods, it is necessary to introduce some basic terms. The first term and the most important one is the band structure of the PhC.

The band structure of the PhC is the characteristic which gives the most general information about the PhC properties. It is represented by a number of eigen-states or eigen-frequencies of an infinite periodic structure.

Eigen-frequency is another important term, it is also called resonant frequency of the structure. Since PhC is an infinite periodic structure, a number of Fresnel reflections appear at the media interfaces. Constructive and destructive interference between forward and backward waves causes either transmission or reflection of the radiation.

Each of the eigen-state sets correspond to the specific value of the radiation wave vector. Independent of the dimensionality of the PhC, the band structure is represented by a 2D plot. The example of such a band structure for 1D PhC is given in Fig. 1.4.

The physical meaning of the band structure is to connect the properties of the radiation with properties of optical medium the radiation propagates in.

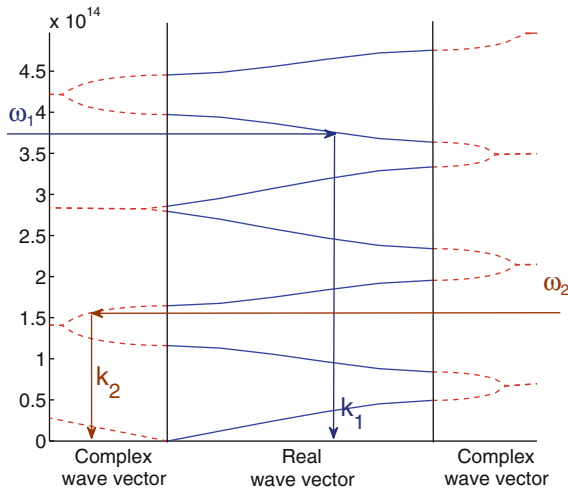


Fig. 1.4. Band structure of 1D PhC

In Fig. 1.4 the horizontal axis corresponds to the wave vector of the radiation and the vertical axis stays for the resonant frequencies of the medium. Let us consider the case when the radiation with frequency ω_1 incidents the PhC. Once it penetrates into the structure, it possesses the exact wave vector which is allowed by the structure. The value of such a wave vector can easily be found from the band structure. We can see from Fig. 1.4 that wave vector value k_1 corresponds to the radiation frequency ω_1 . Possessing this wave vector, the radiation propagates through the structure.

Let us now consider another case. If the radiation has frequency ω_2 , we can see that it falls at the frequency range where there are no allowed real wave vectors. However, it still can possess the complex wave vector k_2 . Later, in Chap. 2, we will see that the imaginary part of the wave vector corresponds to either radiation attenuation or gain. In our case, it corresponds to attenuation. This actually means that the radiation with frequency of this specific range will be reflected from the structure. However, since the attenuation is finite value, it will penetrate to the structure for some distance.

These two cases considered actually contain basic principles of the photonic band structure analysis. Namely, the periodic medium possesses allowed and forbidden frequency ranges. The radiation propagates inside the structure within allowed frequencies only. Otherwise, it will be reflected.

The forbidden frequency ranges are usually referred to as photonic band gaps.

If the radiation possesses allowed frequency, it takes the value of the wave vector which can be found from the band structure. The last statement is more important for 2D and 3D PhCs since the wave vectors for this structures are connected with radiation propagation direction. This allows the PhC to set the radiation propagation direction leading to a number of interesting effects such as strong angular dispersion.

Of course, the list of terms considered here is not complete. Some new terms will be introduced in subsequent chapters.

1.4 Historical Notes

Now, we can briefly consider the PhCs' evolution as well as methods for their design and investigation.

In spite of the fact that PhCs have attracted high attention only during the last several decades, first assumptions of possibility to control the light propagation using the periodic structures relate to 1887 [1]. Those were the investigations of 1D periodic structures.

Almost after 100 years in 1972, Soviet Union scientist V.P. Bykov published a paper where he described the possibility to use periodic structures for the spontaneous emission control [2].

However, the first works assumed to start the intensive progress of PhC are the works of E. Yablonovitch and S. John which was issued in 1987 in *Physical*

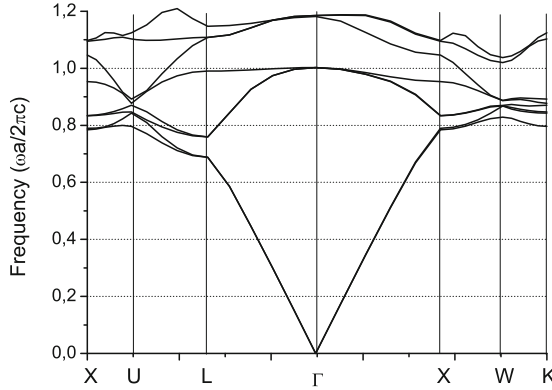


Fig. 1.5. The band structure of 3D PhC with FCC lattice

Review Letters [3], [4]. Papers are dedicated to the possibility of spontaneous emission management as well as the possibility of the radiation propagation control using periodic structures. After publication of these articles, a number of publications dedicated to PhC physics and technology doubles every year.

In 1990, K.M. Ho, C.T. Chan and C.M. Soukoulis [5] obtained the band structure of the PhC with FCC lattices (opal structure) which consisted of dielectric spheres with high refractive index placed in air. Example of such a band structure computed by the PWE method is shown in Fig. 1.5.

As it can be seen from the figure, the first band lies within the relative frequency range of 0–0.8. The second one coincides with the first band at the wave vector section $\Gamma - L$ (within the frequency range of 0–0.7) and $\Gamma - X$ (within the frequency range of 0–0.79). Moreover, within all the investigated frequency ranges at least one eigen-state exists, so no complete PBG appears. For instance, in Γ -point the eigen-frequency is equal to zero. At wave vector range $\Gamma - L$ the eigen-frequency smoothly grows from 0 to 0.8.

The existence of eigen-states at each point of the investigated frequency range tells about the absence of complete PBG. Moreover, it appears that the PhC with such type of lattice does not have the complete PBG at any values of refractive indices. However, considering the band structure, one can conclude that the PhC has wide partial band gaps at some propagation directions (for instance, at the point L within the range from 0.7 to 0.77 there are no eigen-frequencies). This means that the light with frequency in this range propagating in corresponding direction will be reflected. This causes the optical effects typical for all natural and artificial opals.

In the same work, there were also given results of band structure computation for the PhC with diamond lattice made of dielectric spheres placed in air where they found the complete PBG between the second and third bands (see Fig. 1.6).

In 1992, H.S. Sozuer and J.W. Haus [6] computed the band structure of the PhC with inverted FCC lattice (also known as inverted opal) which is

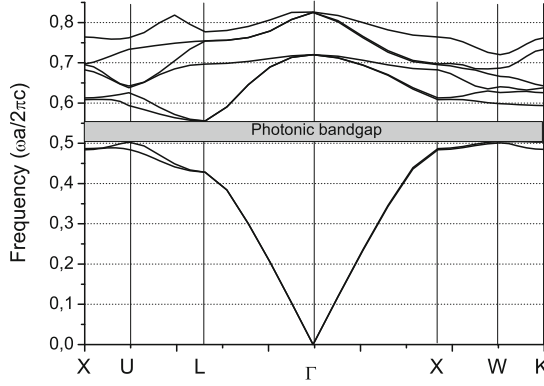


Fig. 1.6. The band structure of 3D PhC with diamond lattice

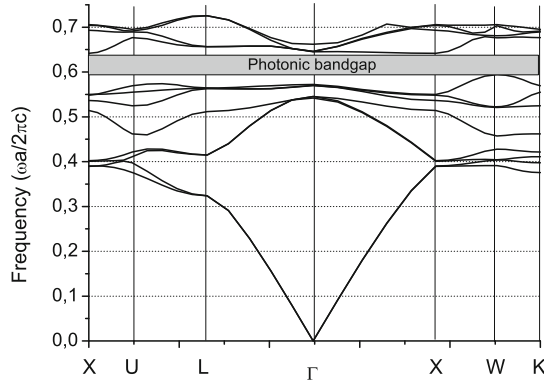


Fig. 1.7. The band structure of the PhC with inverted FCC lattice

presented in Fig. 1.7. The term inverted opal means that instead of dielectric spheres placed in air, the inverted FCC lattice consists of a number of spherical cavities separated by baffles with higher refractive index (see Fig. 1.8). It appeared that such a PhC has complete PBG at relatively high refractive index of material. Investigated inverted opal had complete PBG between the eighth and ninth bands.

The appearance of the complete PBG inside the PhC with inverted FCC lattice attracts a special interest, because today inverted artificial opals provide possibility of mass PhC production.

In 1998, the inverted artificial opal was obtained experimentally [7]. The sphere's diameter in the structure was approximately $1\text{ }\mu\text{m}$, and the distance between the spheres is very low so the spheres are almost touching. From the technological point of view, it is much easier to grow the structure with such parameters than with high distance between spheres because the base FCC lattice consists of dielectric spheres in air so when the spheres touch each other, their position can be easily locked in. The refractive index of the PhC

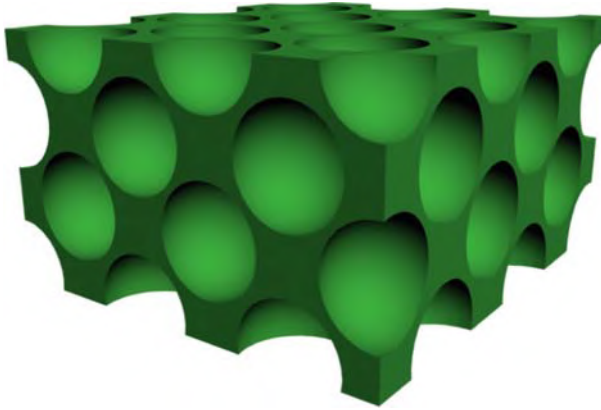


Fig. 1.8. 3D PhC with inverted FCC lattice

material between spheres (TiO_2) is 2.8 and it is too small to form the complete PBG. However, when silica is used as the bulk material, the appearance of the complete PBG is possible at some geometric parameters.

In 2000, the first 3D PhC which had the complete PBG within near infrared range was obtained [8]. Such a PhC consisted of silicon spheres arranged in a diamond lattice.

Starting from 1987 and till 2005 more than 10,000 printed works dedicated to PhCs and PhC-based devices were published. However, the serial production now is available only for microstructured fibers which possess unique properties and the possibility to manage the parameters and characteristics within wide range and 1D PhCs which are produced in the form of distributed Bragg reflectors of vertical cavity surface emitting lasers or in form in the form of fiber Bragg gratings.

In spite of quite undeveloped technology for production of 2D and 3D PhCs, there exist a number of optoelectronics directions such structures can be applied to. The most important are the spontaneous radiation management, optical insulators, nonlinear elements and microstructured fibers. Let us consider each of these directions in detail.

- Spontaneous radiation management [3–9]. This property of PhCs was predicted on dawn of PhCs and it plays important role for the design of light sources on the basis of PhCs. For instance, PhCs can be used to increase the efficiency and to lower the threshold current of semiconductor lasers. 1D, 2D or 3D PhCs can also take a function of distributed reflector [10–15]. The second way to use the PhC as the element for the spontaneous radiation management is the design of principally new radiation sources [16–19]. In such sources, both pure PhCs and PhCs with defects which form high-quality resonators and provide strong radiation localization inside the defect can be used for spontaneous radiation management and improvement

of laser characteristics [9, 20–25]. Depending on what type of PhC is used (with or without the defect), the source can be monochromatic or polychromatic, i.e., lasers or light-emitting diodes [26–35].

- Optical insulators. Utilization of the PhC as an optical insulator, as a rule, is reduced to the utilization of the PhC possibility to localize the radiation inside the defect of the periodic structure. At that, the radiation wavelength must lie inside the PBG of the PhC. Main devices which can be developed on the basis of such a PhC property are microcavities [36–43], waveguides [44–55] and sharp waveguide bends [56–65], splitters [66–73], couplers [74–82] and combiners [83–89]. Main function of microresonators is based on the possibility of the PhC to localize the radiation inside the defect area of the periodic structure. In fact, the defect can be represented by the shift, variation of the parameters or missing of some elements or group of elements.
- PhC waveguides [36, 44–55] are represented by so-called linear defects of periodic structure. Such linear defects possess waveguiding properties within quite a wide range of wavelengths. One of the unique PhC waveguide properties is the possibility to form very sharp bends under the angle up to 90° [90–98] and even more [99–106]. In contrast to planar waveguides, the principle of which is based on the total internal reflection, the PhC waveguides localize the light due to the presence of the complete PBG. Thus, waveguide bend made on the basis of linear defect has higher efficiency and is much more compact than that on the basis of planar waveguide.
- Splitters represent a class of optical devices which allow dividing an optical power in given proportion or splitting it into polarized beams [66–73], [107–110]. The PhC-based splitter can be represented by a number of optical waveguides connected at a single point. In this case, the power passing from the input waveguide is divided at the connection point. Another type of splitter is based on coupling of parallel waveguides with low distance between them [111–113]. The radiation from one waveguide smoothly flows from the input waveguide to the output one. Varying waveguide parameters, one can easily vary a portion of power to be transmitted to the output waveguide.
- Dispersion management [114, 115]. A unique dispersion property of the PhC allows to use them as super-prisms [116–120], super-lenses [121–125], multiplexers and demultiplexers [126–130].
- When investigating the super-prism-effect, the PhC is considered as a bulk media. At that it possesses some effective refractive index which strongly depends on the PhC geometry and the radiation wavelength. In some cases, the refractive index can be negative [75, 131–135].
- Super-lens effect [121–125] allows to use the PhC in order to focus an optical radiation. Moreover, dispersion properties of PhCs allow to create compact and highly-efficient wavelength division demultiplexers [126–130]. The wavelength division demultiplexer allows to separate information channels which are transmitted at different wavelengths over a single waveguide

channel. The PhC-based demultiplexer will be a compact one because the PhC waveguides and waveguide bends size is of order of the wavelength. Moreover, the channel's density can be dramatically increased if necessary in comparison to commonly used demultiplexers on the basis of dispersion elements.

- Nonlinear elements [136–141]. The introduction of nonlinear materials into the periodic structure can cause the appearance of very interesting and unexpected effects. Nonlinear materials change their refractive index under high intensity radiation passing over them. Such variations of the refractive index can cause essential variation of device fundamental characteristics. These possibilities give rise to a new class of optical devices such as optical information storage elements [142–146], logical elements [147–150] and optical power limiters [138–153]. Discrete optical solitons [154–156] inside the nonlinear PhC may be used for information storage. Such solitons managed by the radiation allow to implement the information writing and reading. A principle of the optical logical elements is based on the fact that the power of a single optical signal is not enough to essentially change the structure properties. However, when two signals incident the nonlinear structure, the refractive index variation appears such that the optical properties of the whole PhC are changed as well, particularly, transmittance and reflectance. At that, some situations may happen. The first one, when the optical gate was closed at low radiation intensity and it opens at high intensity, thus implementing AND gate. The second case is vice versa. At low radiation intensity, the gate is opened and the growth of the intensity leads to the gate closure. This situation is for AND-NOT gate.
- Optical power limiters [151–153] can be used to avoid the optical sensors damage due to the high intensity radiation and for the normalization of the optical source intensity at the input of the optical circuit. Their principle consists of the growth of the reflectance of the nonlinear PhC structure with the radiation intensity. At that, the output optical intensity stays constant.
- Microstructured fibers [157–173]. Such optical fibers consist of finite-size PhC with one or several defects introduced to the center. The radiation is concentrated inside the defect. There are two different types of microstructured fibers. The first one is based on the effect of total internal reflection. In this case, the PhC represents the reflecting cladding with lower refractive index. Such fibers are usually singlemode within wide wavelength range in contrast to ordinary step-index fibers. The principle of the second type of microstructured fibers is based on the radiation localization inside the defect due to the complete PBG. Such fibers are usually multimode, however, they allow to localize high radiation power inside the defect area. Thus, they can be used for transmittance of high radiation power and for achievement of some nonlinear effects. Currently, a variety of applications devices is proposed and implemented, which utilize unique properties of microstructured fibers [174–200].

- Slow light is another important application which is being extensively developed [16–18]. It employs PhC's ability to possess ultra-low group velocity at specific wavelength. The devices based on slow-light effect can be used as photonic routers in transparent optical networks, low modal volume microlaser, optical delay lines, etc.

1.5 Problems and Questions

Problem 1.1. Describe similarities and differences between solids and photonic crystals.

Problem 1.2. Give the definition of the photonic band gap.

Problem 1.3. Describe the lattice structure of square and hexagonal crystals.

Problem 1.4. Describe the different kinds of 3D PhC lattices.

Problem 1.5. Characterize the main terms used for band structure description.

Problem 1.6. What happens to radiation which possesses complex wave vector?

Problem 1.7. Describe the opal structure and its band structure.

Problem 1.8. Describe the inverted opal structure and its band structure.

Problem 1.9. Give examples of PhCs application in passive components of optical systems.

Problem 1.10. Specify examples of the elements controlling optical radiation which are based on PhCs.

Fundamentals of Wave Optics

Summary. Chapter 2 discusses the basics of wave optics and briefly introduces the reader into the wave propagation in an optical medium, which simplifies the study of the material presented in following chapters. Such terms as optical medium and its theoretical description are described shortly. The Maxwell's equations are written and principal conception of plane wave propagation is discussed. Then, optical wave behavior in a dielectric medium is considered by means of general solution of the wave equation and such crucial parameters as polarization, refractive index and group velocity are considered.

2.1 What is an Optical Medium? – Theoretical Models

The interaction between electromagnetic field and medium is the main question for understanding of fundamentals of optical wave propagation in waveguides and operation of many other passive and active optical devices.

Discussion of the optical wave fundamentals should consist of the following questions: what optical medium is; what properties the medium has; how optical medium influences electromagnetic field; and, at last, how to describe the electromagnetic field and its interaction with optical medium. Generally, that problem is illustrated in Fig. 2.1 where the spherical electromagnetic wave irradiated from the point source incidents the object. To solve the problem of their interaction, we should characterize the field inside and outside the medium placed in the free space, taking into account its modification at the boundary of the object.

The distances between atoms are one of the key points in characterization of interaction with light. In optical devices and optical structures the thickness of layers in case of layered structure or elements size in case of PhC can be comparable with the wavelength. In such a case, interaction of light with the medium may have different effects like transparency, total or partial reflections and refraction. In optical media used in lightwave technology, the distance between atoms is of the order of 0.1 nm, which is small compared to the wavelength of light that is used in optical communications (these

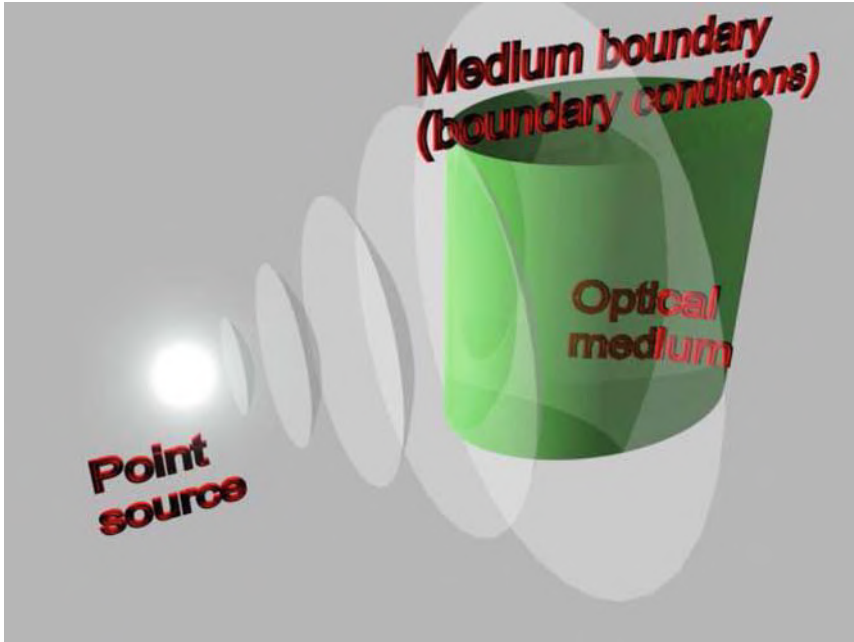


Fig. 2.1. Problem of interaction between EM field radiated from the point source and optical medium

wavelengths are in range of $0.8\text{--}1.6\ \mu\text{m}$). With this, the medium is assumed to be a homogeneous medium. Moreover, in many cases, optical medium can be assumed to be isotropic and time invariant. Hereafter, it will be assumed that the properties of an optical medium are described by the permittivity ε , the permeability μ and the conductivity σ .

In special cases, an optical medium has nonlinear response to an external influence. Nonlinear effects like second harmonic generation, Kerr effect, solitons and vortices formation, etc., plays a more important role in advanced optoelectronics and photonics.

2.1.1 Wave Optics

When ε , μ and σ for the material are defined, then Maxwell's equations solution is a good starting point for analyzing the propagation of light also known as the wave optics. The wave optics provides, particularly, the problem solution of electromagnetic waves propagation in optical waveguides, namely, determination of the electric and magnetic components' amplitudes of the optical field, as well as its phase and amplitude distribution in space. If the thickness of the core of the optical waveguide is of the order of the wavelength, then the propagation can be described with a few modes which are functions of the optical waveguide parameters and the wavelength of the light. If, on

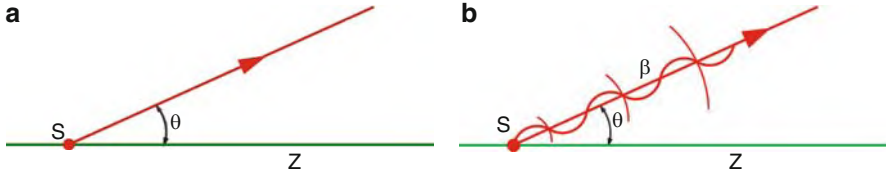


Fig. 2.2. Optical radiation representation in the geometrical (a) and wave (b) optics

the other hand, the core radius is large as compared to the wavelength, then many propagating modes appear. In this case, it will be more effective to solve the problem by means of geometric optics.

2.1.2 Geometric Optics

When dimensions of objects are large compared to the wavelength of the light, an approximate method can be used to study the light propagation. The geometric optics or ray optics uses the methods of geometry in order to formulate the laws of optics. In geometric optics the concept of light rays is introduced in order to describe optical phenomena. The paths taken by the light rays in heterogeneous and compound media are derived from the so-called eikonal equation [201].

Figure 2.2 schematically shows correspondence of both methods. The light irradiated from the point source can be represented like a ray (light beam shown on the Fig. 2.2a) directed angularly from the point source with the angle θ to the optical axis z . This angle θ corresponds to the propagation vector β , which has the same angle to the axis (see Fig. 2.2b) and characterizes the direction of wave propagation with the same angle θ and its phase. The propagation vector is perpendicular to the constant phase surfaces of the propagating wave which are marked by concentric arcs with the center in the point S.

2.2 Wave Propagation: Maxwell's Equations

Light consists of an electric field and magnetic field that oscillate at very high rates, of the order of 10^{14} Hz. This field propagation is described by periodical functions. Transfer of electromagnetic wave energy through empty space is realized by electric and magnetic fields which exchange the energy obeying Ampere's and Faraday's laws. Magnetic field variation is perpendicular to the electric field. A single frequency electromagnetic wave exhibits harmonic variation of electric and magnetic fields in space. In any fixed location, the field amplitude varies with optic frequency. The magnitude of the field repeats itself after one period of the oscillation. The wave repeats itself in space after a distance λ called wavelength which is actually spatial period of the wave. The reciprocal quantity is called wave number.

Within the classic theory, all the electromagnetic phenomena are described by the system of Maxwell's equations which gives the time dependence of electric and magnetic fields and their interaction with optical medium.

Before discussing light propagation in complex optical structures such as PhCs, we consider its propagation in free space. For a medium with free charges and with current, Maxwell's equations are taken in the following form

$$\nabla \times \mathbf{E} = -\frac{\partial \mathbf{B}}{\partial t}, \quad (2.1)$$

$$\nabla \times \mathbf{H} = \mathbf{J} + \frac{\partial \mathbf{D}}{\partial t}, \quad (2.2)$$

$$\nabla \cdot \mathbf{D} = \rho, \quad (2.3)$$

$$\nabla \cdot \mathbf{B} = 0, \quad (2.4)$$

where t denotes the time, ∇ is the nabla operator, “ \cdot ” and “ \times ” denotes scalar and vector products. In Cartesian coordinates,

$$\nabla = \mathbf{x} \frac{\partial}{\partial x} + \mathbf{y} \frac{\partial}{\partial y} + \mathbf{z} \frac{\partial}{\partial z},$$

where $\mathbf{x}, \mathbf{y}, \mathbf{z}$ are unit vectors. The vectors \mathbf{E} and \mathbf{H} are the coordinate- and time-dependent vectors of electric and magnetic fields, respectively, \mathbf{D} and \mathbf{B} are corresponding dielectric displacement and magnetic inductance. The sources of the electromagnetic field are the charge density ρ and the current density \mathbf{J} . They are connected by the continuity equation, which is given by taking divergence of (2.2) and using (2.3) and the relation $\nabla \cdot \nabla \times \mathbf{H} = 0$:

$$\nabla \cdot \mathbf{J} = -\frac{\partial \rho}{\partial t}.$$

In case of nonconductive medium like silica or other material used for optical waveguiding in passive devices like optical fiber or planar waveguide, $\mathbf{J} = 0$ and $\rho = 0$. The flux densities are related to the field vectors by the material relations

$$\mathbf{D} = \varepsilon_0 \mathbf{E} + \mathbf{P}, \quad (2.5)$$

$$\mathbf{B} = \mu_0 \mathbf{H} + \mathbf{M}, \quad (2.6)$$

where

$$\varepsilon_0 = 8.85 \cdot 10^{-12} - \left[\frac{As}{Vm} \right]$$

is the electric constant,

$$\mu_0 = 4 \cdot 10^{-7} \left[\frac{Vs}{Am} \right]$$

is the magnetic constant, \mathbf{P} is the electric polarization of the medium induced by the electric field \mathbf{E} in the medium and \mathbf{M} is the magnetic polarization of

the medium. For optical fibers $\mathbf{M} = 0$ because of the nonmagnetic nature of silica glass. The product of constants ε_0 and μ_0 is equal to

$$\varepsilon_0 \cdot \mu_0 = 1/c^2, \quad (2.7)$$

where $c \approx 3 \cdot 10^8$ m/s is the light speed in vacuum. The concept of \mathbf{P} will be explained below. The response of individual electric charges to an electric field can be described by Newton's laws. The behavior of a charged fluid has a field description that will not be discussed here. The behavior of many solids in response to an electric field can be described well with the same kind of approximation which are usually made for stress and strain. If we think of stress as the perturbation applied to a sample and the strain as the response of the sample to the perturbation, we can say that in our model the response is proportional to the perturbation. The response of many common solids to an applied electric field is such that the electric field inside the sample is less than the applied one. It is similar to the solid that has produced its own charge distribution, i.e., becomes polarized, so that it produces an electric field which is added in opposition to the applied field. Materials which possess such properties are called dielectrics.

We consider the polarization of the material as the response in this case. It turns out that in many useful situations the polarization is proportional to the applied electric field. We need to define the polarization in a way that allows us to measure it.

Evaluation of the electric polarization \mathbf{P} requires a microscopic quantum mechanical approach. Although such an approach is essential when the optical frequency is near a medium resonance, a phenomenological relation between \mathbf{E} and \mathbf{P} can be used far from the medium resonance. This is the case for optical fibers at the wavelength region $0.5 - 2 \mu\text{m}$, a range that covers the low-loss region of optical fibers and is of interest for fiber-optic communication systems. In a homogeneous linear and isotropic dielectric medium, which are considered in the book, polarization is aligned with and proportional to the electric field \mathbf{E} . In an anisotropic material, the polarization and the field are not necessarily in the same direction. In general, the relation between \mathbf{E} and \mathbf{P} can be nonlinear. Although the nonlinear effects in optical waveguides deserve consideration according to [202], they can be ignored in a following description of fiber modes.

Electromagnetic waves carry energy as they travel through empty space. There is an energy density associated with both the electric and magnetic fields. The amount of energy transport per unit area is described by the vector

$$\mathbf{S} = \frac{1}{\mu_0} \mathbf{E} \times \mathbf{B}, \quad (2.8)$$

which is called the Poynting vector. This expression is a vector product, and since the magnetic field is perpendicular to the electric field, \mathbf{S} will be perpendicular to \mathbf{E}, \mathbf{B} - plane and coincides with a wave propagation direction.

2.3 Wave Equation in Vacuum

In a vacuum, there is no medium. As a result, there is no induced polarization or current. In other words, both \mathbf{P} and \mathbf{J} are equal to zero. Therefore, the Maxwell's equations are reduced to

$$\nabla \times \mathbf{E} = -\frac{\partial \mathbf{B}}{\partial t}, \quad (2.9)$$

$$\nabla \times \mathbf{H} = \frac{\partial \mathbf{D}}{\partial t}, \quad (2.10)$$

$$\nabla \cdot \mathbf{D} = 0, \quad (2.11)$$

$$\nabla \cdot \mathbf{B} = 0. \quad (2.12)$$

Four equations (2.1)–(2.4) describe the interdependence between \mathbf{E} and \mathbf{H} . To solve the set of equations (2.9)–(2.12) one can eliminate \mathbf{H} and derive an equation for \mathbf{E} only. Taking the curl of $\nabla \times \mathbf{J}$ and employing the material equation (2.6) gives

$$\nabla \times \nabla \times \mathbf{E} = \nabla \times \left(-\frac{\partial \mathbf{B}}{\partial t} \right) = -\varepsilon_0 \mu_0 \frac{\partial^2}{\partial t^2} \mathbf{E}, \quad (2.13)$$

since

$$\nabla \times \left(-\frac{\partial \mathbf{B}}{\partial t} \right) = -\frac{\partial}{\partial t} (\nabla \times \mu_0 \mathbf{H}) = -\mu_0 \frac{\partial}{\partial t} (\nabla \times \mathbf{H}) = -\varepsilon_0 \mu_0 \frac{\partial^2}{\partial t^2} \mathbf{E}.$$

Vector calculus gives the identity

$$\nabla \times \nabla \times \mathbf{E} = \nabla (\nabla \cdot \mathbf{E}) - \nabla^2 \mathbf{E} = -\nabla^2 \mathbf{E}. \quad (2.14)$$

Here,

$$\nabla^2 = \frac{\partial^2}{\partial x^2} + \frac{\partial^2}{\partial y^2} + \frac{\partial^2}{\partial z^2}$$

is the Laplace operator and equation (2.5) was used which gives $\nabla \cdot \mathbf{E} = \nabla \cdot (\varepsilon_0 \mathbf{D}) = \varepsilon_0 \nabla \cdot \mathbf{D} = 0$. Therefore, the wave equation for the electric field in vacuum is

$$\nabla^2 \mathbf{E} - \frac{1}{c^2} \frac{\partial^2}{\partial t^2} \mathbf{E} = 0. \quad (2.15)$$

The similar wave equation can be obtained for magnetic component by eliminating \mathbf{E} from equations (2.9)–(2.10). The general form of the solution of the Eq. (2.15) has the form:

$$E(x, y, z, t) = a_+ E^+(\mathbf{k} \cdot \mathbf{r} - \omega t) + a_- E^-(\mathbf{k} \cdot \mathbf{r} + \omega t), \quad (2.16)$$

where $\mathbf{r} = (x, y, z)$ is the coordinate vector, $\mathbf{k} = (k_x, k_y, k_z)$ is the wave vector, $\omega = 2\pi/\lambda$ is the angular frequency and λ is the wavelength. Functions E^+

and E^- describe the wave behavior in space (argument $\mathbf{k} \cdot \mathbf{r}$) and time (argument ωt), and a_+ and a_- are amplitude coefficients depending on boundary conditions.

A wave vector is a vector which specifies the wavenumber and direction of propagation of the wave. The magnitude of the wave vector indicates the wavenumber. The orientation of the wave vector indicates the direction of wave propagation. Wavenumber indicates the number of electric and magnetic vectors oscillations per unit of space and is measured in m^{-1} . Components of the wave vector corresponds to the wave numbers in x , y and z directions as follows

$$\frac{\omega^2}{c^2} = k_x^2 + k_y^2 + k_z^2. \quad (2.17)$$

The physical meaning of the wave solution given by (2.16) can be understood as follows. First, let us consider the special case when $k_x = k_y = 0$. In this case the argument $(\mathbf{k} \cdot \mathbf{r} - \omega t)$ is reduced to

$$k_x r_x - \omega t = k_x \left(r_x - \frac{\omega}{k_x} t \right).$$

This means that the wave E^+ is a wave propagating in positive \mathbf{k} direction at velocity of ω/k_x . Similarly, E_- represents a wave propagating in negative \mathbf{k} direction. In general, when all components of the wave vector are non-zero, wave propagates in \mathbf{k} direction with a velocity of light. The special case is important for understanding of wave propagation and for practical applications in wave equation solution (2.15) in case when the field has only one component. This solution is called the plane wave. This case is described as

$$E(x, y, z, t) = E e^{j(\omega t - k_z \cdot z)} \mathbf{x}. \quad (2.18)$$

Here, the electric field has only one component in the x -direction and propagates in the z -direction. Figure 2.3 shows a plane sine wave in two dimensions. The large arrow is a wave vector, which defines the direction of wave propagation by its orientation perpendicular to the wave fronts. As in case of spherical wave shown on the Fig. 2.2 the wave fronts of the plane wave are constant phase plane surfaces separated by one wavelength. The evolution time of the wave is defined by a term (ωt) . For a plane sine wave, the formula (2.18) is transformed to

$$E(x, y, z, t) = \sin(\mathbf{k} \cdot \mathbf{r} - \omega t) = \sin(k_x x + k_y y + k_z z - \omega t).$$

If we assume that a wave front is a line along the comb of the wave, then the wave fronts are lines or surfaces of constant phase, and the equation defining a wave front is simply $\mathbf{k} \cdot \mathbf{r} = \text{const}$. For one dimensional propagation of light just along the x axis we obtain the scalar wave number

$$k_x = \frac{\omega}{c} = \frac{2\pi}{\lambda}. \quad (2.19)$$

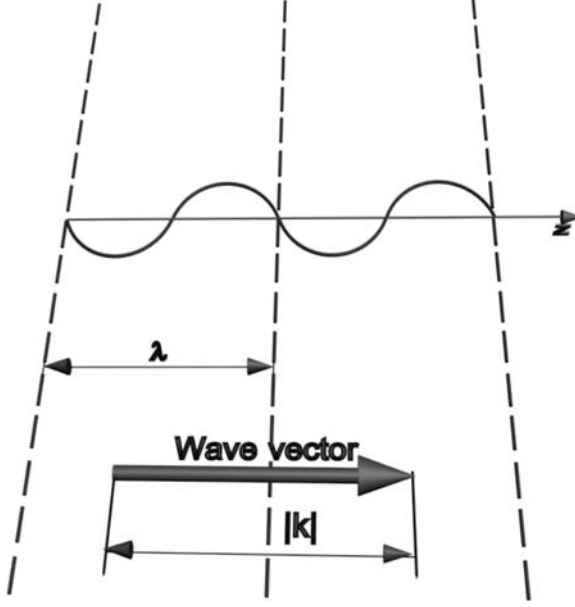


Fig. 2.3. Plane sine wave definition

Substituting electric field equation (2.18) into (2.9) and integrating over time, we obtain:

$$\mathbf{H} = \frac{k}{j\mu_0\omega} E_x e^{j(\omega t - k_z \cdot z)} \mathbf{y} = -j \sqrt{\frac{\epsilon_0}{\mu_0}} E e^{j(\omega t - kz)} \mathbf{y}. \quad (2.20)$$

Thus, both the electric field and magnetic fields are perpendicular to the wave propagation.

2.4 Waves in Dielectric Media

In a dielectric medium, a nonzero polarization \mathbf{P} is induced by an external electric field \mathbf{E} . To understand the physical meaning of \mathbf{P} , we consider a medium made of positive and negative charges (e.g., protons and electrons). When an electric field is present, it separates the positive and negative charges. This charge separation results in an additional electric field. This additional electric field is called the induced polarization.

Various media respond differently to a given external electric field. When the medium is linear and isotropic, \mathbf{P} is linearly proportional to \mathbf{E} and can be expressed as

$$\mathbf{P} = \epsilon_0 \cdot \chi \mathbf{E}, \quad (2.21)$$

where χ is called the electric susceptibility. It is the proportion coefficient between polarization and electric field.

Linear susceptibility is, in general, a second-rank tensor but reduces to a scalar for an isotropic medium such as silica glass. Optical fibers become slightly birefringent because of unintentional variations in the core shape or in local strain. In general, the susceptibility is a function of the frequency ω of the applied field. When the field is an arbitrary function of time t , the polarization is a convolution of the Fourier transform of $\chi(\omega)$ with the $\mathbf{E}(t)$. This reflects the fact that the dipoles in the material cannot respond instantaneously to the applied field, and causality considerations lead to the Kramers–Kronig relations.

With this definition, the electric displacement is

$$\mathbf{D} = \varepsilon_0 \mathbf{E} + \mathbf{P} = \varepsilon_0 \varepsilon \mathbf{E}, \quad (2.22)$$

where

$$\varepsilon = 1 + \chi \quad (2.23)$$

is called the dielectric constant or the relative permittivity of a dielectric material. The dielectric constant of a material affects how electromagnetic signals (light, millimeter-waves, etc.) move through the material. A high value of dielectric constant makes the distance inside the material look bigger. This means that light travels more slowly. It also compresses the waves to behave as if the signal had a shorter wavelength.

2.4.1 Refractive Index of Dielectric Medium

For an electromagnetic field in a dielectric medium without current, Eq. (2.10) reduces using (2.22) to

$$\nabla \times \mathbf{H} = \varepsilon \varepsilon_0 \frac{\partial \mathbf{E}}{\partial t}. \quad (2.24)$$

Using the same procedure described earlier for Eq. (2.15), the wave equation for the electric field is

$$\nabla^2 - \frac{\varepsilon}{c^2} \frac{\partial^2 \mathbf{E}}{\partial t^2} = 0. \quad (2.25)$$

Therefore, the only difference of this equation from (2.15) is that the wave propagation velocity changes from c to c/n , where $n = \sqrt{\varepsilon}$ is the refractive index of the medium. Consequently, the refractive index of a medium is a measure for how much the speed of light (or other waves) is reduced inside the medium.

2.4.2 Lossy Dielectric Medium

The current term in the wave equation can be included to represent the power loss during wave propagation. In this case, the induced current is related to the electric field by $\mathbf{J} = \sigma \mathbf{E}$, where σ is the conductivity. If the electric

field has a time dependence $e^{j\omega t}$, the induced current density also has the same time dependence. Therefore, this current effect is included in the electric susceptibility as follows. From (2.2),

$$\mathbf{J} + \frac{\partial \mathbf{D}}{\partial t} = \frac{\partial}{\partial t} \left(\frac{\mathbf{J}}{j\omega} + \mathbf{D} \right) = \frac{\partial}{\partial t} (\varepsilon \mathbf{E}), \quad (2.26)$$

with the dielectric constant ε .

In general, $\varepsilon(r, \omega)$ is complex. Its real and imaginary parts correspond to the refractive index n and the absorption coefficient α by the definition [202]

$$\varepsilon = (n + j\alpha c/2\omega)^2, \quad (2.27)$$

By using (2.26) and (2.27), n and α are related to χ as

$$n = (1 + \text{Re}\{\chi\})^{1/2}, \quad (2.28)$$

$$\alpha = (\omega/nc) \text{Im}\{\chi\}, \quad (2.29)$$

where Re and Im stand for the real and imaginary parts, respectively. Both n and α are frequency dependent. The imaginary part of the refractive index represents either losses (if negative) or gain (if positive). The frequency dependence of n is referred to as chromatic dispersion. In case of losses present in medium, the radiation exponentially decays as shown in Fig. 2.4.

If \mathbf{D} is substituted in (2.2) from (2.5), the wave equation for the electric field is reduced to

$$\nabla \mathbf{E} - \frac{1}{c^2} \frac{\partial^2}{\partial t^2} \mathbf{E} = \mu_0 \frac{\partial^2}{\partial t^2} \mathbf{P}. \quad (2.30)$$

Using the Fourier transform of $\mathbf{E}(\mathbf{r}, t)$ formula (2.31)

$$\tilde{\mathbf{E}}(\mathbf{r}, \omega) = \int \mathbf{E}(\mathbf{r}, t) \exp(j\omega t) dt \quad (2.31)$$

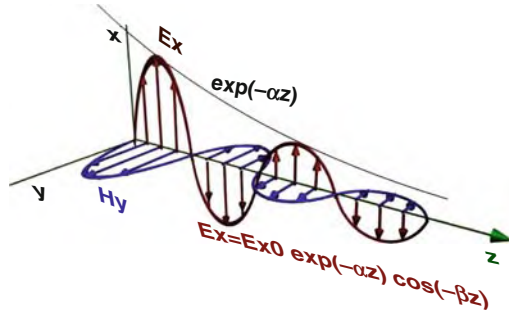


Fig. 2.4. Wave in lossy dielectric medium

and similar relation for $\mathbf{P}(\mathbf{r}, t)$ together with (2.7), one can write wave equation (2.15) in the frequency domain

$$\nabla \times \nabla \times \tilde{E} = -\varepsilon(\mathbf{r}, \omega) \frac{\omega^2}{c^2} \tilde{E}, \quad (2.32)$$

with the frequency-dependent permittivity

$$\varepsilon(\mathbf{r}, \omega) = 1 + \tilde{\chi}(\mathbf{r}, \omega) \quad (2.33)$$

and $\tilde{\chi}(\mathbf{r}, \omega)$ is the temporal Fourier transform of $\chi(\mathbf{r}, t)$. In term of frequencies the wave equation can be obtained as

$$\nabla^2 \tilde{E} + n^2(\omega) k_0^2 \tilde{E} = 0, \quad (2.34)$$

where the free-space wave number k_0 is defined as

$$k_0 = \omega/c = 2\pi/\lambda_0 \quad (2.35)$$

and λ_0 is the vacuum wavelength of the optical field oscillating at the frequency ω . Equation (2.34) is solved next to obtain the optical modes.

2.5 Group Velocity

The concept of group velocity is important for understanding lightwave propagation and quantifying fiber dispersion. In general, there are two different velocities: group velocity and phase velocity. To see the meanings of these velocities, let us first consider a traveling wave of the following form:

$$E(t, z) = E_0 \cos(\omega_0 t - \beta z). \quad (2.36)$$

Its Fourier transform with respect to time is

$$E(\omega, z) = E_0 \pi [\delta(\omega - \omega_0) e^{-j\beta z} + \delta(\omega + \omega_0) e^{j\beta z}]. \quad (2.37)$$

This means that a plane wave has a constant frequency. This constant frequency wave is called a monochromatic wave and is also called a continuous wave (CW). In this case, the phase velocity is defined as

$$v_p = \frac{\omega_0}{\beta}. \quad (2.38)$$

Thus, phase velocity is the velocity of a constant phase plane that moves in the propagation direction.

For the plane wave considered, its amplitude or power is constant over the entire space, time- and position-independent. In other words, one cannot tell

“where” the wave is. Actually, it is everywhere. On the other hand, for two plane waves with a little difference in frequency and wave number,

$$E(t, z) = E_0 \cos(\omega_1 t - \beta_1 z) + E_0 \cos(\omega_2 t - \beta_2 z), \quad (2.39)$$

after trigonometric transformations, takes form:

$$E(t, z) = 2E_0 \cos(\Delta\omega t/2 - \Delta\beta z) \cos(\bar{\omega} t - \bar{\beta} z), \quad (2.40)$$

where $\Delta\omega = \omega_2 - \omega_1$ and $\Delta\beta = \beta_2 - \beta_1$ are assumed to be small, compared to $\bar{\omega} = (\omega_1 + \omega_2)/2$ and $\bar{\beta} = (\beta_1 + \beta_2)/2$, respectively. Thus, the envelope of the combined wave has a velocity

$$v_g = \frac{\Delta\omega}{\Delta\beta}. \quad (2.41)$$

This is called the group velocity. As the derivation shows, it means the propagation velocity of energy.

The concept of group velocity can be generalized from the two monochromatic waves to a “Wave packet”. This form gives a possibility to represent the group velocity like

$$v_g = \frac{\partial\omega}{\partial\beta}. \quad (2.42)$$

The above presentation shows that each component at a different frequency travels at the same speed of v_g . In other words, the wave packet or its amplitude travels at the group velocity v_g .

2.6 Summary

1. Electromagnetic waves are described by a wave equation arising from Maxwell’s equations. Electromagnetic waves provide energy transport described by the Poynting vector.
2. In general, in a homogeneous linear and isotropic dielectric medium, the polarization is aligned with and proportional to the electric field \mathbf{E} . In an anisotropic material, the polarization and the field are not necessarily in the same direction.
3. The phase velocity is the velocity of constant phase plane.
4. The group velocity is the velocity of the energy propagation.
5. A wave vector is a vector which specifies the wavenumber and direction of propagation for a wave. The magnitude of the wave vector indicates the wavenumber. The orientation of the wave vector indicates the direction of wave propagation. Wavenumber is a measure of the number of repeating units of a propagating wave per unit of space and is measured in m^{-1} .
6. The refractive index of a medium is a measure for how much the speed of light (or other waves) is reduced inside the medium.

2.7 Problems and Questions

Problem 2.1. What is permittivity of the medium?

Problem 2.2. How the refractive index is connected to permittivity?

Problem 2.3. Derive the wave equation from the Maxwell's equations in vacuum.

Problem 2.4. Derive the frequency domain Helmholtz equation in dielectric medium.

Problem 2.5. Show that Maxwell's equation $\nabla \times \mathbf{E} = -\partial B/\partial t$ and $\nabla \cdot \mathbf{E} = 0$ are consistent, i.e., they do not contradict each other.

Problem 2.6. Explain terms “plane wave” and “polarization”.

Problem 2.7. Search out the magnetic strength H for nonuniform plane wave in a medium with parameters ε and μ , if the electric strength is given by: $E_y = E_0 \exp(i(\omega t - k_z \cdot z) - k_x \cdot x)$, $E_x = E_y = 0$.

Fundamentals of Computation of Photonic Crystal Characteristics

Summary. Chapter 3 gives solutions for simplest problems such as calculation of field distribution and reflectance spectrum for one-dimensional (1D) photonic crystal. Starting from the Maxwell's equations for dielectric nonmagnetic structure, we show the derivation of the Helmholtz equation and find its solution for 1D layered structure. In addition, the boundary conditions and equation transformation to set of linear equations which are solved using Cramer's method are described thoroughly. This mathematical technique is then applied for computation of the reflectance spectra of 1D perfectly periodic structure and structures with different defects. These results can be easily applied for design of VCSELs, DFBs, or optical demultiplexers. At the end of the chapter the example of an original Matlab program for computation of reflectance spectrum of 1D user-defined layered structure is presented and several problems and questions for self-training are given.

3.1 Computation of the Field Distribution in One-Dimensional (1D) Photonic Crystal

The best understanding of physical properties of periodic structures when they are irradiated by the radiation of the specific wavelength can be given by consideration of the simplest case of the field distribution computation in an arbitrary layered structure. An arbitrary layered structure denotes the structure represented by a number of dielectric layers with arbitrary values of thickness and permittivity. At that, the structure is strictly uniform within a single layer.

In order to start the computation of the 1D structure characteristics, it is first necessary to derive the wave equation from the system of Maxwell's equations as was shown in Chap. 2. We restrict ourselves to the simplest case of isotropic and non-conductive media. Moreover, we consider non-magnetic

media only. With this, we consider the corresponding Maxwell's equation (2.24). The material equations for non-magnetic medium take the following form:

$$\begin{aligned}\mathbf{B}(\mathbf{r}, t) &= \mu_0 \mathbf{H}(\mathbf{r}, t), \\ \mathbf{D}(\mathbf{r}, t) &= \varepsilon_r(\mathbf{r}) \varepsilon_0 \mathbf{E}(\mathbf{r}, t),\end{aligned}\tag{3.1}$$

where μ is the vacuum permeability, and ε_r and ε_0 are the relative permittivity and electric constant. As long as we suppose the medium to be non-magnetic, its relative permeability is equal to 1. Thus, the selected form of the equations pair is written down for the medium which is susceptible to the electric field and unsusceptible to the magnetic field.

Writing the equations in the abovementioned form, we completely determined the variations of environment parameters. For instance, within our model we will not be able to consider magnetic properties of the medium as well as its anisotropy.

First, we will substitute the material equations to Maxwell's equations to obtain the system without electric displacement and magnetic inductivity.

$$\begin{aligned}\nabla \times \mathbf{E}(\mathbf{r}, t) &= -\frac{\partial \mu_0 \mathbf{H}(\mathbf{r}, t)}{\partial t}, \\ \nabla \times \mathbf{H}(\mathbf{r}, t) &= \frac{\partial \varepsilon_r(\mathbf{r}) \varepsilon_0 \mathbf{E}(\mathbf{r}, t)}{\partial t}.\end{aligned}\tag{3.2}$$

Taking curl from both left and right sides of the first equation, we substitute the second equation into the first one to obtain the following relation:

$$-\nabla \times \nabla \times \mathbf{E}(\mathbf{r}, t) = \varepsilon_r(\mathbf{r}) \mu_0 \varepsilon_0 \frac{\partial \mathbf{E}(\mathbf{r}, t)}{\partial t^2}.\tag{3.3}$$

Taking into account relation (2.14), the wave equation can be written in the following form:

$$\Delta \mathbf{E}(\mathbf{r}, t) + \frac{\varepsilon_r(\mathbf{r})}{c^2} \frac{\partial \mathbf{E}(\mathbf{r}, t)}{\partial t^2} = 0,\tag{3.4}$$

where $\Delta = \nabla^2$ is the Laplace operator.

However, the analytic solution of such a non-stationary equation is quite complex. Moreover, in case of propagation of the radiation with constant amplitude, there is no necessity in solution of non-stationary equation. In order to simplify the problem, we will derive the Helmholtz equation. This means that the time derivative should be eliminated. For this reason we represent electric field as the product of the complex amplitude and the time-dependent harmonic function:

$$\mathbf{E}(\mathbf{r}, t) = \mathbf{E}_0(\mathbf{r}) e^{i(\mathbf{k}(\mathbf{r}) \cdot \mathbf{r} + \omega \cdot t)} = \mathbf{E}_0(\mathbf{r}) e^{i(\mathbf{k}(\mathbf{r}) \cdot \mathbf{r})} e^{i(\omega \cdot t)},\tag{3.5}$$

where \mathbf{k} is the radiation wave vector and ω is the radiation angular frequency.

Substituting the expression for the electric field presented in the form of (3.5) to the wave equation and taking the second time-derivative from

time-dependent harmonic function we obtain the Helmholtz equation in the following form:

$$\nabla^2 \mathbf{E}_0(\mathbf{r}) + \varepsilon_r(\mathbf{r}) \frac{\omega^2}{c^2} \mathbf{E}_0(\mathbf{r}) = 0. \quad (3.6)$$

The Helmholtz equation does not contain time-dependent functions. By solving this equation, it is possible to find the reflectance and transmittance of the finite structure, as well as the field distribution and eigen-frequencies of an infinite structure.

Let us now consider a finite 1D layered structure. The description of the radiation propagation inside such a structure can be found by the solution of the Helmholtz equation presented in the following form:

$$\frac{\partial^2 E_z(x)}{\partial x^2} + \varepsilon_r(x) \frac{\omega^2}{c^2} E_z(x) = 0. \quad (3.7)$$

Here we have the coordinate derivative along one direction only because the variation of the permittivity takes place along this direction only. Thus, we consider the case of light propagating perpendicularly to layer-to-layer interface.

After the 1D Helmholtz equation is written down, it is necessary to define the structure and to find out which parameters of this structure will be taken into account and, thus, should be correctly defined. 1D layered structure can be defined by layer thicknesses, their placement and refractive indices. Figure 3.1 depicts an example of the definition of 1D arbitrary layered structure. Each layer has some specific thickness (d_1, d_2, \dots, d_{N-1}) and refractive index (n_1, n_2, \dots, n_{N-1}). The structure is surrounded by material with refractive index $n_0 = n_N$. Arrows indicate forward wave and backward wave inside each layer. Backward waves appear due to the Fresnel reflection from layer-to-layer interface.

Solution of the Helmholtz equation for such a structure consists in determination of amplitudes of forward and backward waves inside each layer.

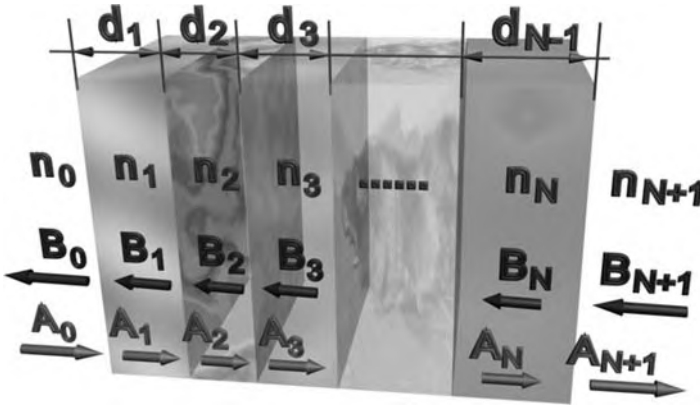


Fig. 3.1. Definition of an arbitrary layered structure

After this, it is possible to obtain the field distribution inside the structure as well as to determine the reflectance and transmittance of the structure.

The general solution of the Helmholtz equation for j -th layer takes the following form:

$$E_j(x) = A_j e^{j \cdot n_j k \cdot x_j} + B_j e^{-j \cdot n_j k \cdot x_j}, \quad (3.8)$$

where A and B are the amplitudes of forward and backward waves correspondingly. As it was shown in Chap. 2, forward and backward waves present in each layer. Their superposition forms the field distribution. However, general solution of the equation is not enough to find wave amplitudes. In order to do this it is necessary to satisfy initial and boundary conditions. In our case, the initial conditions are those ones which determine the radiation source. If the radiation incidents the structure from free space, the initial conditions are defined at the border of the considered computation region. If there are light sources inside the structure (e.g., an active layer) the initial conditions will be defined in the correspondent layer.

Let us consider our case in detail. For instance, the light incidents the structure from free space to the first layer. At that, we assume that after the last interface of the structure there are no more interfaces, hence the reflectance is absent. Thus, as one of the boundary conditions, we can use equivalence to zero of the backward wave amplitude behind the last interface. Moreover, as an initial condition, we are free to choose the amplitude of the forward wave before the first layer, thus, defining the amplitude of the wave which incidents the structure.

As for other boundary conditions, they determine the way how the field distribution functions, or wave functions, are “bonded” at the interfaces. In case of 1D layered structure, we consider the tangential component of the electric field only so boundary conditions are formulated as the equality of wave functions and their first derivatives at the interface:

$$\begin{aligned} E_j(x_j) &= E_{j+1}(x_j), \\ \frac{\partial}{\partial x} E_j(x_j) &= \frac{\partial}{\partial x} E_{j+1}(x_j), \end{aligned} \quad (3.9)$$

where x_j is the coordinate of j -th interface. We now substitute the general solution (3.8) to the expressions (3.9) so the resulting system has the following form:

$$\begin{aligned} A_j e^{j \cdot n_j k \cdot x_j} + B_j e^{-j \cdot n_j k \cdot x_j} &= A_{j+1} e^{j \cdot n_{j+1} k \cdot x_j} + B_{j+1} e^{-j \cdot n_{j+1} k \cdot x_j}, \\ j \cdot n_j \cdot k \cdot A_j e^{j \cdot n_j k \cdot x_j} + j \cdot n_j k \cdot B_j e^{-j \cdot n_j k \cdot x_j} &= \\ = j \cdot n_{j+1} \cdot k \cdot A_{j+1} e^{j \cdot n_{j+1} k \cdot x_j} - j \cdot n_{j+1} k \cdot B_{j+1} e^{-j \cdot n_{j+1} k \cdot x_j}. \end{aligned} \quad (3.10)$$

Writing down such an equation system for each structure interfaces, we obtain the system of linear equations containing $2N + 2$ equations for the structure with N layers. The system contains $2N + 4$ of unknowns.

$$\begin{aligned}
A_0 e^{ikn_0 x_0} + B_0 e^{-ikn_0 x_0} &= A_1 e^{ikn_1 x_0} + B_1 e^{-ikn_1 x_0} \\
ikn_0 A_0 e^{ikn_0 x_0} - ikn_0 B_0 e^{-ikn_0 x_0} &= ikn_1 A_1 e^{ikn_1 x_0} - ikn_1 B_1 e^{-ikn_1 x_0} \\
A_1 e^{ikn_1 x_1} + B_1 e^{-ikn_1 x_1} &= A_2 e^{ikn_2 x_1} + B_2 e^{-ikn_2 x_1} \\
ikn_1 A_1 e^{ikn_1 x_1} - ikn_1 B_1 e^{-ikn_1 x_1} &= ikn_2 A_2 e^{ikn_2 x_1} - ikn_2 B_2 e^{-ikn_2 x_1} \\
&\dots \\
&\dots \\
A_N e^{ikn_N x_N} + B_N e^{-ikn_N x_N} &= A_{N+1} e^{ikn_{N+1} x_N} + B_{N+1} e^{-ikn_{N+1} x_N} \\
ikn_N A_N e^{ikn_N x_N} - ikn_N B_N e^{-ikn_N x_N} &= ikn_{N+1} A_{N+1} e^{ikn_{N+1} x_N} \\
&\quad - ikn_{N+1} B_{N+1}
\end{aligned} \tag{3.11}$$

In order to solve the system it is necessary to eliminate two extra variables. For this reason we use the last boundary condition defining the amplitude of the backward wave behind the last layer B_{N+1} to be equal to zero. We also use the initial condition assigning some specific value to the amplitude of the forward wave before the first layer A_0 .

Obtained linear system of equations is solved by some standard methods such as Cramer's method [203]. As a result of the solution we have a set of amplitudes of forward and backward waves inside each layer. In order to obtain the field distribution inside the structure, it is necessary to substitute amplitudes A and B to the solution in the general form (3.8). Making this for each layer and plotting the obtained function as a dependence of coordinate we will obtain the electric field component distribution inside 1D layered structure. The example of such a distribution inside the structure containing one layer with refractive index 3.5 surrounded by air is shown in Fig. 3.2. Here, red vertical lines mark interfaces. It is an obvious fact that the wave function frequency inside the high-index medium is higher than in air because

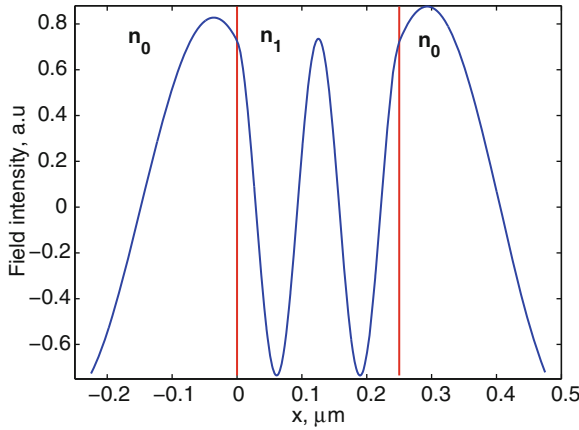


Fig. 3.2. Field distribution inside 1D structure with one layer

the argument of the exponent in the expression (3.8) contains refractive index. Besides, the function is smooth and continuous because of the boundary conditions (3.9) which give the continuity of the function and its derivative at the interfaces.

3.2 Applications of the Field Distribution Computation

Let us assume that we have not just an arbitrary, but some finite-size periodic structure; that is, the structure where a group of two or more layers is translated several times. The behavior of such a structure is quite easy to predict if we know its layers' parameters. Such a periodic structure is usually referred to as Bragg grating or distributed Bragg reflector. The peculiarity of the Bragg grating is the possibility to fine-tune the transmittance and reflectance spectrum by the variation of layer parameters. At that, the structure has very high reflectance at some specific wavelengths while at another wavelength it may be transparent.

In case of the structure containing periodically repeated pair of layers, the wavelength of maximum reflectance also known as Bragg wavelength, can be found from the following expression:

$$\lambda_{\text{Br}} = 2(n_a d_a + n_b d_b), \quad (3.12)$$

where n_a and d_a is the refractive index and thickness of the first layer in pair while n_b and d_b are the same quantities of the second layer. Thus, the Bragg condition is satisfied when half-wavelength equals optical thickness of the pair of layers.

The condition for maximum transmittance is very similar to the expression (3.12) and takes the following form:

$$\lambda_{\text{transmittance}} = (n_a d_a + n_b d_b). \quad (3.13)$$

The expression indicates that the wavelength of the radiation should be equal to the optical thickness of the layer pairs to meet the conditions of maximum transmittance.

Figure 3.3 depicts a typical view of the reflectance spectrum of 1D periodic structure. It is computed by multiple solution of the equation system (3.11). Each solution is carried out at different wavelengths; hence, the computation gives a number of amplitudes of backward waves B_0 before the first layer of the structure. Dividing this amplitude by the incident wave amplitude A_0 and raising the result to the second power we obtain the reflectance of the structure at each wavelength. As is seen from the Fig. 3.3, the reflectance is quite different at different wavelengths. The Bragg wavelength here falls at the wavelength $1.55 \mu\text{m}$. This means that the maximum of reflectance is observed at this wavelength.

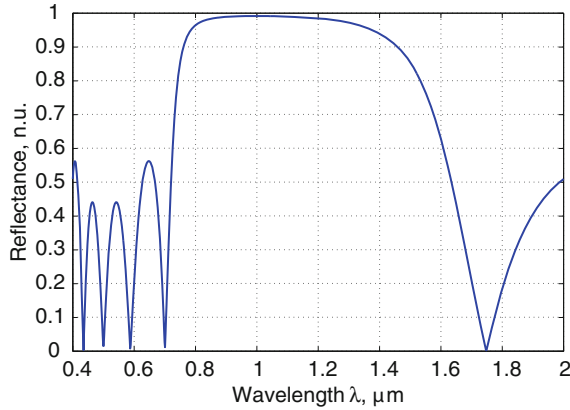


Fig. 3.3. Typical reflectance spectrum of 1D PhC

The computation process shown above is quite easy to understand and use. However, it has a wide range of applications. Using the above described method it is possible to design different passive optical devices such as high-efficiency reflectors, anti reflection films, distributed Bragg reflectors for vertical-cavity surface-emitting lasers (VCSEL), wavelength division multiplexers/demultiplexers on the basis of fiber Bragg gratings (FBG), mirrors of tunable lasers, etc.

As an example of such an application, we will consider here the wavelength division demultiplexer on the basis of FBG [204]. It should be designed to separate in space the optical channels propagating initially in a single fiber at different wavelengths.

The optical scheme of such a demultiplexer is depicted in Fig. 3.4. Input optical fiber is connected to optical insulator which prevents the radiation from propagation back to the input channel. Behind the insulator there are a number of optical circulators connected in series. The radiation falling to one input of such a circulator goes out through the port next to the input one. After that, the radiation incidents the Bragg reflector with defect and is almost totally reflected, except for a single wavelength which is resonant to the defect. After that, the radiation falls at the second circulator and the second Bragg reflector which defect differs from previous one and, consequently, transmits the radiation at another wavelength. The process is repeated until all the channels are separated such that they could be detected, reshaped or amplified.

The main elements of the described demultiplexer are the distributed Bragg reflectors with defect which allow one wavelength of wide range to pass while other wavelengths are reflected. Let us consider in detail the peculiarities of their design.

The Bragg reflector with defect is represented by layered periodic structure where the periodicity is broken by the variation of some parameter (the refractive index or the thickness) of one of the layers. The structure now represents

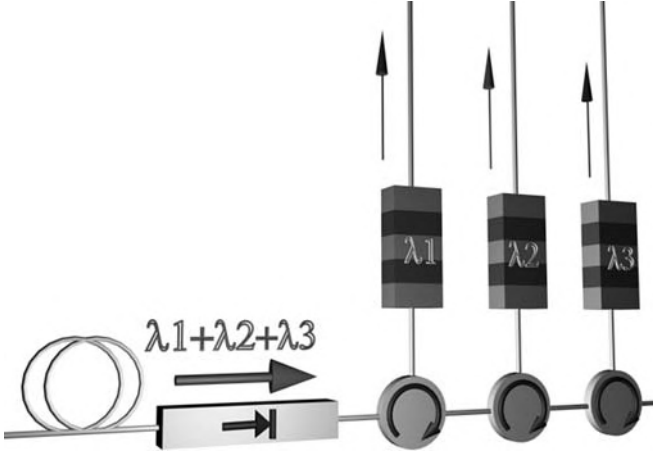


Fig. 3.4. WDM demultiplexer on the basis of FBG

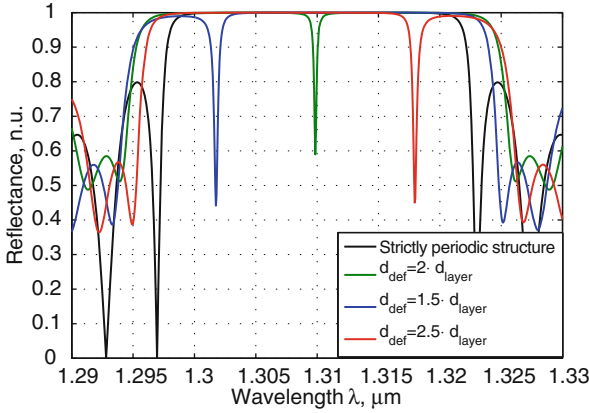


Fig. 3.5. Reflectance spectra of PhCs with defects of different width

the resonator (the defect layer) with two mirrors (distributed Bragg reflectors from both sides of the defect layer). At that, the reflectance spectrum of the whole structure is changed. As a rule, when the parameters of defect layer are properly selected, sharp transmittance peak appears within the main reflectance band as shown in Fig. 3.5. The wavelength of the transmittance peak corresponds to the resonant wavelength of the defect. For instance, if the thickness of the defect layer is twice larger than it was in defectless structure, the transmittance peak appears at the Bragg wavelength of the corresponding defectless structure. Thus, if the radiation with wavelength equal to Bragg wavelength of defectless reflector falls at this structure it will pass the structure almost without the reflectance. If the defect thickness is slightly different, the wavelength of the transmittance peak will be different as well. However, it still may fall at the main reflectance peak of the defectless structure.

If the signal containing a number of the wavelength channels falls at the Bragg reflector with defect, only one channel will pass through while others will be reflected. Properly selected thickness of defect layer of each of the reflector in Fig. 3.4 allows carrying out the spatial separation of all channels. The method described in current chapter allows to automate such a procedure and makes the task purely engineering.

3.3 Summary

1. The Helmholtz equation for electric field component is convenient to use for computation of the field distribution in 1D layered structure.
2. Main computation stages include: definition of the refractive index profile, definition of boundary and initial conditions and solution of system of linear equations.
3. Among the applications of the field distribution computation inside 1D layered structures there are the reflectance spectrum computation of an arbitrary layered structure including distributed Bragg reflectors and design of FBGs with defects for the wavelength division demultiplexers.

3.4 MATLAB Program Reflectance Spectrum Computation of 1D PhC

```
%The program computes the reflectance spectrum
%of the user-defined layered structure by the method
%described in this chapter. The solution of the
%linear equations system is carried out by Cramer's
%method. For this reason, two matrices are composed.
%The first one contains coefficients at the unknowns
%of the system while the second one contains free
%terms.
```

```
%Input parameters: layers thicknesses and refractive
%indices, the range of the wavelengths for the
%spectrum computation.
```

```
%Output data: The plot of the layered structure
%reflectance spectrum within required range
%-----
clear all;
```

```
%The array lambda defines the set of the wavelength
%where the reflectance computation will be carried
```

```

%out.
lambda=1:0.01:2;

%The array layerWidth defines the thickness of each
%layer. The number of elements in this array defines
%the number of layers in the structure.
layerWidth=[0.15 0.25 0.15 0.25 0.15...
            0.25 0.15 0.25 0.15];

%The array layerRI defines the refractive indices of
%layers. I should have the same length as layerWidth.
%Here, it is assumed that surrounding material
%refractive index equals 1 i.e. the structure is
%surrounded by air.
layerRI=[3.5 1 3.5 1 3.5 1 3.5 1 3.5];

%The cycle over wavelength. The variable wavelength
%is counter and it takes on values from 1 to length
%of the array lambda
for wavelength=1:length(lambda)

%Here we compute the wave number
    k=2*pi/lambda(wavelength);

%Clearing the arrays from the values written at
%previous cycle step.
    clear coefMatrix;
    clear freeMemberMatrix;

%Two-dimensional array coefMatrix contains the
%coefficients at unknowns of the
%system of linear equations. Because the coefficient
%A0 is user-defined (as we determined from initial
%conditions) first two rows of the matrix contains
%coefficients B0, A1, B1 only. Consequently, they
%should be defined outside the cycle. Moreover, the
%coordinate of the first interface is assumed to be
%equal to zero so all the exponents here vanish.
coefMatrix(1,1:3)=[1 -1 -1];
coefMatrix(2,1:3)=[-i*k*1 -i*k*layerRI(1) ...
                  i*k*layerRI(1)];

%The variable xCurrent contains the coordinate of
%current interface i.e. the interface we currently

```

```

%writing boundary conditions for
    xCurrent=layerWidth(1);

%The following cycle scans over all interfaces. The
%scanning begins from the interface between two first
%layers
    for countBoundary=1:length(layerWidth)-1
%Defining the function equality condition at the
%boundary.
        coefMatrix(countBoundary*2+1,2*countBoundary:...
2*countBoundary+3)=...
            [exp(i*k*layerRI(countBoundary)*xCurrent)...
            exp(-i*k*layerRI(countBoundary)*xCurrent)...
            -exp(i*k*layerRI(countBoundary+1)*xCurrent)...
            -exp(-i*k*layerRI(countBoundary+1)*xCurrent)];

%Defining the function derivatives equality condition
%at the boundary.
        coefMatrix(countBoundary*2+2,2*countBoundary:...
2*countBoundary+3)=...
            [1i*k*layerRI(countBoundary)*...
exp(1i*k*layerRI(countBoundary)*xCurrent)...
            -1i*k*layerRI(countBoundary)*...
exp(-1i*k*layerRI(countBoundary)*xCurrent)...
            -1i*k*layerRI(countBoundary+1)*...
exp(1i*k*layerRI(countBoundary+1)*xCurrent)...
            1i*k*layerRI(countBoundary+1)*...
exp(-1i*k*layerRI(countBoundary+1)*xCurrent)];

%The coordinate of current interface is increased by
%the thickness of current layer. After that it
%contains the coordinate of the next interface
        xCurrent=xCurrent+layerWidth(countBoundary+1);
    end

%The boundary conditions at the last interface are
%defined manually as it was done for the first one
%because we constituted the coefficient BN+1 to be
%equal to zero.
        coefMatrix(length(layerWidth)*2+1,2*...
length(layerWidth):2*length(layerWidth)+2)=...
            [exp(1i*k*layerRI(length(layerRI))*xCurrent)...
            exp(-1i*k*layerRI(length(layerRI))*xCurrent)...
            -exp(1i*k*1*xCurrent)];

```

```

        coefMatrix(length(layerWidth)*2+2,2*...
length(layerWidth):2*length(layerWidth)+2)=...
        [1i*k*layerRI(length(layerRI))*...
exp(1i*k*layerRI(length(layerRI))*xCurrent)...
        -1i*k*layerRI(length(layerRI))*...
exp(-1i*k*layerRI(length(layerRI))*xCurrent)...
        -1i*k*1*exp(1i*k*1*xCurrent)];

%Defining column matrix containing the array of free
%terms.
%Nonzero elements of this array are only two first
%elements because we assumed A0 to be equal to 1. For
%all other equations free terms equal to zero
        freeMemberMatrix=zeros(length(layerWidth)*2+2,1);
        freeMemberMatrix(1)=-1;
        freeMemberMatrix(2)=-1*1i*k*1;

%Cycle for Cramer's method solution
%Cashing the matrix to some temporary variable.
        tempMatrix=coefMatrix;
%Substituting free-terms column matrix instead of
%column with number corresponding the number of
%solution we are searching for.
        tempMatrix(:,1)=freeMemberMatrix;
%Searching for the solution by dividing the
%determinant of temporary matrix by the
%determinant of the matrix composed of coefficients
%at the unknowns
        solution(wavelength)=...
                1/det(coefMatrix)*det(tempMatrix);
    end

%Plotting the solution
plot(lambda,abs(solution).^2,'LineWidth',2);
xlabel('\lambda, \mu m','FontSize',16);
ylabel('Refrectance, r.u.','FontSize',16);

```

Let us consider the above listed Matlab program. It consists of several steps. In the first step, the structure is defined. As we discussed earlier in this chapter, the structure is defined by its layer thicknesses and refractive indices. These parameters of the layers are written to corresponding arrays.

The next step is the solution itself. We are about to find the spectrum such that the external loop scans over the wavelength. Inside this loop, we

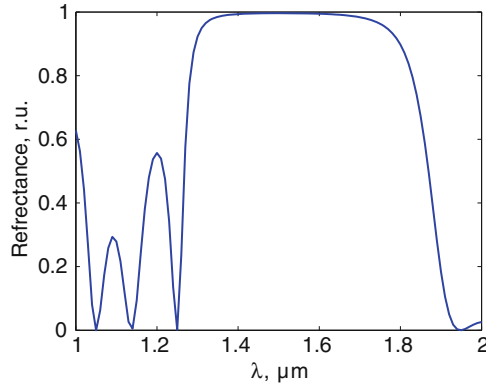


Fig. 3.6. Results of the program. Reflectance spectrum of 1D layered structure

first compute the wave number and then compose the matrix of coefficients at the variables A_n and B_n of the system (3.11). The matrix can be composed inside the cycle except the first and last two rows which correspond to the first and the last interface boundary conditions. The reason is as follows: in order for the system to have a solution, the input forward wave amplitude should be set manually to any value and the backward wave amplitude at the last layer is equal to zero. This eliminates two variables from the system (3.11). The column vector of free terms is then composed. In case of the system (3.11), all free terms are equal to zero except the first and the second ones. They are set in correspondence to the incident wave amplitude. After the matrices are composed, the Cramer's method is applied. The Cramer's method itself works as follows. To find the n -th solution, we exchange the n -th matrix column by the free terms vector. Then, the determinant of resulting matrix is divided by the determinant of the initial matrix. However, since we are interested only in coefficient B_0 , there is no need to compute all coefficients; hence, we limit ourselves by computing the first solution only.

At the last step, we are plotting the solution and sign the axes.

The result of the program is shown in Fig. 3.6 which represents the reflectance spectrum. Main reflectance maximum falls at $1.55 \mu\text{m}$ and coincides with the Bragg wavelength which can be obtained by the formula (3.12).

3.5 Problems and Questions

Problem 3.1. Which parameters define the layered structure?

Problem 3.2. What are forward and backward waves?

Problem 3.3. In which case does the Fresnel reflection appear?

Problem 3.4. Derive Helmholtz equation for magnetic field.

Problem 3.5. Derive the Helmholtz equation for electric field for the medium with magnetic and dielectric properties ($\mu = \mu(\mathbf{r})$, $\varepsilon = \varepsilon(\mathbf{r})$).

Problem 3.6. Derive the Helmholtz equation for magnetic field for the medium with magnetic properties only ($\mu = \mu(\mathbf{r})$, $\varepsilon = \text{const}$).

Problem 3.7. By solving Helmholtz equation for electric field and non-magnetic medium, derive the formula for Fresnel reflection from one interface: $R = (n_1 - n_2)/(n_1 + n_2)$.

Problem 3.8. Write the program for field distribution computation inside 1D arbitrary layered structure. Use the same structure as in the example program.

Band Structure Computation of 1D Photonic Crystals

Summary. Chapter 4 is dedicated to the detailed description of the plane wave expansion method used for computation of the band structure of 1D photonic crystals. We describe all steps of the band structure computation applied for simplest photonic crystal. After the problem formulation, terms such as unit cell, lattice vector, reciprocal lattice and reciprocal lattice vectors as well as the first Brillouin zone are introduced and their physical and mathematical essence is discussed in detail. Peculiarities of the band structure computation are considered and such crucial problems as Bloch theorem, Fourier expansion of a dielectric function and general model formulation are analyzed. Finally, the eigen-value problem for the matrix is considered which gives an idea of the eigen-states computation of the differential operator presented in matrix form. The described model is also applied to off-axis radiation propagation. At the end of the chapter the example of original Matlab-code for band structure computation with additional comments is presented and several problems and questions for self-training are given.

4.1 Problem Definition

In the previous chapter, we have considered computation of the electromagnetic field distribution inside arbitrary 1D layered structure. The field distribution allows one to obtain basic structure characteristic such as the transmittance and reflectance spectra. The method is quite good for 1D structures because of their simplicity. However, it cannot be applied to complex 2D and 3D structures.

In order to obtain the most general idea of PhCs characteristics as well as to effectively design PhC-based devices, it is convenient to use band structures. Band structures give full information about radiation behaviour when propagating within the specific direction inside the PhC. Using the band structure, the parameter values of the PhC can be accurately determined for each application. Moreover, band structure of such non-periodic structures as point, linear and bulk defects allow to find accurate values of resonant wavelengths or, in case of optical waveguide, to determine its modal and dispersive properties.

In this chapter, the idea of the computation of the band structure of 1D PhC will be given. The plane wave expansion (PWE) method which is one of the most important for computation of the PhCs band structures will be described in detail here.

The problem of the band structure computation of a PhC is finding the dispersion relation, that is, the dependence of eigen-frequencies or resonant frequencies of the PhC on the wave vector of the radiation passing through it. In order to obtain the dispersion relation, it is necessary to solve the eigen-problem formulated for the Helmholtz equation inside infinite periodic structure.

The eigen-problem for the Helmholtz equation inside linear, non-dispersive medium written in CGS system, has the following form [205]:

$$\hat{\Theta}\mathbf{H} = \left(\frac{\omega^2}{c^2}\right)\mathbf{H}, \quad \hat{\Theta} = -\frac{\partial}{\partial x} \frac{1}{\varepsilon(x)} \frac{\partial}{\partial x}. \quad (4.1)$$

This equation can easily be derived from the system of Maxwell's equations by eliminating the electric field component similar to how it was made for equation (3.6).

The equation (4.1) should be read in the following manner: if \mathbf{H} is an eigen-function of some periodic structure which is defined by periodic dielectric function $\varepsilon(x)$, the influence of the operator $\hat{\Theta}$ upon this function is equal to the multiplication of this function by the constant which is called the eigen-value. In our case, an eigen-value is represented by the expression ω^2/c^2 which includes frequency ω of an eigen-function. Thus, the problem consists of searching for eigen-functions of a specific periodic structure and corresponding eigen-values.

First, let us find the dispersion relation in case of the radiation propagating inside the uniform medium, that is, in a medium without interfaces.

In order to solve the eigen-problem in case of an infinite periodic structure, the Bloch theorem is usually used which will be discussed later in this section. The Bloch theorem says that the eigen-function inside an infinite periodic medium can be represented in the form of a plane wave multiplied by a periodic function with periodicity of lattice [206]:

$$H(x) = h(x) \exp(ik_x x), \quad (4.2)$$

where $h(x) = h(x + T)$ is a periodic function with periodicity T of the lattice. However, if we consider the uniform medium where no modulation of the refractive index appears, period of the dielectric function is infinite. Thus, the eigen-function can be represented in the form of a plane wave multiplied by a constant. Substituting the wave eigen-function written in this form to the Helmholtz equation, we obtain the following equation:

$$-\frac{\partial}{\partial x} \frac{1}{\varepsilon(x)} \frac{\partial}{\partial x} h \cdot \exp(ik_x x) = \left(\frac{\omega^2}{c^2}\right) h \cdot \exp(ik_x x). \quad (4.3)$$

Taking into account the fact that dielectric function is also constant in case of the uniform medium, we take the derivative and obtain the following relation:

$$\frac{1}{\varepsilon} h \cdot k^2 \exp(ik_x) = \left(\frac{\omega^2}{c^2} \right) h \cdot \exp(ik_x). \quad (4.4)$$

This leads to the following expression:

$$k = \frac{n\omega}{c}. \quad (4.5)$$

Thus, the dispersion relation inside the uniform medium is represented by linear function. Let us consider a situation when a medium which is periodic in one dimension is taken instead of a uniform medium. The medium is assumed to be uniform within all other dimensions. As it was made previously, the field is represented in the form of Bloch functions (4.2). Substitution to the Helmholtz equation gives us the expression which is very similar to (4.4):

$$-\frac{\partial}{\partial x} \frac{1}{\varepsilon(x)} \frac{\partial}{\partial x} h(x) \cdot \exp(ik_x) = \left(\frac{\omega^2}{c^2} \right) h(x) \cdot \exp(ik_x) \quad (4.6)$$

In this expression, however, functions $h(x)$ and $\varepsilon(x)$ are not constants anymore, because of periodicity of the permittivity distribution. Therefore, solution of such kind of problems is much more complex than it was in the case of the uniform medium and, consequently, the dispersion relation will take a more complex form.

Typical form of the dispersion relation of 1D PhC in comparison to the dispersion relation of the uniform medium is given in Fig. 4.1. We can see

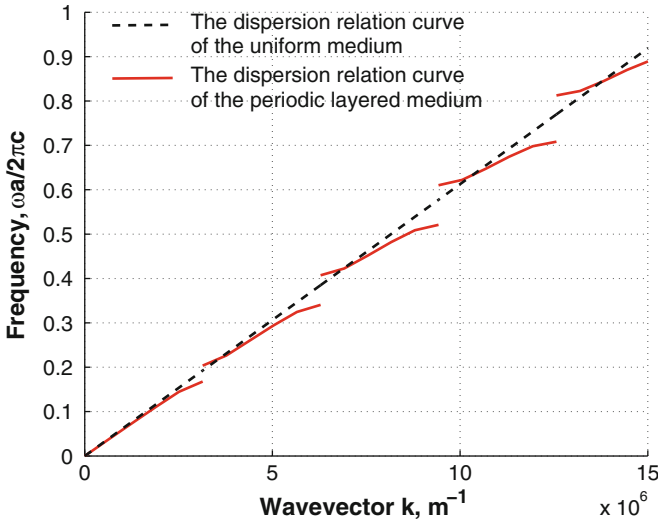


Fig. 4.1. Dispersion characteristics of the uniform medium versus periodic one

frequency gaps which appear within the dispersion relation of the periodic layered structure. Now we have to take into account the complicity of the band structure computation of the PhC.

Now let us consider in detail the eigen-problem definition. As we said previously, the problem consists of searching for eigen-functions and eigen-values of the structure with a known dielectric function. The dielectric function is included into the operator as is shown in expression (4.1). Thus, in order to define and solve the eigen-problem for a PhC it is necessary to define the mathematical description of its structure. Hence, the first step of the computation is to determine the parameters which allow us to define the structure of a PhC.

4.2 Unit Cell

First, let us remind that PhC is presented by an infinite periodic structure. If this is true, the information of a single period is enough to define the whole structure. A section of the PhC which, being translated over all possible dimensions fills a whole space is referred to as unit cell. For instance, if we have 2D PhC, we have two possible dimensions for the translation of the unit cell and, consequently, we are able to fill a whole 2D space with these translated cells.

Unit cell is a spatial domain where each point is closer to the selected base point than to any other neighbour base points. Unit cell of the PhC is defined by its shape and the permittivity or refractive index distribution inside the cell. As it was mentioned in the first chapter, the shape of the unit cell of a PhC defines the type of the PhC lattice. Determination of the unit cell can be made in several ways. Here, we consider the easiest one (see Fig. 4.2). The example is given for a case of 2D PhC, because of simple visualization. However, the technique may be applied to the PhC of any dimensionality:

1. Selecting the base element of the PhC (see Fig. 4.2(a)). As the base element, any peculiarity of the permittivity distribution can be used. For instance, if the PhC consists of rods in air, any rod can be selected as the base element.
2. Connecting the point of the base element with corresponding points of neighbouring elements by line segments (see Fig. 4.2(b)). If we select the central point of the circular base element as the base point, we should connect it with central points of neighbouring elements.
3. Drawing straight lines (in 2D case) or planes (in 3D case) through the center of each of the previously drawn line segments and perpendicular to them (see Fig. 4.2(c)).
4. The figure formed by these lines (in 2D case) or planes (in 3D case) is the unit cell of the PhC and is also known as Wigner-Zeits cell (see Fig. 4.2(d)).

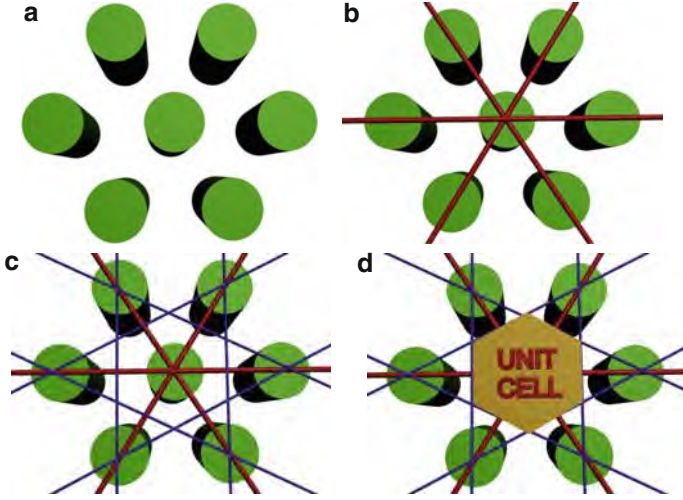


Fig. 4.2. Process of the unit cell determination

As it was mentioned above, the method described is not the only possible one to determine the unit cell; thus, there are different possible shapes of the unit cell. The choice of the unit cell shape is stipulated by the simplicity of its mathematical definition.

The unit cell of 1D PhC is represented by the line segment with a length of a single period of the PhC. Later, in Chap. 5, when computation examples will be considered, mathematical description of some specific kinds of unit cells will be discussed and detailed description will be given.

4.3 Lattice Vectors

After the unit cell of the PhC is determined and its mathematical description is made, it is necessary to determine and describe the translation rules for this cell. The translation rules are defined by so-called lattice vectors. The set of lattice vectors should be selected in a way to completely fill the space with the unit cell. On the other hand, we deal with an infinite structure; hence, it is impossible to define an infinite number of lattice vectors. And again we will use the periodicity of the structure to avoid an infinite set of the lattice vectors. We define a set of basis vectors whose number is equal to the number of dimensions allowed. These vectors are referred to as primitive lattice vectors. The shift of the unit cell by a linear combination of primitive lattice vectors translates it to the similar one. Consequently, the lattice vector can be written in the general form [205]:

$$\mathbf{R} = l\mathbf{a}_1 + m\mathbf{a}_2 + n\mathbf{a}_3, \quad (4.7)$$

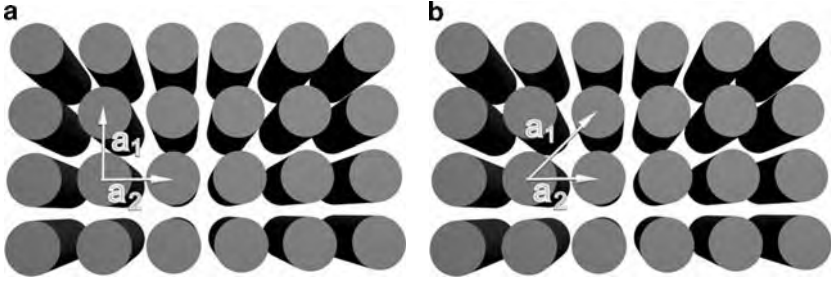


Fig. 4.3. Possible choice of primitive lattice vectors

where l, m, n are integers and $\mathbf{a}_1, \mathbf{a}_2, \mathbf{a}_3$ are primitive lattice vectors. The expression (4.7) is written in the most general form for 3D lattice. 2D and 1D PhC require two and one primitive lattice vectors, correspondingly.

The choice of the lattice vectors as well as the choice of the unit cell is not standardized. The examples of different sets of primitive lattice vectors for the PhC with square lattice is shown in Fig. 4.3. The only requirement is the possibility of the unit cell translation.

Thus, we have the mathematical description of the PhC lattice, which can be used for computation of the PhC band structure.

4.4 Reciprocal Lattice

Now we turn to the expression (4.6) and analyze the part including the medium dielectric function.

Since the PhC is an infinite periodic structure, the dielectric function is infinite as well. Thus, solution of the equation as represented in the expression (4.6) is impossible. However, there are methods which allow avoiding the infinity inside the equation. One such method is derived from the theory of representations which is widely used in quantum mechanics [207], [208]. The theory of representations says that any function represented as a dependence of one variable can be represented as a dependence of another variable by the expansion over basis functions. The basis function expansion is carried out by the integral transform. The theory of representations is widely used in quantum mechanics. For instance, the coordinate representation of the wave function of the particle $\psi(x, t)$ can be derived from the impulse representation using the following transform:

$$\psi(x, t) = \int c(p, t) \cdot \psi_p(x), \quad (4.8)$$

where the set of amplitudes $c(p, t)$ can be considered as the wave function describing the same state of the particle, however, in impulse representation. $\psi_p(x)$ in the expression (4.8) presents the basis functions.

In the theory of PhCs we can proceed in a similar way. When we work with dielectric function in coordinate representation (as a dependence of coordinate), the function appears to be an infinite one. However, when we represent the function as a dependence of the wave vectors, that is, dealing with wave vector representation, we have some decaying function instead, which can be truncated at some point to obtain an approximate solution. Moreover, previously we defined the problem as searching for the dependence of eigen-values on the radiation wave vectors so that the wave vector representation will be very convenient to use.

Thus, in order to derive the dielectric function in wave vector representation, we will expand it over basis functions using the integral transform. In the most basic case, the basis functions take form of plane waves with frequencies which are proportional to the length of the wave vector:

$$\varepsilon(\mathbf{r}) = \int g(\mathbf{k}) \cdot e^{j \cdot \mathbf{k} \cdot \mathbf{r}} d\mathbf{k}, \quad (4.9)$$

where $g(\mathbf{k})$ is the dielectric function in wave vectors representation and \mathbf{k} is the wave vector. Actually, such an expansion can be carried out for the basis functions of any form. However, in the simplest case the system of basis functions is represented by a set of plane waves. Such an integral transform is referred to as Fourier transform. It is usually used to obtain the spectrum of some function dependent on time or coordinate. Now we write down the periodicity condition which says that the values of the function are repeated with some period \mathbf{R} :

$$\varepsilon(\mathbf{r}) = \varepsilon(\mathbf{r} + \mathbf{R}), \quad (4.10)$$

Substituting this condition into the expression (4.9) we obtain:

$$\varepsilon(\mathbf{r} + \mathbf{R}) = \int g(\mathbf{k}) \cdot e^{j \cdot \mathbf{k} \cdot \mathbf{r}} \cdot e^{j \cdot \mathbf{k} \cdot \mathbf{R}} d\mathbf{k} = \varepsilon(\mathbf{r}) = \int g(\mathbf{k}) \cdot e^{j \cdot \mathbf{k} \cdot \mathbf{r}} d\mathbf{k}. \quad (4.11)$$

This condition is met when $g(\mathbf{k}) = 0$ or $e^{j \cdot \mathbf{k} \cdot \mathbf{R}} = 1$ only. In other words, $g(\mathbf{k}) = 0$ everywhere except those values of \mathbf{k} which satisfy condition $e^{j \cdot \mathbf{k} \cdot \mathbf{R}} = 1$ for any lattice vector \mathbf{R} .

Thus, when synthesizing the periodic function of the plane waves, it is necessary to use only those wave vectors which satisfy the condition $e^{j \cdot \mathbf{k} \cdot \mathbf{R}} = 1$ for all lattice vectors \mathbf{R} . There is a simple analogy in 1D case. If we synthesize the function with period τ of harmonic functions, we have to use only fundamental ones in which period equals τ , $\tau/2$, $\tau/3$ and so on. Those wave vectors \mathbf{k} which satisfy the condition $e^{j \cdot \mathbf{k} \cdot \mathbf{R}} = 1$ or $\mathbf{k} \cdot \mathbf{R} = n2\pi$, where n are integers, are called reciprocal lattice vectors and usually designated as \mathbf{G} . These vectors form their own periodic lattice. As far as we found that we have non-zero amplitudes of plane waves only for those ones which argument

is multiple of a reciprocal lattice vector, we can write down the sum of plane waves over reciprocal lattice vector instead of the integral (4.9):

$$\varepsilon(\mathbf{r}) = \sum_{\mathbf{G}} g_{\mathbf{G}} \cdot e^{j \cdot \mathbf{G} \cdot \mathbf{r}}, \quad (4.12)$$

where $g_{\mathbf{G}}$ are coefficients at correspondent plane waves. Thus, instead of the Fourier transform we obtained the expansion to the Fourier series of the dielectric function.

4.5 Reciprocal Lattice Vectors and Brillouin Zone

In the previous section we have defined conditions which determine exactly the set of reciprocal lattice vectors. It can be evaluated via the lattice vector of the PhC by means of the relation:

$$\mathbf{G} \cdot \mathbf{R} = n2\pi. \quad (4.13)$$

We now represent the reciprocal lattice vector in terms of basis vector as we made for lattice vectors:

$$\mathbf{G} = l\mathbf{b}_1 + m\mathbf{b}_2 + n\mathbf{b}_3, \quad (4.14)$$

where $\mathbf{b}_1, \mathbf{b}_2, \mathbf{b}_3$ are basis of primitive reciprocal lattice vectors. Substituting (4.14) and (4.7) into (4.13) we obtain:

$$\mathbf{G} \cdot \mathbf{R} = (l\mathbf{a}_1 + m\mathbf{a}_2 + n\mathbf{a}_3) \cdot (l'\mathbf{b}_1 + m'\mathbf{b}_2 + n'\mathbf{b}_3) = N \cdot 2\pi. \quad (4.15)$$

Taking advantage of the rule of scalar multiplication, we obtain the following relation:

$$a_i \cdot b_i = \delta_{ij} 2\pi, \quad (4.16)$$

where δ_{ij} is Kronecker delta. It is equal to 1 when $i = j$ and 0 otherwise. Using the relation (4.15) we obtain the expressions for primitive reciprocal lattice vectors [205]:

$$\begin{aligned} b_1 &= 2\pi \frac{a_2 \times a_3}{a_1 \cdot a_2 \times a_3}, \\ b_2 &= 2\pi \frac{a_3 \times a_1}{a_1 \cdot a_2 \times a_3}, \\ b_3 &= 2\pi \frac{a_1 \times a_2}{a_1 \cdot a_2 \times a_3}. \end{aligned} \quad (4.17)$$

Thus, if we have the information about primitive lattice vectors of the PhC, we can obtain the primitive reciprocal lattice vectors. Reciprocal lattice just like lattice in coordinate space possesses the periodicity, that is, the translation symmetry. It means that if we take one of the cells and translate it over all possible reciprocal lattice vectors, we will fill whole wave vector space. Such a

unit cell of the reciprocal lattice is selected in a similar way as it was shown for lattice in coordinate space and is defined as the part of the reciprocal space which is closer to the selected base point than to any other base points. The part of the reciprocal space defined in such a way is referred to as the first Brillouin zone or, simply, the Brillouin zone. Because of the translation symmetry, the eigen-frequencies of the structure are usually computed within the Brillouin zone. In case of the computation outside the Brillouin zone, the solutions may duplicate. The process of the Brillouin zone determination consists of several steps:

1. Determination of the unit cell of the PhC.
2. Determination of primitive lattice vectors.
3. Computation of the primitive reciprocal lattice vectors by formulas (4.17).
4. Building several base points of reciprocal lattice from known reciprocal lattice vectors (see Fig. 4.4(a)).
5. Selecting the base element of the PhC.
6. Connecting the point of the base element with corresponding points of neighbour elements by line segments (see Fig. 4.4(b)).
7. Drawing straight lines or planes (in 3D case) through the center of each of the previously drawn line segments and perpendicular to them.
8. The figure formed by these lines or planes (in 3D case) is the unit cell of the reciprocal lattice is the Brillouin zone (see Fig. 4.4(c)).

As we see, the scheme is very similar to the one we used to determine the unit cell. Actually, the Brillouin zone is the Wigner–Zelts cell in the reciprocal space. Figure 4.4, schematically depicts the determination process of the Brillouin zone of the 2D PhC with hexagonal lattice.

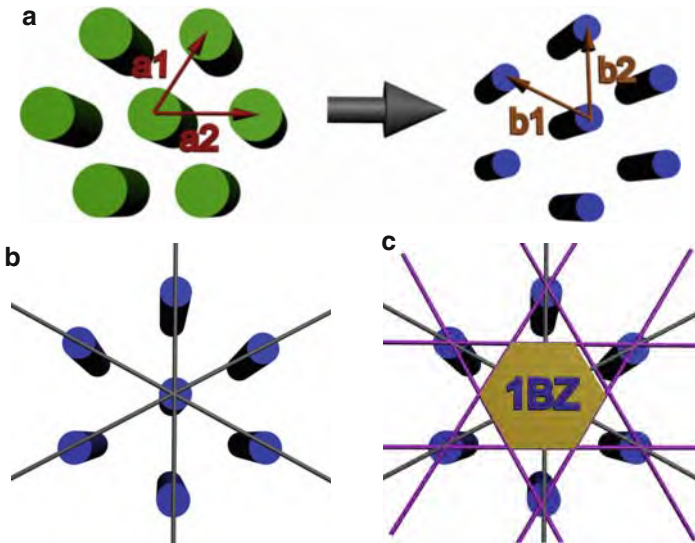


Fig. 4.4. The scheme of the Brillouin zone selection for 2D PhC Brillouin zone

Reciprocal lattice and the Brillouin zone plays an important role in the computation process. It allows to obtain the limits of the variation of the wave vectors where computation of the eigen-states will be carried out.

4.6 Band Structure Computation

In order to compute the band structure of 1D PhC, it is necessary to solve the eigen-problem for the 1D Helmholtz equation. The derivation of Helmholtz equation was given in Chap. 3. The form of the Helmholtz equation for the electric field is shown in (3.7). However, computation of the band structure is more convenient to carry out using the equation for magnetic field component. The equation in this case takes the following form:

$$\frac{\partial}{\partial x} \frac{1}{\varepsilon(x)} \frac{\partial}{\partial x} H(x) + \frac{\omega^2}{c^2} H(x) = 0. \quad (4.18)$$

The difference of this equation from equation (3.7) lies in an operator. Here, the dielectric function stands inside one of the coordinate derivatives while in the equation (3.7) it is outside all derivatives. The dielectric function inside the operator causes some difficulties when searching for field distribution inside the structure; however, such a form of Helmholtz equation is quite convenient for band structure computation. As this will be shown later, the differential operator in such a Helmholtz equation is Hermitian in contrast to the equation for the electric field where the operator should be modified [205].

In order to solve the eigen-value equation (4.18), some approximate methods should be used which employ the periodicity of the permittivity distribution. For instance, we know that the eigen-function of an infinite periodic structure will also be infinite and periodic. That's why the Bloch theorem should be used for representation of the eigen-function of the PhC. The Bloch theorem says that eigen-function of an infinite periodic structure can be represented in the form of plane wave multiplied by some kind of periodic function with periodicity of lattice. Such a function has the following form [206]:

$$H(x) = h_{k,n}(x) \cdot \exp(j \cdot k \cdot x), \quad (4.19)$$

where $h_{k,n}(x)$ is the periodic function with periodicity of lattice, which corresponds to wave vector \mathbf{k} and the state number n .

As mentioned earlier, we cannot proceed with the computation of an infinite functions inside the equations, so we expand the function (4.19) to Fourier series by reciprocal lattice vectors.

$$H(x) = \sum_G h_{k,n}(G) \cdot \exp(j \cdot (k + G) \cdot x), \quad (4.20)$$

where $h_{k,n}(G)$ is previously defined periodic function in representation of wave vectors. It is also the Fourier expansion coefficient.

The dielectric function is a periodic function as well, so it should also be expanded into Fourier series. However, for convenience of further operations, we will expand the Fourier series not permittivity but the inverted dielectric function as it is written down in (4.18):

$$\frac{1}{\varepsilon(x)} = \sum_{G'' \in G} \chi(G'') \cdot \exp(j \cdot G'' \cdot x), \quad (4.21)$$

where $\chi(G'')$ are Fourier expansion coefficients of the inverted dielectric function.

After the expansion of all the infinite functions we substitute them in equation (4.18):

$$\begin{aligned} & \sum_{G''} \frac{\partial}{\partial x} \chi(G'') \cdot \exp(j \cdot G'' \cdot x) \frac{\partial}{\partial x} \sum_{G'} h_{k,n}(G') \cdot \exp(j \cdot (k + G') \cdot x) + \\ & + \frac{\omega^2}{c^2} \sum_G h_{k,n}(G) \cdot \exp(j \cdot (k + G) \cdot x) = 0. \end{aligned} \quad (4.22)$$

Taking into account that $G = G' + G''$ [209], [210], we reduce the first summand of the expression to a common summation index:

$$\begin{aligned} & \sum_G \sum_{G'} \frac{\partial}{\partial x} \chi(G - G') \cdot \exp(j \cdot (G - G') \cdot x) \cdot h_{k,n}(G') \cdot \frac{\partial}{\partial x} \exp(j \cdot (k + G') \cdot x) + \\ & + \frac{\omega^2}{c^2} \sum_G h_{k,n}(G) \cdot \exp(j \cdot (k + G) \cdot x) = 0. \end{aligned} \quad (4.23)$$

Then, taking derivatives and combining the exponents we obtain:

$$\begin{aligned} & \sum_G \sum_{G'} \chi(G - G') \cdot h_{k,n}(G') \cdot \exp(j \cdot (k + G) \cdot x) \times \\ & \times (j \cdot (k + G') \cdot j \cdot (k + G)) + \\ & + \frac{\omega^2}{c^2} \sum_G h_{k,n}(G) \cdot \exp(j \cdot (k + G) \cdot x) = 0. \end{aligned} \quad (4.24)$$

The projection to the basis $\exp(j \cdot (k + G) \cdot x)$ gives the equation:

$$- \sum_{G'} \chi(G - G') ((k + G') \cdot (k + G)) \cdot h_{k,n}(G') + \frac{\omega^2}{c^2} h_{k,n}(G) = 0, \quad (4.25)$$

which is known as “Master equation” for 1D PhC.

Main peculiarity of the equation (4.25) is the absence of the coordinate dependence. All the variables depend on the reciprocal lattice vector only

that is a consequence of the theory of representations which was given above. Moreover, it should be mentioned that instead of one differential equation containing infinite functions we have the system with an infinite number of linear equations and infinite number of unknowns. The information about the permittivity distribution inside the structure is now given in the form of Fourier expansion coefficients of corresponding function.

In spite of the fact that we have an infinite number of linear equations, it can be truncated to some quite low number of equations depending on the accuracy required. This is the crucial moment of the plane waves expansion method. The differential operator in equation (4.25) is presented in the form of a matrix whose element can be found from the following expression:

$$\hat{\theta}_{G,G'} = \chi(G - G')((k + G') \cdot (k + G)). \quad (4.26)$$

A set of solutions of the equations system (4.25) can be found as eigenvalues of matrix differential operator which has the following form:

$$\hat{\theta} = \begin{vmatrix} \hat{\theta}_{G_1 G'_1} & \hat{\theta}_{G_2 G'_1} & \dots & \hat{\theta}_{G_N G'_1} \\ \hat{\theta}_{G_1 G'_2} & \hat{\theta}_{G_2 G'_2} & \dots & \hat{\theta}_{G_N G'_2} \\ \vdots & \vdots & \ddots & \vdots \\ \hat{\theta}_{G_1 G'_N} & \hat{\theta}_{G_2 G'_N} & \dots & \hat{\theta}_{G_N G'_N} \end{vmatrix} \quad (4.27)$$

The process of the selection of G and G' will be shown in the section dedicated to the Fourier expansion of the dielectric function. Here, it just should be mentioned that the set of G must be the same as G' such that the matrix will be square.

The set of wave vectors the computation is carried out for should be selected taking into account the specificity of the problem. For instance, the determination of eigen-states of the periodic structure with irregularity (variation of one of PhC elements' permittivity or thickness which causes the light localization) one value of wave vector is enough, while computation of pure periodic structure requires a set of wave vectors taken in some specific points within the Brillouin zone. In order to compute a more complex characteristic such as photonic density of states it is necessary to compute the eigen-states in all points of the Brillouin zone.

Main peculiarity of the matrix (4.27) is that it is a Hermitian one. Hermitian matrix is the one with elements which satisfy the following condition:

$$\hat{\theta}_{G,G'} = \hat{\theta}_{G',G}^*. \quad (4.28)$$

This means that diagonal-symmetric elements are complex conjugated. In other cases, the eigen-values of such a matrix will be complex which does not make sense, since eigen-values have a form of ω^2/c^2 such that the eigen-frequency of the structure will be complex as well.

4.7 Eigen-Values and Eigen-Vectors of a Matrix

The general form of matrix eigen-problem has the form

$$Ax = \lambda x, \quad (4.29)$$

where $A = \|a_{i,j}\|^m$ is a square matrix, λ are eigen-values of the matrix and x are eigen-vectors of matrix corresponding the specific eigen-value. Let us now represent eigen-vectors of matrix in an arbitrary basis e_1, e_2, \dots, e_m :

$$x = \sum_{i=1}^m x_i e_i. \quad (4.30)$$

Substituting (4.30) in (4.29) we obtain the system of scalar equations

$$\begin{aligned} a_{11}x_1 + a_{12}x_2 + \dots + a_{1m}x_m &= \lambda x_1 \\ a_{21}x_1 + a_{22}x_2 + \dots + a_{2m}x_m &= \lambda x_2 \\ &\vdots \\ a_{m1}x_1 + a_{m2}x_2 + \dots + a_{mm}x_m &= \lambda x_m \end{aligned}, \quad (4.31)$$

which can be re-written in the following form:

$$\begin{aligned} (a_{11} - \lambda)x_1 + a_{12}x_2 + \dots + a_{1m}x_m &= 0 \\ a_{21}x_1 + (a_{22} - \lambda)x_2 + \dots + a_{2m}x_m &= 0 \\ &\vdots \\ a_{m1}x_1 + a_{m2}x_2 + \dots + (a_{mm} - \lambda)x_m &= 0 \end{aligned}. \quad (4.32)$$

In order for the system (4.32) to have non-trivial solutions, it is necessary for the determinant of the system to be equal to zero:

$$\begin{vmatrix} (a_{11} - \lambda) & a_{12} & \dots & a_{1m} \\ a_{21} & (a_{22} - \lambda) & \dots & a_{2m} \\ \vdots & \vdots & \ddots & \vdots \\ a_{m1} & a_{m2} & \dots & (a_{mm} - \lambda) \end{vmatrix} = 0. \quad (4.33)$$

The determinant (4.33) represents an algebraic equation of the n -th order which is called characteristic equation and its left part is known as characteristic polynomial. Thus, each eigen-value is the root of characteristic equation.

Substituting each the eigen-value to the system (4.32) and solving it, we obtain corresponding eigen-vector. For more detailed information about matrix computations, reader may consult the book [211].

In our case the eigen-value means value of ω^2/c^2 which gives the eigen-frequency of the structure.

4.8 Computation Results

The result of the eigen-problem solution for 1D PhC is usually presented as the band structure like the one shown in Fig. 4.5.

On the x -axis of the band structure of 1D PhC lies the wave vector. On the y -axis lies the so-called normalized frequency $\omega a/2\pi c$. It is convenient to use normalized frequency. In the considered case, the frequency is normalized by the period of the PhC so it does not depend on the scale of the structure. The period of the PhC may be of order of either microns or millimeters, but the view of the band structure remains unchanged due to the employment of the normalized frequency while the layer thickness ratio and their permittivities are kept constant.

Let us now consider the band structure in detail. The eigen-frequencies of the PhC start from zero frequency at a point $k = 0$ except the case of so-called off-axis propagation when the angle between the radiation propagation direction and the medium interface differs from 90° . This case will be considered in detail in the final section of this chapter. Higher on the frequency axis the photonic band gap (PBG) appears. The PhC does not have eigen-states within the PBG. The bands and PBGs appear one-by-one on the frequency axis, except those cases when the PBG width is equal to zero. In the case of 1D PhCs, the PBG appears between almost each pair of the bands. In case of 2D and 3D PhCs the PBG appears much more rear.

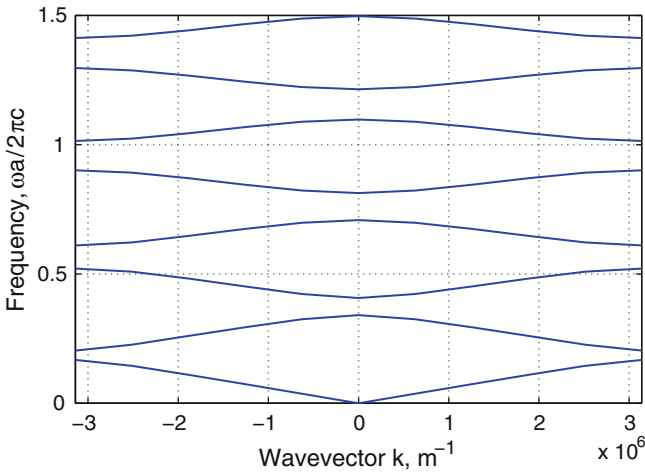


Fig. 4.5. Typical band structure of 1D PhC

4.9 Fourier Expansion of the Dielectric Function

Fourier expansion of the dielectric function in 1D case is written down as follows:

$$\frac{1}{\varepsilon(x)} = \sum_G \chi(G) \cdot \exp(j \cdot G \cdot x) = \sum_{l'=-\infty}^{\infty} \chi_{l'} \cdot \exp(j \cdot l' \cdot G_0 \cdot x). \quad (4.34)$$

Here l' is the number of period of the reciprocal lattice as was defined in (4.14) and G_0 corresponds to the length of the primitive reciprocal lattice vector. The Fourier expansion written in the form of (4.34) is for 1D case only. In the expression, χ_n are Fourier expansion coefficients which are determined in following manner:

$$\chi_n = \chi(l' \cdot G_0) = \frac{1}{T} \int_{x_1}^{x_2} \frac{1}{\varepsilon(x)} \cdot e^{-j \cdot l' \cdot G_0 \cdot x} dx, \quad (4.35)$$

where T is the period of the PhC in coordinate space and x_1 and x_2 are coordinates of starting and ending points of a single PhC period. In the simplest case, the permittivity profile or dielectric function is step-like, that is, the has following mathematical description:

$$\varepsilon(x) = \left\{ \begin{array}{l} \varepsilon_1, x = (0 + l \cdot T; a + l \cdot T) \\ \varepsilon_2, x = (a + l \cdot T; (a + b) + l \cdot T) \end{array} \right\}, \quad l \in Z, \quad (4.36)$$

where ε_1 and ε_2 are permittivities of each layer, and a and b are integers. Consequently, inverted dielectric function is described by the following expression:

$$\frac{1}{\varepsilon(x)} = \left\{ \begin{array}{l} \frac{1}{\varepsilon_1}, x = (0 + l \cdot T; a + l \cdot T) \\ \frac{1}{\varepsilon_2}, x = (a + l \cdot T; (a + b) + l \cdot T) \end{array} \right\}, \quad l \in Z. \quad (4.37)$$

In case of such a profile it is possible to find the analytical expressions for the Fourier expansion coefficients. For this reason, we substitute (4.37) in (4.35) and obtain:

$$\begin{aligned} \chi_{l'} &= \frac{1}{T} \int_0^a \frac{1}{\varepsilon_1} \cdot e^{-j \cdot l' \cdot G_0 \cdot x} dx + \frac{1}{T} \int_a^{a+b} \frac{1}{\varepsilon_2} e^{-j \cdot l' \cdot G_0 \cdot x} dx = \\ &= -\frac{1}{T \cdot j \cdot l' \cdot G_0} \left(\frac{1}{\varepsilon_1} \left(e^{-j \cdot l' \cdot G_0 \cdot a} - 1 \right) + \frac{1}{\varepsilon_2} \left(e^{-j \cdot l' \cdot G_0 \cdot (a+b)} - e^{-j \cdot l' \cdot G_0 \cdot a} \right) \right) = \\ &= \frac{i}{T \cdot l' \cdot G_0} \left(\frac{1}{\varepsilon_1} \left(e^{-j \cdot l' \cdot G_0 \cdot a} - 1 \right) + \frac{1}{\varepsilon_2} \left(e^{-j \cdot l' \cdot G_0 \cdot (a+b)} - e^{-j \cdot l' \cdot G_0 \cdot a} \right) \right). \end{aligned} \quad (4.38)$$

Here, we have a simple expression which gives us the possibility to obtain the Fourier expansion coefficient at each reciprocal lattice vector within the selected set.

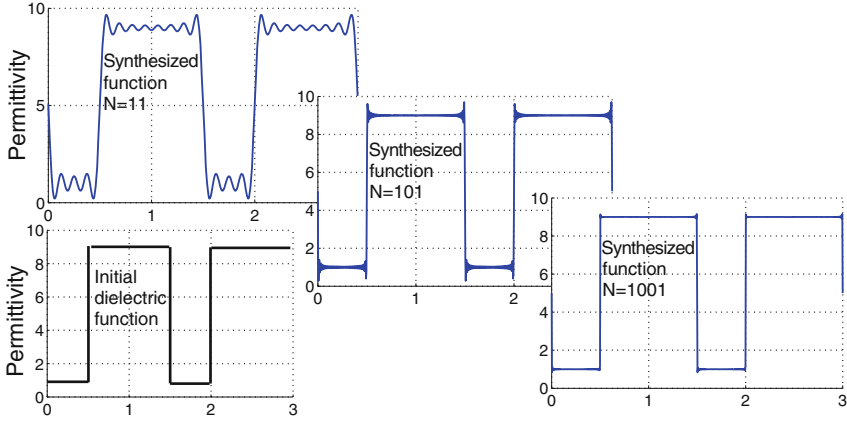


Fig. 4.6. Results of validation of the 1D dielectric function Fourier transform (different number of plane waves)

Now, before the computation process starts, it is necessary to verify the correctness of the dielectric function Fourier expansion. For this reason it is convenient to synthesize the dielectric function from plane waves with previously defined amplitudes and compare it with initial one. Now we will show two examples of such a validation. In the first one (Fig. 4.6), the synthesis of the permittivity distribution is carried out using different number of plane waves, namely, 11, 101 and 1001 plane waves. At that, the value of the reciprocal lattice cell number l' in formula (4.35) is varied, respectively, within the range from -5 to 5 , from -50 to 50 and from -500 to 500 . It can be easily seen that improvement of the shape of that the synthesized function grows with the number of plane waves. However, the initial values of permittivities $\varepsilon_1 = 1$ and $\varepsilon_2 = 9$ are reproduced even at lowest number of plane waves. Thus, growth of number of plane waves used for synthesis of the function does not influence qualitative results but only the quantitative ones. From the point of view of the band structure computation this means that qualitatively right result can be obtained even at low number of equations in system (4.25) such that the computation will take less time. The increase of number of equation in this case will lead to a slight frequency shift of the band structure.

The second example illustrates the situation when the set of the reciprocal lattice cell number l' is not zero-symmetrical. This situation is shown in Fig. 4.7.

In this example, in both cases of synthesis, an equal number of plane waves is taken. However, in the first case the range of n is taken from 0 to 100 while in the second case this range is from -50 to 50 . At that, both functions are very similar to initial function. However, in the first case the value of ε_1 appears to be 3.7 instead of 1, and ε_2 is 7.6 instead of 9 while in the second case ε_1 and ε_2 correspond to the initial values. Thus, asymmetry of n relatively to zero

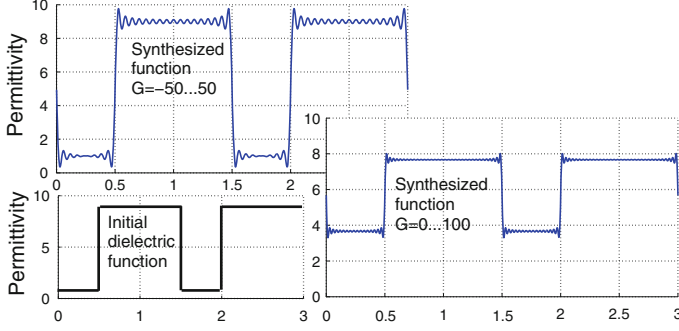


Fig. 4.7. Results of validation of the 1D dielectric function Fourier transform (testing the asymmetric set of reciprocal lattice vectors)

can qualitatively influence the synthesized function. This means that in case of such an error, we will compute the band structure of different PhC and, consequently, the achievement of the right result is impossible at any number of plane waves.

4.10 The Eigen-Value Problem for Electric Field

Previously, it was mentioned that it is convenient to use the Helmholtz equation for magnetic component of the electromagnetic field. Let us consider the reason, why it is inconvenient to use the electric field.

The Helmholtz equation for electric field is written in the following form:

$$\nabla^2 \mathbf{E}_0(\mathbf{r}) + \varepsilon(\mathbf{r}) \frac{\omega^2}{c^2} \mathbf{E}_0(\mathbf{r}) = 0. \quad (4.39)$$

The eigen-value equation for the electric field component in terms of reciprocal lattice can be obtained in the same manner as for magnetic field and takes the following form:

$$-\sum_{\mathbf{G}'} \chi(\mathbf{G} - \mathbf{G}') (\mathbf{k} + \mathbf{G}') (\mathbf{k} + \mathbf{G}') \mathbf{e}_{\mathbf{k}n}(\mathbf{G}') = \frac{\omega_{\mathbf{k}n}^2}{c^2} \mathbf{e}(\mathbf{G}). \quad (4.40)$$

Thus, the matrix for the eigen-values computation will be composed of coefficients of the following view:

$$\hat{\theta}_{G,G'} = \chi(\mathbf{G} - \mathbf{G}') (\mathbf{k} + \mathbf{G}') (\mathbf{k} + \mathbf{G}'). \quad (4.41)$$

In order for the eigen-values to be real and, thus, have a physical meaning, the matrix must be Hermitian, that is, the following relation must be true for any reciprocal lattice vector:

$$\chi(\mathbf{G} - \mathbf{G}') (\mathbf{k} + \mathbf{G}') (\mathbf{k} + \mathbf{G}') = (\chi(\mathbf{G}' - \mathbf{G}) (\mathbf{k} + \mathbf{G}) (\mathbf{k} + \mathbf{G}))^*. \quad (4.42)$$

Here, we can see that the matrix is not Hermitian because expression (4.41) is not invariant to the exchange of \mathbf{G} and \mathbf{G}' . This shows the impossibility of the plane waves expansion method application to the equation for electric field component given in such a form.

There are, however, some artificial methods which allows the differential operator for electric field to be an Hermitian. For instance, we can rewrite the Helmholtz equation 4.39 for electric field as follows [205]:

$$\frac{1}{\sqrt{(\varepsilon(\mathbf{r}))}} \nabla^2 \frac{1}{\sqrt{(\varepsilon(\mathbf{r}))}} \mathbf{F}_0(\mathbf{r}) + \frac{\omega^2}{c^2} \mathbf{F}_0(\mathbf{r}) = 0, \quad (4.43)$$

where

$$F_0(\mathbf{r}) = \frac{1}{\sqrt{(\varepsilon(\mathbf{r}))}} \mathbf{E}_0.$$

The operator

$$\hat{\theta} = \frac{1}{\sqrt{(\varepsilon(\mathbf{r}))}} \nabla^2 \frac{1}{\sqrt{(\varepsilon(\mathbf{r}))}}$$

is now Hermitian. However, the computation of the eigen-values by means of solution of the equation (4.43) is not as fast as for magnetic field.

4.11 Algorithm of PWE Method

Concluding the chapter dedicated to the band structure computation of 1D PhC, the whole computation process can be described as a consequence of operations:

1. Writing down the expression for the computation of Fourier expansion coefficients.
2. Limiting the variation of wave vector within the Brillouin zone $k = -\pi/T \dots \pi/T$.
3. Sets of G and G' vary within the limits of $-2\pi N/T \dots 2\pi N/T$, where $2N + 1$ is the number of plane waves taken into account.
4. According to formulas (4.25) and (4.27) writing down the matrix differential operator for each wave vector within the selected range and computing the eigen-states of obtained matrix.

4.12 Off-Axis Band Structure of 1D PhC

Before this moment we considered only normal incidence of the radiation to medium interface, that is, pure 1D case. However, those situations where the radiation incidents the structure under some angle different from 90° may be interesting from the point of view of the devices design. The example of such propagation is shown in Fig. 4.8.

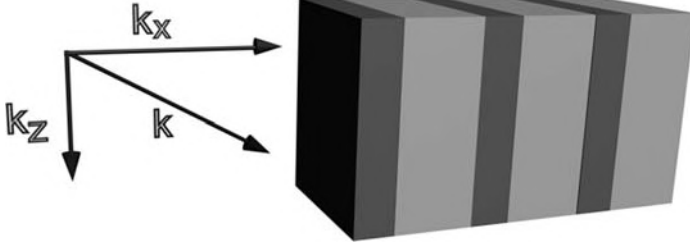


Fig. 4.8. Off-axis radiation propagation inside 1D PhC

So what is the difference of such a case in comparison to pure 1D case? It consists of additional component of the radiation wave vector which ought to be taken into account when composing matrix differential operator. Now the matrix element has the following form:

$$\hat{\theta}_{\mathbf{G}_x, \mathbf{G}'_x} = \chi(\mathbf{G}_x - \mathbf{G}'_x)((\mathbf{k}_{x,z} + \mathbf{G}_x) \cdot (\mathbf{k}_{x,z} + \mathbf{G}'_x)). \quad (4.44)$$

where $\mathbf{k}_{x,z} = \mathbf{k}_x + \mathbf{k}_z$ stands for total wave vector including in-axis and off-axis component while \mathbf{G}_x and \mathbf{G}'_x denote in-axis reciprocal lattice vector. Pay attention that this time these variables are vectors in contrast to the Eq. 4.26 where we had pure 1D case and therefore scalar variables could be used.

This expression shows that in case of the off-axis propagation, when the component \mathbf{k}_z is non-zero, total wave vector is non-zero as well independent on the value of \mathbf{k}_x . Consequently, minimum eigen-frequency will no longer be zero as it was previously. This will lead to frequency shift of the whole band structure and thinning all the bands. At some quite large values of the off-axis wave vector component \mathbf{k}_z , the variation of \mathbf{k}_x within the limits of Brillouin zone will be negligible and therefore the bands will degenerate to a thin level and the band structure will take the form of a system of discrete levels. When computing the band structure for different values of the radiation incidence (which means just varying \mathbf{k}_z component of wave vector) the reduced band structure will have the view presented in Fig. 4.9.

Fig. 4.9(a) depicts the computation result of the reduced off-axis band structure of 1D PhC TE polarization and Fig. 4.9(b) the band structure for TM polarization. The process of the computation of reduced band structure consists of multiple computation of the band structure at different values of some parameter. Then, only the information about the complete PBG is taken and is drawn as a dependence of the parameter value. Here, the reduced band structure depicts presence of complete PBG at different angles of the radiation propagation. Here, dark areas correspond to the range of frequencies with eigen-states and light areas indicate the PBG.

One important fact should be mentioned. The behavior of the reduced off-axis band structure strongly depends on the radiation polarization [205]. In case of TE polarization the growth of the off-axis wave vector component

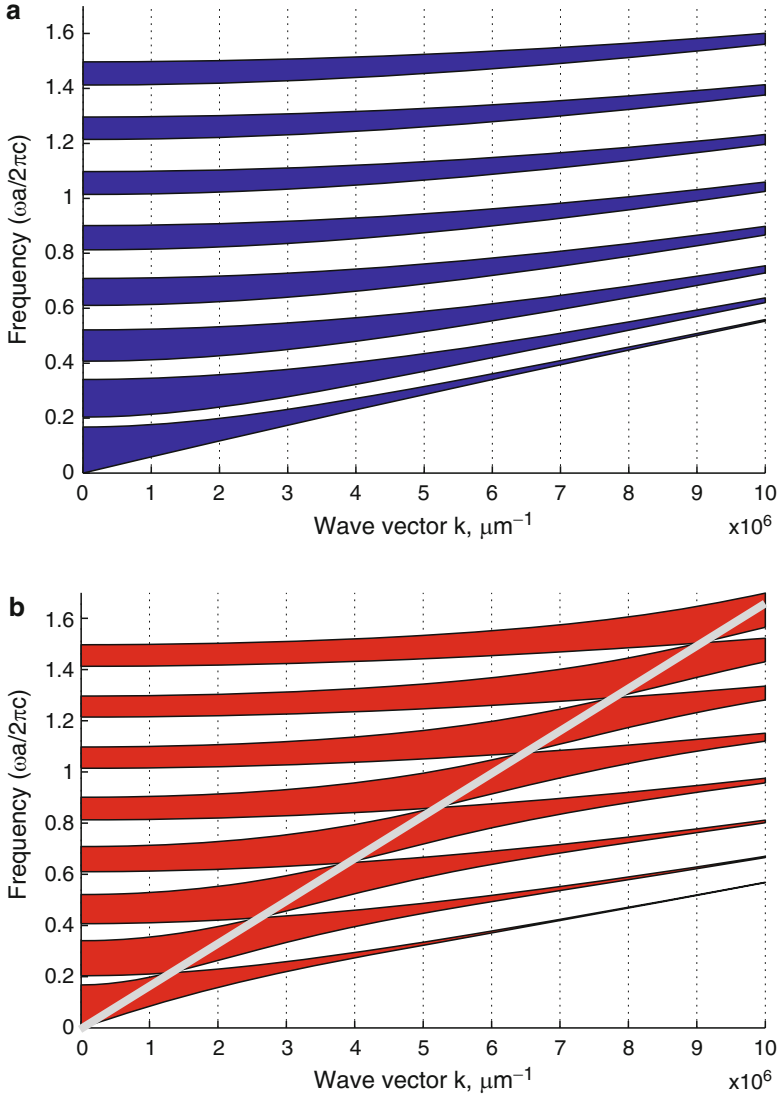


Fig. 4.9. Off-axis band structure of the 1D PhC. (a) TM polarization, (b) TE polarization

results in growth of PBGs while in case of TM polarization there are some kind of waists at some specific values of frequency and wave vector. At that, k_z possesses the value of:

$$k_z = \left(\frac{\omega}{c} \right) \cdot n_2 \cdot \sin(\theta_B), \quad (4.45)$$

where θ_B is the Brewster angle. When the radiation of TM polarization incidents the interface under this angle, the Fresnel reflection is absent. Consequently, the radiation in the neighboring layers appears to be unbound so the reflection from the whole structure is absent as well. The straight line in Fig. 4.9(b) indicates values of frequency and off-axis component of the wave vector which satisfy the condition (4.45).

4.13 Summary

1. 1D PhC is represented by an infinite layered periodic structure. Each period of such a structure is a unit or translational cell of the PhC. By translation of such a cell over all possible lattice vectors it is possible to fill whole space.
2. The band structure of the PhC is one of the most important characteristics. The PWE method is widely used for the computation of the band structures.
3. The PWE method allows to solve the eigen-problem formulated for the specific periodic structure.
4. The PWE requires mathematical description of the PhC lattice and the Bloch theorem is used for representation of the eigen-functions in the general form.
5. The solution is carried out within the wave vector space. For this reason the Fourier expansions of the dielectric function as well as the Bloch function are taken instead of functions themselves. The problem formulated within the wave vector space is then numerically solved.

4.14 MATLAB Program for 1D PhC Band Structure Computation by Means of PWE Method

```
%Program for photonic band structure computation of
%1D photonic crystal. Unit cell consists of two
%layers.
%Structure is defined by the thickness of layers
%within the unit cell as well as their refractive
%index

%Input parameters: thickness of layers and
%refractive index of each layer inside the unit cell

%Output data: dependence of normalized frequency
%on wave vector (photonic band structure)
```

```

%Variables l1 and l2 contain thicknesses of each
%layer within unit cell
l1=0.2e-6;
l2=0.8e-6;

% Variables eps1 and eps2 contain permittivities of
%each layer within unit cell
eps1=1;
eps2=9;

%Variable a is lattice constant
a=l1+l2;

%Variable numG defines number of plane waves in
%Fourier series expansion. Note: due to the
%requirement to the Fourier series to be zero-
%symmetric, actual number of plane waves is
%calculated by formula  $N=numG*2+1$ 
numG=50;

%Variables count_k, countG and countG1 are counters
%for wave vector inside the
%Brillouin zone, reciprocal lattices vector G and G'
%respectively, which are required for definition of
%matrix differential operator

count_k=0;
countG=1;
countG1=1;

%Loop to obtain Fourier expansion coefficients
for G=-numG*2*pi/a:2*pi/a:numG*2*pi/a %G
    for G1=-numG*2*pi/a:2*pi/a:numG*2*pi/a %G'

%Matrix chi contains Fourier expansion coefficients
%for the structure.
%Case of  $(G-G')=0$  is considered separately.
        if (G-G1)==0
            chi(countG1,countG)=1/(l1+l2)*...
            (1/eps1*l1+1/eps2*l2);
        else
            chi(countG1,countG)=1i/(l1+l2)/(G-G1)*...
            (1/eps1*(exp(-1i* (G-G1)*l1)-1)+1/eps2*...
            (exp(-1i* (G-G1)*(l1+l2))-exp(-1i* (G-G1)*l1)));
        end
    end
end

```

```

        countG=countG+1;
    end
    countG1=countG1+1;
    countG=1;
end

%Resetting counters before next loop
countG=1;
countG1=1;

%The loop of band structure calculation. External
%loop is for scanning over the wave vector inside
%the Brillouin zone. Boundaries of the Brillouin
%zone are  $-\pi/a$  and  $\pi/a$ . However, due to symmetry
%a half of the Brillouin zone is enough to
%consider.

for k=-pi/a:0.2*pi/a:pi/a
%The loop over reciprocal lattice vectors G and G'
    for G=-numG*2*pi/a:2*pi/a:numG*2*pi/a %G
        for G1=-numG*2*pi/a:2*pi/a:numG*2*pi/a %G'
%Using previously calculated Fourier expansion
%coefficients we define
%differential operator matrix elements writing
%results to matrix M
            M(countG1,countG)=chi(countG1,countG)*...
                                (k+G1)*(k+G);

            countG=countG+1;
        end
        countG1=countG1+1;
        countG=1;
    end
    countG1=1;

%Computing eigen-values of matrix M
    V=eig(M);
    count_k=count_k+1;
%Here we sort eigen-values obtained and normalize
%them
    dispe(count_k,:)=sqrt((sort(abs(V))))*a/2/pi;
    ks(count_k)=k;
end

%Plotting the band structure
%Creating new window to plot a graph

```

```

figure(1);
%Disabling window cleaning before plot of next graph
hold on;
%Plotting first 8 bands
for u=1:8
    plot(ks,dispe(:,u),'LineWidth',2);
end;
%Making labels and limiting the output area
xlabel('Wave vector k, m^{-1}','FontSize',20);
ylabel('Relative frequency...
        \omega_r=\omega_{aa}/2\pi c','FontSize',20);
xlim([-pi/a pi/a]);

```

If we consired the program, we will see that it consists of four blocks.

In the first block, the variables which determine the structure parameters such as layers thickness and refractive indices as well as period of the structure are introduced.

In the second block, the Fourier expansion coefficients are found. Since the structure is simple, the Fourier expansion coefficients are obtained from analytical expression (4.38). We separated this procedure from the loop for computation of the eigen-values since it is not necessary to compute the coefficients for each value of the wave vector.

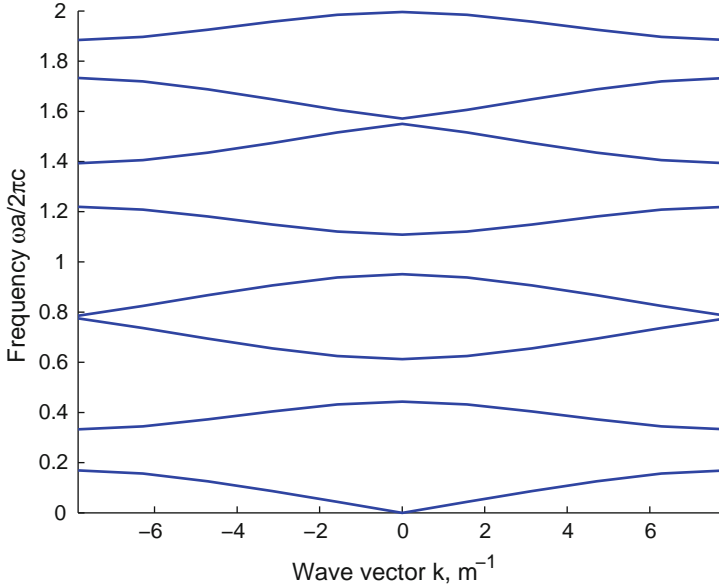


Fig. 4.10. Results of the program. Band structure of 1D PhC

The next block is for the computation of the band structure itself. Here, the scan over all wave vectors within considered range is performed. For each value of the wave vector, the matrix differential operator (4.27) is composed from elements (4.26). Then, the eigen-values of the matrix are found and are written to the corresponding array.

The last block is responsible for plotting the solution and signing the axes.

As a result of the program, we obtain the 2D plot which band structure of the 1D PhC (see Fig. 4.10). The relative frequency $\omega_r = \omega a / 2\pi c = a / \lambda$ lies over the vertical axis while the wave vector is over the horizontal one. The structure parameters are the same as in the program of Chap. 3. Thus, we expect the wavelength $1.55 \mu\text{m}$ to fall at the band gap since it corresponds to the reflection maximum. We can find the relative frequency by the formula $\omega_r = a / \lambda = (0.15 + 0.25) / 1.55 = 0.2581$. This value of relative frequency corresponds to the first band gap as was expected.

4.15 Problems and Questions

Problem 4.1. Derive the eigen-value equation for electric field.

Problem 4.2. Derive the dispersion relation for the uniform medium with refractive index n .

Problem 4.3. What is the unit cell of the PhC? What parameters unambiguously define the unit cell?

Problem 4.4. What is the Wigner–Zits cell? How can it be found?

Problem 4.5. What are lattice vectors? Write down the expression for the lattice vector of the PhC with hexagonal lattice.

Problem 4.6. What is the Brillouin zone?

Problem 4.7. Write down the expression for primitive reciprocal lattice vectors.

Problem 4.8. Find the primitive reciprocal lattice vectors for the PhC with hexagonal lattice.

Problem 4.9. Write down the master equation for 1D PhC.

Problem 4.10. Derive the expression for Fourier expansion coefficient of the PhC with unit cell which contains three layers with widths d_1 , d_2 , d_3 and permittivities ε_1 , ε_2 , ε_3 .

Problem 4.11. Write down the element of matrix differential operator for off-axis radiation propagation.

Problem 4.12. Write the program for band structure computation of 1D PhC with unit cell containing three layers with widths d_1 , d_2 , d_3 and permittivities ε_1 , ε_2 , ε_3 .

Band Structure Computation of 2D and 3D Photonic Crystals

Summary. Chapter 5 discusses the plane wave expansion method applied to the band structure computation of 2D and 3D photonic crystals. The main attention is given to computational peculiarities, characteristics of PhC structures, which are different from 1D PhCs discussed in Chap. 4. Particularly, we discuss the choice of the wave vectors and reciprocal vectors as well as dielectric function Fourier expansion. Then, illustrative examples are given which include band structures with full and partial band gaps, photonic band-gap maps, photonic density of states and off-plane band structures. Finally, the advantages and disadvantages of PWE method for 2D and 3D photonic crystals computation are discussed. At the end of the chapter, the example of original Matlab code for 2D PhC band structure computation by means of PWE method is presented and several problems and questions for self-training are given.

5.1 Problem Definition for 3D Photonic Crystal

Since 3D PhCs possess periodicity in three directions, their band structure computation will be considered first and then the method for 2D PhCs will be discussed which allows some approaches and simplifications such as polarization separation so that it can be derived from one for 3D PhC.

Just as in the case of 1D photonic crystal, computation of the band structure requires the Helmholtz equations obtained from the Maxwell's equations. Then, it is necessary to determine the range of wave vectors variation to compute the Fourier expansion coefficients of the dielectric function, to form the matrix differential operator and to obtain the eigen-values of the matrix.

We will start with Helmholtz equation. Its derivation is the same as for 1D case. However, 3D case implies the permittivity variation in all possible

directions. Thus, the Helmholtz equations can be written down in the following form [206]:

$$\begin{aligned} \frac{1}{\varepsilon(\mathbf{r})} \nabla \times \{ \nabla \times \mathbf{E}(\mathbf{r}) \} &= \frac{\omega^2}{c^2} \mathbf{E}(\mathbf{r}), \\ \nabla \times \left\{ \frac{1}{\varepsilon(\mathbf{r})} \nabla \times \mathbf{H}(\mathbf{r}) \right\} &= \frac{\omega^2}{c^2} \mathbf{H}(\mathbf{r}), \end{aligned} \quad (5.1)$$

where \mathbf{r} is a 3D vector in coordinate space.

Since we are searching for eigen-states of infinite periodic structure, spatial distribution of the field components \mathbf{E} and \mathbf{H} may be represented in the form of Bloch functions, namely, the plane waves multiplied by periodic function with periodicity of lattice [206]:

$$\begin{aligned} \mathbf{E}(\mathbf{r}) &= \mathbf{E}_{\mathbf{k}n}(\mathbf{r}) \cdot e^{j \cdot \mathbf{k} \cdot \mathbf{r}}, \\ \mathbf{H}(\mathbf{r}) &= \mathbf{H}_{\mathbf{k}n}(\mathbf{r}) \cdot e^{j \cdot \mathbf{k} \cdot \mathbf{r}}, \end{aligned} \quad (5.2)$$

where $\mathbf{E}_{\mathbf{k},n}$ and $\mathbf{H}_{\mathbf{k},n}$ are periodic functions with periodicity of lattice. Indices indicate that the periodic function is different for each wave vector \mathbf{k} and number of eigen-state n . Since the functions are periodic ones, they satisfy the following conditions:

$$\begin{aligned} \mathbf{E}_{\mathbf{k}n}(\mathbf{r} + \mathbf{R}) &= \mathbf{E}_{\mathbf{k}n}(\mathbf{r}), \\ \mathbf{H}_{\mathbf{k}n}(\mathbf{r} + \mathbf{R}) &= \mathbf{H}_{\mathbf{k}n}(\mathbf{r}), \end{aligned} \quad (5.3)$$

where \mathbf{R} is the lattice vector.

When we apply the Bloch theorem to represent the wave functions, we constrain the shape of these functions within some limits. The shape is determined by the periodicity of the medium. Thus, instead of an arbitrary function shape, we now have some periodic functions with periodicity of the photonic crystal lattice. These functions which are represented in form of Bloch waves (5.2), also depend on the wave vector \mathbf{k} and on the number of eigen-state n .

As in case of 1D photonic crystal, direct solution of Helmholtz equation for infinite periodic structure is impossible. However, periodicity of wave functions (5.2) leads to possibility of their Fourier expansion over reciprocal lattice vectors. Thus, we can represent the wave function in wave vectors space instead of coordinate space:

$$\begin{aligned} \mathbf{E}_{\mathbf{k}n}(\mathbf{r}) &= \sum_{\mathbf{G}} \mathbf{E}'_{\mathbf{k}n}(\mathbf{G}) \exp(j(\mathbf{k} + \mathbf{G}) \cdot \mathbf{r}), \\ \mathbf{H}_{\mathbf{k}n}(\mathbf{r}) &= \sum_{\mathbf{G}} \mathbf{H}'_{\mathbf{k}n}(\mathbf{G}) \exp(j(\mathbf{k} + \mathbf{G}) \cdot \mathbf{r}), \end{aligned} \quad (5.4)$$

where \mathbf{G} is the reciprocal lattice vector.

By analogy with above mentioned transformation, the dielectric function can also be expanded to the Fourier series due to the periodicity:

$$\frac{1}{\varepsilon(\mathbf{r})} = \sum_{\mathbf{G}} \chi(\mathbf{G}) \cdot \exp(j\mathbf{G} \cdot \mathbf{r}), \quad (5.5)$$

where $\chi(\mathbf{G})$ are Fourier expansion coefficients which depend on the reciprocal lattice vectors. Thus, employing the basis functions $\exp(\mathbf{G} \cdot \mathbf{r})$, we made the transformation of the wave functions from the coordinate representation to the wave vectors representation. The wave functions within wave vectors representation are written down as functions of the discrete argument \mathbf{G} in the form of $\mathbf{E}'_{\mathbf{k}\mathbf{n}}(\mathbf{G})$ and $\mathbf{H}'_{\mathbf{k}\mathbf{n}}(\mathbf{G})$ for electric and magnetic field components, respectively. The wave vector representation of the dielectric function has also discrete argument and is written in the form of $\chi(\mathbf{G})$. Thus, instead of coordinate dependencies of the electromagnetic field distribution, we will use their Fourier expansion coefficients in wave vector representation. Substituting (5.4) and (5.5) into (5.1), and performing the simplification procedure described in Chap. 4, we obtain the following eigen-value equations for the Fourier expansion coefficients of electric and magnetic fields [206]:

$$\begin{aligned} - \sum_{\mathbf{G}'} \chi(\mathbf{G} - \mathbf{G}') (\mathbf{k} + \mathbf{G}') \times \{(\mathbf{k} + \mathbf{G}') \times \mathbf{E}_{\mathbf{k}\mathbf{n}}(\mathbf{G}')\} &= \frac{\omega_{\mathbf{k}\mathbf{n}}^{(E)2}}{c^2} \mathbf{E}_{\mathbf{k}\mathbf{n}}(\mathbf{G}), \\ - \sum_{\mathbf{G}'} \chi(\mathbf{G} - \mathbf{G}') (\mathbf{k} + \mathbf{G}') \times \{(\mathbf{k} + \mathbf{G}') \times \mathbf{H}_{\mathbf{k}\mathbf{n}}(\mathbf{G}')\} &= \frac{\omega_{\mathbf{k}\mathbf{n}}^{(H)2}}{c^2} \mathbf{H}_{\mathbf{k}\mathbf{n}}(\mathbf{G}). \end{aligned} \quad (5.6)$$

These equations represent so called “Master equations” for 3D PhC [206]. Their solutions are the eigen-states of the photonic crystal. Using the expression for matrix differential operator, we compose the matrix and searching for its eigen-values which are being computed for different wave vectors of the radiation gives the band structure.

It is necessary to pay attention to the convergence of the PWE method for 3D case. The problem appears when one needs to compute the band structure for such a 3D photonic crystal because of its complexity. Computation of the Fourier expansion coefficients for 3D case as well as computation of the matrix eigen-values takes a lot of time and it strongly depends on the accuracy required for the specific task.

When we use equation for magnetic field, the number of matrix elements of the matrix differential operator is $2N$ for 3D case, where N is the number of plane waves in Fourier expansion of dielectric function. When equation for electric field is used, the number of matrix elements is $3N$ because of incomplete set of basis functions provided by this equation and, consequently, the necessity of their extension. Taking into consideration the fact that computation time is proportional to N^3 , time consumption in 3D case can be the great value. At that, computation of the band structure even with an error less than 5% requires more than 3000 plane waves to be involved [206].

The convergence of the method can be greatly improved when using the alternative systems of basis functions. For instance, the spherical waves basis can be used for 3D PhC represented by periodically placed spheres. This method is called the spherical wave expansion method or vectorial Korringa–Kohn–Rostoker (KKR) method [212], [213]. Though the application of such a method is limited by the spherical or cylindrical structures, the convergence of the KKR method is much better as compared to PWE method.

5.2 Problem Definition for 2D Photonic Crystal

When one investigates the light propagation in some 2D PhC which is formed by the system of rods with the generatrix along z-axis, two different forms of reduced Maxwell's equations can be considered, which correspond to different radiation polarizations. At that, the radiation can be separated to TE and TM-polarizations (H and E, respectively) depending on which field vector has the component perpendicular to the plane of photonic crystal. The radiation has TE or H-polarization when it has nonzero H_z , E_x and E_y components of the field. At that, the Maxwell's equations can be reduced to the following form [206], [205]:

$$\begin{aligned}\frac{\partial}{\partial x}E_y - \frac{\partial}{\partial y}E_x &= -\frac{1}{c}\frac{\partial}{\partial t}B_z, \\ \frac{\partial}{\partial y}H_z &= \frac{1}{c}\frac{\partial}{\partial t}D_x, \\ -\frac{\partial}{\partial x}H_z &= \frac{1}{c}\frac{\partial}{\partial t}D_y.\end{aligned}\tag{5.7}$$

The radiation which has nonzero E_z , H_x , H_y field components is referred to as TM or E-polarized radiation. The Maxwell's equations for TM polarization differ from the ones for TE polarization and take the following form:

$$\begin{aligned}\frac{\partial}{\partial y}E_z &= -\frac{1}{c}\frac{\partial}{\partial t}B_x, \\ -\frac{\partial}{\partial x}E_z &= -\frac{1}{c}\frac{\partial}{\partial t}B_y, \\ \frac{\partial}{\partial x}H_y - \frac{\partial}{\partial y}H_x &= \frac{1}{c}\frac{\partial}{\partial t}D_z.\end{aligned}\tag{5.8}$$

The above given definition of TE and TM polarization is commonly used and is described in a lot of books dedicated to PhC physics. However, in some computation tools such as RSoft, the opposite TE and TM polarization definition is used in order to make the terms agree with other software modules. In these cases, the TE polarization corresponds to the radiation with nonzero E_z , H_x and H_y components and the term TM polarization is used for the field with nonzero H_z , E_x and E_y . Thus, in view of ambiguity of terminology, it is necessary to pay attention to definition of polarization used when

reading publications or using computation tools. During all the chapters in the book, the commonly-used definition of the TE and TM polarization is used [206], [205].

The Helmholtz equations obtained for TE and TM polarizations from Maxwell's equations (5.7) and (5.8) have some differences as compared to those for 3D PhC. Helmholtz equations for 2D case take the following form:

$$\begin{aligned} - \left\{ \frac{\partial}{\partial x} \frac{1}{\varepsilon(\mathbf{r}_{||})} \frac{\partial}{\partial x} + \frac{\partial}{\partial y} \frac{1}{\varepsilon(\mathbf{r}_{||})} \frac{\partial}{\partial y} \right\} H_z(\mathbf{r}_{||}) &= \frac{\omega^2}{c^2} H_z(\mathbf{r}_{||}), \\ - \frac{1}{\varepsilon(\mathbf{r}_{||})} \left\{ \frac{\partial^2}{\partial x^2} + \frac{\partial^2}{\partial y^2} \right\} E_z(\mathbf{r}_{||}) &= \frac{\omega^2}{c^2} E_z(\mathbf{r}_{||}). \end{aligned} \quad (5.9)$$

Here $\mathbf{r}_{||}$ is 2D vector in coordinate space which lies in plane of 2D PhC (in our case, in plane (X, Y)). At that, we have in mind that permittivity variation of the PhC in Z direction as well as the variation of the electro-magnetic field is absent.

Subsequent band structure computation process is very similar to that one for 1D and 3D PhCs considered previously. First, we represent the wave functions in the form of Bloch waves and expand them into the Fourier series over the reciprocal lattice vectors. Then we also expand the inversed dielectric function into Fourier series. Substituting these expressions into Helmholtz equations (5.9) we obtain the eigen-value equations for the Fourier expansion coefficients:

$$\begin{aligned} \sum_{\mathbf{G}_{||}} \chi(\mathbf{G}_{||} - \mathbf{G}'_{||}) \left| \mathbf{k}_{||} + \mathbf{G}'_{||} \right|^2 E_{z, \mathbf{k}_{||}n}(\mathbf{G}'_{||}) &= \frac{\omega_{\mathbf{k}_{||}n}^{(E)2}}{c^2} E_{z, \mathbf{k}_{||}n}(\mathbf{G}_{||}), \\ \sum_{\mathbf{G}_{||}} \chi(\mathbf{G}_{||} - \mathbf{G}'_{||}) (\mathbf{k}_{||} + \mathbf{G}_{||}) (\mathbf{k}_{||} + \mathbf{G}'_{||}) H_{z, \mathbf{k}_{||}n}(\mathbf{G}'_{||}) &= \frac{\omega_{\mathbf{k}_{||}n}^{(H)2}}{c^2} H_{z, \mathbf{k}_{||}n}(\mathbf{G}_{||}), \end{aligned} \quad (5.10)$$

which is “Master equation” for 2D PhC.

Here $\mathbf{G}_{||}$ and $\mathbf{G}'_{||}$ are in-plane reciprocal lattice vectors, $\mathbf{k}_{||}$ is in-plane wave vector, and $\omega_{\mathbf{k}_{||}n}^{(E)}$ and $\omega_{\mathbf{k}_{||}n}^{(H)}$ are eigen-frequencies for TM and TE polarization, respectively (in case of 2D PhC the values of these frequencies are different).

The complexity of subsequent computation process consists mainly in definition of the Brilluoin zone, discovering the set of wave vectors the computation will be carried out for and expansion of dielectric function into Fourier series.

In the simplest cases of the PhC configuration, like periodically arranged dielectric rods in 2D PhC or dielectric spheres in 3D case, it is possible to obtain analytical expression for the Fourier expansion coefficients. However, if the structure slightly differs from the strictly periodic one, analytical expression of the Fourier coefficients is impossible to obtain. In such a case, numerical method should be involved.

5.3 Fourier Expansion of the Dielectric Function

General view of the Fourier expansion of inversed dielectric function is given by expression (5.5). Calculation of the Fourier expansion coefficients is made by the following expression:

$$\chi(\mathbf{G}) = \frac{1}{V_0} \int_{V_0} \frac{1}{\varepsilon(\mathbf{r})} \exp(-j\mathbf{G} \cdot \mathbf{r}) d\mathbf{r}, \quad (5.11)$$

where V_0 corresponds to the volume of the unit cell of the PhC.

5.3.1 Dielectric Spheres

Let us consider the 3D PhC which consists of dielectric spheres placed in a uniform medium [206]. In this case, the inversed dielectric function takes the following form:

$$\frac{1}{\varepsilon(\mathbf{r})} = \frac{1}{\varepsilon_2} + \left(\frac{1}{\varepsilon_1} - \frac{1}{\varepsilon_2} \right) S(\mathbf{r}), \quad (5.12)$$

where ε_1 is the spheres' permittivity and ε_2 is the permittivity of the medium the dielectric spheres are placed in. $S(\mathbf{r})$ represents the step function and has the following form:

$$S(\mathbf{r}) = \begin{cases} 1, & |\mathbf{r}| \leq r_a \\ 0, & |\mathbf{r}| > r_a \end{cases}, \quad (5.13)$$

where r_a is the sphere radius. Representing the dielectric function in such a way we have $(1/\varepsilon(\mathbf{r})) = 1/\varepsilon_1$ when $|\mathbf{r}| \leq r_a$ and $(1/\varepsilon(\mathbf{r})) = 1/\varepsilon_2$ when $|\mathbf{r}| > r_a$. Substituting (5.13) in (5.11) we obtain the following expression for the Fourier expansion coefficients:

$$\chi(\mathbf{G}) = \frac{1}{\varepsilon_2} \delta_G + \frac{1}{V_0} \left(\frac{1}{\varepsilon_1} - \frac{1}{\varepsilon_2} \right) \int_{V_0} S(\mathbf{r}) \exp(-j\mathbf{G} \cdot \mathbf{r}) d\mathbf{r}, \quad (5.14)$$

where δ_G is equal to 1 when $\mathbf{G} = 0$, and 0 elsewhere. Because 3D PhC here is formed by dielectric spheres, it is quite convenient to use spherical coordinate system to calculate the integral in the expression (5.14). After the expression is represented in the spherical coordinate system, it takes the following form:

$$\begin{aligned} \int_{V_0} S(\mathbf{r}) \exp(-j\mathbf{G} \cdot \mathbf{r}) d\mathbf{r} = \\ 2\pi \int \int r^2 \sin \theta \cdot \exp(-iGr \cos(\theta)) dr d\theta = \\ \frac{4\pi}{G^3} (\sin Gr_a - Gr_a \cos(Gr_a)), \end{aligned} \quad (5.15)$$

where $G = |\mathbf{G}|$. We now designate the part of unit cell volume occupied by the dielectric sphere via the expression $f = 4\pi r_a^3/3V_0$. Here $4\pi r_a^3/3$ is the volume

of the dielectric sphere and V_0 is full volume of the unit cell. Substituting this expression into (5.15) we obtain the following expression for the Fourier expansion coefficients:

$$\chi(\mathbf{G}) = 3f \left(\frac{1}{\varepsilon_1} - \frac{1}{\varepsilon_2} \right) \cdot \left(\frac{\sin Gr_a}{(Gr_a)^3} - \frac{\cos Gr_a}{(Gr_a)^2} \right). \quad (5.16)$$

Here, we consider separately the case of $\mathbf{G} = 0$. The reason is the division by zero which appears in the expression (5.16). However, if we substitute $\mathbf{G} = 0$ into the expression (5.14) and derive the expression for the Fourier expansion coefficient, we can avoid zero-division:

$$\chi(0) = \frac{f}{\varepsilon_1} + \frac{f-1}{\varepsilon_2}. \quad (5.17)$$

The expression (5.16) also demonstrates the reason for the Fourier expansion convenience for the band structure computation of an infinite periodic structure. The part

$$\left(\frac{\sin Gr_a}{(Gr_a)^3} - \frac{\cos Gr_a}{(Gr_a)^2} \right)$$

in the expression (5.16) and, consequently, the whole expression is reduced while G increases. Taking into account the fact that G determines the plane wave frequency, it is obvious that contribution of plane waves with lower frequencies to the χ is much larger than those with high frequencies. Thus, it is enough to limit our consideration by only several plane waves with lower frequencies.

5.3.2 Dielectric Rods

The simplest case of 2D PhC is the system of periodically arranged dielectric rods in uniform medium. At that, it is supposed that rods have infinite length [206]. The expression for the Fourier expansion coefficients of such a dielectric function is reduced from (5.11) and takes the following form:

$$\chi(\mathbf{G}_{||}) = \frac{1}{V_0^{(2)}} \int_{V_0^{(2)}} \frac{1}{\varepsilon(\mathbf{r}_{||})} \exp(-j\mathbf{G}_{||} \cdot \mathbf{r}_{||}) d\mathbf{r}_{||}. \quad (5.18)$$

Here $V_0^{(2)}$ is 2D volume of the 2D PhC unit cell. The designation $||$ points to the values which are considered within the plane of the PhC only.

The dielectric function of the 2D PhC can be written down by the analogy with 3D case (5.12):

$$\frac{1}{\varepsilon(\mathbf{r}_{||})} = \frac{1}{\varepsilon_2} + \left(\frac{1}{\varepsilon_1} - \frac{1}{\varepsilon_2} \right) S^{(2)}(\mathbf{r}_{||}), \quad (5.19)$$

where ε_1 is the permittivity of the rod, ε_2 is the permittivity of the surrounding material and $S^{(2)}(\mathbf{r}_{||})$ is the step function.

Substituting (5.19) into (5.18), we obtain the following expression:

$$\chi(\mathbf{G}_{||}) = \frac{1}{\varepsilon_2} \delta_{G_{||}} + \frac{1}{V_0^{(2)}} \left(\frac{1}{\varepsilon_1} - \frac{1}{\varepsilon_2} \right) \int_{V_0^{(2)}} S^{(2)}(\mathbf{r}_{||}) \exp(-j\mathbf{G}_{||}\mathbf{r}_{||}) d\mathbf{r}_{||}. \quad (5.20)$$

In order to compute the integral in the expression (5.20), in 2D case it is convenient to use polar coordinate system. At that, the integral takes the following form:

$$\begin{aligned} \int_{V_0^{(2)}} S^{(2)}(\mathbf{r}_{||}) \exp(-j\mathbf{G}_{||} \cdot \mathbf{r}_{||}) d\mathbf{r}_{||} &= \int \int r \cdot \exp\left(iGr \cdot \sin\left(\phi - \frac{\pi}{2}\right)\right) dr d\phi = \\ &= \int \int r \cdot \sum_{l=-\infty}^{\infty} J_l(Gr) \exp\left(il\left(\phi - \frac{\pi}{2}\right)\right) = 2\pi \int r J_0(Gr). \end{aligned} \quad (5.21)$$

The part of the 2D volume occupied by the rod is determined as the ratio of the rod 2D volume to the unit cell 2D volume $f = (\pi r_a^2 / V_0^{(2)})$. Here πr_a^2 is the cross-section area of the rod and $V_0^{(2)}$ is the total 2D volume of the unit cell. Substituting this expression and (5.21) into (5.20) we obtain:

$$\chi(\mathbf{G}_{||}) = 2f \left(\frac{1}{\varepsilon_1} - \frac{1}{\varepsilon_2} \right) \frac{J_1(Gr_{||})}{Gr_{||}}, \quad (5.22)$$

where $J_1(Gr_{||})$ is the first order Bessel function which appears to be decreasing with increasing argument.

By the analogy with 3D PhC, we consider separately the case of $G_{||} = 0$ and obtain:

$$\chi(0) = \frac{f}{\varepsilon_1} + \frac{f-1}{\varepsilon_2}. \quad (5.23)$$

The term $(J_1(Gr_{||})/Gr_{||})$ in the expression (5.22) decreases as its argument increases. Thus, in 2D case the value of the expression decreases with G . So in 2D case we have also the Fourier expansion coefficients which decrease with absolute value of the reciprocal lattice vector and, consequently, the main contribution to the dielectric function is made by plane waves with lower frequencies.

5.3.3 Fourier Expansion Coefficient of an Arbitrary Dielectric Function

As already mentioned above, analytical expression for the Fourier expansion coefficients can only be obtained for the simplest cases. And even in those cases the derivation of final expressions is quite complicated. In case of PhC with irregularities or in case when the shape of the PhC elements differs from

the shape of the sphere or the rod, it is necessary to use numerical methods to compute the Fourier expansion coefficients. In this section, one of the possible ways of the Fourier expansion coefficient computation is given. The method is based on discretization of the unit cell space and replacement of the integral by a summation.

First, it is necessary to discretize the unit cell. The easiest way to do this is to divide the unit cell by the uniform square mesh (the mesh with identical cells). Discretization process is shown in Fig. 5.1. The nodes of the mesh contain the information about the permittivity of the medium in the point with corresponding coordinates. When this operation is complete, we have the set of discrete values corresponding to the specific points of the space instead of dielectric function in the analytical form.

Discretization accuracy should be considered separately. If the size of the mesh cell is large in comparison to the smallest structure element of the PhC (for instance, only one or two mesh cells fall at single PhC element), the

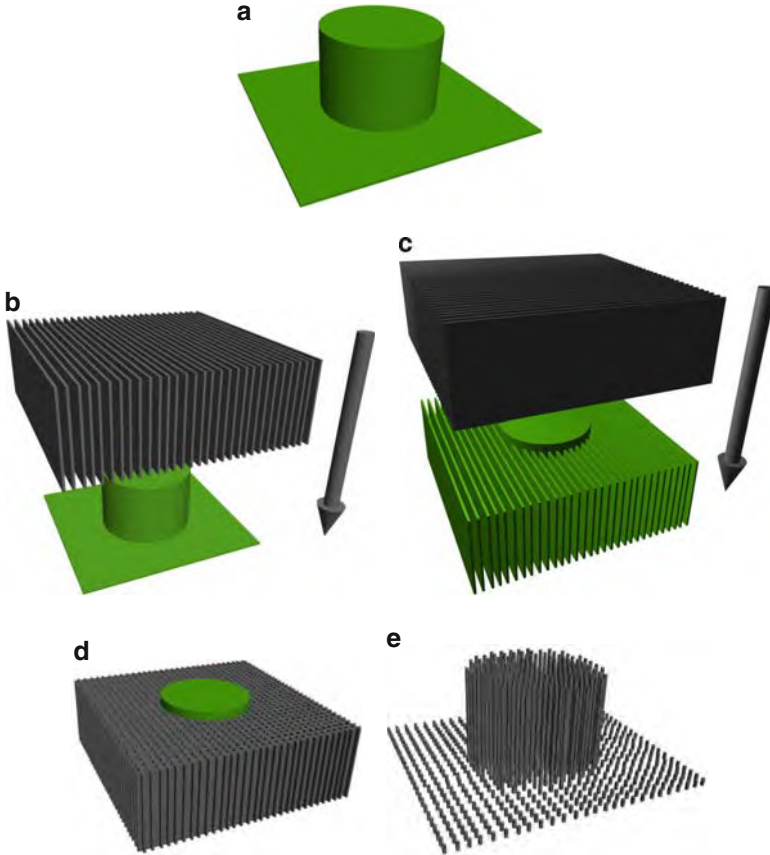


Fig. 5.1. Step-by-step discretization of the PhC unit cell

discretization is bad and computation results will contain large errors. Moreover, the mesh must be dense enough to reproduce the shape of the elements' boundary. However, if the density of the mesh is very high (for instance, 1000 nodes fall at single PhC element), the computation process will take a lot of time and, possibly, machine resources.

After discretization of the unit cell, the integrals (5.11) and (5.18) for 3D and 2D case, respectively, can be replaced by the summation:

$$\chi(\mathbf{G}) = \frac{1}{V_0} \int_{V_0} \frac{1}{\varepsilon(\mathbf{r})} \exp(-j\mathbf{G} \cdot \mathbf{r}) d\mathbf{r} = \frac{1}{a \cdot b \cdot c} \int \int \int \frac{1}{\varepsilon(x, y, z)} \exp(j(G_x x + G_y y + G_z z)) dx dy dz = \quad (5.24)$$

$$\frac{1}{a \cdot b \cdot c} \sum_{j=0}^{N_x} \sum_{k=0}^{N_y} \sum_{u=0}^{N_z} \frac{1}{\varepsilon(x_j, y_k, z_u)} \times \\ \times \exp(j(G_x x_j + G_y y_k + G_z z_u)) \cdot \Delta x_j \cdot \Delta y_k \cdot \Delta z_u,$$

$$\chi(\mathbf{G}_{||}) = \frac{1}{V_0^{(2)}} \int_{V_0^{(2)}} \frac{1}{\varepsilon(\mathbf{r}_{||})} \exp(-j\mathbf{G}_{||} \cdot \mathbf{r}_{||}) d\mathbf{r}_{||} =$$

$$\frac{1}{a \cdot b} \int \int \frac{1}{\varepsilon(x, y)} \exp(j(G_x x + G_y y)) dx dy = \quad (5.25)$$

$$\frac{1}{a \cdot b} \sum_{j=0}^{N_x} \sum_{k=0}^{N_y} \frac{1}{\varepsilon(x_j, y_k)} \exp(j(G_x x_j + G_y y_k)) \cdot \Delta x_j \cdot \Delta y_k.$$

Here, a, b, c are the unit cell dimensions, N_x, N_y, N_z are the numbers of mesh nodes in x, y and z directions, respectively.

Defining the set of the reciprocal lattice vectors and carrying out summation over all the elements, we obtain the Fourier expansion coefficients.

5.3.4 Validation of the Fourier Expansion

In Chapter 4 that is dedicated to the band structure computation for 1D PhC, we mentioned the necessity of the Fourier expansion validation before further computation process. In case of 2D and 3D PhC this should also be done. Here, the example of the validation of 2D dielectric function Fourier expansion will be demonstrated by the Fourier synthesis of dielectric function. The example of computation accuracy examination will also be given.

In order to carry out the validation, it is necessary to synthesize the initial dielectric function using the plane waves and previously computed Fourier expansion coefficients. For 2D case it is necessary to substitute Fourier expansion coefficients into the expression (5.5). In Figs. 5.2 and 5.3, examples of such a validation are given. The PhC with unit cell represented by the rectangular area with dielectric rod inside is taken as an example.

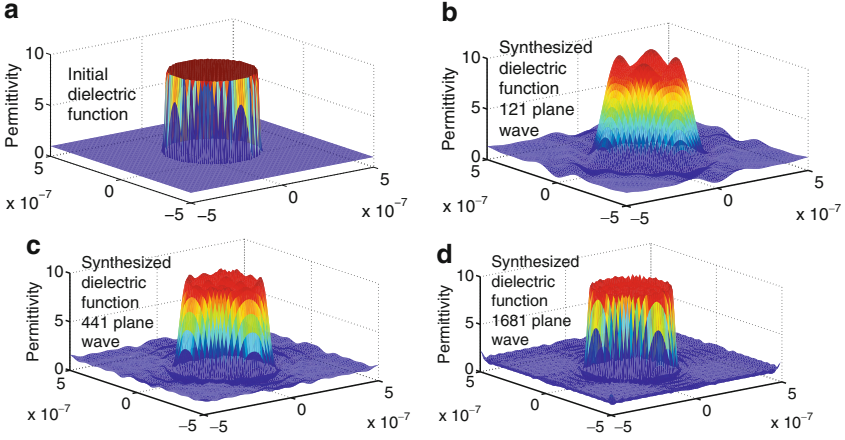


Fig. 5.2. The validation results of the Fourier expansion coefficients computation under constant number of the mesh elements. (a) Initial permittivity distribution within nit cell, (b) Permittivity distribution synthesized from 121 plane waves, (c) Permittivity distribution synthesized from 441 plane waves, (d) Permittivity distribution synthesized from 1681 plane waves

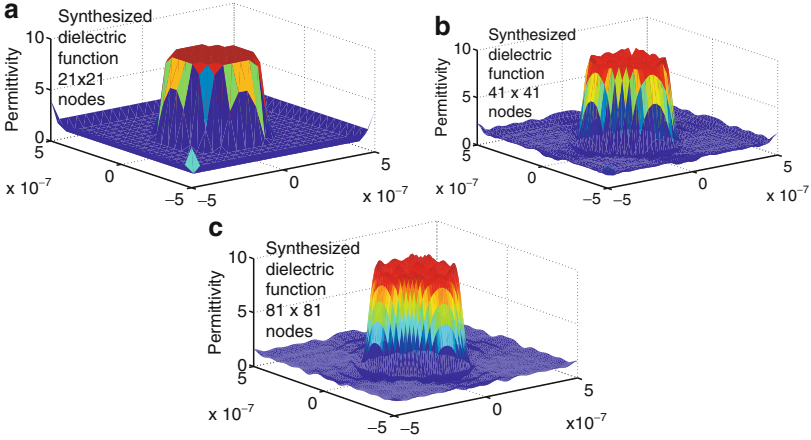


Fig. 5.3. The validation results of the Fourier expansion coefficients computation under constant number of plane waves. (a) Permittivity distribution synthesized for 21×21 mesh elements, (b) Permittivity distribution synthesized for 41×41 mesh elements, (c) Permittivity distribution synthesized for 81×81 mesh elements

In the first case (Fig. 5.2), the number of mesh nodes is constant value (81×81). At that, the number of plane waves for the initial function to be synthesized from, varies from 121 to 1681. It can be easily seen in the

figure that the synthesized function shape approaches stepwise shape shown in sample when the number of plane waves grows.

Figure 5.3 shows the validation results of the Fourier expansion coefficients computation at constant number of plane waves the dielectric function is synthesized from, but for different number of mesh elements. In this case, it is seen that growth of the mesh element number leads to inessential growth of the function quality while neither shape nor permittivity values of the function change.

Thus, after the validation is finished, we can conclude that number of plane waves is the only crucial factor which determines the shape of the synthesized function. The number of mesh elements in this case is not so important while the mesh cell is small enough to provide good discretization. However, it is necessary to remember that large number of plane waves can dramatically increase computation time.

5.4 Wave Vectors Set

When we considered the band structure computation procedure of 1D PhC, variation of the wave vector was limited by the first Brillouin zone. However, due to one-dimensionality of the Brillouin zone, the wave vectors set selection was not the problem. In case of 2D and 3D PhC, variation limits of the wave vectors are still the same and are determined by the first Brillouin zone. However, in contrast to 1D case, the computation of the band structure for all of points inside the Brillouin zone can take a lot of time and is hard to analyze. Instead of this, the high-symmetry points of the Brillouin zone are only considered, which are determined by the group theory [207]. Briefly, the high-symmetry points are those points of the Brillouin zone, which are translated into themselves when rotating Brillouin by 90° , 180° , 30° or 60° depending on the PhC lattice. It is supposed that the band structure is extreme in these points only and between these points it monotonically decreases or increases. Computation of the band structure usually begins from the center of the Brillouin zone. This point is designated by the Greek letter Γ . In this point, the wave vector equals to zero. Then, computation is carried out for all high-symmetry points and returns to the point Γ . The contour obtained by the connection of high-symmetry points is called k -path. As a rule, the PhCs with typical lattices have determined k -path.

The k -paths for the 2D PhC with square and hexagonal lattices are shown in Fig. 5.4(a) and (b), respectively.

For 3D PhC there are a large number of PhC lattice types and the k -paths. Here, in Fig. 5.5 we show the k -path for the PhC with cubic lattice only. As it is seen, the k -path has now a quite complicated shape. Like in 2D case it begins and finishes in Γ point.

To achieve a smoother band structure both in 2D and 3D cases, additional eigen-states may be computed for intermediate wave vectors on the k -path.

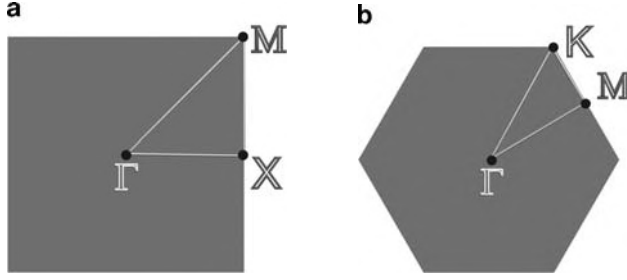


Fig. 5.4. k -Path of the PhC with square (a) and hexagonal (b) lattices

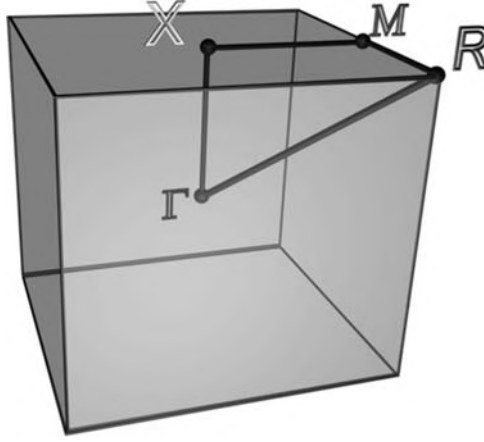


Fig. 5.5. k -Path of the Brillouin zone for the PhC with cubic lattice

5.5 Reciprocal Lattice Vectors Set

The set of the reciprocal lattice vectors should now be selected to provide correct Fourier expansion of the dielectric function and the Bloch functions. When we described the band structure computation of 1D PhC, we pointed out that reciprocal lattice vectors must be selected to form zero-symmetric set. In case of 2D and 3D PhCs, the selection procedure is the same. However, here we have 2D and 3D reciprocal lattice vectors. In this case, the number of the reciprocal lattice vectors in the set is discrete. For instance, for 2D PhC it can take values 1, 9, 25, 49, 81, 121 and so on. The example of the reciprocal lattice vectors set selection is shown in Fig. 5.6. In the figure, the vectors which connect point $(k_x = 0, k_y = 0)$ with corresponding points of neighbour cells of the reciprocal lattice are depicted. These vectors provide translation of the Brillouin zone. Since the number of the reciprocal lattice vectors has to be zero-symmetric, it cannot take an arbitrary number of plane waves such as 80 or 42. Otherwise, this leads to qualitative errors.

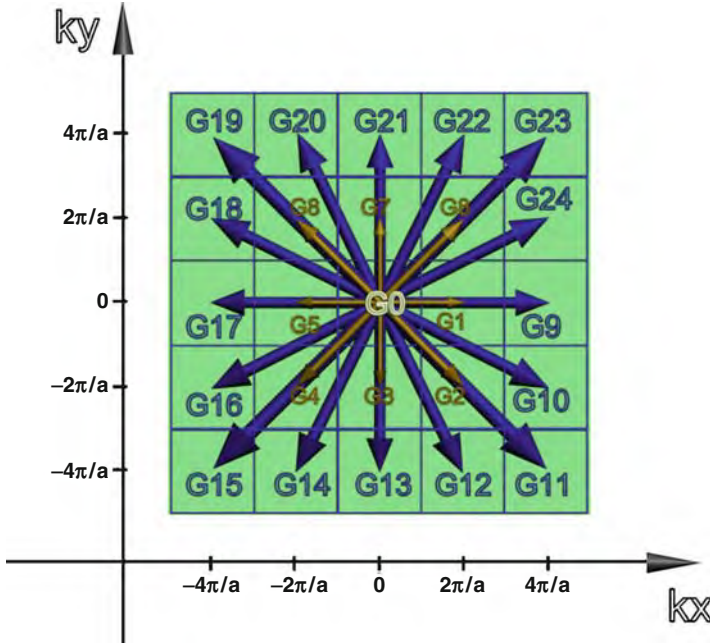


Fig. 5.6. Definition of the set of reciprocal lattice vectors

5.6 Results of the Band Structure Computation

Now, when all preparations are done, we can start the computation itself. For this reason, we find elements of matrix differential operator by formula (4.26) and compose the matrix for 2D of 3D PhC likewise for 1D PhC. Then we are searching for eigen-states of the matrix, which are the set of eigen-states for each value of the wave vector on the k -path.

It is necessary to pay attention to the method of the band structure plotting. If the band structures are plotted directly, the band structure for 2D PhC will be the surface in 3D coordinate system (k_x, k_y, ω) and the band structure for 3D PhC will be represented in 4D coordinate system (k_x, k_y, k_z, ω) . This means that we have to plot 3D or even 4D plots. But 3D plots are very hard to analyze and 4D plots are impossible to draw with standard methods.

In order to avoid such problems, the following can be done. In the plot, high symmetry points lie along horizontal axis while frequency lies along another one. In this case, we will have 2D plot independent of the dimensionality of the PhC. Such a plot is easy to analyze and draw. The example of such a plot is given in Fig. 5.7.

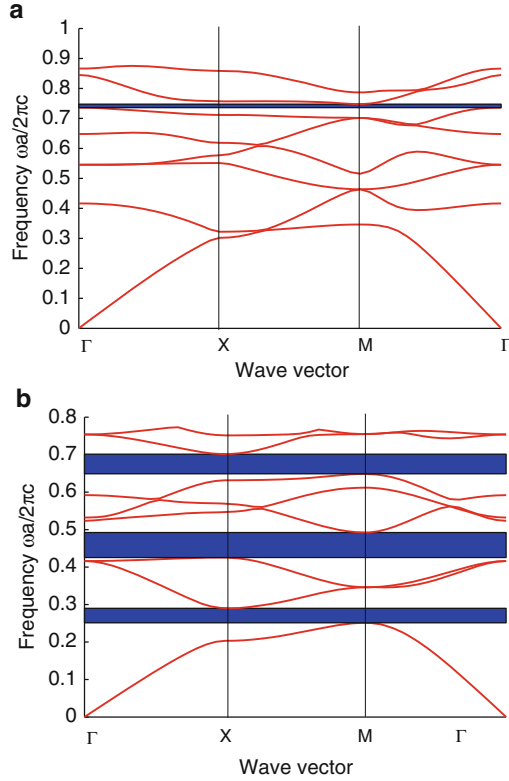


Fig. 5.7. Examples of the band structure of rods arranged to square lattice with $r/a = 0.4$ computed for TE (a) and TM (b) polarizations

5.7 Analysis of the Band Structure

Because the wave vector space is connected with the coordinate space via the relations (4.17), it is quite easy to connect some points of the Brillouin zone with the radiation propagation direction inside the PhC. Thus, we can claim that for each of the directions inside PhC there exist band gap areas as it is shown in Fig. 5.8(a). This means that radiation of the given wavelength cannot propagate inside the PhC under some specific angle. Such areas of wavelengths or frequencies are referred to as partial photonic band gaps.

At some specific frequencies, the band gaps are overlapped forming so-called complete photonic band gap (PBG) (see Fig. 5.8(b)). This means that radiation will not propagate inside the PhC under any angle. The PBG of the PhC can be designated in different ways. One of the ways is to specify frequencies where PBG appears. The second way is to specify percentage which is calculated by formula:

$$\text{PBG} = \frac{\Delta\omega}{\omega_0} \cdot 100\%, \quad (5.26)$$

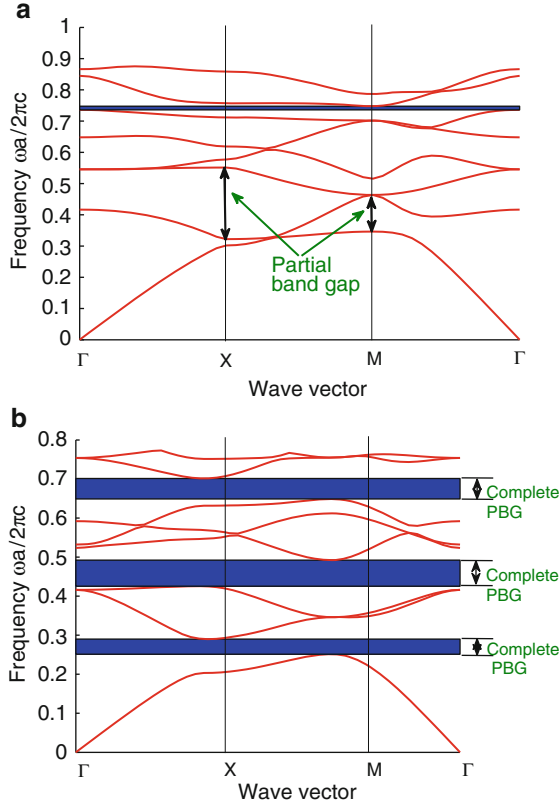


Fig. 5.8. Partial (a) and complete (b) photonic band gaps of the PhC

where $\Delta\omega$ is the half width of the PBG and ω_0 is its center frequency. Besides, investigating the band structure, it is possible to obtain the group velocity of the radiation inside the PhC. The group velocity is determined as the first wave vector derivative of the band structure. Consequently, the more flat the band of the PhC, the lower the group velocity at corresponding frequency.

Thus, the band structure of PhC gives the possibility to find and analyze the PBG which is the crucial moment for a number of practical applications and group velocities which allows to predict the radiation propagation conditions in different directions inside the PhC.

5.8 Photonic Band Gap Maps

When designing a PhC device, it is usually necessary to solve the problem, which aims not to obtain the band structure but to determine PhC parameters from known frequency characteristics. For instance, it is necessary to design

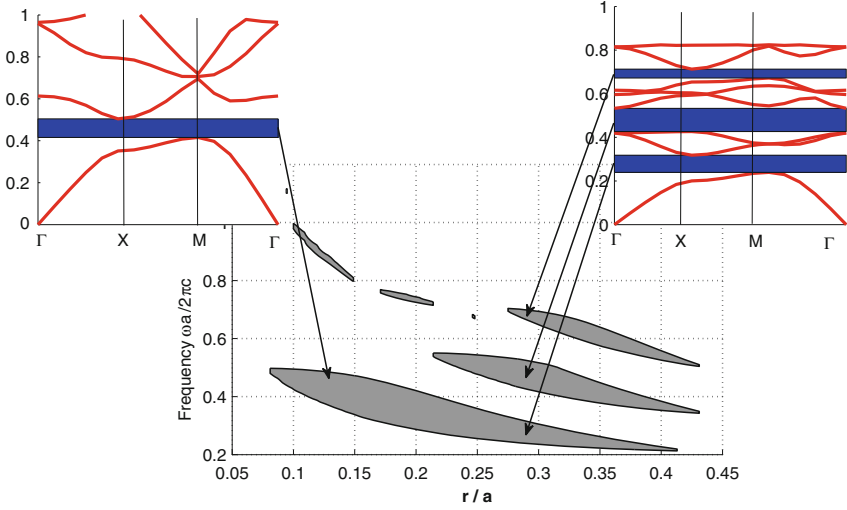


Fig. 5.9. Example of the PBG map formation

a PhC with the PBG at the specific frequency. For this, we need to specify the permittivities of the PhC materials, the size of elements and kind of the PhC lattice.

In order to solve such kind of problems, it is convenient to use so-called PBG maps also known as reduced band structures. The PBG maps are represented by the projection of the complete PBG obtained at different values of the PhC parameter (refractive index, PhC elements size, etc.). The example of such a PBG map is given in Fig. 5.9.

In order to obtain PBG map, computation of the band structure at different values of the PhC parameter is carried out. Then one obtains the information about complete PBG and draws it upon a separate plot as a dependence of parameter's value. This is shown in Fig. 5.9. In the figure, the PBG map of the 2D PhC of the rods arranged to square lattice and the initial band structures computed for two values of the PhC elements radius is also shown. Such band structures form the PBG map. In order to build the PBG map, only the information about complete PBG is taken from the band structure and is presented on the plot as a dependence on the radius. When investigating the PBG map in Fig. 5.9, it is seen that such a PhC have more than one PBG at some frequency range (e.g., in the range of radius from 0.25 to 0.4). When increasing the permittivities contrast, the number of PBGs as well as their width will grow.

The PBG maps can be applied to a broad class of problems when designing complex active and passive devices of the PhC basis. The information provided by these maps gives the possibility to determine PhC parameters at which the PhC has maximum reflectance or partially transmits radiation.

5.9 Photonic Density of States

Just like in semiconductors there is a conception of the density of states; in PhC there is a similar conception of the photonic density of states (PhDOS) or density of modes. The PhDOS is the number of the PhC eigen-states inside the unit frequency range [209].

The PhDOS provides much more information in comparison to the PBG maps from the point of view of spectral properties of the PhC, because it has information about the PhC behavior outside the PBGs while the PBG maps give only the knowledge about the PBGs. However, in order to compute the PhDOS, it is not enough to compute the PhC eigen-sates at several points of the Brilluoin zone because the information obtained in such a wave is not complete. As it was mentioned in the section dedicated to the band structure computation, the band structure computed for all points inside the Brilluoin zone, is the surface. The example of such a band structure is depicted in Fig. 5.10. Each point on the surfaces represents one of the eigen-states of the PhC. If the high-symmetry points are marked on the k_x and k_y axis, connect them with lines and then make a vertical cut at these lines, the cut will form the band structure shown in Fig. 5.8(b).

The computation of the PhDOS consists in counting the number of eigen-states having the specific frequency which can be expressed by the following formula:

$$N(\omega) = \sum_n \int_{\text{BZ}} d^2k \delta(\omega - \omega_n(\mathbf{k})). \quad (5.27)$$

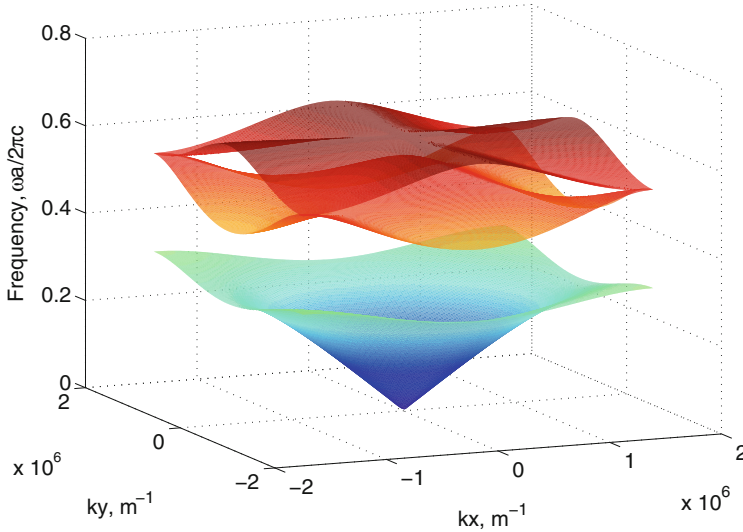


Fig. 5.10. The band structure computed for all k -points inside the Brilluoin zone

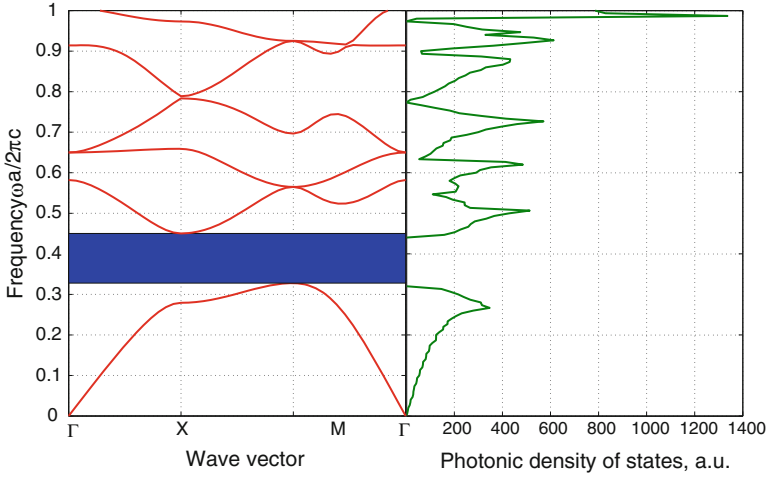


Fig. 5.11. Photonic density of states of 2D PhC

Here the multiplication by the delta-function $\delta(\omega - \omega_n(\mathbf{k}))$ corresponds to making the extract of the eigen-states with the same frequency. After the extraction, integration is carried out. This means summation of eigen-states with the same frequencies within one band. After integration, the summation over all the bands is carried out.

The typical PhDOS has view shown in Fig. 5.11.

Low or zero PhDOS corresponds to the absence of the eigen-states within corresponding frequency range, that is, the PBG. If the PhDOS is large, this corresponds to high number of eigen-states. In other words, the large number of eigen-states correspond to large number of paths the radiation can pass through the PhC and, consequently, the larger the PhDOS, the larger the transmittance of the PhC.

Thus, the PhDOS is the characteristic which allows to take into account spectral properties of the PhC without direct computation of the transmittance coefficients. The characteristic carries more information in comparison to PBG maps and to the band structure. At that it does not require a lot of computer recourses and computation time.

5.10 Off-Plane Band Structure for 2D Photonic Crystal

In case of 2D PhC, situations are possible where the radiation propagates not in the plane of the PhC but under some angle (see Fig. 5.12). The examples of devices utilizing such kind of propagation are the PhC fibers where the radiation propagates along the PhC elements. In case of the off-plane propagation, the k_z -component of the wave vector appears, which is perpendicular to the PhC plane. The band structure in this case can be dramatically modified [205].

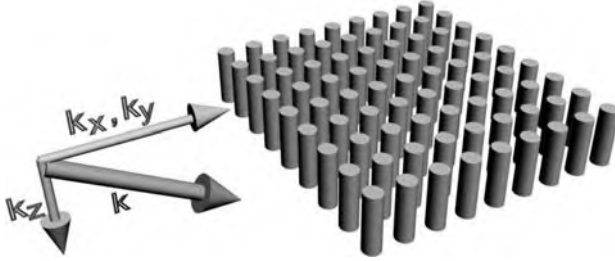


Fig. 5.12. Off-plane radiation propagation inside the PhC

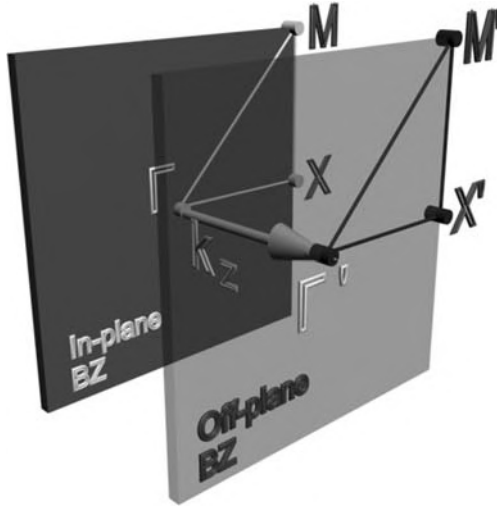


Fig. 5.13. The Brillouin zone for computation of the off-plane band structure

Lets us consider the variations of the band structure which appear with non-zero k_z component. The band structure computation is carried out over the k -path which includes high-symmetry points discussed in Sect. 5 of this chapter. However, since the k_z component of the wave vector is no longer equal to zero, the Brillouin zone appears to be shifted in the z -direction to the value of k_z (see the Fig. 5.13). At that, even in-point of the total wave vector length is no longer equal to zero. And if previously frequency of the first PhC eigen-state in-point was equal to zero, the situation is now changed so that minimum frequency of the first state now differs from zero. Besides, because k_z is now non-zero and for some cases its value can be quite large, for example, in PhC fibers, the variation of k_x and k_y components will make lower contribution to the variation of the total wave vector length. This leads to interesting effect. The variation of the frequency within a single band will be as lower as larger the k_z value. Consequently, the band will be more flat than at $k_z = 0$.

The computation of the off-plane band structure requires the modification of the Brilluoin zone. The modification consists in parallel transition of the Brilluoin zone to along the z -direction by the value of k_z wave vector component. At that, the shape of the Brilluoin zone does not change (see Fig. 5.13). The modification of the Brilluoin zone leads to the matrix differential operator modification. The modification consists of the additional component k_z of the wave vector:

$$\hat{H}_{G,G'} = \chi \left(\mathbf{G}_{x,y} - \mathbf{G}'_{x,y} \right) \left((\mathbf{k}_{x,y,z} + \mathbf{G}'_{x,y}) \cdot (\mathbf{k}_{x,y,z} + \mathbf{G}_{x,y}) \right). \quad (5.28)$$

where $\mathbf{k}_{x,y,z} = \mathbf{k}_x + \mathbf{k}_y + \mathbf{k}_z$ is the 3D wave vector. In Fig. 5.14 the results of in-plane and off-plane band structure computations are shown. The band

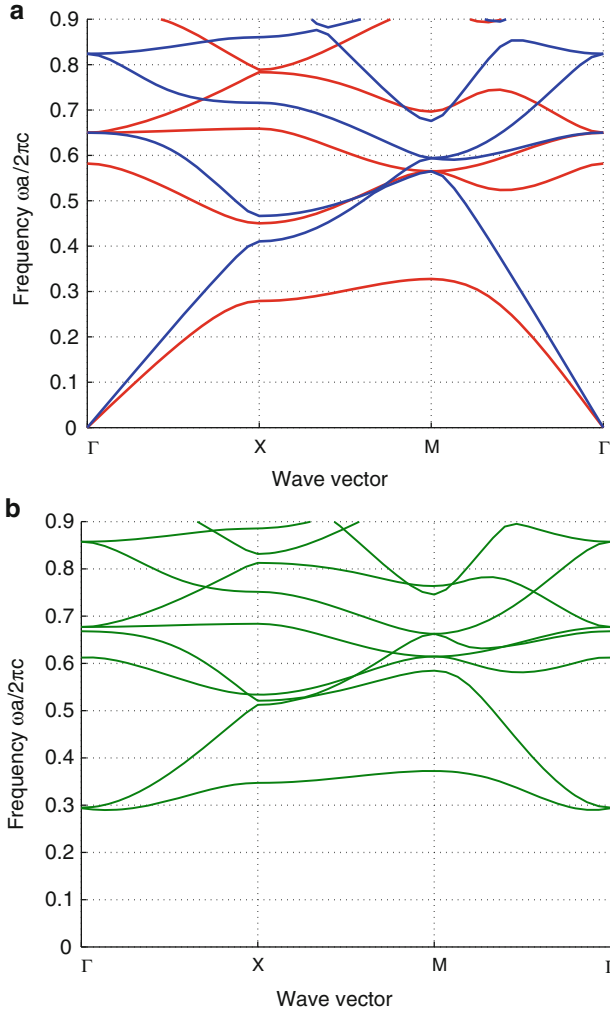


Fig. 5.14. In-plane (a) and off-plane (b) band structures

structures were computed for the same PhC but for different k_z values. The obvious difference of obtained band structures is the fact that the off-plane band structure starts from non-zero value of the frequency. Moreover, if we consider bands with the same number (for instance, the first ones), it can be pointed out that the band of the in-plane band structure lies inside the range of frequencies from 0 to 0.24 while for the off-plane structure the limits are from 0.23 to 0.33, that is, it occupies the frequency range which is 2.4 times smaller for in-plane band structure.

As a result of the lowering of the frequency range occupied by the separate bands, at some high values of the k_z the PBGs can appear which are not present when the in-plane propagation is considered. Such an effect will be considered in detail in Chap. 6 which is dedicated to the PhC fibers. Due to the existence of the PBG at high values of k_z , it becomes possible for the waveguiding effect appearance which is fundamentally different from the total internal refraction effect used in conventional step-index fiber.

5.11 Band Structure Computation of the PhC with Defect

The defect of the periodic structure means some kind of violation of the PhC strict periodicity. This may be, for instance, missing rod or hole as well as elements displacement. In any case, the optical properties of such kind of structures differ from ones of pure PhC. In the introduction, we mentioned the similarities between solid-state crystal and photonic crystal. One of crucial similarities was connected with defect embedded to the structure. In both solid-state and photonic crystals, the eigen-states appear inside the forbidden energy range which allows the radiation or particles with such energies to exist inside the structure.

We will now investigate this phenomenon in detail and consider the method for the band structure computation of the PhC with defect.

One of the most convenient methods used in this case is the plane wave expansion method described in this chapter as well as in Chap. 4. As we know, the PWE method deals with strictly periodic structures only. That is why we have to use artificial method for the structure with defect. We extract from the PhC the area with defect inside it. The area may be of 5 or 6 elements in each dimension. Then we translate this area over all directions and obtain a new structure where the selected area forms new unit cell of the PhC. Corresponding lattice vectors are changed as well. After that, we compute the band structure of the PhC with new unit cell as we made this for strictly periodic one.

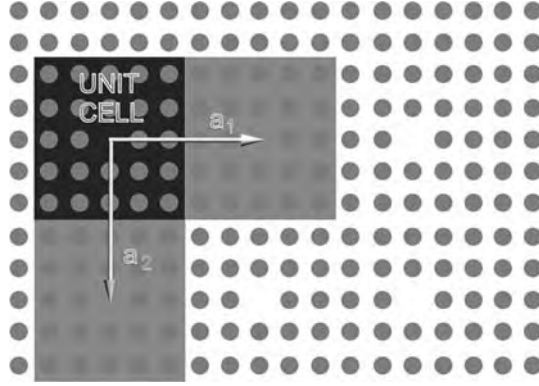


Fig. 5.15. Translated defect of the PhC, its unit cell and lattice vectors

The computation procedure now is the following:

1. Determine the unit cell of the PhC containing defect. In our case, the unit cell should be large enough to insulate translated defects from interaction with each other. For this, we should take the unit cell including at least 5 or 6 PhC elements as shown in Fig. 5.15. On the other hand, the unit cell should not be too large to avoid long computation time.
2. The range of the wave vectors is still limited by a Brillouin zone.
3. Define the set of the reciprocal lattice vectors. Since the PhC unit cell possesses complex refractive index profile and it has relatively small elements as compared with unit cell size, the number of reciprocal lattice vectors should be larger than that for strictly periodic structure. This allows to take into account more harmonics with higher frequencies to reproduce in detail the refractive index profile.
4. Form the matrix differential operator for each wave vector value within defined set and compute its eigen-values. This step is similar to the one for strictly periodic PhC.

Figure 5.16 shows the band structure of the PhC with defect and corresponding defectless structure. We can see that the eigen-state appears within forbidden frequency range. This means that the radiation possessing this frequency can propagate inside such a PhC.

There is another important detail the attention should be paid to. The eigen-frequency of the defect state does not depend on the radiation wave vector. This means that the defect eigen-frequency is the same for all propagation directions. This property of the defect is very important for modeling of such applications as PhC fibers or PhC waveguides since we may proceed with computation for a single value of the wave vector \mathbf{k} .

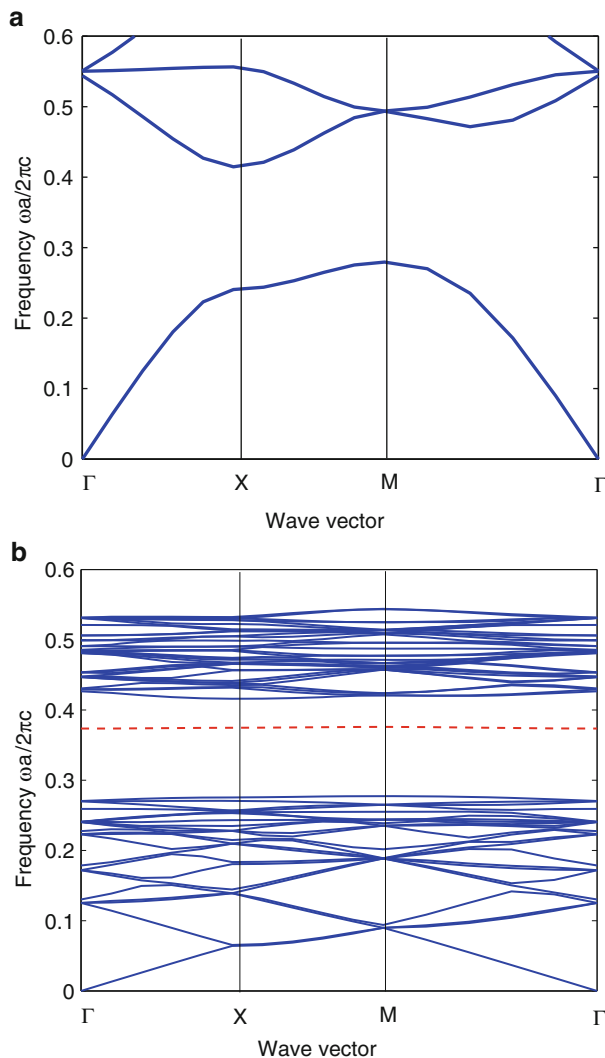


Fig. 5.16. The band structure of the PhC with defect (b) and corresponding defectless structure (a)

5.12 Experimental Verification of the PWE Method

Let us consider a simple example of the band structure computation of the real structure.

The band structure may be obtained in many different ways such as PWE method or finite-difference time domain method which will be discussed in Chap. 8. Another way is to analyze the reflectance spectra obtained for different radiation propagation directions. In [214], such an experimental

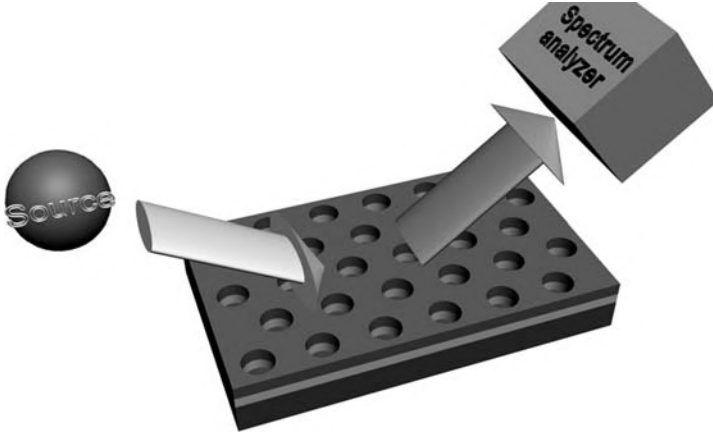


Fig. 5.17. The experimental setup for the band structure measurement

investigation of the band structure is described. The investigation was carried out for the PhC etched inside the layered structure which consists of $Al_{12}Ga_{88}As$ surrounded by $Al_{35}Ga_{65}As$ and $GaAs$. Such a sandwich structure formed the waveguide. Employing electron beam lithography with further ion etching, the periodic pattern of holes was created arranged to hexagonal lattice. The period of the structure was 360 nm and radius of the holes was taken to be equal to 100 nm.

In order to obtain the band structure, the structure was irradiated by plane parallel white light from a tungsten-halogen lamp as shown in Fig. 5.17. The spectrum of the radiation reflected from the sandwich was analyzed by the grating spectrometer. The measurement was carried out for different angles which corresponded to different directions in the band structure. After the analysis of the reflectance spectrum, the eigen-values were obtained and compared with theoretically obtained band structures.

Here, we use results obtained in [214] to verify the PWE method. Since we use the numerical method, we introduce some simplifications. First, we neglect finite thickness of the waveguide and assume that we have pure 2D PhC which has uniform dielectric constant distribution along the third dimension. Another approximation used here is that all the holes' radii and shapes are the same while in real structure some deviations take place. At last, we neglect the chromatic dispersion and the absorption of the material the PhC is made of. The only approximation which may cause essential difference between experimental and theoretical results is the first one which actually neglects total internal reflection from the layers interface. The analysis of experimental results carried out in [214] shows also the effect of planar waveguide to appearance of narrow gaps at the anti-crossing points obtained by the PWE method.

The experimental data and the band structure obtained by the PWE method as described in this chapter, are presented in Fig. 5.18. The insertion of the figure shows whole band structure of the PhC obtained by the PWE method. The rectangle in the insertion indicated the area depicted in the main figure we consider in detail. Let us now consider the main figure. As we discussed above, we do not take into account the “sandwich” structure the PhC is made in. However, this may be corrected by introducing “light lines” which correspond to conditions of total internal reflection from the lower layer and, therefore, only the computation results above the “light lines” should be considered. The blue lines in figure correspond to “light lines” of the PhC considered and were also introduced by the authors of [214]. Then, we proceed with the analysis of the experimental data. The red solid lines correspond to experimental data of the band structure. The method of such an experimental measurement of the band structure is concluded in the transmittance spectrum measurement of the PhC for the radiation that incidents the structure under different angles. The transmittance spectra had local minima and maxima which actually correspond to certain phase conditions which are determined by the wave vector. Namely, when the phase conditions provide constructive interference, the maximum of transmittance takes place. On the other hand, the situation is vice versa in case of the destructive interference. For example, when we have the finite-size PhC formed by N unit cells, the conditions of constructive interference along the ΓM direction may be written as follows:

$$k = \pi m / Na, \quad (5.29)$$

where m is an integer varying from 1 to N .

Taking corresponding transmittance peaks and plotting them versus wave vector, we obtain the band structure.

Now we compare the experimental results with the ones obtained by the PWE method. The computed band structure for TE polarization is shown by solid black line while dashed black lines represent TM band structure.

We can see good qualitative agreement between the theoretical and experimental results. Particularly, within $\Gamma - M$ direction there are two experimentally obtained anti-crossing points which differ from the theoretical ones by 5–10 meV while the anti-crossing point within $\Gamma - K$ direction almost coincides with the one obtained by PWE method. As a whole, the deviation between experimentally obtained bands and corresponding theoretical data does not exceed 10 meV. This indicates that assumptions described above do not introduce essential error to the computation results.

Thus, it can be concluded that the PWE method appears to be a powerful and quite an accurate method which can be effectively used for the design of such passive PhC-based devices as filters, waveguides, splitters, demultiplexers, etc.

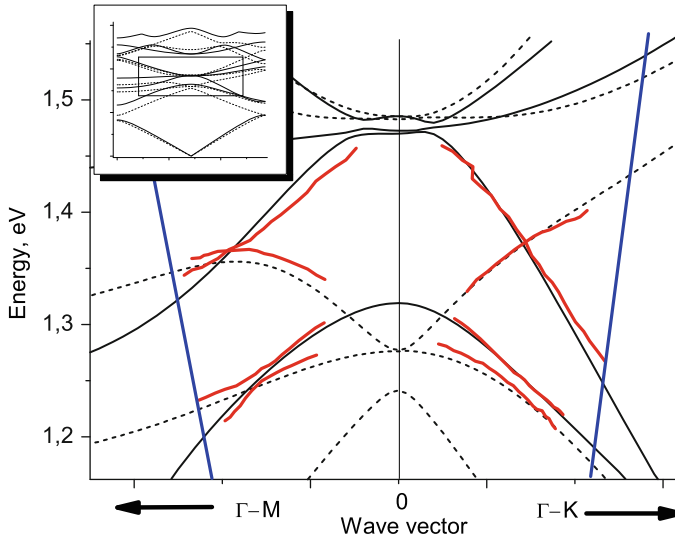


Fig. 5.18. The band structure obtained by PWE method with corresponding experimental data

5.13 Advantages and Disadvantages of the Plane Wave Expansion Method

Concluding the PWE method description, it is necessary to mention its main advantages and disadvantages and the limits of its applicability.

1. The main advantage of the PWE method is high performance. For the simplest structure, computation takes several seconds. At that, the system requirements are very unpretentious.
2. The PWE method allows to compute the band structure not only for the simplest PhCs like infinite periodic structures but for more complicated structures such as point defects, PhC waveguides and PhC fibers.
3. Besides, the method allows to compute the field distribution for each of eigen-states of the PhC which is extremely convenient when designing PhC-based active devices as well as investigating PhC fibers.

However, except the irrefutable advantages, it should be mentioned that the method has some essential disadvantages:

1. Inability to treat losses. The differential operator in Helmholtz equation is Hermitian only in case of lossless material. When one considers materials with losses, the imaginary part of the refractive index appears which makes the application of the method impossible.
2. As it was shown, the method consists of searching for the set of eigen-frequencies at the specific value of the wave vector. In order for the algorithm to make sense, the permittivity should be the same at all frequencies

within the computation range. Thus, without additional modifications, the method is unable to treat dispersive materials.

However, in spite of all the disadvantages, the area of the method applications is very large. The method gives the possibility to estimate the characteristics of linear and nonlinear devices. For more precise analysis, some other methods such as the finite differences time domain method can be used.

5.14 Summary

1. 3D PhC is represented by an infinite structure which is periodical in 3 dimensions. 2D PhC is represented by the structure which is periodical in 2 dimensions while in the 3rd dimension the permittivity is constant. Each of periods of such a PhC is the unit cell. The translation of the unit cell over all possible lattice vectors allows to fill the whole space.
2. Mathematical description of the unit cell, lattice vectors and reciprocal lattice vectors is much more complicated for 2D and 3D than for 1D PhC, because of large number of lattice types.
3. The method of the band structure computation is similar to that for 1D case. Main difference consists of the fact that the band structure is computed for only several points inside the Brillouin zone which are high symmetry points.
4. The derivation of the Fourier expansion coefficient for 2D and 3D PhC in analytical form is possible for the simplest cases only.
5. The most important applications are PBG maps which allow to solve the optimal parameters selection problem, PhDOS computation which provides the information about spectral properties of the PhC and the computation of eigen-states of PhC waveguides and fibers.
6. The computation of the PhDOS is carried out by the analysis of the band structure obtained for all points inside the Brillouin zone. The PhDOS provides the information about transmittance of the PhC outside the PBG which allows to carry out the precise analysis.
7. Off-plane band structures can be used for the investigation of modal properties as well as for the design of PhC optical fibers.

5.15 MATLAB Program for Band Structure Computation of 2D PhC by Means of PWE Method

```
%The program for the computation of the PhC photonic
%band structure for 2D PhC.
%Parameters of the structure are defined by the PhC
%period, elements radius, and by the permittivities
%of elements and background material.
```

```

%Input parameters: PhC period, radius of an
%element, permittivities
%Output data: The band structure of the 2D PhC.

clear all;

%The variable a defines the period of the structure.
%It influences on results in case of the frequency
%normalization.
a=1e-6; % in meters

%The variable r contains elements radius. Here it is
%defined as a part of the period.
r=0.4*a; % in meters

%The variable eps1 contains the information about
%the relative background material permittivity.
eps1=9;

%The variable eps2 contains the information about
%permittivity of the elements composing PhC. In our
%case permittivities are set to form the structure
%perforated membrane
eps2=1;

%The variable precis defines the number of k-vector
%points between high symmetry points
precis=5;

%The variable nG defines the number of plane waves.
%Since the number of plane waves cannot be
%arbitrary value and should be zero-symmetric, the
%total number of plane waves may be determined
%as  $(nG*2-1)^2$ 
nG=4;

%The variable precisStruct defines contains the
%number of nodes of discretization mesh inside in
%unit cell discretization mesh elements.
precisStruct=30;

%The following loop carries out the definition
%of the unit cell. The definition is being
%made in discreet form by setting values of inversed

```

```

%dielectric function to mesh nodes.
nx=1;
for countX=-a/2:a/precisStruct:a/2
    ny=1;
    for countY=-a/2:a/precisStruct:a/2
        %The following condition allows to define the circle
        %with of radius r
        if(sqrt(countX^2+countY^2)<r)
            %Setting the value of the inversed dielectric
            %function to the mesh node
            struct(nx,ny)=1/eps2;
        %Saving the node coordinate
            xSet(nx)=countX;
            ySet(ny)=countY;
        else
            struct(nx,ny)=1/eps1;
            xSet(nx)=countX;
            ySet(ny)=countY;
        end
        ny=ny+1;
    end
    nx=nx+1;
end

%The computation of the area of the mesh cell. It is
%necessary for further computation of the Fourier
%expansion coefficients.
dS=(a/precisStruct)^2;

%Forming 2D arrays of nods coordinates
xMesh=meshgrid(xSet(1:length(xSet)-1));
yMesh=meshgrid(ySet(1:length(ySet)-1))';

%Transforming values of inversed dielectric function
%for the convenience of further computation
structMesh=struct(1:length(xSet)-1,...
    1:length(ySet)-1)*dS/(max(xSet)-min(xSet))^2;

%Defining the k-path within the Brilluoin zone. The
%k-path includes all high symmetry points and precis
%points between them
kx(1:precis+1)=0:pi/a/precis:pi/a;
ky(1:precis+1)=zeros(1,precis+1);

```

```

kx(precis+2:precis+precis+1)=pi/a;
ky(precis+2:precis+precis+1)=...
    pi/a/precis:pi/a/precis:pi/a;
kx(precis+2+precis:precis+precis+1+precis)=...
    pi/a-pi/a/precis:-pi/a/precis:0;
ky(precis+2+precis:precis+precis+1+precis)=...
    pi/a-pi/a/precis:-pi/a/precis:0;

%After the following loop, the variable numG will
%contain real number of plane waves used in the
%Fourier expansion
numG=1;

%The following loop forms the set of reciprocal
%lattice vectors.
for Gx=-nG*2*pi/a:2*pi/a:nG*2*pi/a
    for Gy=-nG*2*pi/a:2*pi/a:nG*2*pi/a
        G(numG,1)=Gx;
        G(numG,2)=Gy;
        numG=numG+1;
    end
end

%The next loop computes the Fourier expansion
%coefficients which will be used for matrix
%differential operator computation.
for countG=1:numG-1
    for countG1=1:numG-1
        CN2D_N(countG,countG1)=sum(sum(structMesh.*...
            exp(1i*((G(countG,1)-G(countG1,1))*...
                xMesh+(G(countG,2)-G(countG1,2))*yMesh)))));
    end
end

%The next loop computes matrix differential operator
%in case of TE mode. The computation
%is carried out for each of earlier defined
%wave vectors.
for countG=1:numG-1
    for countG1=1:numG-1
        for countK=1:length(kx)
            M(countK,countG,countG1)=...
CN2D_N(countG,countG1)*((kx(countK)+G(countG,1))*...
                (kx(countK)+G(countG1,1))+...
            (ky(countK)+G(countG,2))*(ky(countK)+G(countG1,2)));

```



```

    end
  end
end

%The computation of eigen-states is also carried
%out for all wave vectors in the k-path.
for countK=1:length(kx)
%Taking the matrix differential operator for current
%wave vector.
    MM(:,:)=M(countK,,:);
%Computing the eigen-vectors and eigen-states of
%the matrix
    [D V]=eig(MM);
%Transforming matrix eigen-states to the form of
%normalized frequency.
    dispe(:,countK)=sqrt(V*ones(length(V),1))*a/2/pi;
end

%Plotting the band structure

%Creating the output field
figure(3);
%Creating axes for the band structure output.
ax1=axes;
%Setting the option
%drawing without cleaning the plot
hold on;
%Plotting the first 8 bands
for u=1:8
    plot(abs(dispe(u,:)), 'r', 'LineWidth', 2);
%If there are the PBG, mark it with blue rectangle
    if(min(dispe(u+1,:))>max(dispe(u,:)))
        rectangle('Position',[1,max(dispe(u,:)),...
            length(kx)-1,min(dispe(u+1,:))-...
                max(dispe(u,:))], 'FaceColor', 'b', ...
                    'EdgeColor', 'b');
    end
end
%Signing Labeling the axes
set(ax1, 'xtick', ...
    [1 precis+1 2*precis+1 3*precis+1]);
set(ax1, 'xticklabel', ['G'; 'X'; 'M'; 'G']);
ylabel('Frequency \omega a/2\pi c', 'FontSize', 16);
xlabel('Wavevector', 'FontSize', 16);

```

```
xlim([1 16])
set(ax1,'XGrid','on');
```

The program for the computation of 2D PhC band structure is much more complex than the one for 1D PhC. There are more peculiarities such as definition of permittivity distribution inside unit cell. That is why the program has seven blocks. Let us consider them in detail.

The first block is for the variables initialization. Here, the parameters of the structure and the computation accuracy are defined. The PhC is defined by the lattice constant and the elements radius. The number of plane waves and the number of points in k -path determine the accuracy of the computation.

In the second block, the permittivity distribution inside the unit cell is defined. Here, we consider the PhC with square lattice and circular elements so the definition is carried out by one loop. After this block is computed, we have three 2D arrays containing x -coordinate of each point, y -coordinate of each point and the permittivity values within these points.

The third block sets up the k -path and the set of reciprocal lattice vectors. Since we consider the PhC with square lattice with side a , the Brillouin dimensions are equal to $2\pi/a$ in both k_x and k_y directions. Taking this into account, we are setting up the k -path through points Γ , X , M , Γ (see Fig. 5.4(a)). The size of the reciprocal lattice vectors can be found from the expression $(2 \cdot nG + 1)^2$. The x and y components of the set is written to the corresponding array.

In the fourth block, the Fourier expansion coefficients are computed for each value of \mathbf{G} and \mathbf{G}' within the above selected set. The computation is carried out in accordance with the expression (5.25). The result is stored in 2D array. As in case of 1D PhC, the Fourier expansion coefficients are computed before the matrix differential operator formation since it does not depend on the wave vector.

The fifth block forms the matrix differential operator using stored values of the Fourier expansion coefficients in accordance with expression (4.26).

In the sixth block, the eigen-values of matrix differential operator are found at each value of wave vector within the k -path and stored to the array.

The stored eigen-values are then plotted as function of the wave vectors taken from the k -path array. We may plot several lower eigen-values only since the PBGs are usually observed at low frequencies in strictly periodic 2D PhCs. The axes are then signed.

The program results are shown in Fig. 5.19. We can see three PBGs between the first and the second bands, between the second and the third bands and between the fourth and fifth bands. As discussed in the previous chapter, the relative frequency $\omega a/2\pi c$ lies on the vertical axis. However, the values on the horizontal axis differ from those of 1D band structure. Here, we set the wave vector values from the Brillouin zone symmetry points as shown in Fig. 5.4(a). Only with this technique we can plot the 2D PhC band structure

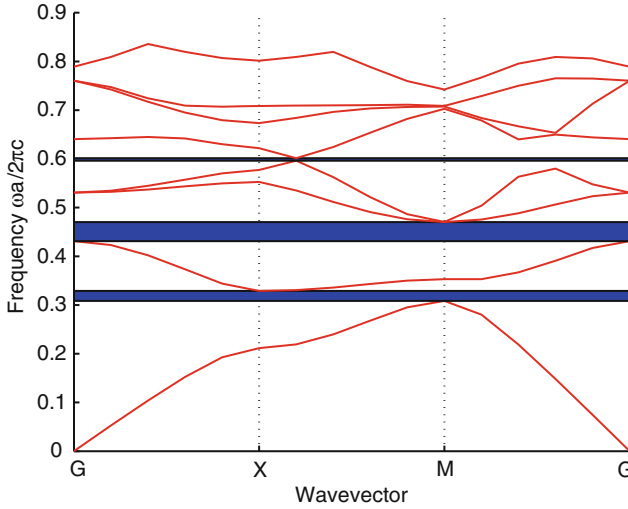


Fig. 5.19. Results of the program. The band structure of 2D PhC

on the 2D plot. Otherwise, the results should be presented in 3D plot or surface as shown in Fig. 5.10.

5.16 Problems and Questions

Problem 5.1. Derive the 3D Helmholtz equation for electric and magnetic fields.

Problem 5.2. Write down the Bloch function.

Problem 5.3. Write down the master equations for 3D case.

Problem 5.4. What is the difference between TE and TM polarizations for 2D PhC?

Problem 5.5. Write down the analytical expression for Fourier expansion coefficient of the 3D PhC unit cell presented by spheres in vacuum.

Problem 5.6. Write down the analytical expression for Fourier expansion coefficient of the 2D PhC unit cell presented by rods in vacuum.

Problem 5.7. Derive the expression for the Fourier expansion coefficient of the unit cell with arbitrary variation of the permittivity.

Problem 5.8. What are PBG maps? How can they be computed?

Problem 5.9. What is photonic density of states? Write down the expression for the photonic density of states computation.

Problem 5.10. Which case is referred to as off-plane radiation propagation?

Problem 5.11. Write down the element matrix differential operator for off-plane band structure computation.

Problem 5.12. Modify the example program to compute the band structure of 2D PhC with hexagonal lattice.

Problem 5.13. Modify the example program to compute the band structure of 2D PhC with square lattice the unit cell of which contains two rods of different radius.

Finite-Difference Time-Domain Method for PhC Devices Modeling

Summary. Chapter 6 provides an introduction to finite-difference time-domain method. Problem formulation for field distribution computation by means of this method is discussed in this chapter. Then all stages of solution are analyzed in detail based on the practical experience of the authors. Discretization of Maxwell's equations and definition of the dielectric function are presented. All steps of the initial and boundary conditions definition are analyzed and stability of the method is discussed. Finally, the original Matlab codes for computation of optical field distribution in nonuniform optical medium is discussed and several problems and questions for self-training are given.

6.1 Problem Formulation for the Field Distribution Computation: Finite-Difference Time-Domain Method

In the previous chapters plane wave expansion method was given which allows eigen-states calculation for an infinite periodic structure. The method also allows calculation of field distributions which correspond to those states. However, if we need to find field distribution in complicated structure or investigate dynamic characteristics, plane wave expansion method is inapplicable.

For investigation of the field distribution in complicated PhC devices numerical methods are used such as finite-difference time-domain method (FDTD), beam propagation method, mode matching method, coupling modes method, matrix methods, multipole method, ray tracing method, method of lines, method of moments, etc. However, the FDTD method will be considered in detail here due to its flexibility to treat almost any problem.

The FDTD method is one of the most advanced methods today for computation of the field distribution inside the PhC-based devices which are actually optical structures with non-uniform refractive index distribution. This is one of the simplest and universal numerical methods. Briefly, it consists of discretization of the space, i.e., in replacement of the continuum space by a discrete set of nodes. After that, derivatives in Maxwell's equations are

replaced by finite differences that results in a system of algebraic equations which are linear on coordinates. Such a system is solved sequentially starting from initial and boundary conditions.

Thus, the FDTD method allows to find the field distribution by solving the system of Maxwell's equations upon the discrete mesh. The solution is based on the following data:

- Permittivity distribution function which determines radiation propagation conditions.
- Initial conditions which constitute such radiation parameters as the wavelength (or the radiation spectrum for non-monochromatic wave), the amplitude and the initial phase.
- Boundary conditions which determine the radiation behavior at the boundary of the computation region.

After all these conditions are set, the field distribution is computed step-by-step starting from the radiation source.

6.2 Maxwell's Equations Discretization

Before the computation starts, it is first necessary to derive the Maxwell's equations in terms of finite differences [215]. To do this, we write down the equations for the medium without the dispersion, absorption or the light generation:

$$\begin{aligned}\nabla \times \mathbf{E}(\mathbf{r}, t) &= -\frac{1}{c} \frac{\partial \mathbf{B}(\mathbf{r}, t)}{\partial t}, \\ \nabla \times \mathbf{H}(\mathbf{r}, t) &= \frac{1}{c} \frac{\partial \mathbf{D}(\mathbf{r}, t)}{\partial t}.\end{aligned}\tag{6.1}$$

We now expand the curl operators and write separately the equations by vector components. Each equation corresponds to one direction so we obtain:

$$\begin{aligned}\frac{\partial}{\partial y} E_z - \frac{\partial}{\partial z} E_y &= -\frac{1}{c} \frac{\partial}{\partial t} B_x, \\ \frac{\partial}{\partial z} E_x - \frac{\partial}{\partial x} E_z &= -\frac{1}{c} \frac{\partial}{\partial t} B_y, \\ \frac{\partial}{\partial x} E_y - \frac{\partial}{\partial y} E_x &= -\frac{1}{c} \frac{\partial}{\partial t} B_z, \\ \frac{\partial}{\partial y} H_z - \frac{\partial}{\partial z} H_y &= \frac{1}{c} \frac{\partial}{\partial t} D_x, \\ \frac{\partial}{\partial z} H_x - \frac{\partial}{\partial x} H_z &= \frac{1}{c} \frac{\partial}{\partial t} D_y, \\ \frac{\partial}{\partial x} H_y - \frac{\partial}{\partial y} H_x &= \frac{1}{c} \frac{\partial}{\partial t} D_z.\end{aligned}\tag{6.2}$$

Main principle of the FDTD method is discretization of the space, i.e. replacing all of partial derivatives by differences $\partial/\partial x \approx \Delta/\Delta x$, $\partial/\partial y \approx \Delta/\Delta y$,

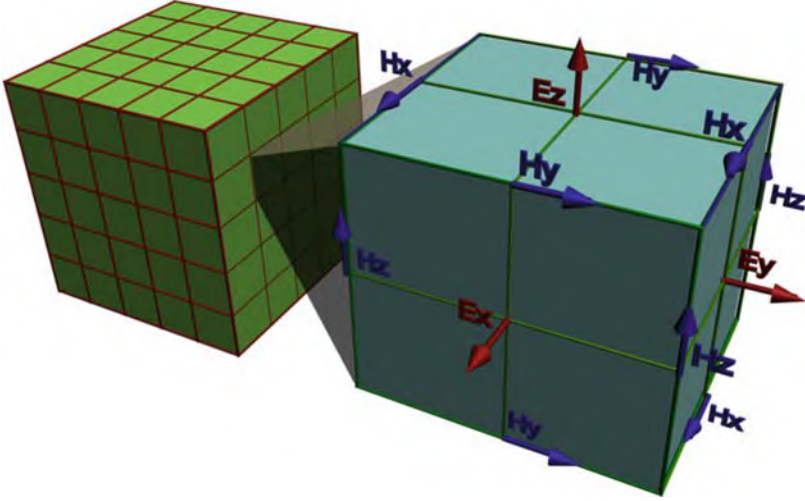


Fig. 6.1. 3D mesh and calculation scheme within single cell used for FDTD method

$\partial/\partial z \approx \Delta/\Delta z$. Thus, the derivative is now represented by its approximate value which is function variation divided by the argument variation taken at different mesh nodes (Fig. 6.1). In the figure, discretization of the computation region by the square mesh is shown. To the right, a single cell of the mesh is shown with all corresponding components of the field vectors. Solving the system of Maxwell's equations by the FDTD method, we obtain values of the fields intensity in each mesh node.

Having the system (6.2) and changing the derivatives by differences it is quite easy to obtain recurrent expression which gives the value of the field component in some node of the mesh using known values of the field components in adjacent nodes. It is also necessary to apply the material equations (2.5) and (2.6) to the system (6.2), which give the relation between electric intensity and displacement and between the magnetic intensity and induction. It is convenient now to work within the CGS system of units instead of SI system. The permittivity and permeability in this unit system are equal to one so the expressions become much easier. The obtained recurrent formula are as follows:

$$\begin{aligned}
 H_{x(i,j,k)}^{n+1/2} &= H_{x(i,j,k)}^{n-1/2} + \frac{c\Delta t}{\mu\Delta z} \left(E_{y(i,j,k+1/2)}^n - E_{y(i,j,k-1/2)}^n \right) - \\
 &\quad - \frac{c\Delta t}{\mu\Delta y} \left(E_{z(i,j+1/2,k)}^n - E_{z(i,j-1/2,k)}^n \right), \\
 H_{y(i,j,k)}^{n+1/2} &= H_{y(i,j,k)}^{n-1/2} + \frac{c\Delta t}{\mu\Delta x} \left(E_{z(i+1/2,j,k)}^n - E_{z(i-1/2,j,k)}^n \right) - \\
 &\quad - \frac{c\Delta t}{\mu\Delta z} \left(E_{x(i,j,k+1/2)}^n - E_{x(i,j,k-1/2)}^n \right),
 \end{aligned}$$

$$\begin{aligned}
H_{z(i,j,k)}^{n+1/2} &= H_{z(i,j,k)}^{n-1/2} + \frac{c\Delta t}{\mu\Delta y} \left(E_{x(i,j+1/2,k)}^n - E_{x(i,j-1/2,k)}^n \right) - \\
&\quad - \frac{c\Delta t}{\mu\Delta x} \left(E_{y(i+1/2,j,k)}^n - E_{y(i-1/2,j,k)}^n \right), \\
E_{x(i,j,k)}^{n+1} &= E_{x(i,j,k)}^n + \frac{c\Delta t}{\varepsilon\Delta y} \left(H_{z(i,j+1/2,k)}^{n+1/2} - H_{z(i,j-1/2,k)}^{n+1/2} \right) - \\
&\quad - \frac{c\Delta t}{\varepsilon\Delta z} \left(H_{y(i,j,k+1/2)}^{n+1/2} - H_{y(i,j,k-1/2)}^{n+1/2} \right), \\
E_{y(i,j,k)}^{n+1} &= E_{y(i,j,k)}^n + \frac{c\Delta t}{\varepsilon\Delta z} \left(H_{x(i,j,k+1/2)}^{n+1/2} - H_{x(i,j,k-1/2)}^{n+1/2} \right) - \\
&\quad - \frac{c\Delta t}{\varepsilon\Delta x} \left(H_{z(i+1/2,j,k)}^{n+1/2} - H_{z(i-1/2,j,k)}^{n+1/2} \right), \\
E_{z(i,j,k)}^{n+1} &= E_{z(i,j,k)}^n + \frac{c\Delta t}{\varepsilon\Delta x} \left(H_{y(i+1/2,j,k)}^{n+1/2} - H_{y(i-1/2,j,k)}^{n+1/2} \right) - \\
&\quad - \frac{c\Delta t}{\varepsilon\Delta y} \left(H_{x(i,j+1/2,k)}^{n+1/2} - H_{x(i,j-1/2,k)}^{n+1/2} \right).
\end{aligned} \tag{6.3}$$

Expressions (6.3) indicate that values of the magnetic field intensity are taken with time shift as related to the electric field. This fact allows us to carry out the step-by-step (recurrent) computation of the electric field and then the magnetic field starting from one side of the computation mesh and moving to another side. The values of the electric and magnetic field components are taken from the internodes $(i+1/2, j+1/2, k+1/2)$ and $(i-1/2, j-1/2, k-1/2)$ to allow central differences approximation. Computation is carried out over and over again for different time moments until required computation time is achieved. In case of 2D PhC, the problem is separated into two independent cases, namely, we consider separately TE and TM polarizations. In case of TM polarization, as it was defined in the Chap. 5, we have a non-zero electric field component which is parallel to the PhC elements and magnetic field components lying in the plane of PhC. All other electric and magnetic field components are equal to zero. At that, the system (6.2) is significantly simplified acquiring the following form:

$$\begin{aligned}
\frac{\partial}{\partial y} E_z &= -\frac{1}{c} \frac{\partial}{\partial t} B_x, \\
-\frac{\partial}{\partial x} E_z &= -\frac{1}{c} \frac{\partial}{\partial t} B_y, \\
\frac{\partial}{\partial x} H_y - \frac{\partial}{\partial y} H_x &= \frac{1}{c} \frac{\partial}{\partial t} D_z.
\end{aligned} \tag{6.4}$$

Recurrent formula for computation of the field distribution taken in this case is of the following form:

$$H_{x(i,j)}^{n+1/2} = H_{x(i,j)}^{n-1/2} - \frac{c\Delta t}{\mu\Delta y} \left(E_{z(i,j+1/2)}^n - E_{z(i,j-1/2)}^n \right),$$

$$\begin{aligned}
H_{y(i,j)}^{n+1/2} &= H_{y(i,j)}^{n-1/2} + \frac{c\Delta t}{\mu\Delta x} \left(E_{z(i+1/2,j)}^n - E_{z(i-1/2,j)}^n \right), \\
E_{z(i,j)}^{n+1} &= E_{z(i,j)}^n + \frac{c\Delta t}{\varepsilon\Delta x} \left(H_{y(i+1/2,j)}^{n+1/2} - H_{y(i-1/2,j)}^{n+1/2} \right) - \\
&\quad - \frac{c\Delta t}{\varepsilon\Delta y} \left(H_{x(i,j+1/2)}^{n+1/2} - H_{x(i,j-1/2)}^{n+1/2} \right).
\end{aligned} \tag{6.5}$$

In the case of TM polarization we have an opposite situation. Magnetic field component which is parallel to the PhC elements and electric field components lying in the plane of PhC are now non-zero while other components equal to zero which leads to the following system:

$$\begin{aligned}
\frac{\partial}{\partial x} E_y - \frac{\partial}{\partial y} E_x &= -\frac{1}{c} \frac{\partial}{\partial t} B_z, \\
\frac{\partial}{\partial y} H_z &= \frac{1}{c} \frac{\partial}{\partial t} D_x, \\
-\frac{\partial}{\partial x} H_z &= \frac{1}{c} \frac{\partial}{\partial t} D_y.
\end{aligned} \tag{6.6}$$

Replacing the derivatives by differences we obtain the following recurrent formula:

$$\begin{aligned}
H_{z(i,j)}^{n+1/2} &= H_{z(i,j)}^{n-1/2} + \frac{c\Delta t}{\mu\Delta y} \left(E_{x(i,j+1/2)}^n - E_{x(i,j-1/2)}^n \right) - \\
&\quad - \frac{c\Delta t}{\mu\Delta x} \left(E_{y(i+1/2,j)}^n - E_{y(i-1/2,j)}^n \right), \\
E_{x(i,j)}^{n+1} &= E_{x(i,j)}^n + \frac{c\Delta t}{\varepsilon\Delta y} \left(H_{z(i,j+1/2)}^{n+1/2} - H_{z(i,j-1/2)}^{n+1/2} \right), \\
E_{y(i,j)}^{n+1} &= E_{y(i,j)}^n - \frac{c\Delta t}{\varepsilon\Delta x} \left(H_{z(i+1/2,j)}^{n+1/2} - H_{z(i-1/2,j)}^{n+1/2} \right).
\end{aligned} \tag{6.7}$$

In 1D case when both electric and magnetic field components are parallel to media interfaces, system (6.2) can be reduced to the following one:

$$\begin{aligned}
\frac{\partial}{\partial y} E_z &= -\frac{1}{c} \frac{\partial}{\partial t} B_x, \\
-\frac{\partial}{\partial y} H_x &= \frac{1}{c} \frac{\partial}{\partial t} D_z.
\end{aligned} \tag{6.8}$$

In this 1D case, it is supposed that radiation propagates along the y -axis. When propagation occurs in another direction, the other field components will be non-zero but general view of the system remains unchanged. The recurrent formula in 1D case is derived in a similar way as for 3D and 2D case and takes the following form:

$$\begin{aligned}
H_{x(i,j)}^{n+1/2} &= H_{x(i,j)}^{n-1/2} - \frac{c\Delta t}{\mu\Delta y} \left(E_{z(i,j+1/2)}^n - E_{z(i,j-1/2)}^n \right), \\
E_{z(i,j)}^{n+1} &= E_{z(i,j)}^n - \frac{c\Delta t}{\varepsilon\Delta y} \left(H_{x(i,j+1/2)}^{n+1/2} - H_{x(i,j-1/2)}^{n+1/2} \right).
\end{aligned} \tag{6.9}$$

Solution of Maxwell's equations represented in discrete form require information about the permittivity and permeability in computation nodes. Besides, the field distribution at least at one boundary should be specified to start the computation.

6.3 Definition of the Dielectric Function

The FDTD method means digitization of the computation region by rectangular mesh. At that, in case of continuous permittivity distribution function, the node of such a mesh contains the exact value of the function within the corresponding coordinate. If the function is discontinuous, i.e., it has step-like permittivity change, there are two ways for definition of the discrete permittivity function. The first one is direct method which means the node values are set as is. This method is the simplest one but gives low accuracy in approximation or otherwise requires high-density mesh. The second method consists of smoothing the step by changing it to some analytic function. At that, the step area can be artificially extended such that the nearest mesh elements will also be involved. The interpolation is made within the selected area so that the permittivity monotonically changes from one side of the step to another one. The linear interpolation may be used within the PhC computation when the permittivity inside the undefined region (i.e., the neighborhood of the permittivity step) will be defined by the following formula:

$$\varepsilon(x, y) = \varepsilon_1 + (\varepsilon_2 - \varepsilon_1)(1 - (\sqrt{(x^2 + y^2) - r})/dr), \quad (6.10)$$

where ε_1 and ε_2 are permittivities of PhC elements and background material respectively, r is elements radius and dr is the thickness of undefined region which may be set manually. If $dr = 0$, we have the case with no interpolation. However, if dr is taken to be a large value, the shape of the elements will be very smooth and large computation inaccuracy appears.

Examples of two space discretization methods are shown in Fig. 6.2.

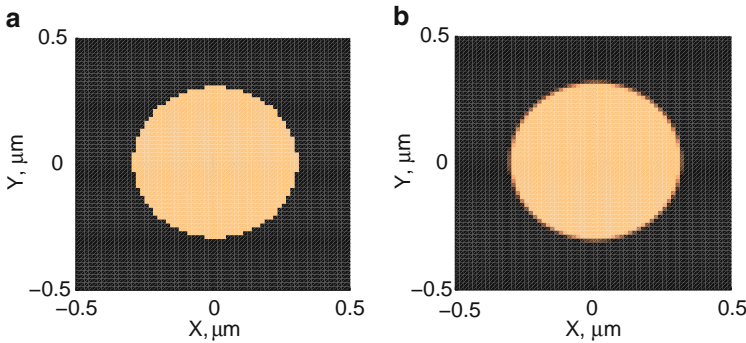


Fig. 6.2. Example of the space discretization without (a) and with (b) interpolation

The case of the space discretization without the interpolation appears to be satisfactory only when computation region is small, and thus, high-density mesh can be used. However, in case of large computation region mesh density may become critical, hence the method employing the interpolation is preferable.

6.4 Definition of Initial and Boundary Conditions

6.4.1 Initial Conditions

When computation region is discretized, initial values of the electric and magnetic fields should be assigned to the mesh nodes before the start of computation. Usually, these values are assumed to be zero, and therefore, initially we have 6 (in 3D case), 4 (in 2D case) or 2 (in 1D case) arrays filled with zeros. Later these arrays will contain information about each field component values with correspondent coordinate.

Besides the above mentioned arrays initialization it is necessary to introduce radiation into the structure under investigation. For this reason, some array elements should be initialized with non-zero values. Moreover, the radiation source is varying in time so nodes-sources should be initialized at each time step. The radiation parameters such as amplitude and frequency are defined in a specific way. Because of discreteness of time in equations (6.3), (6.5), (6.7), (6.9) as well as coordinate, radiation source will be defined by samples both in time and space.

Let us consider example of the source defined by harmonic oscillation with frequency ω in time and Gaussian transverse profile.

The pulse time and space profiles are shown in Fig. 6.3. It can be seen that sampling in this example is quite good, hence the shape of the pulse profiles is not distorted. However, if one takes the mesh with low density or large time step, the pulse will be essentially distorted and will not remind the analytical function.

The nodes-sources also take part in general process of field computation described in this section. Taking this into account, the source value should be added to the value contained by the source node.

6.4.2 Conditions at the Boundaries of Computation Region

Besides the boundary conditions defined at the media interface inside the computation region, we should define the radiation behavior at the boundaries of the computation region. The computation region has finite size and we suppose that radiation outside the region is not perturbed. However, at the boundary of the region radiation can be totally or partially reflected. Such kind of boundary conditions are represented by a equation or a set of equations defining the field distribution behavior near the boundary of computation region.

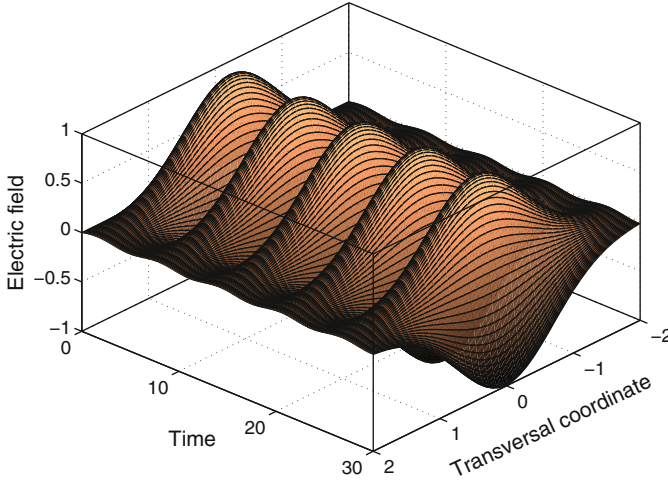


Fig. 6.3. Example of source field definition

There are five commonly used types of boundary conditions used when solving the radiation propagation problem:

1. Dirichlet boundary conditions (or first type boundary conditions) [216] defines the field component values at the computation region

$$kE_{(i,j,k)} = F.$$

This actually means that before the field distribution computation at each time step we set some specific values of the field components to the boundary node of computation mesh. For instance, if the field intensity at the boundary is set to zero at each node, this means total reflection from the boundary.

2. Neumann boundary conditions (or second type boundary conditions) [216] define the derivatives of the function at the computation region boundary:

$$C \left(\frac{\partial E}{\partial n} \right)_{(i,j,k)} = F.$$

In this case, the function values at the computation region boundary are not frozen but depend on the node values of the neighboring ones. For instance, when the function derivative is defined to be zero, the values at the boundary nodes are exactly the same as the values of the nodes next to them. Mathematically this means lowest reflection from the boundary.

3. Mixed boundary conditions are defined when the boundary is divided by several contours. The Dirichlet conditions are defined at one of the contours while Neumann conditions are defined within the second contour:

$$kE_{(i,j,k)} \Big|_{\Gamma_1} = F_1,$$

$$C \left(\frac{\partial E}{\partial n} \right)_{(i,j,k)} \Big|_{\Gamma_2} = F_2.$$

4. Robin boundary conditions [217] are weighted combination of Dirichlet and Neumann boundary conditions in contrast to mixed boundary conditions where separate conditions are used at different subsections of the boundary. Robin conditions are also called impedance boundary conditions because of their application in electromagnetic theory.

$$kE_{(i,j,k)} + C \left(\frac{\partial E}{\partial n} \right)_{(i,j,k)} = F.$$

5. Periodic boundary conditions emulate the translation of the computation region over infinite space. Such boundary conditions are consequence of Bloch theorem and they are usually used to simulate the radiation propagation inside some infinite periodic structure.

$$E_{(i=0,j,k)} = E_{(i=i_{\max},j,k)},$$

$$E_{(i,j=0,k)} = E_{(i,j=j_{\max},k)},$$

$$E_{(i,j,k=0)} = E_{(i,j,k=k_{\max})}.$$

When the problem of electromagnetic field propagation inside the PhC is solved, it is usually supposed that the radiation floats out of the computation region without any perturbation so transparent Neumann boundary conditions are employed. Unfortunately, even in case of Neumann boundary conditions, the non-physical reflection from the computation region boundary is present due to space discretization employed in the FDTD method. Solution of the problem was proposed by J. Berenger and later was developed by other groups [218]-[221]. Solution consists of introduction of relatively thin layer with high artificial absorption. This layer is called the perfectly matched layer (PML). Passing through this layer radiation decays exponentially according to the absorption coefficient. After reflection from the computation region boundary it passes the layer once again so if the absorption coefficient is correctly set, no radiation returns to the computation region.

Absorption of the PML is introduced due to the conductivity of the material. At that, the conductivity is different for different propagation directions so each field component is subdivided into two parts which leads to the following view of Maxwell's equations:

$$-\frac{\partial}{\partial y}(E_{zx} + E_{zy}) = \sigma_y^* H_{xy} + \mu \frac{1}{c} \frac{\partial}{\partial t} H_{xy},$$

$$\frac{\partial}{\partial z}(E_{yz} + E_{yx}) = \sigma_z^* H_{xz} + \mu \frac{1}{c} \frac{\partial}{\partial t} H_{xz},$$

$$\begin{aligned}
-\frac{\partial}{\partial z}(E_{xy} + E_{zx}) &= \sigma_z^* H_{yz} + \mu \frac{1}{c} \frac{\partial}{\partial t} H_{yz}, \\
\frac{\partial}{\partial x}(E_{zx} + E_{zy}) &= \sigma_x^* H_{yx} + \mu \frac{1}{c} \frac{\partial}{\partial t} H_{yx}, \\
-\frac{\partial}{\partial x}(E_{yz} + E_{yx}) &= \sigma_x^* H_{zx} + \mu \frac{1}{c} \frac{\partial}{\partial t} H_{zx}, \\
\frac{\partial}{\partial y}(E_{xy} + E_{xz}) &= \sigma_y^* H_{zy} + \mu \frac{1}{c} \frac{\partial}{\partial t} H_{zy}, \\
\frac{\partial}{\partial y}(H_{zx} + H_{zy}) &= \sigma_y E_{xy} + \varepsilon \frac{1}{c} \frac{\partial}{\partial t} E_{xy}, \\
-\frac{\partial}{\partial y}(H_{yz} + H_{yx}) &= \sigma_z E_{xz} + \varepsilon \frac{1}{c} \frac{\partial}{\partial t} E_{xz}, \\
\frac{\partial}{\partial y}(H_{xy} + H_{xz}) &= \sigma_z E_{yz} + \varepsilon \frac{1}{c} \frac{\partial}{\partial t} E_{yz}, \\
-\frac{\partial}{\partial y}(H_{zx} + H_{zy}) &= \sigma_x E_{yx} + \varepsilon \frac{1}{c} \frac{\partial}{\partial t} E_{yx}, \\
\frac{\partial}{\partial y}(H_{yz} + H_{yx}) &= \sigma_x E_{zx} + \varepsilon \frac{1}{c} \frac{\partial}{\partial t} E_{zx}, \\
-\frac{\partial}{\partial y}(H_{xy} + H_{xz}) &= \sigma_y E_{xy} + \varepsilon \frac{1}{c} \frac{\partial}{\partial t} E_{xy}.
\end{aligned} \tag{6.11}$$

Here $\sigma_x, \sigma_y, \sigma_z$ are electric conductivities within the directions x, y, z , and $\sigma_x^*, \sigma_y^*, \sigma_z^*$ are magnetic conductivities within directions x, y, z . Corresponding recurrent formula will be similar to formulas 6.3. However, each equation will be subdivided into two parts containing only one part of the field component. Besides, the part with conductivity will present in these equations. Resulting field component can be found by summation of its parts:

$$\begin{aligned}
E_x &= E_{xy} + E_{xz}, & H_x &= H_{xy} + H_{xz}, \\
E_y &= E_{yx} + E_{yz}, & H_y &= H_{yx} + H_{yz}, \\
E_z &= E_{zx} + E_{zy}, & H_z &= H_{zx} + H_{zy}.
\end{aligned} \tag{6.12}$$

In the section of the computation region when the conductivity is equal to zero (which actually contains the considered optical structure) the summation of corresponding equations of system (6.12) gives the system (6.2).

The PMLs in 2D and 3D cases are shown in Fig. 6.4. It is seen from the figure that conductivities for all directions are non-zero only within corners of the computation region. In other sections of the PML only two or four conductivity components are non-zero.

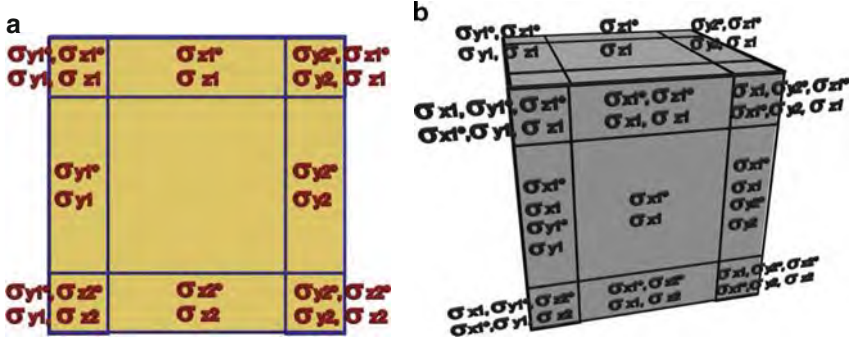


Fig. 6.4. 2D (a) and 3D (b) computation regions with perfectly matched layer

6.5 FDTD Method Stability

After the cell size of the computation mesh is selected it is necessary to determine the time step. The time step limitation comes from the condition that radiation should not propagate through more than one computation mesh cell during a single time step.

Thus, taking the light speed in vacuum as the radiation propagation speed (here we consider the electromagnetic field propagation only) we can estimate the time step allowed for stable computation:

$$c\Delta t \leq \left(\frac{1}{(\Delta x)^2} + \frac{1}{(\Delta y)^2} + \frac{1}{(\Delta z)^2} \right)^{-1/2}, \quad (6.13)$$

where Δx , Δy , Δz are linear dimensions of computation mesh cell.

The condition (6.13) is known as Courant condition and is always used in FDTD computation technique. In practice, the sign of equality may be set in the expression (6.13) instead of less or equal. In this case, the computation time is minimal while the accuracy stays high. Low value of time step should only be taken in case of structure containing high conductivity or nonlinear materials.

6.6 FDTD Method Application for Experimentally Obtained PhC with Hexagonal Lattice Structure

In this section, we will consider the example of the computation of the specters of the real PhC. In [222], the transmittance spectra of the PhC represented by holes arranged to the hexagonal lattice and having following parameters have been investigated: filling factor $f = 0.25, \dots, 0.3$, number of PhC layers $N = 3, \dots, 15$, refractive index $n = 3.3$ (GaAs). The experimental investigation was carried out using scaling technique because of the

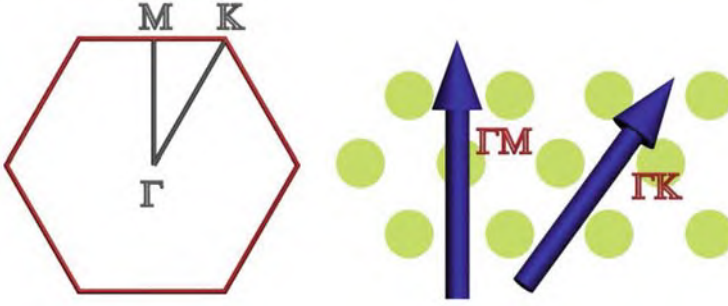


Fig. 6.5. Correspondance between high-symmetry points and the radiation propagation direstion inside the PhC

limitations of the quantum dot tunability range. Thus, the structure was reproduced seven times with different scales with corresponding lattice constant $a = 180, 200, 220, 240, 260, 280, 300$ nm. The transmittance spectrum of each structure was scaled in frequency and then “glued” to the common plot. Obtained transmittance spectrum then was analyzed.

In [222], the transmittance was taken at some specific direction of the radiation propagation inside the PhC. As mentioned in the Chap. 4, the direction in real space is connected to the direction in the reciprocal space via the expressions (4.17). Thus, the designation of the radiation propagation in this work is the same as the desingnations of the high-symmetry points directions in the Brillouin zone. Such correspondance is shown in Fig. 6.5.

We will now compare the experimental specters with the ones obtained by the FDTD technique. There are, however, some peculiarities of the computation of the field distribution of the real structure. The first one is the chromatic dispersion. However, in this particular case, this inaccuracy may be neglected since the experimental technique employing the scaling of the structure is unable to take into account the chromatic dispersion. The second peculiarity is the definition of the computation area and the definition of the point where the field value will be taken after it passes the PhC. Let us consider the field distribution just after the PhC (See Fig. 6.6). As we can see, the radiation is diffracted by the PhC and propagates in different directions after the PhC. However, as we mentioned earlier, we are interested in single propagation direction, namely ΓK or ΓM . In order to avoid the parasitic effects, we have to move the source as far as possible from the structure. Unfortunately, the computation time may significantly increase in this case and, therefore, we set the receiver at the distance of 30 periods from the PhC. As we have seen, such placement of the receiver provides low error at relatively low computation time. We consider here only the case when the PhC contains 15 rows of holes since it is considered in [222] in great detail.

As for the FDTD computation of the transmittance spectrum, there are two different ways. The first one is to use the CW pulse as the source and

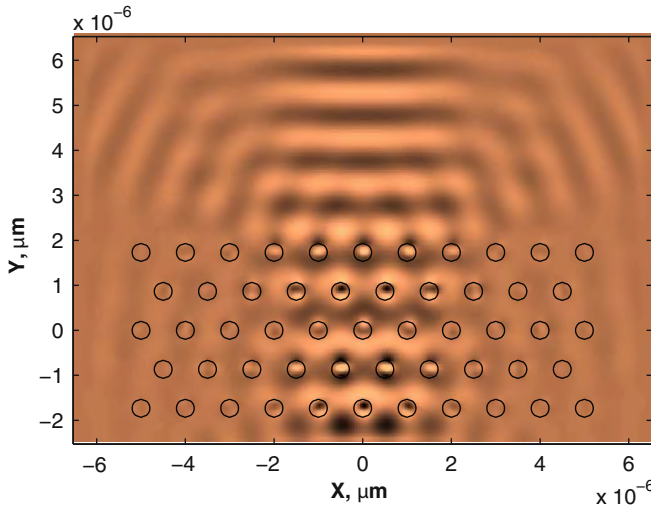


Fig. 6.6. Demonstraion of the field diffraction after the PhC

measure the transmittance at each wavelength within the selected range. This is the most basic technique. However, it takes a lot of time since we have to compute the field distribution starting from zero-time for each wavelength.

Another computation technique employs fast Fourier transform. In this case, we launch the Gaussian-shaped pulse with broad spectrum (i.e., the temporal width of the shape is low). After the computation is complete, we have temporal response of the structure. Then we apply fast Fourier transform to the temporal response, divide it by the spectrum of the launched pulse and obtain the transmittance spectrum of the structure. In order to understand this technique, we can represent the broad-spectrum as a number of narrow-spectrum pulses with magnitudes A_1, A_2, \dots, A_8 launched together to the structure (see Fig. 6.7). Each pulse “tests” the structure at the specific wavelength so after the structure each initial pulse has magnitude multiplied by the PhC transmittance at its wavelength $A_1 \cdot T_1, A_2 \cdot T_2, \dots, A_8 \cdot T_8$. When we apply Fourier transform, we obtain the information about all these pulses. However, since an initial pulse had Gaussian shape, we have to normalize the output spectrum by the spectrum of launched pulse. After this final operation, we obtain the transmittance spectrum of the PhC.

As we have seen, the second computation is very similar to the first one. The only difference is that we compute the transmittance sparately when we use CW initial pulse while Gaussian-shaped beam allows to scan over whole frequency range. Due to this fact, the computation time in the second technique is much lower.

Now let us consider the computation results. They are presented in Fig. 6.8. The blue lines in the middle of Fig. 6.8 present the band structure of the PhC considered in [222]. The TE PBG of such a PhC lies between the first

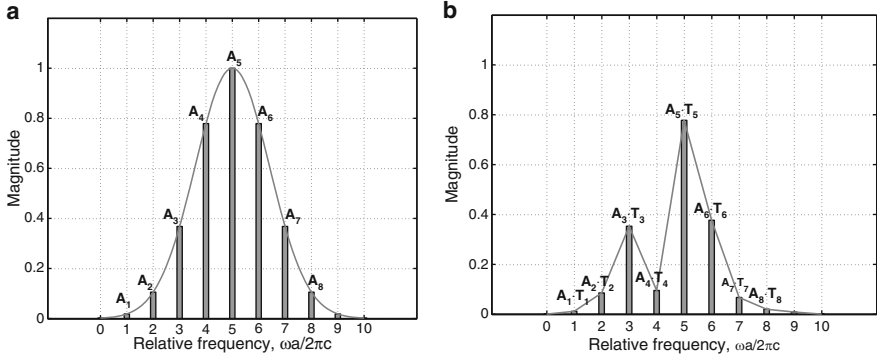


Fig. 6.7. The spectrum of the probe pulse before (a) and after (b) the structure

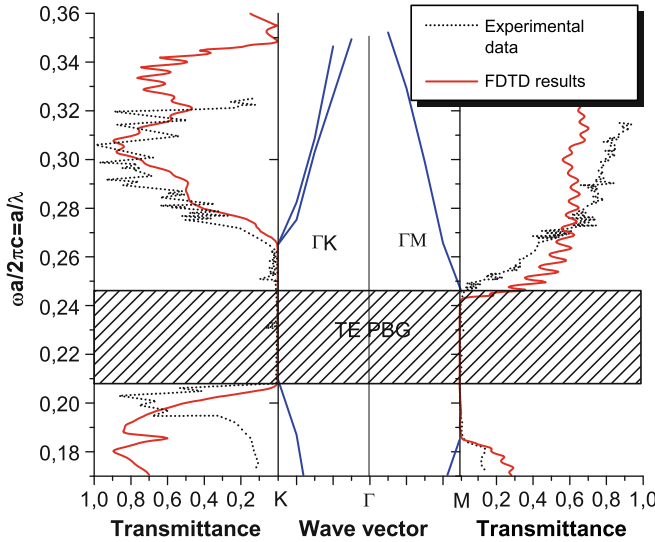


Fig. 6.8. The band structure with corresponding theoretically and the experimentally obtained transmittance spectra within different propagation direction

and the second bands within the limits of relative frequency from 0.208 to 0.248. However, partial PBGs along the directions ΓK and ΓM are slightly wider and are shifted by frequency, one related to another. The computed transmittance spectra are compared to the band structure. The spectrum along the direction ΓK is shown to the left and the one for direction ΓM is to the right from the band structure. As we can see, due to strict determination of the radiation propagation direction, the transmittance minima correspond to partial PBGs. The computed transmittance minima in both ΓM and ΓK directions are in good agreement with experimental data. However, outside

the PBG, there is no full correspondence between theoretical and experimental results. This can be explained partially by the inaccuracy of the experimental technique which is analyzed in detail in [222] and, partially, by neglecting the material properties such as absorption, when applying FDTD technique. Anyway, such an inaccuracy does not cause large error when the theoretically obtained results are used for the design of the real devices.

The experimental verification of the method gives an opportunity to consider it as a convenient tool for design and optimization of real PhC devices which gives good qualitative agreement with experiment and may be easily applied for arbitrary structures as well as for complex optical circuits.

6.7 Summary

1. One of most widespread methods for computation of electromagnetic field distribution in optical structures is the FDTD method.
2. FDTD method is based on digitization of Maxwell's equations. Field is defined in nodes of the square mesh.
3. Inputs for FDTD computations are dielectric permittivity within the computation domain, boundary and initial conditions. After inputs are defined computation of the field distributions are calculated step-by-step.
4. FDTD is a universal method. However, in special cases analytical and approximate methods can be used resulting in decreasing of computation time.

6.8 Problem Solution Example

Problem:

Compute 1D field distribution in air during five time steps. Computation domain size is $2\text{ }\mu\text{m}$. Excitation source is delta pulse of magnetic field. Discretization step is $\Delta y = 0.2$. Dirichlet boundary conditions should be used.

Solution:

First, basing on Courant condition of the method stability, we have to find the computation time step. Substituting the discretization step to the expression (6.13), we obtain:

$$c\Delta t \leq \Delta y \Rightarrow \Delta t \leq \frac{\Delta y}{c}$$

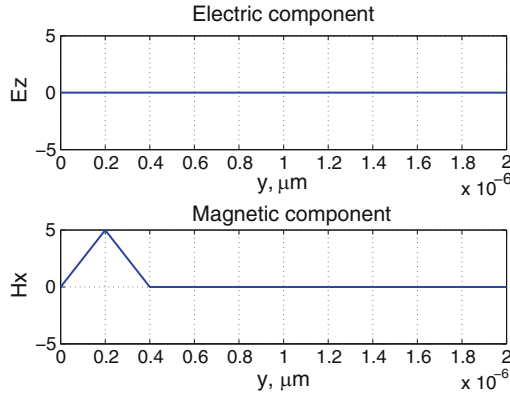
In this problem, we select time step to be equal to $\Delta t = \Delta y / 2c$

Then, we create the arrays which contain values of electric and magnetic field.

Now, we set the initial field distribution inside the computation area. As follows from the statement of the problem, the excitation is performed by the

Table 6.1. Electric and magnetic field strengths within mesh nodes after the first computation step

| | | | | | | | | | | | |
|-------|---|---|---|---|---|---|---|---|---|---|---|
| E_z | 0 | 0 | 0 | 0 | 0 | 0 | 0 | 0 | 0 | 0 | 0 |
| H_z | 0 | 5 | 0 | 0 | 0 | 0 | 0 | 0 | 0 | 0 | 0 |

**Fig. 6.9.** Electric and magnetic field distributions after the first (initial) step

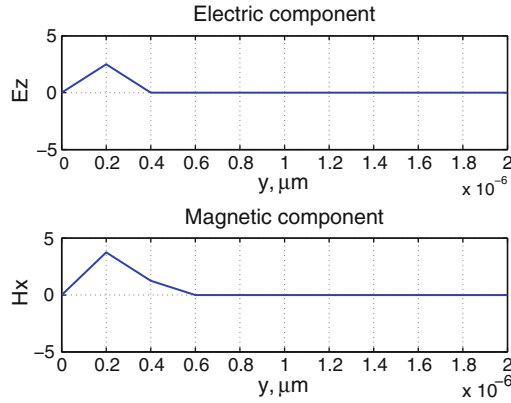
magnetic delta-pulse. With this, all values of the electric field are initially equal to zero while one of magnetic field values takes value of delta-pulse magnitude. Here we have taken the delta-pulse with magnitude 5. The values of the initial electric and magnetic fields are presented in Table 6.1 while Fig. 6.9 depicts both initial fields distribution.

After the initial field distribution is given, we will use equations (6.9). When we considered the computation domain discretization, we mentioned that grid points of magnetic field is shifted by half-of-cell as related to magnetic field. The time moments the magnetic field is computed in, is also shifted by half of time-step. This gives us strict sequence of the field components computation. Therefore, we first take the first equation from the system (6.9) and compute the electric field distribution from known initial electric and magnetic fields. It should be mentioned that we start the computation from the second point of the computation mesh since we use the Dirichlet boundary conditions. With these conditions, field values at the boundary of the computation region (which actually means the first and the last points of the mesh) should be manually set. In our case, we set them to zero. Then, we use the second equation from the set (6.9) and calculate the magnetic field distribution. In this case, we use previously found electric field distribution as a basis for this calculation. New values of electric and magnetic fields are given in Table 6.2 and are plotted in Fig. 6.10.

We can see in Fig. 6.10 that the field distribution now differs from the one given in Fig. 6.9. The maximum of the field starts to move right and values of

Table 6.2. Electric and magnetic field strengths within mesh nodes after the second computation step

| | | | | | | | | | | | |
|-------|---|------|------|---|---|---|---|---|---|---|---|
| E_z | 0 | 2.5 | 0 | 0 | 0 | 0 | 0 | 0 | 0 | 0 | 0 |
| H_z | 0 | 3.75 | 1.25 | 0 | 0 | 0 | 0 | 0 | 0 | 0 | 0 |

**Fig. 6.10.** Electric and magnetic field distributions after the second step**Table 6.3.** Electric and magnetic field strengths within mesh nodes after the third computation step

| | | | | | | | | | | | |
|-------|---|-------|-------|------|---|---|---|---|---|---|---|
| E_z | 0 | 3.75 | 0.625 | 0 | 0 | 0 | 0 | 0 | 0 | 0 | 0 |
| H_z | 0 | 1.875 | 2.81 | 0.31 | 0 | 0 | 0 | 0 | 0 | 0 | 0 |

electric and magnetic fields are now equal to zero at the boundaries. Boundary conditions should be considered separately. In the system (6.9), we can see that the electric field is a result of difference between magnetic field values in the neighboring elements. Similar situation is for magnetic field. Thus, since we manually set zeros to boundary elements, the difference including these elements will give us exactly the same values the neighboring elements contain. This produces the effect of complete field reflection from the boundary which is very similar to perfect conductor.

The field computation at the third, fourth and fifth steps does not actually differ from the one at the second computation step. Therefore, the field values are presented only in Tables 6.3–6.5 and field components distributions are given in Figs. 6.11–6.13.

Thus, we obtain the field distribution after five computation steps. If we track the field evolution during the computation steps, we will find out that its behavior is very similar to any type of wave propagating in any medium. During the propagation, the pulse is reflected from the left boundary and

Table 6.4. Electric and magnetic field strengths within mesh nodes after the fourth computation step

| | | | | | | | | | | | |
|-------|---|------|------|-------|-------|---|---|---|---|---|---|
| E_z | 0 | 3.28 | 1.87 | 0.156 | 0 | 0 | 0 | 0 | 0 | 0 | 0 |
| H_z | 0 | 0.23 | 3.51 | 1.17 | 0.078 | 0 | 0 | 0 | 0 | 0 | 0 |

Table 6.5. Electric and magnetic field strengths within mesh nodes after the fifth computation step

| | | | | | | | | | | | |
|-------|---|-------|------|------|-------|-------|---|---|---|---|---|
| E_z | 0 | 1.64 | 3.04 | 0.70 | 0.039 | 0 | 0 | 0 | 0 | 0 | 0 |
| H_z | 0 | -0.58 | 2.81 | 2.34 | 0.41 | 0.019 | 0 | 0 | 0 | 0 | 0 |

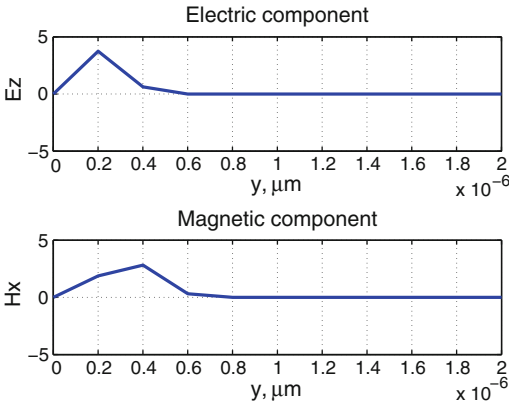


Fig. 6.11. Electric and magnetic field distributions after the third step

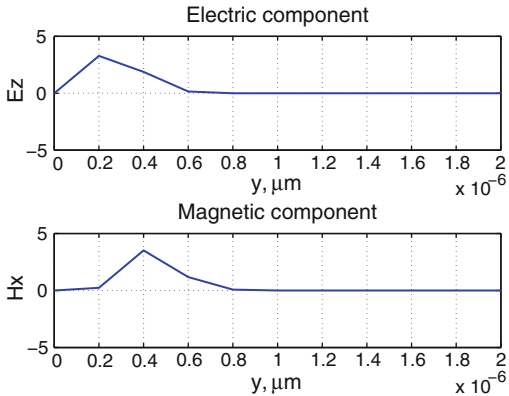


Fig. 6.12. Electric and magnetic field distributions after the fourth step

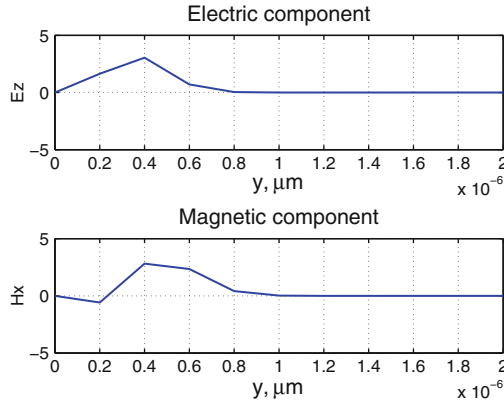


Fig. 6.13. Electric and magnetic field distributions after the fifth step

then propagates to the right one. If the number of computation steps was high enough, we could observe the pulse reflection from the right boundary and its propagation to an opposite direction.

6.9 MATLAB Program for Computation of Field Distribution in Nonuniform Optical Medium

```
%Program for computation of temporal field
%evolution in rectangular computational domain
%containing several regions of low refractive index.
%Dirichlet boundary conditions are used.
```

```
clear all;
%Variables maxX maxY contain linear sizes of
%computational domain. Here they are 3 and 10
%microns
maxX=3e-6;
maxY=10e-6;
```

```
%Variable r contains radius of the region in the
%center of computational domain
r=0.45e-6;
```

```
%Variable maxT defines maximum computational time.
%It is set to 50 picoseconds
maxT=50e-12;
```

```

%Variable lambda contains radiation wavelength
lambda=2.04e-6;

%Constant  is the speed o light in vacuum
c=3e8;

%Variable  contains distance between low-index
%regions
a=1e-6;

%Variables accuracyX and accuracyY define
%discretization quality
accuracyX=120;
accuracyY=400;

%Time step Dt is calculated using Courant
%condition
Dt=1/c/sqrt(1/(maxX/accuracyX)^2+...
            1/(maxY/accuracyY)^2);

%After that we calculate number of time steps
accuracyT=round(maxT/Dt);

%Space steps are also calculated
Dx=maxX/accuracyX;
Dy=maxY/accuracyY;

%Material under consideration is nonmagnetic
mu=1;

%Assign mesh nodes by dielectric permittivity.
%The background material will have permittivity
%of 9
eps=9*ones(accuracyX, accuracyY);

%Array drw will contain contours of interfaces.
%It is initially filled in by zeros.
drw=zeros(accuracyX, accuracyY);

%Calculate the optical frequency to be used in
%definition of harmonic excitation source
w=2*pi/lambda;

%Create a region for plotting
figure('Position',[200,0,accuracyX*2+40,...
                    accuracyY*2+40]);

```



```

%Initialize 2D arrays of the field components
Ez=zeros(accuracyX,accuracyY);
Hx=zeros(accuracyX,accuracyY);
Hy=zeros(accuracyX,accuracyY);
%Next loop assign by 1 each element of the array,
%which appears inside one of the 4 circle low-index
%regions On the interface corresponding element of
%the array drw is assigned by 1.
for countX=1:accuracyX
    for countY=1:accuracyY
        if sqrt((countX*Dx-maxX/2)^2+...
                (countY*Dy-maxY/2)^2)<r
            eps(countX,countY)=1;
        elseif sqrt((countX*Dx-maxX/2)^2+...
                (countY*Dy-maxY/2)^2)<r+r/5;
            drw(countX,countY)=1;
        end
        if sqrt((countX*Dx-maxX/2)^2+...
                (countY*Dy-maxY/2-a)^2)<r
            eps(countX,countY)=1;
        elseif sqrt((countX*Dx-maxX/2)^2+...
                (countY*Dy-maxY/2-a)^2)<r+r/5;
            drw(countX,countY)=1;
        end
        if sqrt((countX*Dx-maxX/2)^2+...
                (countY*Dy-maxY/2+a)^2)<r
            eps(countX,countY)=1;
        elseif sqrt((countX*Dx-maxX/2)^2+...
                (countY*Dy-maxY/2+a)^2)<r+r/5;
            drw(countX,countY)=1;
        end
        if sqrt((countX*Dx-maxX/2)^2+...
                (countY*Dy-maxY/2+2*a)^2)<r
            eps(countX,countY)=1;
        elseif sqrt((countX*Dx-maxX/2)^2+...
                (countY*Dy-maxY/2+2*a)^2)<r+r/5;
            drw(countX,countY)=1;
        end
    end
end

%calculate coefficients at field components
eps_x=c*Dt/Dx./eps;
eps_y=c*Dt/Dy./eps;
mu_x=c*Dt/mu/Dx;
mu_y=c*Dt/mu/Dy;

```

```

%Variable counter allows plotting skipping several
%passages of loop
counter=1;

%In the next loop we calculate field distribution.
%Change of the counter of the outer loop corresponds
%to change of time.
for t=1:accuracyT
%Before each calculation of the space field
%distribution excitation function is saved.
    Ez(2:accuracyX,1)=Ez(2:accuracyX,1)+...
        0.1*exp(-(Dx*((2:accuracyX)-accuracyX/2)')...
            .^2/((maxX/4)^2))*sin(w*Dt*c*t);

%Next loop calculates magnetic field based on values
%of electric field in the mesh nodes
for y=2:accuracyY-1
    for x=2:accuracyX-1
        Hx(x,y)=Hx(x,y)-mu_x*(Ez(x,y)-Ez(x,y-1));
        Hy(x,y)=Hy(x,y)+mu_y*(Ez(x,y)-Ez(x-1,y));
    end
end
%Next loop calculates electric field based on values
%of magnetic field in the mesh nodes
for y=2:accuracyY-2
    for x=2:accuracyX-2
        Ez(x,y)=Ez(x,y)+eps_x(x,y)*(Hy(x+1,y)-Hy(x,y))-...
            eps_y(x,y)*(Hx(x,y+1)-Hx(x,y));
    end
end

%Next condition control if the number inside the
%counter is multiple of 2, and plots the field
    if mod(counter,5)==0
        Edisp=Ez';
%In the next two loops we plot interface contour
        for i=1:accuracyY
            for j=1:accuracyX
                if drw(j,i)~=0;
                    Edisp(i,j)=1.5;
                end
            end
        end
    end
end

```

```

% Image is plotted in the output region
image((0:accuracyX)/accuracyX*maxX,...
      (0:accuracyY)/accuracyY*maxY,30*real(Edisp));
drawnow;
end
counter=counter+1;
end

```

We now consider the program in detail. The program consists of three blocks.

During the first block, the program initialization is carried out. Here, we are setting up parameters of the computation domain and initialize arrays for permittivity distribution, field components computation and the graphical output. Inside this block we are also computing the time step by means of expression (6.13). This gives stability to the method.

In the next block, we are setting up the permittivity distribution inside the computation domain. We consider here the structure of three holes, but the reader may set the permittivity distribution by just changing the contents of the array *eps*.

The third block is for FDTD computation itself. Here, we consider the TM polarization so we were governed by the set of equations (6.4). However, the reader may use analogous computation technique for the method implementation in case of TE polarizatón as well as in case of 1D or 3D FDTD. It should also be mentioned that there is no necessity in redrawing the field distribution at each computation step. That is why we introduced the computation step counter and redrawing the field each fifth step.

The computation results are shown in Fig. 6.14(b) and (b). The first figure depicts the field distribution at almost the beginning of the computation process while the second one is after a time interval. We can see the interaction between the radiation and the structure. Setting up custom structures and taking into consideration the material properties, it is possible to compute the field distribution inside any optical device.

6.10 Problems and Questions

Problem 6.1. Derive the discreet system of Maxwell's equations for 2D TE case.

Problem 6.2. Derive the discreet system of Maxwell's equations for 1D case for field components E_x , H_y

Problem 6.3. Write the program for computation of TE-wave propagation in 2D computational domain $10\mu\text{m} \times 10\mu\text{m}$ with permittivity of air under excitation by harmonic electrical field with the period $T = \Delta t \cdot 10$ placed in

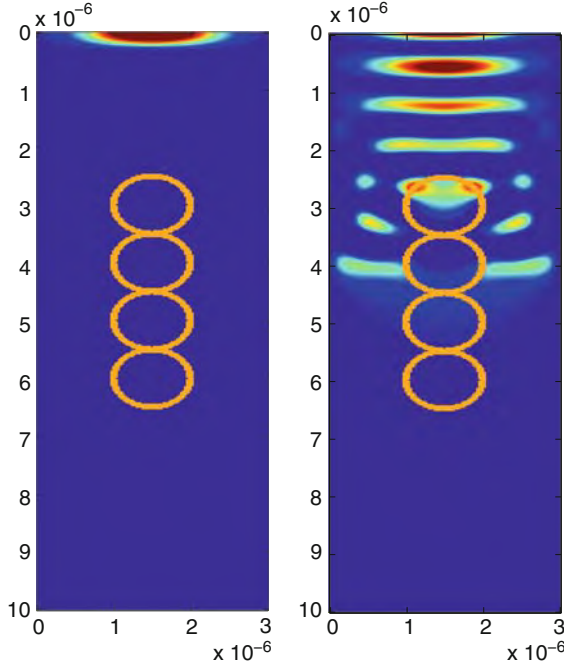


Fig. 6.14. Results of the program. Field distribution at different moments inside the considered structure

the center of the computational domain. Discretization step is $\Delta y = 0.2 \mu\text{m}$. Apply Dirichlet boundary conditions.

Problem 6.4. Solve the Problem 6.1 using meander with the period $\Delta t \cdot 10$ as an excitation source.

Problem 6.5. Solve the Problem 6.1 for the TM-wave and non-uniform medium. Consider square silicon region $2 \mu\text{m} \times 2 \mu\text{m}$ in the center as non-uniformity. Neglect the absorption.

Problem 6.6. Derive recurrent formula for calculation of TE and TM waves in 2D case for wave propagation in computational domain bounded by perfectly matched layer.

Problem 6.7. Solve Problem 6.1 in computation domain bounded by PML of $1 \mu\text{m}$ thickness. Apply absorbing boundary conditions.

Problem 6.8. Solve problem 6.2 in computation domain bounded by PML of $1 \mu\text{m}$ thickness.

Photonic Crystal Optical Fibers

Summary. Chapter 7 gives an idea of computation of principal characteristics of the photonic crystal fibers (PCF). Similarities and distinctions between PCF and conventional optical fibers are considered. The first part of the chapter deals with theoretical relations and characteristics of conventional fibers. The second part gives classification and characteristics computation of PhC fibers. The chapter gives detailed analysis of the index-guided photonic crystal fibers, as well as PBG fibers. The computations technique for their eigen-states and field distribution are demonstrated and analysis of results is carried out. At the end of the chapter, the example of original Matlab-code for computation of fundamental mode distribution in microstructured fiber by means of PWE method is presented and several problems and questions for self-training are given.

7.1 Photonic Crystal Fibers: New Class of Optical Waveguides

Current field of optical waveguides is not limited by conventional step-index optical fibers or special-profiled dispersion-shifted of polarization-maintained fibers. New kinds of fibers with microstructured cladding should also be included to existing fibers classification.

At the end of the the twentieth century, the variety of optical fibers was significantly extended by introducing a new class of optical fibers which provided the effective solutions to a number of existing problems in such fields as telecommunications, fiber lasers, high-power transmission, nonlinear devices, sensor applicaions, and others.

This special class of photonic crystal fibers is also referred to as microstructured optical fibers. The main difference between these fibers and the conventional ones is the index profile of core/cladding. In microstructured fibers the cross section of either lightguiding core, cladding, or both are represented by 2D photonic crystal.

Cylindrical shape of the cross section and huge length of such structures in aggregate with their assignment to transfer optical radiation, allows to

sort them out into separate class of PhC devices. In addition, similarity to conventional fiber lightguides found application of analysis methods from the theory of propagation of optical radiation in dielectric cylindrical waveguides.

In this chapter we consider methods for computation of photonic crystal fibers. However, due to similarity to conventional fibers we first give a small historical introduction after which basic relations and characteristics describing radiation propagation in conventional fibers will be presented. Crucial steps of the fiber optics history can be found in [223].

Guiding properties of the optical fiber are based on the phenomena of total internal reflection (TIR). Such fibers consist of optically transparent medium surrounded by a material with smaller optical density. Light rays incident on the front edge of such a structure are captured and guided by the fiber if an incident angle is smaller than TIR angle. After the wave properties of light were taken into account, it was found that only limited number of rays with discrete set of angles inside the TIR angle can form guided waves of the structure. Such rays must satisfy phase synchronism condition in addition to the total internal reflection. Phase synchronism condition is the requirement for waves to be in phase after two sequential reflections and thus interfere constructively. Only in that case waves will form self-consistent field distribution of the guided waves (modes). If that condition is not satisfying, waves will interfere destructively and therefore vanish. Quantization of waves into discrete series of guided modes was discovered only after solution of Maxwell's equations for particular kinds of guided structures. Such solutions for dielectric cylinder of the round cross section was obtained for the first time by D.Hondors and P.Debye [224]. Majority of theoretical and experimental works before the 1950s have concerned propagation of microwaves along the dielectric waveguides. This has resulted in creation of transmission lines and system components as well as antennas for microwaves. Quasioptical properties of dielectric waveguides received a little attention in this time, except perhaps one detailed theoretical work after H.Buchholz [225].

The first dielectric waveguide in which discrete modes on optical frequencies have been studied was glass fiber with glass cladding. Such a fiber was discovered by N.S.Kapany [226] for the purpose of application of fiber optics in imaging systems.

Research of the optical waveguides has received strong impulse due to the laser forthcoming at the beginning of 1960s and consequently due to possibility of coherent light application in telecommunications and other areas where previously microwaves were used. A glass fiber lightguide was proposed as a transmission line for the first time by Kao and Hockham [227]. After losses in silica fibers were reduced down to 20 dB/km, wide perspectives of application of fiber lightguides in optical telecommunications become evident.

Against the background of colossal development in technology of the fiber-optical telecommunications, forthcoming of photonic crystals, structures which allow radiation localization not only due to the total internal reflection, but due to photonic band gap as well, has allowed obtaining totally new class

of the optical transmission media. Photonic crystal fibers or microstructured fibers have unique modal properties which can be controlled via modification of photonic crystal geometry. Microstructured fiber proposed by Birks, Knight, and Russel [228], possess single-mode properties in much wider wavelength range than conventional fiber made by core doping. In addition, such a fiber has larger core that allows transmission of more powerful signals and increases capacity of transmission line.

7.2 Modes in Conventional Optical Fibers

Conventional optical fibers are represented by an optical guiding structure consisting of several annular layers, namely, core, reflective cladding, and protective coating (on the top part of the Fig. 7.1). The index profile of such kinds of fibers may have various shapes, however, it is always axially symmetric.

In contrast to the conventional fibers, layers of microstructured fibers may consist of several different materials and contain PhC-like microstructure (see the bottom part of Fig. 7.1). The size of microstructure elements is of the order of radiation wavelength propagating over this fiber. Main peculiarity of such fibers is strong dependence of its optical properties on the geometry of the microstructure. It gives possibility to design the fiber with any possible characteristics by manipulation with geometry only.

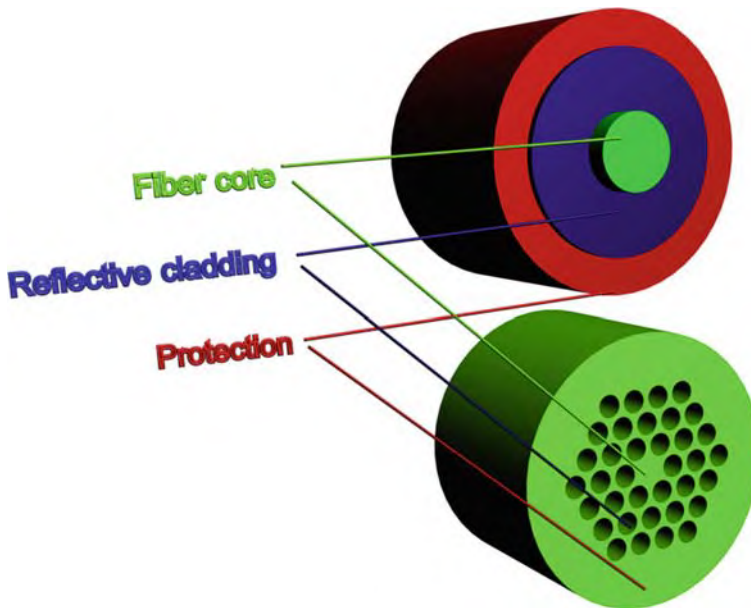


Fig. 7.1. Similarity between conventional fiber and PhC fiber

For best understanding of physics of microstructured fibers, it is first necessary to consider modal properties of conventional fiber.

7.3 Solution of Helmholtz Equation in Axial-Symmetric System

Strong theory for wave propagation in fibers is necessary to obtain good design of telecommunication links. The geometric optics approach gives much important information but characterizes wave propagation roughly. The mode concept is a general concept in optics occurring also, for example, in the theory of lasers, optical waveguides, and fibers. An optical mode refers to a specific solution of the Helmholtz equation

$$\nabla^2 \mathbf{E} + n^2(\omega) k_0^2 \mathbf{E} = 0, \quad (7.1)$$

which satisfies the appropriate boundary conditions and has constant spatial distribution while propagating over the fiber. For simplicity of notation, the frequency dependence of all variables is understood by default. The fiber modes are classified as guided modes, leaky modes, and radiation modes [229]. Signal transmission in fiber-optic communication systems takes place through the guided modes only. The following discussion focuses only on the guided modes of a step-index fiber.

To take advantage of the cylindrical symmetry of the fiber the Helmholtz equation (7.1) is written in the cylindrical coordinates (ρ, ϕ, z) with z -axis lying along the axis of the fiber as in [202]

$$\frac{\partial^2 E_z}{\partial \rho^2} + \frac{1}{\rho} \frac{\partial E_z}{\partial \rho} + \frac{1}{\rho^2} \frac{\partial^2 E_z}{\partial \phi^2} + \frac{\partial^2 E_z}{\partial z^2} + n^2 k_0^2 E_z = 0, \quad (7.2)$$

where the refractive index n is of the form

$$n = \begin{cases} n_1, & \rho \leq a \\ n_2, & \rho > a \end{cases} \quad (7.3)$$

for a step-index fiber of core radius a . Equation (7.1) is written for the longitudinal component E_z , of the electric field vector. Similar equations can be written for the other five components of electromagnetic fields: E_ρ , E_ϕ , H_ρ , H_ϕ and H_z . But because of interconnection of all electromagnetic components which is expressed by Maxwell's equations, it is not necessary to solve all six equations and only two independent components can be used. Because light is transferring in the longitudinal direction components E_z and H_z are selected as independent functions and then E_ρ , E_ϕ , H_ρ , H_ϕ are obtained. Solution of (7.1) is based on the method of separation of variables which represent the function E_z , as

$$E_z(\rho, \phi, z) = F(\rho)\Phi(\phi)Z(z). \quad (7.4)$$

By using (7.4) in (7.1), we obtain three ordinary differential equations:

$$d^2 Z/dz^2 + \beta^2 Z = 0, \quad (7.5)$$

$$d^2 \Phi/d\phi^2 + m^2 \Phi = 0, \quad (7.6)$$

$$\frac{d^2 F}{d\rho^2} + \frac{1}{\rho} \frac{dF}{d\rho} + \left(n^2 k_0^2 - \beta^2 - \frac{m^2}{\rho^2} \right) F = 0. \quad (7.7)$$

Equation (7.5) characterizes longitudinal properties of the field. It has a solution of the form

$$Z = \exp(j\beta z), \quad (7.8)$$

where β stands for the propagation constant. Similarly, (7.6) characterizes the azimuthal behavior. This equation has a solution

$$\Phi = \exp(jm\phi), \quad (7.9)$$

but the constant m possesses integer values only since the field must be periodic in ϕ with a period of 2π . Equation (7.7) describes the field radial behavior. That is the well-known differential equation for the Bessel functions. Its general solution in the core and cladding regions is given by linear combination of two cylindrical functions of the order of m

$$F(\rho) = \begin{cases} AJ_m(\kappa\rho) + BN_m(\kappa\rho), & \rho \leq a \\ CK_m(\gamma\rho) + DI_m(\gamma\rho), & \rho > a \end{cases}, \quad (7.10)$$

where A , B , C , and D are constants and J_m , N_m , K_m , and I_m are different kinds of cylindrical Bessel functions, and a is the fiber core radius. The parameters κ and γ are defined by

$$\kappa^2 = n_1^2 k_0^2 - \beta^2, \quad (7.11)$$

$$\gamma^2 = \beta^2 - n_2^2 k_0^2. \quad (7.12)$$

Bessel function J_m for the core area gives correct physical description of the optical field in the fiber core $\rho < a$. Neumann function N_m has singularity at $\kappa\rho = 0$ and does not satisfy physical representation of the mode in the core. That is why constant D must be equal to zero. The modified Bessel function I_m and the modified Hankel function H_m which are decaying ones, describe field behavior in the cladding.

Essential simplification in Eq. (7.10) occurs when we assume the boundary condition that the optical field for a guided mode should be finite at $\rho = 0$ and decreases to zero at $\rho = \infty$. Function $F(\rho)$ vanishes at infinity only if $D = 0$ and singularity of the function $K(\gamma\rho)$ is not considered when $\rho > a$. The general solution of (7.1) is hereby of the form

$$E_z = \begin{cases} AJ_m(\kappa\rho) \exp(jm\phi) \exp(j\beta z), & \rho \leq a \\ CK_m(\gamma\rho) \exp(jm\phi) \exp(j\beta z), & \rho > a \end{cases}. \quad (7.13)$$

The first two terms of (7.13) describe field behavior in transversal plane. The first term corresponds to radial distribution and the second one represents periodical azimuthal oscillations. Last function in (7.13) shows that optical field decays exponentially in longitudinal z direction with decaying coefficient β . To satisfy the boundary conditions and taking into account the cylindrical symmetry of the system, it is preferable to take all electric fields to have cosine dependence on angle ϕ , and magnetic fields to have sine dependence. Then, we can write the solution for E_z in following form:

$$E_z = \begin{cases} AJ_m(\kappa\rho) \cos(m\phi) \exp(j\beta z), & \rho \leq a, \\ CK_m(\gamma\rho) \cos(m\phi) \exp(j\beta z), & \rho > a \end{cases}. \quad (7.14)$$

The same method can be used to obtain H_z , which also satisfies (7.1). Actually, the solution for H_z has the same form but with different constants A' and C' , such that

$$H_z = \begin{cases} A'J_m(\kappa\rho) \sin(m\phi) \exp(j\beta z), & \rho \leq a, \\ C'K_m(\gamma\rho) \sin(m\phi) \exp(j\beta z), & \rho > a \end{cases}. \quad (7.15)$$

Other four components E_ρ , E_ϕ , H_ρ , and H_ϕ , can be expressed in terms of E_z and H_z by solutions of using Maxwell's equations. For the core region, we have [223]

$$E_\rho = -\frac{j}{\kappa^2} \left(\beta \frac{\partial E_z}{\partial \rho} + \mu_0 \frac{\omega}{\rho} \frac{\partial H_z}{\partial \phi} \right), \quad (7.16)$$

$$E_\phi = -\frac{j}{\kappa^2} \left(\frac{\beta}{\rho} \frac{\partial E_z}{\partial \phi} - \mu_0 \omega \frac{\partial H_z}{\partial \rho} \right), \quad (7.17)$$

$$H_\rho = -\frac{j}{\kappa^2} \left(\beta \frac{\partial H_z}{\partial \rho} - \varepsilon_0 n^2 \frac{\omega}{\rho} \frac{\partial E_z}{\partial \phi} \right), \quad (7.18)$$

$$H_\phi = -\frac{j}{\kappa^2} \left(\frac{\beta}{\rho} \frac{\partial H_z}{\partial \phi} + \varepsilon_0 n^2 \omega \frac{\partial E_z}{\partial \rho} \right). \quad (7.19)$$

After replacing κ^2 by $-\gamma^2$ these equations can be used for the fiber cladding region. Equations (7.13)–(7.19) express the electromagnetic field in the core and cladding regions of an optical fiber in terms of four constants A , A' , C , and C' . These constants are determined by applying the boundary condition which requires that the tangential components of $\mathbf{E}(E_z, E_\phi)$ and $\mathbf{H}(H_z, H_\phi)$ must be continuous across the core-cladding interface. By requiring the continuity of E_ρ , E_ϕ , H_ρ , and H_ϕ at $\rho = a$, we obtain a set of four linear equations [229] as related to A , A' , C , and C' . These equations set is homogeneous and have a nontrivial solution only if the determinant of the coefficient matrix equals to zero. After transformations, this condition leads to the eigen-value equation for guided modes

$$\begin{aligned} \left[\frac{J'_m(\kappa a)}{\kappa J_m(\kappa a)} + \frac{K'_m(\gamma a)}{\gamma K_m(\gamma a)} \right] \left[\frac{J'_m(\kappa a)}{\kappa J_m(\kappa a)} + \frac{n_2^2}{n_1^2} \frac{K'_m(\gamma a)}{\gamma K_m(\gamma a)} \right] \\ = \left[\frac{2m\beta(n_1 - n_2)}{a\kappa^2\gamma^2} \right]^2, \end{aligned} \quad (7.20)$$

where prime indicates differentiation with respect to the argument. That is typical characteristic equation for cylindrical dielectric waveguide with refractive index n_1 surrounded by unbounded medium with refractive index n_2 and has only longitudinal phase constant β as an unknown. This equation was obtained for the first time by Hondors and Debye [224].

For a given set of principal parameters λ_0 , a , n_1 , and n_2 , the characteristic differential equation (7.20) can be solved numerically to determine the mode propagation constant β , or its phase constant. In general, this equation may have multiple solutions for each integer value of m . It is convenient to enumerate these solutions in numerical order and denote them by β_{ml} for a given m ($l = 1, 2, \dots$). Solutions β_{ml} of the characteristic equation (7.20) together with spatial distribution from Eqs. (7.13)–(7.19) describe behavior of the fiber optical modes. Conception of the optical mode is common for all optical guided systems. As we see the optical mode of a fiber is a specific solution of the wave equation, which satisfies all the boundary conditions, and which properties are unchanged during propagation along the fiber.

The propagating mode which transfers information through the fiber links must be guided by the fiber core, and their field and power should be localized inside the core near its axis. Penetration of the field into the cladding and jacket buffer, should be as low as possible to eliminate attenuation of the mode power.

7.4 Hybrid Modes in Fibers and Mode Parameters

The given analysis has shown that in fiber both longitudinal components E_z and H_z are nonzero (except for $m = 0$). That conclusion displays the difference from the strip waveguides, for which one of longitudinal components can be taken to be zero. Fiber modes are therefore hybrid modes and are denoted by HE_{ml} or EH_{ml} , depending on whether H_z or E_z dominates.

Only one special case of symmetrical modes is possible when $m = 0$ for which the periodical azimuthal oscillations in (7.13) are absent, and HE_{0l} and EH_{0l} modes are also denoted by H_{0l} and E_{0l} , respectively, since they correspond to transversal electric ($E_z = 0$) and transversal magnetic ($H_z = 0$) modes. According to the geometric optics approach, mode with $m = 0$ corresponds to the meridional rays propagating in the meridional incident plane crossing the fiber axis.

Mode classification is illustrated in Fig. 7.2. There, space distributions of the electric and magnetic components for the first order mode HE_{11} is also presented.

Depending on fiber parameters, longitudinal components E_z and H_z can be small and main field distribution are presented by transversal components. That is possible in weakly guiding fibers with small difference between core and cladding refractive indices. For mode classification in weakly guiding fibers

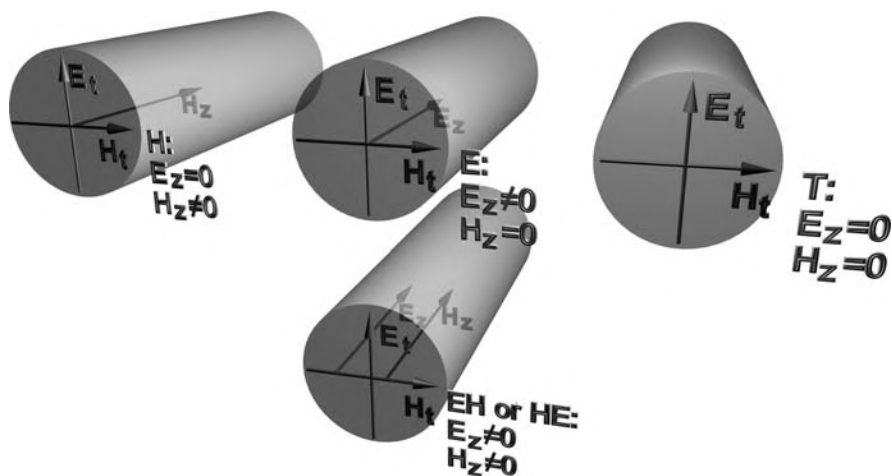


Fig. 7.2. Kinds of fiber guided modes

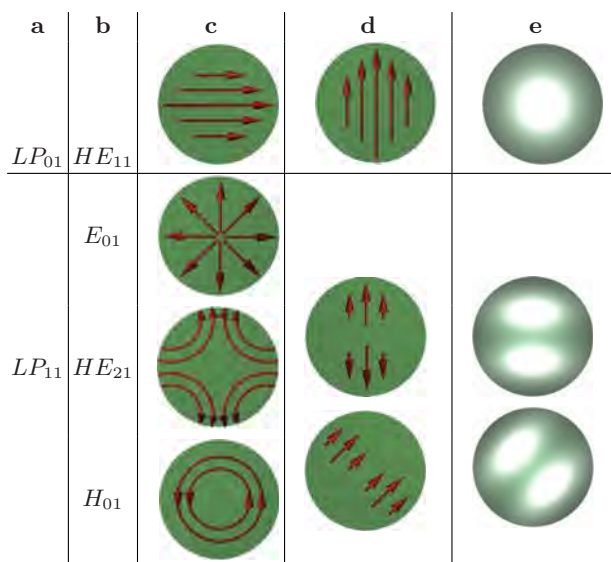


Fig. 7.3. Low-order transverse modes of step-index fiber (a) linearly polarized LP mode indication; (b) exact mode indication; (c) electric field distribution; (d) LP mode electric field distribution (e) intensity distribution

a different notation LP_{ml} (or linearly polarized modes) is also used [223] for which both E_z and H_z are nearly zero. The scheme of linearly polarized mode formation and correspondent hybrid modes in the fiber is shown in Fig. 7.3.

7.4.1 Fundamental Mode Distribution in Weakly Guiding Fibers

The field distribution of the fundamental mode is obtained by using Eqs. (7.13)–(7.19). Hence, the HE_{11} mode is approximately linearly and uniformly polarized for weakly guiding fibers. It is also denoted as LP_{01} , following a to an alternative classification of guiding modes in which all fiber modes are assumed to be linearly polarized [202, 223].

One of the transverse components can be taken as zero for a linearly polarized mode and therefore the mode will have only two transverse components. Polarization description will be more clear by using Cartesian coordinates with transformation from the cylindrical coordinates by the relation

$$\begin{aligned} E_x &= E_r \cos \phi - E_\phi \sin \phi, \\ E_y &= E_r \sin \phi + E_\phi \cos \phi. \end{aligned}$$

If we set $E_y = 0$ into field distribution expressions presented above, the E_x component of the electric field for the HE_{11} mode is given by [202]

$$E_x = E_0 \left\{ \begin{aligned} [J_0(\kappa\rho)/J_0(\kappa a)] \exp(j\beta z), & \quad \rho \leq a \\ [K_0(\gamma\rho)/K_0(\gamma a)] \exp(j\beta z), & \quad \rho > a \end{aligned} \right\}, \quad (7.21)$$

where E_0 is a constant related to the power launched into the mode. The dominant component of the corresponding magnetic field is given by $H_y = n_2 (\varepsilon_0/\mu_0)^{1/2} E_x$. This mode is linearly polarized along the x axis.

The fiber also supports another mode with $E_x = 0$ which is linearly polarized along the y axis. In this respect, a single-mode fiber actually supports two orthogonally polarized modes that are degenerate, as they have the same propagation constant $k_z = \beta$.

Superposition of degenerated HE and EH modes form high-order LP modes with corresponding azimuthal and radial indices.

7.4.2 Effective Mode Index and Cutoff Conditions

From the practical characterization of different modes it is useful to introduce a quantity $\bar{n} = \beta/k_0$, called the mode index or effective index which has following physical meaning: a each fiber mode propagates with a unique effective refractive index \bar{n} whose value lies in the range $n_1 > \bar{n} > n_2$ and is guided until $\bar{n} \leq n_2$. The effective index may be defined in terms of group velocity as $\bar{n} = c/v_g = c\beta/\omega = \beta/k_0$, or taking into account the relation $\beta = k \sin \theta = k_0 n_1 \sin \theta$, we have

$$n_{\text{eff}} = \bar{n} = \beta/k_0 = n_1 \sin \theta.$$

The effective refractive index is the crucial parameter in guided wave propagation, just as the refractive index in free wave propagation. In fact, the

effective refractive index changes the wavelength in the same way as the bulk refractive index does. Following $n = c/v = \lambda_0/\lambda$, the wavelength measured in the waveguide is $\lambda_g = \lambda_0/n_{\text{eff}}$.

This can be explained by noting that the optical field of guided modes decay exponentially inside the cladding layer and by using the asymptotic form for the Hankel function which is correct at large values of the argument [G. Korn and T. Korn, *Mathematical Handbook for Scientists and Engineers*. New York: McGraw-Hill, 1961], [222]

$$K_m(\gamma\rho) = \sqrt{\frac{\pi}{2\gamma\rho}} \exp(-\gamma\rho) \quad \text{for } \gamma > 1. \quad (7.22)$$

When $\bar{n} < n_2$, from (7.12) it follows that $\gamma^2 = \beta^2 - n_2^2 k_0^2 \leq 0$ and the exponential decay does not occur. The mode reach cutoff when γ becomes zero or when $\bar{n} = n_2$. From (7.11), $\kappa^2 = k_0^2(n_1^2 - \beta^2/k_0^2) = k_0^2(n_1^2 - \bar{n}^2)$ and when $\gamma = 0$, or $\bar{n} = n_2$ we have the critical level of the transversal phase parameter

$$\kappa = k_0(n_1^2 - n_2^2)^{1/2}, \quad (7.23)$$

which characterizes the moment when mode stops to be propagating, or cutoff condition.

Like for planar waveguides, it is convenient to express cutoff condition as well as other characteristics of the fiber through the parameter referred to as normalized frequency:

$$V = k_0 a (n_1^2 - n_2^2)^{1/2} \approx (2\pi/\lambda) a n_1 \sqrt{2\Delta}, \quad (7.24)$$

The normalized frequency or simply the V parameter, combines most important fiber parameters: core radius a , material refractive indices of core n_1 and cladding n_2 , and wavelength λ of the light to be transmitted in the fiber. The cutoff condition (7.23) gives

$$V = \kappa a. \quad (7.25)$$

Since transversal parameters values are not as interest as phase constant β in propagation direction, it makes sense to use its universal notation, namely the normalized propagation constant b defined as

$$b = \frac{\beta/k_0 - n_2}{n_1 - n_2} = \frac{\bar{n} - n_2}{n_1 - n_2}. \quad (7.26)$$

7.4.3 bV Diagram

The bv diagram shows how many modes are supported by a waveguide. As we discussed before TE and TM modes are the transverse electric and transverse magnetic modes as defined by the solution of the equation. HE and EH modes are hybrid, and both contain components of electric and magnetic fields along the fiber axis.

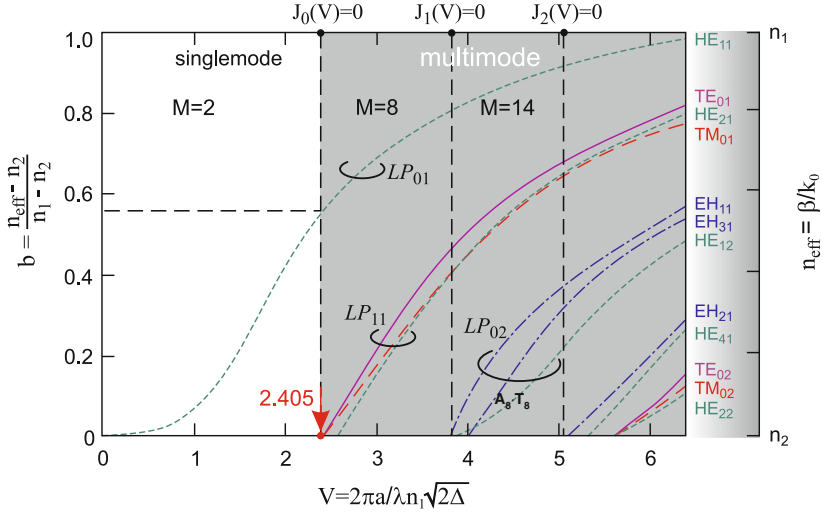


Fig. 7.4. Normalized propagation constant b as a function of normalized frequency V for a few low-order fiber modes. The right scale shows the mode index

Figure 7.4 shows a plot of b as a function of V for a few low-order fiber modes obtained by solving the eigen-value Eq. (7.20) and correspondent LP modes. Each curve actually represents two modes, one orthogonally polarized with respect to the other in the transverse plane.

Conventional fibers do not maintain polarization of the launched wave. Since orthogonally polarized waves associated with the same mode have the same effective refractive index, they travel at the same velocity and easily couple energy between themselves. This exchange occurs at bends, twists, splices, and any other mechanical deformations of the fiber. The effective refractive indices \bar{n} for all modes lie between the index of the cladding and that of the core. For a given mode, \bar{n} varies with wavelength, producing waveguide dispersion. At a fixed value of V , several modes may propagate, each having a different effective index. This situation leads to modal distortion.

The longitudinal propagation factor can be obtained from \bar{n} by taking into account $\beta = k_0 \bar{n}$. Propagation direction Θ in respect to optical axis are determined from $n_{\text{eff}} = \bar{n} = n_1 \sin \theta$.

Propagation in the fiber is quite similar to propagation in the slab. Modes are cutoff when their rays travel at the critical angle, and rays far from cutoff travel close to 90° almost directly down the fiber. In addition, decaying vanishing fields exist outside the core for all of the modes; and the closer a mode comes to cutoff, the deeper its penetration into the cladding. Far from cutoff, a propagating mode travels almost entirely in the core. For large values of V , many modes will propagate. Large V corresponds to a relatively large core radius. The number of modes (including all polarizations) for such a multimode fiber is roughly approximated by the following expression

$$M = V^2/2. \quad (7.27)$$

Typical multimode fiber with $a = 25\mu\text{m}$ and $\Delta = 10^{-2}$ has $V = 24$ at wavelength $\lambda = 1.3\mu\text{m}$ and would support about 576 modes. However, the number of modes decreases rapidly as V is reduced. It is clear from this example that even a fiber with relatively small core diameter can support a large number of modes. Because the normalized frequency is proportional to the difference in refractive indices of the core and cladding, keeping this difference small reduces the number of propagating modes.

Below a certain value of V all modes except the HE_{11} mode reaches cutoff. It appears when V is equal to the first root of Bessel function (see Fig. 7.4). Fibers with such a V parameter support only single first mode and are referred to as single-mode fibers.

7.5 Single-Mode Fibers

Single-mode or monomode fibers support only the lowest-ordered HE_{11} mode, also known as the fundamental mode of the step index fiber.

In such a fiber all of high-order modes must be cut off for operating wavelength fiber is designed such that all higher-order modes are cut off at the operating wavelength. As it was shown in the previous paragraph, the V parameter determines the number of modes supported by a fiber and their propagation condition. The cutoff condition of various modes is also determined by V . The fundamental mode has no cutoff and is always supported by a fiber.

7.5.1 Single-Mode Condition

As it is seen in Fig. 7.4, the single-mode condition is determined by the value of V at which TE_{01} and TM_{01} modes reach cutoff. Assuming $m=0$ in Eqn. (7.20) we can obtain eigen-value equations for these two modes. After that, equation can be separated into two eigen-value equations

$$\frac{J'_0(\gamma a)}{\kappa J_0(\kappa a)} + \frac{K'_0(\gamma a)}{\gamma K_0(\gamma a)} = 0, \quad (7.28)$$

$$\frac{J'_0(\gamma a)}{\kappa J_0(\kappa a)} + \frac{n_2^2}{n_1^2} \frac{K'_0(\gamma a)}{\gamma K_0(\gamma a)} = 0. \quad (7.29)$$

As previously, prime denotes derivative with respect to argument.

$$J_0(V) = 0. \quad (7.30)$$

The root of this equation is $V = 2.405$. If a fiber is designed such that $V < 2.405$, it supports only HE_{11} mode which is fundamental one. Therefore, the case when $V = 2.405$ is called also as the single-mode condition

The key point in single-mode fiber design is small core diameter. This can be understood from the dependence of the cutoff wavelength λ_C of the fiber on the core diameter. The cutoff wavelength is the wavelength above which only one single transverse mode can exist

$$\lambda_C = \frac{2\pi a}{V}(n_1^2 - n_2^2)^{1/2}, \quad (7.31)$$

where $V = 2.405$ for step-index fiber and a is the core radius. When the core diameter of a single-mode fiber is not much larger than the wavelength, there is significant power portion or field penetration in the cladding. Therefore, it is necessary to define mode field diameter or the width of the transverse field. Specifically, it is the root mean square width of the fields if the field is Gaussian. Its transverse field pattern is approximately Gaussian shaped. More strong determination of the field diameter leads to the conception of spot size [202].

$$E_x = A \exp\left(-\frac{\rho^2}{w^2}\right) \exp(j\beta z), \quad (7.32)$$

where w is the mode radius and is referred to as the spot size.

7.6 Microstructured Fibers

Main peculiarity of microstructured fibers is their complex structure of the core and the cladding. The typical PhC-based optical fiber has structure very similar to the one of conventional fibers. However, it has the PhC instead of reflecting cladding. Depending on the problem the PhC can have different spatial configuration and geometric parameters. Simple examples of the PhC-based fibers are shown in Fig. 7.5.

Because of quite complex structure of the PhC, the microstructured fiber can be made upon different principles and technologies. Taking this into account, the number of possible variations of such fibers is huge. The microstructured fiber can have the core, which refractive index is less than claddings one, it can possess either positive or negative dispersion, maintain some specific polarization, it can be single-mode within wide wavelength range even with large core size. These features together with many others provide wide range of applications for microstructured fibers.

Microstructured fibers available on markets today have reflecting cladding made of 1D or 2D PhC. The fibers with cladding made of 1D PhC have mostly technological high-power application to transmit the light to short distances. Due to the air core, the attenuation in these fibers is negligible. Because reflecting coating has the structure similar to the Bragg reflector, such kind of fibers is known as Bragg fibers (see for example [230], [231]).

The fibers which optical confinement is based on 2D PhC, can be used both for technological purposes (including optical pulses compression [232,233], and

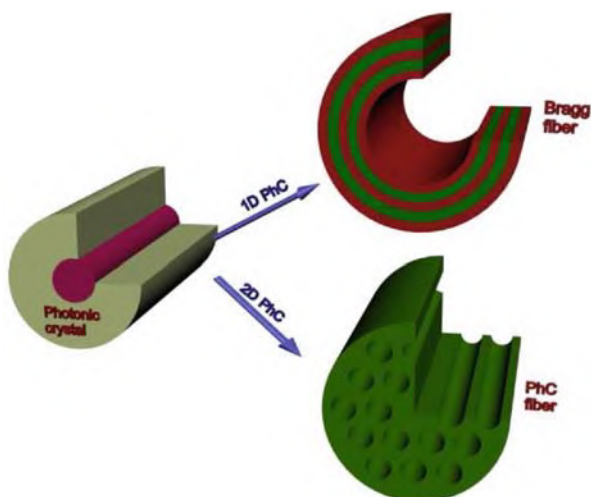


Fig. 7.5. Simple illustration of microstructured fibers geometry

supercontinuum generation [234–236]) and for telecommunication purposes to transmit information and compensate dispersion within short communication line sections.

2D PhC-fibers themselves can be classified by the principle of the radiation confinement within the core. The first class of such fibers utilizes total internal refraction. In this case, the reflective cladding is represented as some solid material with some specific refractive index which actually depends on the wavelength and the PhC elements size. This refractive index appears to be lower than the core index which provides the waveguiding properties of the fiber. Moreover, dependence of the cladding refractive index on the wavelength makes it possible to achieve a single-mode operation within wide wavelength range. The second class of 2D PhC-fibers employs the possibility of the PhC to form complete PBG. The core of such a fiber can possess lower refractive index than surrounding PhC has. Thus, the core of such fibers can be hollow. Examples of two kinds of 2D PhC fibers are given in Fig. 7.6. The only difference between them is the size of elements. Actually, the PBG may appear even at low elements size, however, the refractive index of the fiber material should be quite high. If we work with silica or some kinds of polymers, the PBG appears at large elements size only.

7.6.1 Computation of Eigen-States of Microstructured Fibers

Main characteristic of the fiber intended for long-distance data transmission is the modal structure of the optical radiation propagating inside it. Computation of the modal structure for the step-index conventional fiber was given above. The problem can be easily solved analytically and is reduced

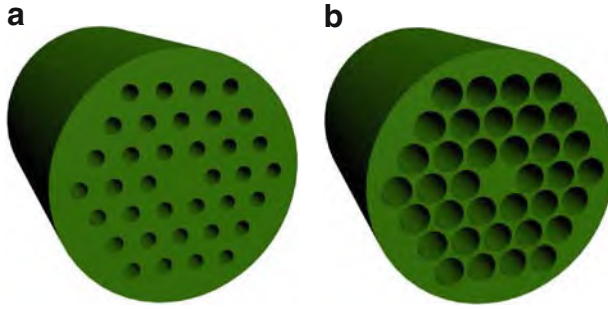


Fig. 7.6. Examples of index-guided (a) and PBG (b) fibers

to the determination of fiber parameters which provide either single-mode or multi-mode operation of the fiber. However, in case of microstructured fiber, the problem becomes much more complex in view of large number of structure elements. This leads to employment of numerical techniques such as plane wave expansion method or approximation methods such as effective refractive index method.

In general, determination of modal structure of the microstructured fiber is reduced to the solution of the eigen-problem formulated for the PhC with a defect which was described in Chap. 5. One of the most convenient methods used in this case is the plane wave expansion method described in Chaps. 4 and 5. In addition, it is necessary to compute the off-plane eigen-states because of radiation propagation along the defect so its off-plane wave vector component is not zero as was shown in Chap. 5. In this case the off-plane component of the wave vector stands for the propagation constant.

The eigen-problem solution consists in computation of eigen-states of an infinite periodic structure formed by the translation of the PhC section with defect. The computation procedure now is as follows:

1. Determine the unit cell of the PhC containing defect. In our case, the unit cell should be large enough to insulate translated defects from each other. For this, we should take the unit cell including at least five or six PhC elements as discussed in Chap. 5.
2. The range of the in-plane wave vector component may be limited by a single value. This may be done because of the independence of the defect eigen-frequency on the wave vector as was also shown in Chap. 5. As for the off-plane wave vector component, it should vary within the limits from zero to the value determined in the specific problem.
3. Define the set of the reciprocal lattice vectors. As was shown in Chap. 5, the number of reciprocal lattice vectors should be larger than that for strictly periodic structure.
4. Form the matrix differential operator for each wave vector value within defined set and compute its eigen-values.

Lets now consider each computation step in detail. Determination of the unit cell of the PhC with defect which the PhC-fiber is, is the crucial moment in the eigen-states computation. If size of the unit cell is too small, the light localization inside each of translated defects will be weak as well. The solid-state analogy here is high probability of the tunneling between defects. Consequently, the eigen-states in this case will widen such that computation results will be rather inaccurate. On the other hand, when the unit cell is selected to be large, the computation performance is dramatically reduced which may be critical in optimization.

The fact that the Brillouin zone of the structure with defect will be several times smaller in each direction than in case of strictly periodic structure should be taken into account. The size of the Brillouin zone is in inverse proportion to the size of the PhC unit cell as follows from (4.17).

The off-plane component of the wave vector is the longitudinal one and, by definition, it is usually referred to as the propagation constant and is designated as β when computing the eigen-states of the PhC-fiber. It represents the change in phase along the path traveled by the wave at any instant.

Determination of the matrix differential operator and solution for the eigen-states is carried out similarly to the procedure described in Chap. 5. One more important moment is the fact that there is no polarization separation of the radiation in contrast to in-plane 2D PhC consideration. Therefore, computation of the PhC-fiber eigen-states requires consideration of both electric and magnetic components of the field.

7.6.2 Computation of the Mode Field Distribution in Microstructured Fibers

In some applications like supercontinuum generation, it is necessary to know the mode field distribution in order to take into account interaction between the optical field and fiber. The solution of such kind of problems can also be carried out by PWE method.

During the derivation of the final expression for the eigen-frequency computation described in Chap. 4, we presented the eigen-function distribution as a product of the plane wave and the periodic function with periodicity of lattice (5.2). We have also obtained the Fourier expansion of this function (5.4). As a result, the system of linear equations have been derived when the eigen-problem was solved. The value of $\frac{\omega^2}{c^2}$ in this system play a role of the eigen-value while $\mathbf{H}_{\mathbf{k}n}(\mathbf{G})$ and $\mathbf{E}_{\mathbf{k}n}(\mathbf{G})$ are eigen-vectors. Solving the eigen-problem by the method described in Chap. 4 it is possible to obtain the sets of eigen-vectors each corresponding to specific eigen-value. The field distribution at the specific eigen-state can easily be found substituting the eigen-vector elements to the expression (5.4), i.e., the field is synthesized from the set of harmonics where the eigen-vector elements play role of harmonics amplitudes. In other words previously, the expansion problem was solved and after

all parameters are determined, the synthesis problem is solved. Let us now consider the example of the field distribution computation of the eigen-state.

We consider the eigen-function computation for 2D PhC fiber represented by the set of holes in bulk material. First, the problem is solved directly in a way described in Chap. 5. Now, we write down the expression which allows to determine the field distribution. The expression (5.4) which is actually a Fourier expansion, takes the following form:

$$\begin{aligned} \mathbf{E}_{\mathbf{k}n}(x, y) &= \sum_u \mathbf{E}'_{\mathbf{k}n}(\mathbf{G}_u) \exp(j((k_x + G_{xu}) \cdot x + (k_y + G_{yu}) \cdot y)), \\ \mathbf{H}_{\mathbf{k}n}(x, y) &= \sum_u \mathbf{H}'_{\mathbf{k}n}(\mathbf{G}_u) \exp(j((k_x + G_{xu}) \cdot x + (k_y + G_{yu}) \cdot y)). \end{aligned} \quad (7.33)$$

Here $\mathbf{H}'_{\mathbf{k}n}(\mathbf{G}_u)$ and $\mathbf{E}'_{\mathbf{k}n}(\mathbf{G}_u)$ are eigen-vectors to be found during the eigen-problem solution.

We solve the eigen-problem and compute the field distribution for some specific wave vector. After the eigen-problem is solved and we have the set of eigen-values and corresponding set of eigen-vector, we can start with field distribution computation. We must consider the transversal field distribution only, so that the off-plane wave vector component is absent within the expression (7.33). When we synthesize the field distribution, the sets of G_x and G_y are taken to be exactly the same as during the solution of eigen-problem since previously we obtained Fourier coefficients for harmonics with exactly these values of G_x and G_y . Otherwise, the synthesis will be carried out for harmonics with frequencies which differ from those used for expansion, so computed eigen-vectors will be meaningless.

The summation is carried out for specific coordinate so that during single summation, the field value in a single point only can be found. In order to find the field distribution within specific region, it is necessary to carry out summation for all points within this region. Resulting electric field distributions of the first and the second nondegenerated modes are shown in Fig. 7.7. The first mode corresponds to the lowest eigen-state and has the lowest frequency. The second mode is actually degenerated to the first one and has almost the same frequency. However, it appears that the third mode (or the second nondegenerated mode) already possesses much higher frequency. Figure 7.7 depicts the field distribution within the unit cell of the considered PhC. It is seen that the field of the first mode is strongly localized inside the defect of the periodic structure while the second one passes through the surrounding PhC and flows out the defect.

The computation of the modes field distribution inside the PhC fiber carried out by the plane wave expansion method can be useful for the determination of modal properties of the fiber as well as for the solution of field-material interaction problem in nonlinear fibers.

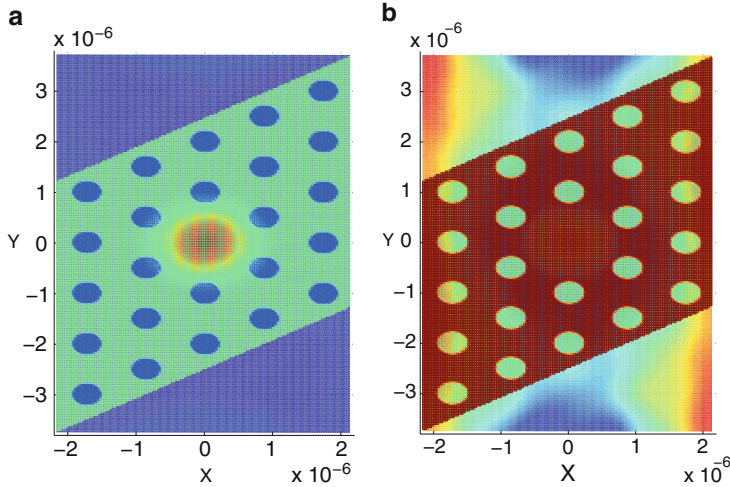


Fig. 7.7. Electric field distribution of the first and second nondegenerated modes inside index-guided microstructured fiber

7.7 Index-Guided Microstructured Fibers

As mentioned above, there are two main classes of microstructured fibers, namely, the fibers employing the principle of total internal reflection (TIR) and the fibers where waveguiding effect is possible due to complete PBG of the PhC cladding. In this section, we consider the first class of such a PhC-fiber. Main peculiarity of the TIR PhC-fibers is their ability to support single-mode operation within wide range of wavelengths.

How can this be achieved? For better understanding of the operation principles of the TIR PhC fibers, we first consider computation of bulk PhC eigen-states with further consideration of the structure with defect and field distribution computation inside the waveguiding area.

The characteristic which describes properties of the PhC as a fiber cladding is referred to as continuum of states. It gives the range of frequencies and propagation constants where strictly periodic PhC has eigen-states so the radiation passes through the PhC. This means that no radiation localization is possible within such radiation parameters. The continuum of states is indicated by filled green area in Fig. 7.8. In order to obtain the information about the continuum of states of the fiber cladding, we first compute the reduced band structure for the PhC without defect. Such a reduced band structure is represented by the characteristic indicating the presence or absence of the PBG at each value of the propagation constant within selected range. Such reduced band structure was computed for the value of holes radius $r = 0.15a$. It is seen from figure that minimum frequency of the continuum of states shifts to high-frequency region while growth of the propagation is constant.

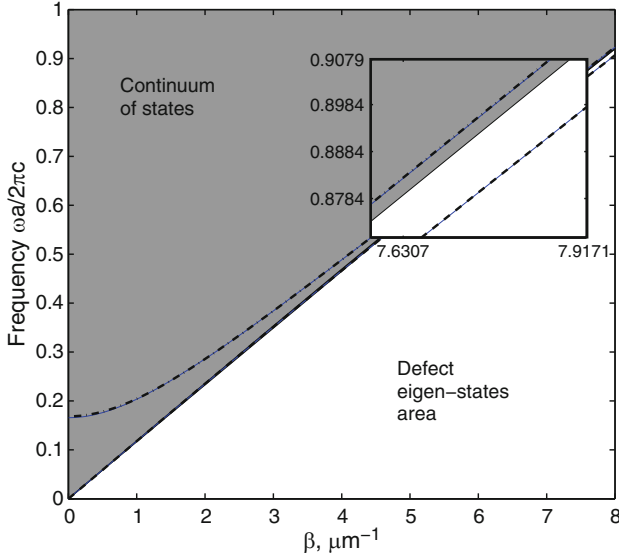


Fig. 7.8. The continuum of states and the defect eigen-states of a single-mode index-guided microstructured fiber

Now we consider the eigen-states of the PhC with defect, which is represented by missing hole creating conditions for the radiation localization and forming the waveguiding area of the fiber. As we decided previously, we will compute the eigen-states for a single wave vector only so that we obtain the set of eigen-frequency dependencies on the wave vector instead of reduced band structure obtained for defectless structure. The computation results indicated by lines in Fig. 7.8. First two eigen-states of the structure with defect appear to be degenerated so their frequencies are very close to each other so that we can see one line only at the bottom of the insertion. It can also be seen that in the insertion, that these eigen-states lie beneath the continuum of states. This indicates the fact that the radiation possessing corresponding wave vectors and frequencies will not be able to pass through the cladding PhC so it will be localized inside the core. Thus, $\omega - \beta$ space is divided by two areas, namely, the continuum of states and the area beneath the continuum. The area beneath the continuum of states is actually the area of guiding modes. The eigen-states lying within this area, correspond to modes localized in the core region. Fibers with eigen-states beneath the continuum of states are referred to as TIR PhC fibers or index guided fibers.

Let us now consider the results obtained from another point of view. The computation results actually demonstrate the fact that the first group of degenerated eigen-states lie below the continuum of states within wide frequency range while the second group of levels lie in the continuum of states area. This allows to conclude that the PhC fiber operating principle is based on the TIR, which is singlemode within wide range of frequencies.

7.7.1 Effective Refractive Index of the PhC-Fiber

In order to characterize the TIR PhC-fiber, the effective refractive index of the cladding is used. The effective index is introduced for each mode and is determined by the expression $n_{\text{eff}} = \beta/k$ as was shown in Sect. 7.4. The dependence of effective refractive index of the first mode on the radiation frequency is shown in Fig. 7.9.

It can be seen from figure that the effective refractive index of the first mode asymptotically approaches to effective index of the boundary of the continuum of states. Thus, the core refractive index is always higher than the effective refractive index of the first mode, which provides the TIR similar to conventional step-index fiber. The effective index of modes lying inside the continuum of states, is always higher than the one of the bulk PhC, hence they will flow out from the core.

7.7.2 Step-Index Fiber Model of the Index-Guided PhC Fibers

The model of the PhC fiber considered earlier in this chapter are quite precise and take into account the exact geometry of the PhC. However, many problems such as computation of numerical aperture or bending losses can be solved much easier when representing the PhC fiber as a step-index fiber. This model was first proposed by Birks et al. [237] and may effectively be used for approximate solution of many problems.

The model itself consists in representation of the PhC fiber by the step-index fiber (the analogy is given in Fig. 7.1). Within this model, the reflecting

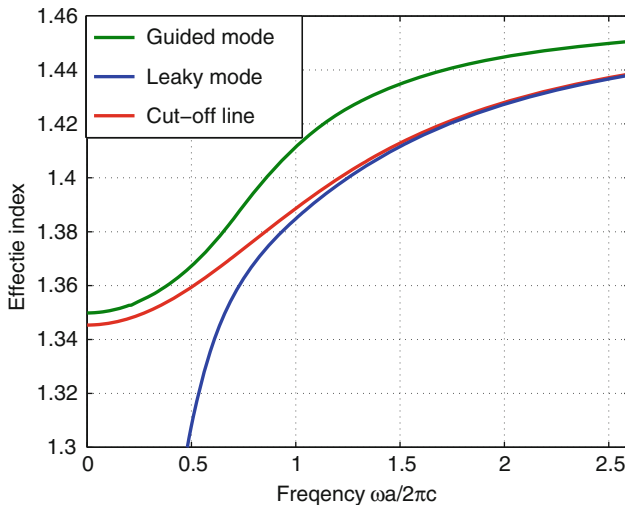


Fig. 7.9. The effective refractive index of the first and second nondegenerated modes and the cutoff line

cladding of the PhC fiber is represented as solid material with specific refractive index which is actually the effective refractive index n_{eff} of the PhC. The defect of the PhC where the radiation is localized, is represented by the fiber core with the same refractive index as a material of the PhC. As we have seen earlier (see Fig. 7.9) for PhC silica fiber, the effective refractive index of the PhC is always lower than that of the solid material, i.e., of the core which provides light localization within high-index region. Thus, representing the PhC fiber by this simple model, we may now analyze simple step-index fiber in a way described at the beginning of the chapter instead of quite complex structure.

However, it should be mentioned that the fact that n_{eff} of the PhC varies with wavelength and, therefore, this approximation may be used for a single wavelength only as long as properties of whole step-index fiber vary as well.

7.7.3 Numerical Aperture of the PhC Fiber

When the mode flows out from the fiber face, its radius usually increases. The amount of such widening can be made by introducing the numerical aperture (NA).

The easiest way to estimate the NA of the index-guided PhC fiber is to approximate it by a step-index fiber as was made above. This technique was applied in the work [238] and it allowed to reduce the problem of computation of the NA of single-mode step-index fiber.

In case of conventional single-mode optical fiber, the mode field distribution is described by Gaussian function and NA is often defined as $NA = \sin \theta$, where θ is the half-divergence angle between the radiation propagation direction and the cone connecting the points where the intensity of Gaussian beam decreases several times.

$$\tan \theta_f = \lim_{z \rightarrow \infty} \frac{r_f(z)}{z}, \quad (7.34)$$

where $r_f(z)$ is determined from the expression

$$\frac{\Psi(z, r = r_f)}{\Psi(z, r = r_0)} = f, \quad (7.35)$$

where Ψ is Gaussian function of width w .

The half-divergence angle has different approximations for different values of f . In case of $f = 1/e^2 = 0.135 = 13.5\%$, it is found as

$$\theta_{13.5\%} \approx \arctan \left(\frac{2}{kw} \right) = \arctan \left(\frac{\lambda}{\pi w} \right), \quad (7.36)$$

In case of $f = 5\%$

$$\theta_{5\%} = \arctan \left(\sqrt{\frac{\ln 20}{2}} \times \tan \theta_{13.5\%} \right). \quad (7.37)$$

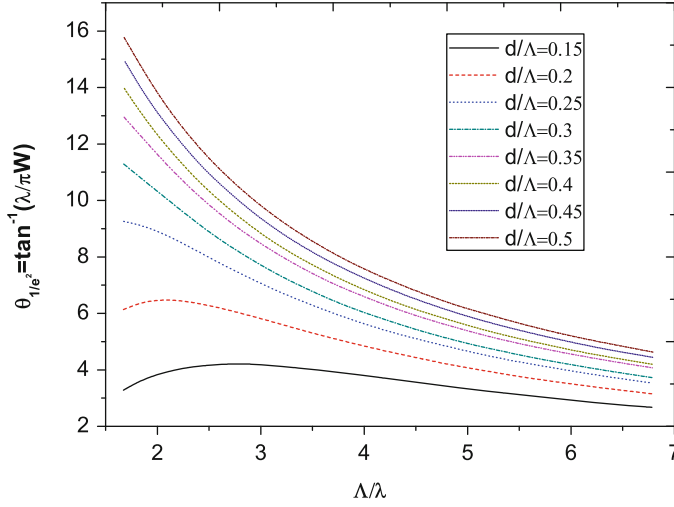


Fig. 7.10. Half-divergence angle of the PhC silica-based fiber with different radii of the PhC holes

These approximate formulas are in good agreement with the exact solution of the scattering problem when $kw \gg 1$. In order to solve the problem accurately for the PhC fiber, the PhC fiber mode field distribution should be taken into account. The field computation technique was presented in the Sect. 7.6.2 using the Eq. (7.33).

In Fig. 7.10, the half-divergence angle $\theta_{13.5\%}$ is given as a function of normalized distance between holes' centers a/λ for different diameters of the PhC holes. In case of low radius the angle is low so that the NA is low as well. This is caused by very low difference between the n_{eff} of the PhC and the refractive index of the core which leads to low localization of the radiation within the fiber core.

7.7.4 Macro-Bending Losses

When the TIR PhC-fiber is straight, the PhC provides light localization inside the core. However, if the fiber appears to be coiled around something or just bent (see Fig. 7.11), the radiation starts to couple to leaky mode which causes losses. If the bending radius is much larger than the wavelength, such bend is referred to as macro-bending.

Similar to material losses, macro-bending losses obey exponential law, and are described by formula:

$$P = P_0 \cdot \exp(-\alpha \cdot z), \quad (7.38)$$

where P_0 is initial optical power, α are losses due to bending.

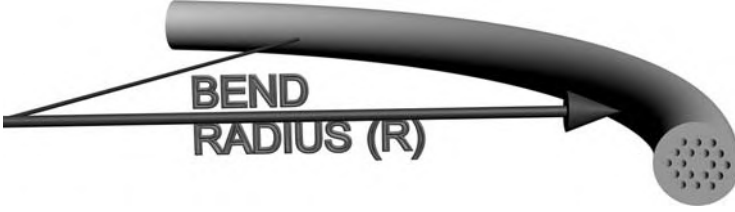


Fig. 7.11. Schematic of the macro-bending of the PhC fiber

The easiest way to compute the bending losses is to apply the step-index approximation to the PhC fiber as it was made in [239].

$$\alpha = \frac{\sqrt{\pi}}{8} \frac{A_e^2}{P} \frac{\rho \exp(-4\Delta W^3 R / (3\rho V^2))}{W \sqrt{WR/\rho + V^2/(2\Delta W)}}, \quad (7.39)$$

where V is normalized frequency, W is normalized decay parameter of the cladding, Δ is relative difference between core and cladding refractive indices, ρ is the radius of the core, A_e is the amplitude coefficient of the field in the cladding, and P is the power carried by fundamental mode.

When we apply this formula to the PhC fiber, we have to use effective parameters instead of real ones. Thus, we replace the normalized frequency by its effective analog [239]:

$$V \rightarrow V_{\text{eff}} = \rho \frac{2\pi}{\lambda} \sqrt{n_{\text{co}}^2 - n_{\text{cl,eff}}^2(\lambda)}, \quad (7.40)$$

as well as normalized decay parameter:

$$W \rightarrow W_{\text{eff}} = \rho \frac{2\pi}{\lambda} \sqrt{n_{\text{co,eff}}^2 - n_{\text{cl,eff}}^2(\lambda)}, \quad (7.41)$$

and

$$\Delta \rightarrow \Delta V_{\text{eff}}(\lambda) = n_{\text{co}} - n_{\text{cl,eff}}(\lambda), \quad (7.42)$$

where n_{co} is the refractive index of the core, $n_{\text{co,eff}}$ is the effective index of the fundamental mode and $n_{\text{cl,eff}}$ is the effective index of the defectless PhC forming the PhC fiber cladding.

The approximation here causes some inaccuracy since the PhC fiber does not possess rotational symmetry in contrast to conventional fiber. Due to this fact, the bending in different directions causes different losses. However, if one wants to estimate losses, this inaccuracy may be neglected.

In Fig. 7.12 it is depicted typical bending losses obtained in the work [239] using this approximation and employing full-vectorial method for PhC characteristics computation. The bending losses are computed for different bending radius. As is seen, the characteristics possess minima at some specific wavelength which does not change with bending radius which gives rise to optimization possibility of such fibers.

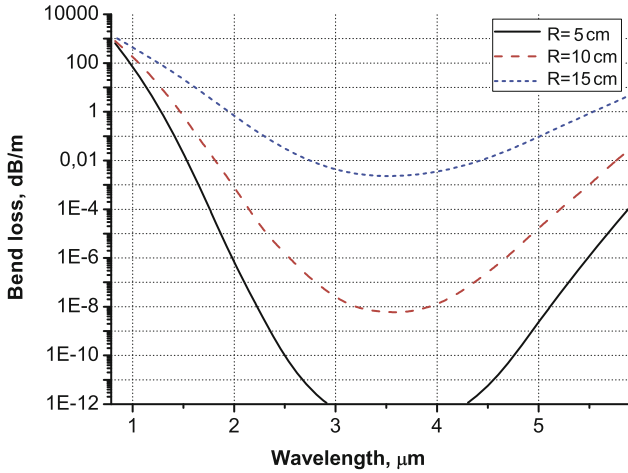


Fig. 7.12. Macro-bending losses obtained by full-vectorial model

7.8 Photonic Band Gap Fibers

A class of microstructured fibers described in the previous section had the core refractive index higher than the effective refractive index of the guided modes. However, for a class of PhC fibers described in this section this requirement is not indispensable because their operating principle is based on the PBG rather than TIR. The core of the fiber which is actually a defect of the periodic structure localizes the radiation due to appearance of the additional eigenstates inside the PBG.

In Chap. 5 it was shown that computation of the off-plane band structure of the PhC requires consideration of both electric and magnetic field components. Appearance of the PBG in this case is possible in very special cases only, for instance, at high refractive index contrast or large radius of holes as compared to the distance between them and at high values of propagation constant when the bands become flat enough. In Fig. 7.13 the reduced off-plane band structure of the defectless PhC with high holes radius values is indicated by filled green area. It can be seen from the figure that the appearance of the PBG is possible at high radius of holes and at high values of the propagation constant. The PBGs are indicated by white areas inside the continuum of states. The first one starts from the relative frequency 1.35 and the relative propagation constant 1.25 and is quite wide while the second one lies within the frequency range from 1.75 to 2.2 and propagation constant range from 1.6 to 2.25, so it is narrow.

When the defect is introduced to the periodic structure, additional eigenstates appear within the PBG so that the radiation with corresponding frequency and wave vector will be guided by the fiber. Here we consider the hollow-core fiber (see Fig. 7.13(a)) to demonstrate the possibility of light localization inside the defect with low refractive index.

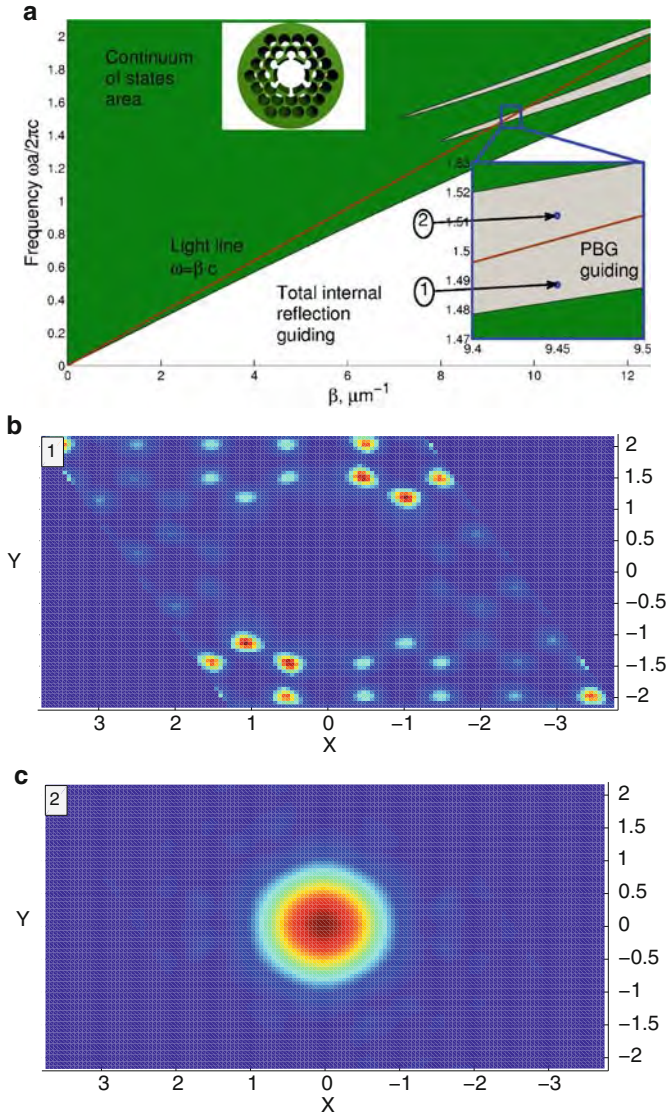


Fig. 7.13. Hollow-core fiber cross section and its dispersion diagram (a) and modes field distribution (b) and (c)

Obviously, the PBG fiber will not be a single mode. The eigen-states of the PBG fibers may appear both beneath the continuum of states and within the PBG so that the number of modes will depend on the number of eigen-states outside the continuum of states.

Two eigen-states of the PBG fiber are shown in Fig. 7.13(a) by blue dots. It is seen that both modes lie inside first PBG so that they both will be localized

by the PhC. In Fig. 7.13(a), the black line indicates the so-called light line. The radiation below this line is affected by the TIR effect at the interface between the material and holes. This means that the light localization appears inside high-index areas of the PhC but not in the PhC defect area which has low refractive index (see Fig. 7.13(b)). These modes are known as cladding modes. On the other hand, if the eigen-frequency lies above the light line, the radiation forms “leaky” modes which are able to flow out from the high-index medium to the low-index defect of the PhC and to be localized there (see Fig. 7.13(c)).

7.9 Band Gap Diagram of the PBG Fiber

As we have seen, the conditions for the radiation localization inside the defect may not be satisfied even in case of presence of the PBG at high values of the propagation constant with defect eigen-states inside. Thus, dispersion characteristic considered in this section does not provide enough information.

To provide complete characterization of the PBG fiber, another kind of characteristics, namely, the band gap diagram, appears to be more convenient. The characteristics (see the right part of the Fig. 7.14) is represented by the contrast picture where green areas inside bold black lines correspond to band gaps of the PhC while white areas correspond to continuum of states. Along the horizontal axis, the frequency lies while effective refractive index lies along vertical one. Such characteristics are described, for instance, in [240] and [241]. Thus, the characteristic indicates ranges of the effective index where the PBG exists. The light line shown in left part of the Fig. 7.14 (the orange one) corresponds to horizontal line at the level of $n_{\text{eff}} = 1$ in the band gap diagram while lines with higher (the gray and green ones) and lower (the red one) effective indices give corresponding horizontal lines inband gap diagram.

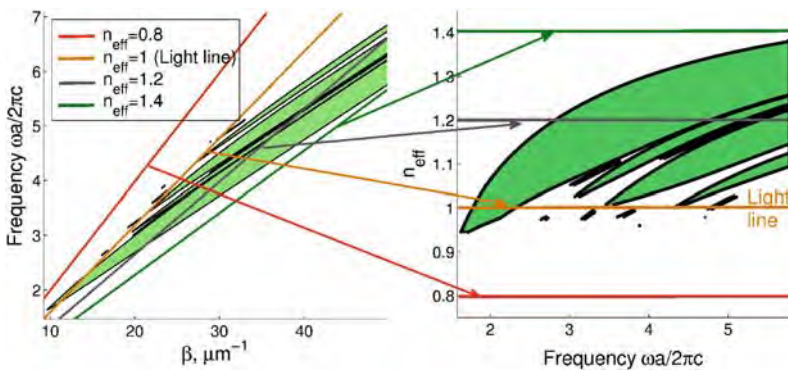


Fig. 7.14. The formation of the band gap diagram of the PhC

As we have seen in the previous section, the light licalization inside the PBG fiber core is possible when eigen-states lie above the light line. In the band gap diagram corresponding area is situated below the orange horizontal line at the level of $n_{\text{eff}} = 1$. Here we can conclude that the PBG-guidance inside the low-refractive index core of the PBG fibers is allowed only for those ones which have the PBG below the line $n_{\text{eff}} = n_{\text{low}}$, where the n_{low} is the refractive index of the core region.

Let us now turn to the computation of the band gap diagram. We first compute the dispersion diagram as we made in previous section. At that, we compute continuum of states and band gaps only. Such a dispersion diagram is shown in left part of the Fig. 7.14.

After that, we “cut” obtained dispersion diagram by the lines corresponding to different constant values of the effective refractive index. These lines are red, orange, gray, and green ones in Fig. 7.14. Then we are moving along the lines of constant n_{eff} and writing down the values of the frequencies where the PBG appears. Then we plot obtained values in the band gap diagram.

We can use another method which is good for analysing the raster images of the dispersion diagrams. Since we have patch plot rather than 2D plot, we can just move along the line $n_{\text{eff}} = \text{const}$ and set the light spot if we found continuum of states at this frequency or the dark spot if the frequency corresponds to the band gap. Scanning over each n_{eff} within the selected range, we finally obtain the band gap diagram.

The band gap diagram is quite simple to obtain if we know the dispersion characteristic. On the other hand, the characteristic is very useful for the determination of the guidance possibility of the PBG fiber and for the determination of frequency range the guidance is allowed for.

7.9.1 Coupling Losses of the PhC Fiber

When the radiation is introduced to fiber as well as in case of fiber splicing, the radiarion lossess appear. They are usually referred to as coupled losses.

The losses themselves may appear, for instance, if the fibers’ geometry parameters do not fit (see Fig. 7.15(a)). It can be easily illustrated that the coupling losses when introducing the radiation from the multimode step-index fiber to the single-mode fiber. As long as their core diameters differ several times, some radiation wich propagated inside the core of the multimode fiber, appears to be out of the core of the single-mode one. If the fibers are connected without specially designed couplers, significant losses appear.

Theoretical background for coupling losses computation is quite simple. They are actually computed as following overlap integral:

$$L_c = -20 \log_{10} \left[\frac{\int_{-\infty}^{\infty} \int_{-\infty}^{\infty} \Psi_1 \cdot \Psi_2 \cdot dxdy}{\sqrt{\int_{-\infty}^{\infty} \int_{-\infty}^{\infty} \Psi_1^2 \cdot dxdy \int_{-\infty}^{\infty} \int_{-\infty}^{\infty} \Psi_2^2 \cdot dxdy}} \right], \quad (7.43)$$

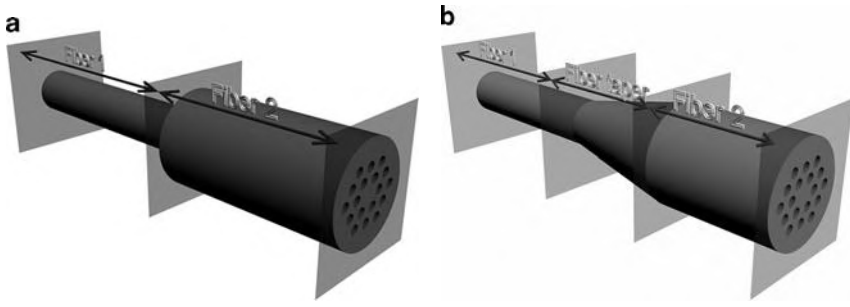


Fig. 7.15. Photonic crystal fibers connection without (a) and with (b) taper

where Ψ_1 and Ψ_2 are field profile of the input and output fibers. The field distribution of the guided modes can be computed either by PWE or by FDTD methods and, after the numerical integration the losses may be easily obtained.

In order to minimize coupling losses, the tapers are usually used. Couplers are exactly designed devices which provide high-efficient coupling from one fiber to another. Some examples of such couplers are shown in Fig. (7.15(b)). The main aim of the coupler is to effectively convert the field profile inside one fiber to the profile introduced to the second fiber. High-performance couplers allow almost total elimination of coupling losses.

7.10 Summary

1. Microstructured fiber is an optical waveguiding structure in which main element is PhC cladding providing light localization inside the core region.
2. Microstructured fiber possesses wide spectrum of features such as single-mode operation within wide frequency range and with large core, strong light localization within the core region, peculiar dispersive properties according to PhC surrounding the core region, namely, 1D or 2D photonic crystal, and according to optical confinement mechanism, namely, total internal reflection or the photonic band gap.
3. Computation of the characteristics of the microstructured fiber as well as mode field distribution can be made by plane wave expansion method.
4. TIR PhC fibers are characterized by wide range of single mode operation due to frequency dependent effective refractive index of the PhC.
5. PBG fibers possess strong light localization within the core region which provides high interaction between the field and the fiber material and, consequently, appearance of high nonlinearities.
6. The band gap diagram is the characteristic of the PBG fiber which allows to determine its operating frequency range.

7.11 MATLAB Program for Computation of the Fundamental Mode Distribution in Microstructured Fiber by Means of Plane Wave Expansion Method

```
%Program for computation of the mode field
%distribution in microstructured fiber based on
%square lattice photonic crystal. Parameters
%of the fiber are: PhC period, radii of its
%elements, refractive indices of the background
%and PhC elements.

%Input parameters are PhC period, radius of an PhC
%element, indice of refraction.

%Output data are mode field distribution.

clear all;

%Variable a contains period of the structure.
a=1e-6;

%Variable r contains PhC element radius. All
%elements are identical. Here radius is expressed
%via period.
r=0.2*a;

%Variable eps1 contains background material
%permittivity.
eps1=1.46^2;

%The variable eps2 contains permittivity of the
%elements composing PhC. In our case
%permittivities are set for the structure
%perforated membrane
eps2=1;

%The variable nG defines the number of plane waves
%which is determined as  $(nG*2-1)^2$ . For
%calculations a few plane waves is enough.
nG=3;

%Variable precisStruct sets number of nodes inside
%the unit cell.
precisStruct=30;
```

```

% We have used a set of wave vectors within the
%Brillouin zone to compute PBG for strictly
%periodic PhC. In this program here we compute
%field distribution for the defect eigen-state
%which is independent on wave vector. Thus we can
%suppose transverse components of the wave vector
%to be zero and longitudinal component to be
%nonzero.
kx=0;
ky=0;
kz=2/a;

% Inside this loop we define unit cell via
%assigning inverse refractive index to each mesh
%node. In contrast to strictly periodic PhC we
%need larger unit cell for microstructured fiber,
%since its refractive index profile is not a
%strictly periodic function, but contains defect
%instead, which localizes radiation. In this case
%here the linear size of the unit cell is 5 times
%larger as compared to the strictly periodic
%structure. Defect is in the center of the
%structure.

for numElemX=1:5
  for numElemY=1:5
    nx=1;
    if(numElemX==3)&&(numElemY==3)
      for countX=0:a/precisStruct:a
        ny=1;
        for countY=0:a/precisStruct:a
          struct(nx+(numElemX-1)*precisStruct,ny+...
                (numElemY-1)*precisStruct)=1/eps1;
          xSet(nx+(numElemX-1)*precisStruct)=countX+...
                (numElemX-1)*a;
          ySet(ny+(numElemY-1)*precisStruct)=countY+...
                (numElemY-1)*a;
        ny=ny+1;
      end
      nx=nx+1;
    end
  else
    for countX=0:a/precisStruct:a
      ny=1;
      for countY=0:a/precisStruct:a

```

```

% Next condition allows definition of a circle of
%the radius r
    if(sqrt((countX-a/2)^2+(countY-a/2)^2)<r)
        struct(nx+(numElemX-1)*precisStruct,ny+...
            (numElemY-1)*precisStruct)=1/eps2;
        xSet(nx+(numElemX-1)*precisStruct)=...
            countX+(numElemX-1)*a;
        ySet(ny+(numElemY-1)*precisStruct)=...
            countY+(numElemY-1)*a;
    else
        struct(nx+(numElemX-1)*precisStruct,ny+...
            (numElemY-1)*precisStruct)=1/eps1;
        xSet(nx+(numElemX-1)*precisStruct)=...
            countX+(numElemX-1)*a;
        ySet(ny+(numElemY-1)*precisStruct)=...
            countY+(numElemY-1)*a;
    end
    ny=ny+1;
end
    nx=nx+1;
end
end
end

%Calculation of the area of the mesh cell can be
%used in calculation of Fourier expansion
%coefficients
dS=(a/precisStruct)^2;

%Two-dimensional arrays formation from the set of
%coordinates of the mesh nodes
xMesh=meshgrid(xSet(1:length(xSet)-1));
yMesh=meshgrid(ySet(1:length(ySet)-1))';

%Values in the mesh nodes are transformed to the
%form convenient for calculation of the Fourier
%expansion coefficients
structMesh=struct(1:length(xSet)-1,1:...
    length(ySet)-1)*dS/(max(xSet)-min(xSet))^2;

%Variable numG contains number of plane waves
%which are used in expansion of Bloch waves and
%refractive index into Fourier series
numG=1;

```

```

%This loop forms the set of inverse lattice
%vectors
for Gx=-nG*2*pi/(a*5):2*pi/(a*5):nG*2*pi/(a*5)
    for Gy=-nG*2*pi/(a*5):2*pi/(a*5):nG*2*pi/(a*5)
        G(numG,1)=Gx;
        G(numG,2)=Gy;
        numG=numG+1;
    end
end

%This loop calculates Fourier expansion
%coefficients which will be used for calculation
%of matrix differential operator.
for countG=1:numG-1
    for countG1=1:numG-1
        CN2D_N(countG,countG1)=sum(sum(structMesh.*...
            exp(1i*((G(countG,1)-G(countG1,1))*...
                xMesh+(G(countG,2)-G(countG1,2))*yMesh))));
    end
end

%In this loop we calculate matrix differential
%operator for TM polarization according to
%formula (4.25).
%Calculation is realized for each wave vector from
%the array defined above. The difference from the
%previously considered case consists in that wave
%vector contains now a component along the
%propagation direction, i.e. component
%perpendicular to the plane of PhC.
for countG=1:numG-1
    for countG1=1:numG-1
        M(countG,countG1)=CN2D_N(countG,countG1)*...
            (kz^2+(kx+G(countG,1))*(kx+G(countG1,1))+...
                (ky+G(countG,2))*(ky+G(countG1,2))));
    end
end

%Calculation of eigen-vectors and eigen-values
[D V]=eig(M);

%We calculate field distribution within the unit
%cell. Actually, field distribution like the
%structure itself will be periodic, and size of
%the area where field distribution will be

```

```

%calculated does not matter. However, in his
%program here we restrict ourselves by elementary
%cell.
%We create an array in which the values of the
%field strength in each point will be saved. The
%size of the array is equal to the size of another
%array which describes unit cell.
field=zeros(size(struct));
for Gc=1:numG-1
    xi=1;
    for x=min(xSet):(xSet(2)-xSet(1)):max(xSet)
        yi=1;
        for y=min(ySet):(ySet(2)-ySet(1)):max(ySet)
            %We calculate field strength in specific point by
            %summation of terms in Fourier series for each
            %inverse lattice vector on which expansion was made.
            %To synthesize the field distribution we take first
            %eigen-vector which corresponds to the first
            %eigen-state of the PhC.
            field(xi,yi)=field(xi,yi)+D(Gc,1)*...
                exp(i*((kx+G(Gc,1))*x+(ky+G(Gc,2))*y));
            yi=yi+1;
        end
        xi=xi+1;
    end
end
end
f=figure(234);
% We plot field strength distribution
surf(ySet,xSet,abs(field),'LineStyle','none');
hold on;
% We plot refractive index of the cell
mesh(ySet,xSet,struct,'FaceColor','none');
xlabel('x, \mum','FontSize',20);
ylabel('y, \mum','FontSize',20);

```

Now let us discuss some crucial moments in the program. It consists of seven blocks.

The first block is variables initialization and structure parameters definition. Here we initially set the lattice constant for defectless PhC and the elements radius as well as discretization precision. Here the PWE method parameters are also defined such as the value nG which determines the number of plane waves. In this program the wave vector definition may also be considered as the part of the first block since here we perform computation for a single wave vector value.

The structure definition is performed within block 2. The structure here is represented by square 5×5 matrix of holes with missed one in the center.

In the third block, the set of reciprocal lattice vectors is initialized. However, in contrast to the program given in Chap. 5, here the primitive reciprocal lattice vectors will be five times smaller since they are in reverse proportion to the unit cell dimensions.

Computation of the Fourier expansion coefficients is carried out within fourth block of the program. The procedure here is exactly the same as was considered in Chap. 5.

Then, in fifth block the matrix differential operator is composed and its eigen-values and eigen-vectors are found. It should be mentioned that here we are interested in eigen-vectors rather than in eigen-values. However, the computation procedure does not differ from the one for defectless PhC.

The sixth block is the most important in the program. Here, the field distribution is computed by means of the expressions (7.33). For this reason we use the eigen-vectors obtained in the previous computation block. The procedure consists in summation over all the reciprocal lattice vectors. The summation gives the field intensity in a single space point. At that, it is not necessary for these points to coincide with nodes of the discretization mesh. Actually, we may compute the field distribution at the 1 km distance from the considered PhC fiber. However, since we have restricted the shape of the field distribution by representing it in the form of Bloch wave, the computation result will be periodically repeated as well with period equal to the dimension of the unit cell. In our case it is $5a$. It should also be mentioned that we may compute the distribution of any mode. The choice is made by the variation of the number in the member $D(Gc, 1)$ of the summation. By default, it computes the field distribution of the first mode.

Seventh block is for plotting the solution. Besides the field distribution, the permittivity distribution is also plotted, so that we can see the field distribution as related to the PhC elements.

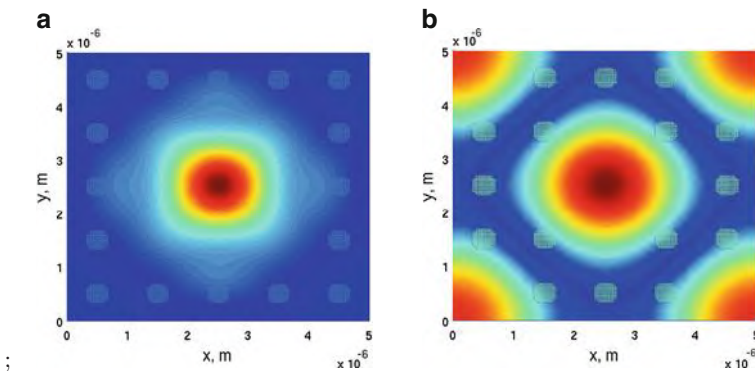


Fig. 7.16. The program result. (a) is field distribution of the first mode and (b) is the second mode

The result of the program is presented in Fig. 7.16. We see here the first and the second modes. We can see also that the first mode is strongly localized inside the defect area and the second one flows out from the core. Analyzing the obtained results, we can conclude that the fiber with considered parameters will be a single-mode one.

7.12 Problems and Questions

Problem 7.1. What is the difference between conventional fiber and PhC fiber?

Problem 7.2. What is the difference between single-mode and multi-mode fiber?

Problem 7.3. Which kind of PhC fibers is applied in telecommunications? What is the reason?

Problem 7.4. What kind of PhC fibers are called index-guided microstructured fibers?

Problem 7.5. What kind of PhC fibers are called PBG-guided fibers?

Problem 7.6. What is continuum of states of the PhC? Why it is necessary to compute the continuum of states together with defect eigen-states?

Problem 7.7. Write down element of matrix differential operator for PhC fiber.

Problem 7.8. Calculate the reciprocal lattice primitive vectors in case of hexagonal PhC unit cell containing 5×5 elements. The distance between centers of elements is a .

Problem 7.9. Calculate the reciprocal lattice primitive vectors in case of square PhC unit cell containing 5×5 elements. The distance between centers of elements is a .

Problem 7.10. Modify the program to compute the continuum of states of the PhC fiber cladding.

Problem 7.11. Modify the program to compute the set of eigen-values within the range of propagation constant from 0 to 10^7 .

Problem 7.12. Modify the program to compute the field distribution inside the fiber on the basis of hexagonal PhC.

FDTD Method for Band Structure Computation

Summary. Principles of photonic band structure computation using FDTD method are considered in this chapter. The general scheme of FDTD method for photonic band structure computation is presented. Peculiarities of different stages like definition of computation domain, definition of Bloch boundary conditions and initial conditions for delta-pulse, and Gaussian-modulated excitations are discussed. The spectral analysis of the temporal response by Fourier transform is carried out for 1D and 2D photonic crystals. The 1D and 2D PhC band structures are compared with those obtained by PWE method. Finally the original Matlab-code for FDTD band structure computation of 1D photonic crystal is given and several problems and questions for self-training are presented.

8.1 Problem Definition

In the chapters dedicated to the plane wave expansion method we discussed some drawbacks of PWE method application to computation of a photonic band structure. Among drawbacks are impossibility to take into consideration the chromatic dispersion, absorption, and gain as well as nonlinear materials whose refractive index depends on the radiation intensity.

One of the possible ways to overcome the problem is to apply the FDTD technique. In contrast to PWE method, the FDTD provides possibility of the refractive index variation during the computation process [215], which allows to take into account losses and nonlinearity when computing the band structure.

Let us now consider in details the basic principles underlying the band structure computation by means of FDTD technique which are briefly discussed, for example, in [172] and [242]. First, it is necessary to pay attention to the time-dependence of the electro-magnetic function obtained as the FDTD solution. The eigen-values of the optical structure is found by the analysis of the time-dependent response of a structure on the pulse excitation. It should also be noted that the field computation is carried out within the unit cell only. The periodicity of the structure is emulated by setting up periodic boundary

conditions. Such conditions provide definition of the radiation wave vector by tuning the phase of the radiation when translating it from one side of the unit cell to another. After the field computation is complete, the Fourier transform is applied, which gives the response spectrum. Eigen-states of the PhC correspond to local maxima of the spectrum since the eigen-state is resonant frequency of the structure. That means that phase conditions, noted above as a way to define the radiation wave vector, support radiation propagation inside the infinite structure.

In general, PBG computation using FDTD should be carried out as follows:

1. Determine the computation area.
2. Set up periodic boundary conditions.
3. Define the radiation excitation function. The radiation spectrum should be wide enough to cover whole investigated frequency range.
4. Carry out the spectral analysis of the time-dependent response of the structure on the probe pulse by searching all of local maxima and plotting them over frequency axis.
5. Repeat steps from 2 to 4 at different values of the phase shift in periodic boundary conditions corresponding to all selected points within the PhC Brillouin zone the band structure is computed for.

Let us now consider in details each step of the problem solution.

8.2 Computation Region Definition

The FDTD technique the band structure will be found with, requires determination and discretization of the computation domain. However, since the PhC is an infinite structure and computation of over an infinite structure takes infinite time period, the response of such a structure is impossible to find. Solution in this case is consideration of a unit cell rather than infinite periodic structure since it carries the information about whole structure. Thus, the computation domain in given a problem consists of a single unit cell of the PhC. The computation domain, therefore, takes the look shown in Fig. 8.1(a). It is represented by segment of 1D space possessing step-index refractive index profile.

In case of 2D PhC the simplest unit cell has square shape (see Fig. 8.1b). However, being more complex than in case of 1D PhC, the shape of computation region for 2D PhC may vary depending on the unit cell shape. The computation region for 3D PhC with cubic lattice is shown in Fig. 8.1c. Discretization of the computation region by rectangular mesh is also shown in Fig. 8.1. As is mentioned in Chap. 7, the FDTD technique allows to find the solutions within the mesh nodes.

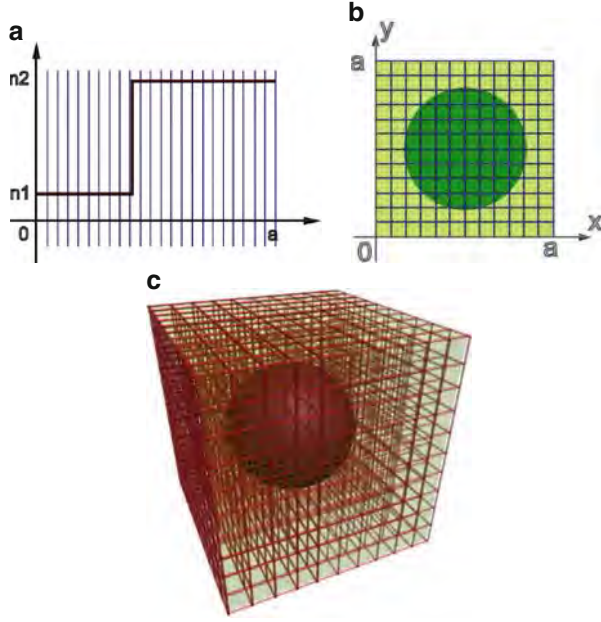


Fig. 8.1. Examples of computation domains for 1D, 2D, and 3D phonic crystals (a) 1D PhC, (b) 2D PhC, (c) 3D PhC

8.3 Boundary Conditions Definition

As long as we determine that computation area should take shape and size of the PhC unit cell, the periodicity emulation of the structure should be set manually. It is achieved by setting up periodic boundary conditions at the edges of the computation domain.

Besides the translation emulation, specially set periodic boundary conditions allow computation of the electro-magnetic field distribution with different wave vectors. Such type of periodic boundary conditions are referred to as Bloch periodic boundary conditions [244]. The expressions of Bloch's periodic boundary conditions for electric and magnetic field components take following form:

$$\begin{aligned} \mathbf{E}(x+a, y+b, z+c) &= \mathbf{E}(x, y, z) \cdot e^{-i \cdot k_x \cdot a - j \cdot k_y \cdot b - k \cdot k_z \cdot c}, \\ \mathbf{H}(x+a, y+b, z+c) &= \mathbf{H}(x, y, z) \cdot e^{-i \cdot k_x \cdot a - j \cdot k_y \cdot b - k \cdot k_z \cdot c}. \end{aligned} \quad (8.1)$$

where a, b, c are linear dimensions of the unit cell along X, Y and Z axes respectively; k_x, k_y, k_z are wave vector components.

Bloch periodic boundary conditions operate in following way; the electric or magnetic field intensity is taken from one boundary of the computation region and is added to the corresponding field component intensity at the opposite boundary according to periodic boundary conditions. However, in contrast to simple periodic conditions, the Bloch ones require multiplication

of the field intensity by the exponent which argument contains radiation wave vector. This corresponds to the phase shift of the radiation while traveling from one unit cell to another.

Let us consider simple example. If the eigen-states computation is carried out for the radiation with zero-equal wave vector, then $e^{-i \cdot 0 \cdot a - j \cdot 0 \cdot b - k \cdot 0 \cdot c} = 1$. It means that field from one boundary will be translated to another one without alteration. In an opposite case, when the wave vector falls at the edge of the Brillouin zone, the wave vector equals to $\mathbf{k} = (\frac{\pi}{a} \cdot i, \frac{\pi}{b} \cdot j, \frac{\pi}{c} \cdot k)$. The exponent in the expression (8.1) will be equal to $e^{-i \cdot \frac{\pi}{a} \cdot a - j \cdot \frac{\pi}{b} \cdot b - k \cdot \frac{\pi}{c} \cdot c} = -1$, so that the field at the opposite boundary of the computation region will be excited in antiphase.

Thus, setting up the Bloch periodic boundary conditions provides the possibility to investigate propagation of radiation with different wave vectors and, therefore, to compute the band structure.

8.4 Initial Conditions

To compute PBG for PhC under investigation, the time-dependent response of the structure on the probe pulse should be found at any point of the computation domain. For this reason the probe pulse possessing wide spectrum should be introduced to the structure first.

The radiation can be introduced to the structure in various ways. However, we will consider excitation from a single point of the computation region. The pulse shape which provides wide spectrum may also be selected in various ways. The simplest shapes are delta-pulse and Gaussian-modulated high-frequency signal. At that, the delta-pulse is introduced in a single moment of time while the modulated signal requires long time to be introduced into the structure. Let us consider example of radiation injection. In case of delta-pulse, the excitation function takes following form:

$$\delta(t - t_0, x - x_0, y - y_0, z - z_0) = 1. \quad (8.2)$$

It is widely known that the spectrum of the delta-pulse is infinitely wide so that it gives structure responses at any frequency. After the delta-pulse is introduced, the excitation is turned off, however, due to periodic boundary conditions, radiation exists infinitely long time in the structure without absorption.

Another case we consider here is the Gaussian-modulated high-frequency excitation. The expression for such a pulse takes following form:

$$E_z(x, y, z) = A \cdot e^{\frac{-(t-t_0)^2}{w^2}} \cdot \sin(\omega \cdot t), \quad (8.3)$$

where t_0 provides the time-delay of the Gaussian envelope function, w is its width, and ω is carrier wave frequency. The Gaussian pulse excitation is carried out during whole computation process in contrast to the computation by

delta-pulse. The spectrum of such a pulse is not so wide as that for delta-pulse. However, varying the carrier frequency, one can focus on some specific spectral range to provide high accuracy and avoid errors when analyzing structure response.

8.5 Structure Response Analysis

After the pulse response of the structure is obtained, it should be analyzed. This analysis gives eigen-states of the PhC under investigation.

The spectral analysis of the time dependent pulse response can be carried out by Fourier transform. The accuracy of the method achieves its maximum when computation time is infinite. However, since we have finite computer resources, the computation time is taken to be finite but very large value.

Fast Fourier transform (FFT) [243] is usually used within this technique since the response function is discrete one and in this case the FFT performance is much faster than general Fourier transform. As a result of the FFT, we have the discrete spectrum as well. The example of the FFT of the structure response to the delta-pulse excitation is shown in Fig. 8.2.

The eigen-states of the structure are searched for local maxima at the response spectrum. Detailed analysis should be made to avoid spurious solutions. Such spurious solutions usually appear as inessential peaks at the spectrum. Therefore, the local maximum appearance does not always correspond to the eigen-state. The maxima corresponding to spurious solutions are just a little bit higher than neighbor spectrum points while valid solutions values are several times larger than neighbor ones.

In Fig. 8.3a example of pulse responses computation of 1D PhC for wave vectors taken within Brillouin zone is shown. Figure 8.3b depicts result of spectra analysis compared to the results obtained by the PWE method.

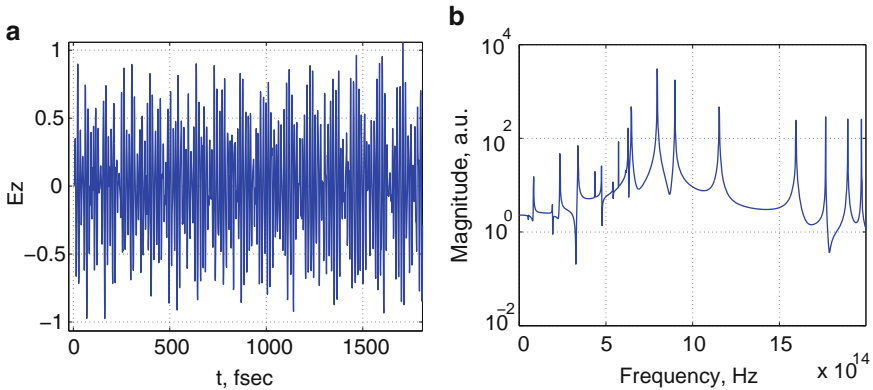


Fig. 8.2. Temporal response (a) and its spectrum obtained by FFT (b)

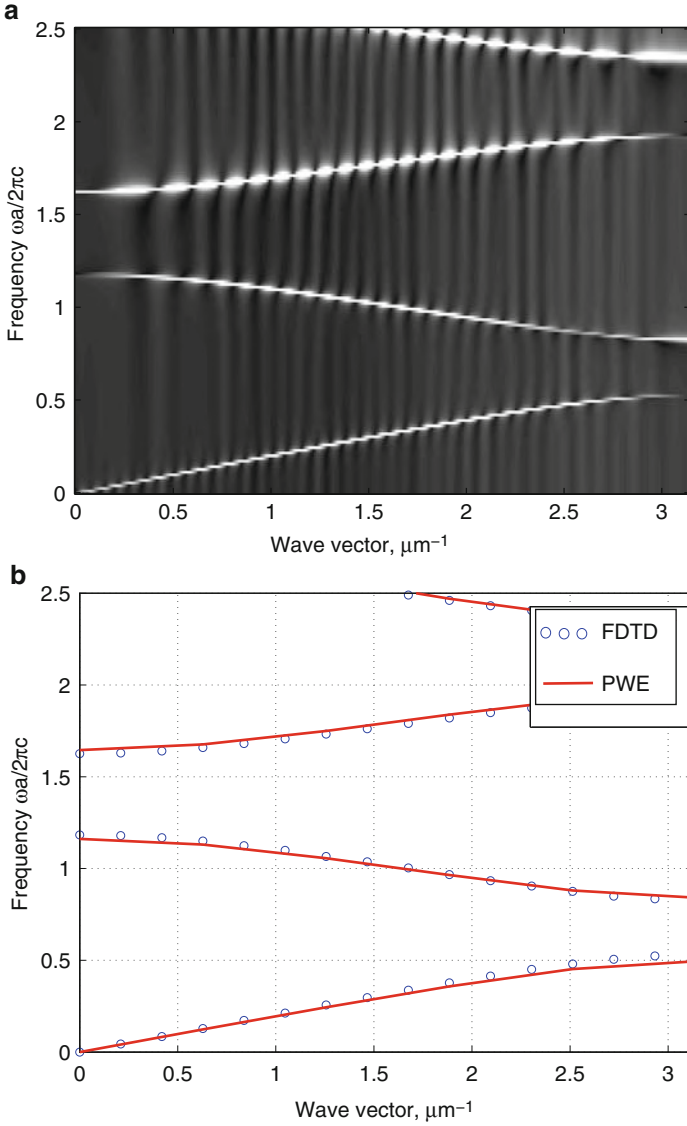


Fig. 8.3. Temporal response spectra (a) and 1D PhC band structure as compared with one obtained by PWE method (b)

In Fig. 8.4 the 2D PhC response spectra as well as the band structures obtained by both methods are shown. Just like in case with 1D PhC, the spectra are not homogenous for the radiation with different wave vectors. However, the analysis may be carried out even in this case since we are interested in frequency of the local maxima rather than in their absolute values. Comparison of results show that both in 1D and 2D cases, some spurious solutions appear

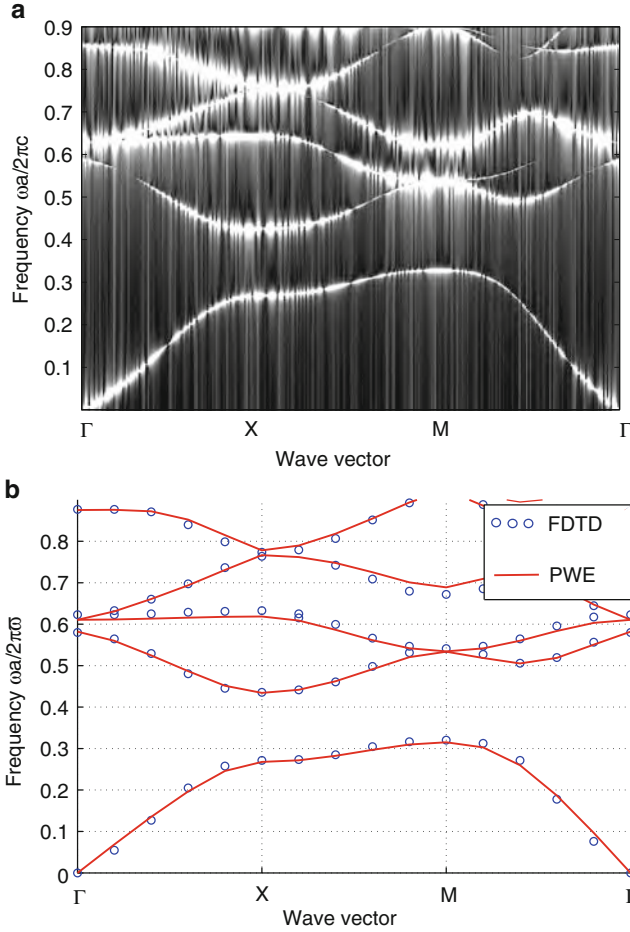


Fig. 8.4. Temporal response spectra (a) and 2D PhC band structure as compared with one obtained by PWE method (b)

which can be avoided by enhancement of the spectrum analysis technique. The deviation from results obtained by PWE method achieves 5% and may be improved by enlarging FDTD computation time.

8.6 Summary

1. In this chapter we have considered the method for the band structure computation by means of the FDTD method.
2. The FDTD method has several advantages as compared to the PWE method. Particularly, it allows to take into account different properties of materials such as the material dispersion, the nonlinearities, losses and gain. All these effects cannot be ignored when modeling active devices.

3. The method has also several disadvantages. The most critical is spurious solutions which appear during the response spectrum analysis. Moreover, the computation time is very large when high accuracy is required.

Thus, the method may be useful for active media such as photorefractive materials or laser resonators modeling. However, in case of simple device, the PWE method is much more effective.

8.7 MATLAB Program for Band Structure Computation of 1D PhC by Means of FDTD Method

```
%The program for 1D PhC band structure computation by
%means of FDTD method.
%Input data: permittivity distribution within
%unit cell
%Output data: 1D PhC band structure

clear all;

%The variable a is lattice constant
a=1e-6;

%c is the light speed in vacuum
c=3e8;

%Variable accuracyY determines the number of
%mesh elements at the space discretization stage
accuracyY=48;

%dy determines the size of the mesh cell
dy=a/accuracyY;

%dt is time step
dt=1/c/sqrt(1/dy^2);

%Variables eps1 and eps2 determine permittivities
eps1=1;
eps2=9;

%Variables l1 and l2 are the layers thicknesses
%defined as fractions of the period
l1=0.3;
l2=1-l1;
```

```

%tMax determines number of time steps.
%To obtain Fourier-image using fast Fourier transform
%the number of time steps should be multiple of 2
tMax=2^14;

%numK is the counter of wave vectors which
%are used for PBG formation
numK=0;

%Determine coefficients at field components
dt1=c*dt/dy/eps;
dt2=c*dt/dy/eps2;

figure(1);
ax=axes;
hold on;
%Loop on wave vectors. This is the main loop.
for K=0:1/20*pi/a:pi/a
%Increment of counter for wave vectors
    numK=numK+1;
%Initialize arrays containing components of field
%distribution by assigning their components by zeros
    Ez=zeros(1,accuracyY);
    Hx=zeros(1,accuracyY);

%Calculate coefficient which define phase rotation
%when the field will passes through the boundary
%with Bloch's boundary conditions
    rotate=exp(i*K*a);

%Clear the variable Time which will receive values of
%one of the field components in designated space
%point in various time moments
    clear Time;

%Next loop calculates field variation in time
    for t=0:dt:tMax*dt-dt
%Define initial conditions like excitation by complex
%harmonic function in a point of unit cell
        Ez(round(1*accuracyY/5))=Ez(round(1*accuracyY/5))...
            +exp(-(t-0.5e-12).^2/1e-25)*5.*exp(i*5e15*t);

%Define boundary conditions for magnetic component
        Hx(1)=Hx(1)-dt1*eps*(Ez(1)-Ez(length(Ez))*rotate);
    end
end

```



```

%Calculate magnetic component of the field
for coord=2:accuracyY
    if coord<accuracyY*11
        Hx(coord)=Hx(coord)-dt1*eps*(Ez(coord)-...
                                Ez(coord-1));
    else
        Hx(coord)=Hx(coord)-dt2*eps2*(Ez(coord)-...
                                Ez(coord-1));
    end %if
end % for coord
%Calculate electric component of the field
for coord=1:accuracyY-1
    if coord<accuracyY*11
        Ez(coord)=Ez(coord)-dt1*(Hx(coord+1)-Hx(coord));
    else
        Ez(coord)=Ez(coord)-dt2*(Hx(coord+1)-Hx(coord));
    end %if
end %for coord
%Define boundary conditions for electric field
Ez(accuracyY)=Ez(accuracyY)-dt2*(Hx(1)/rotate-...
                                Hx(length(Ez)));
%Receive intensity of electric component of the field
%in a point of unit cell. That point should be
%in some distance from the excitation point
Time(round(t/dt+1))=Ez(round(2*accuracyY/5));
end % for t

%Obtain Fourier-image of the time-dependent pulse
%response of the structure
fourier=abs(fft(Time));

%Obtain absolute frequency values.
%Each element of the array obtained corresponds
%to the element of the array which we have obtained
%using fast Fourier Transform
f=1/dt*(0:length(fourier))/length(Time);

%wCount - is the counter of eigen-frequencies
%obtained for current value of the wave vector.
wCount=1;

%Analyze the spectrum of the pulse response.
%First element of the array fourier we process
%separately.

```

```

if(fourier(1)/fourier(2)>1.0001)
    wEigen(numK, wCount)=f(1);
    wCount=wCount+1;
end % if

%In the next loop we process all other elements
%of the array fourier.
%Current element is compared with previous and next
%one. If current element is larger it is considered
%as an eigen-state and corresponding frequency is
%recorded into the array of eigen-states of the PhC
for u=2:length(fourier)-1
    if(fourier(u)/fourier(u-1)>1.0001)&&...
        (fourier(u)/fourier(u+1)>1.0001)
        wEigen(numK, wCount)=f(u);
        wCount=wCount+1;
    end %if
end %for u

%Display the eigen-states.
%Create a figure. If figure exists, it becomes
%the current figure

%If 16 or more eigen-states are found,
%only 16 eigen-states are shown.
%In other case all eigen-states are displayed.
if(wCount-1>=16)
    plot(ones(1,16)*K,abs(wEigen(numK,1:16)),...
        'o','LineWidth',3);
else
    plot(ones(1,wCount-1)*K,...
        abs(wEigen(numK,1:wCount-1)),...
        'o','LineWidth',3);
end % if

%Mark the axes
ylim([0 3e14]);
xlim([0 3.15e6]);
xlabel('k,m^{-1}','FontSize',20);
ylabel('Frequency, Hz','FontSize',20);
set(ax,'XGrid','on');
set(ax,'YGrid','on');
%Draw results
drawnow;
end % main loop for K

```

Let us consider the program. It consists of four blocks.

The program initialization is performed inside the first block. In this program we have to initially set up the structure geometry, particularly, the period and thicknesses of the layers, as well as permittivity distribution inside each layer. Here, the structure is very simple so we are setting up only the fraction of the period instead of absolute thickness of the layer. In this section the time step from the Courant conditions is also determined.

The second, the third, and the fourth blocks are inside the loop which scans over wave vectors.

The second block implements the FDTD technique for 1D case. The temporal response within a selected point is obtained at the block output.

The temporal response analysis is performed in the third block. Here, the fast Fourier transform is applied to the temporal response which gives its spectrum. Then, the spectrum is scanned and local maxima found. Each maximum corresponds to eigen-state of the PhC at given value of the wave vector.

The eigen-states obtained for the specific value of the wave vector are then plotted one by one in the figure. Since the eigen-states are found for different values of the wave vector, we finally obtain the band structure.

The result of the band structure computation is given in Fig. 8.5. As it is seen, some additional solutions appear in the figure which are drop out from

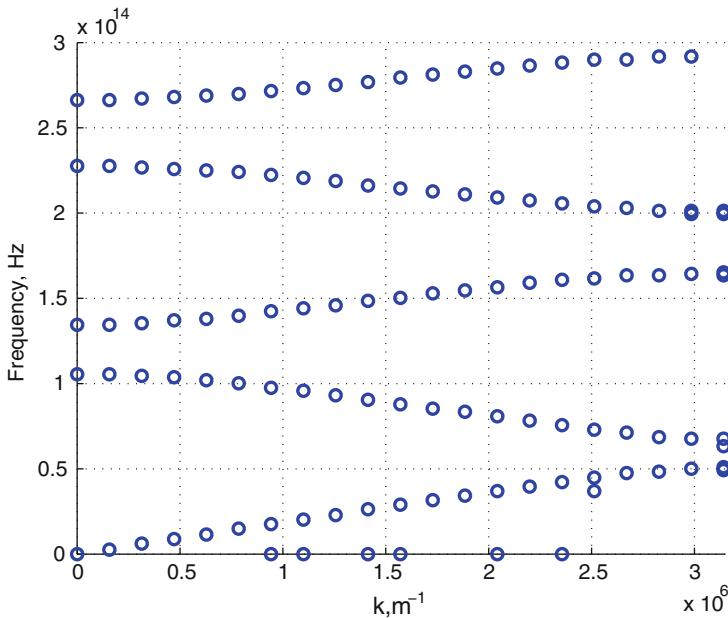


Fig. 8.5. Results of the program. Band structure of 2D PhC obtained by FDTD technique

the general set. They are called spurious solutions. Such solutions appear due to space discretization and because of finite solution time interval. Such solutions may easily be eliminated even manually.

8.8 Problems and Questions

Problem 8.1. How the infinite periodic structure can be defined for the band structure computation by the FDTD method?

Problem 8.2. What is the Bloch periodic boundary conditions? Write down corresponding expression.

Problem 8.3. Modify the program to compute the band structure of the PhC with sinusoidal refractive index profile.

Problem 8.4. Modify the program to excite the radiation by the delta-pulse.

Problem 8.5. Write the program to compute the band structure of 2D PhC with square lattice.

Problem 8.6. Modify the program to use simple discrete Fourier transform (write your own function) rather than FFT.

Photonic Crystal Waveguides

Summary. Chapter 9 is dedicated to photonic crystal waveguides, as they are one of the crucial elements of the optical integrated circuits. Using PWE method computation of band structure and dispersion diagrams of 2D photonic crystal waveguides is demonstrated. Peculiarities of PWE method as applied to 2D photonic crystal waveguides are considered. In addition, to give an opportunity to compare photonic crystal waveguides and conventional integrated optical waveguides, the basics of planar waveguides are given at the beginning of the chapter. Finally, the original Matlab-code for computation of dispersion diagram of 2D photonic crystal waveguides is presented at the end of the chapter along with the problems and questions for self-training.

9.1 Conventional Planar Waveguides

Guiding effect in integrated optical waveguides is achieved by surrounding the core with a lower refractive index cladding. If refractive index decreases gradually away from the axis, waveguide is called graded-index waveguide.

Waveguides for integrated optics are usually made of transparent dielectric materials like glass or semiconductors like *GaAs* or *InP*. Symmetric slab waveguide and strip waveguides are of particular interest, serving as simple models for the waveguiding regions of optoelectronic integrated circuits or semiconductor lasers.

The slab waveguide forms a starting point for the development of integrated optical circuits which concern mainly three or more different media and have more than two interfaces between the media. Due to the importance of slab waveguides for understanding the principles of operation of the integrated optical devices, we will start as in case of photonic crystal fibers, with basic mathematical and physical points related to radiation propagation in conventional slab waveguides.

9.1.1 Guided Modes in a Slab

To start considering the radiation propagation in PhC waveguides, it is reasonable before to consider the principles of mode formation and propagation in conventional slab waveguides. Modal properties of the slab waveguides can be derived using geometric optics approach since they are represented by a simple structure. Let us consider the light propagation inside a simple step-index slab waveguide.

Under plane wave excitation of a slab waveguide, the waveguide mode is formed only, if the phase angle is kept constant after each consecutive reflection from the waveguide walls. This condition leads to the characteristic equation of the form

$$-2k_1d\sin\theta_1 + \Phi_{10} + \Phi_{12} = -2m\pi. \quad (9.1)$$

Here k_1 is the wave vector, d the thickness of the slab, and Φ_{10} and Φ_{12} are phase shifts. This equation defines the value of angle θ_1 which corresponds to the specific slab mode. The homogeneous plane wave propagating on zigzag way under such an angle forms the slab mode.

Phase shifts Φ_{10} and Φ_{12} depend on the plane wave polarization and can be obtained via analysis of the boundary conditions using methods of geometrical optics. To do that, it is convenient to represent the homogeneous plane wave incident on the interface of two media with different refractive indices as a composition of two waves with transversal electric and transversal magnetic polarizations. In a slab these waves form slab modes. That is why slab modes have different polarizations. If magnetic component \mathbf{H} of the plane wave is parallel to the incidence plane, we have H or TE (transverse electric) mode and that mode has only one component in propagation direction, H_z . Correspondingly, if electric component \mathbf{E} is parallel to the incidence plane, it leads to an electric E or TM (transverse magnetic) mode.

Boundary condition is illustrated in Fig. 9.1, where wave vector $\mathbf{k} = \beta - j\alpha$ in lossless ($\alpha = 0$) medium and its longitudinal k_z and transversal k_x components in both media are depicted in consistent with the description given in Chap. 2.

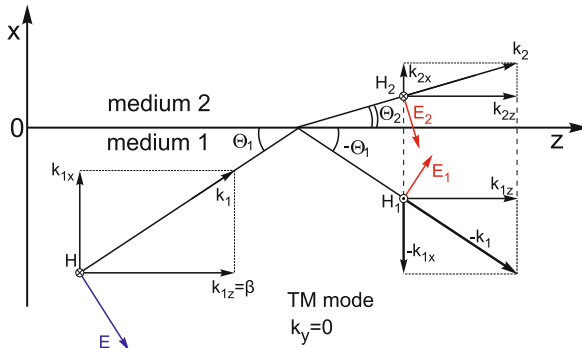


Fig. 9.1. Wave vector components on the boundary for TM wave

Boundary condition require continuity of the tangential components at the interface ($k_{1z} = k_{2z}$ at $x = 0$) [223]. The incident wave vector \mathbf{k}_1 in 2D case has components

$$k_{1x} = k_1 \sin \theta_1, \quad k_{1y} = 0, \quad k_{1z} = k_1 \cos \theta_1 \quad (9.2)$$

with $\mathbf{k}_1 \cdot \mathbf{k}_1 = k_{1x}^2 + k_{1z}^2 = k_1^2 = \omega^2 n_1^2 \varepsilon_0 \mu_0$. Hence, for reflected and refracted waves we should have the same z -component $k_{2z} = k_{1z}$, and it is obvious that

$$\mathbf{k}_2 \cdot \mathbf{k}_2 = k_{2x}^2 + k_{2z}^2 = k_2^2 = \omega^2 n_2^2 \varepsilon_0 \mu_0, \quad \text{where} \quad k_{2z} = k_2 \cos \theta_2. \quad (9.3)$$

Amplitudes of the transmitted and reflected waves may be obtained after matching of the tangential components on the interface. In case of TM polarized incident wave the following components:

$$H_{y1} \quad \text{and} \quad E_{z1} = -\frac{k_1}{\omega \varepsilon_0 n_1^2} H_{y1} \sin \theta_1,$$

must be added to the components of the reflected wave

$$H_{yr} \quad \text{and} \quad E_{zr} = \frac{k_1}{\omega \varepsilon_0 n_1^2} H_{yr},$$

and the result must be set equal to the refracted wave components

$$H_{y2} \quad \text{and} \quad E_{z2} = -\frac{k_2}{\omega \varepsilon_0 n_2^2} H_{y2} \sin \theta_2.$$

Then boundary conditions can be written as follows:

$$H_{y1} + H_{yr} = H_{y2}, \quad (9.4)$$

$$E_{z1} + E_{zr} = E_{z2}. \quad (9.5)$$

From these equations, it follows the reflection coefficient r which is equal to the quotient of amplitudes of the reflected and incident waves, and transmission coefficient t which is equal to the quotient of amplitudes of the refracted and incident waves.

Expressing both coefficients through the wave admittance for the incident and refracted waves [223] we can write

$$r_H = \frac{n_2^2 k_{1x} - n_1^2 k_{2x}}{n_2^2 k_{1x} + n_1^2 k_{2x}}, \quad t_H = \frac{2n_2^2 k_{1x}}{n_2^2 k_{1x} + n_1^2 k_{2x}}. \quad (9.6)$$

These expressions show the dependence of the reflection and transmission coefficients from the normal components of the wave vector and the refractive index.

Similar analysis of TE polarization case gives us the following expressions for the reflection and transmission coefficients

$$r_E = \frac{k_{1x} - k_{2x}}{k_{1x} + k_{2x}}, \quad t_E = \frac{2k_{1x}}{k_{1x} + k_{2x}}. \quad (9.7)$$

Here we do not have dependence on the refractive index. Both coefficients for TE polarization are defined by normal components only.

In ordinary case of wave transmission through the interface, when incident optical power is divided into equal parts, we have real coefficients for both t and r . In case of wave propagation in more dense medium $n_2 < n_1$ with total reflection effect, the refracted wave has $\theta_2 = 0$ and $k_{2x} = 0$. Then the reflection coefficient r is increased up to 1. Under incident angles smaller than critical angle we have $k_z = k_1 \cos \theta_1 > k_2$ and from (9.3) it follows:

$$k_{2x}^2 = k_2^2 - k_z^2 < 0.$$

Thus as of $\theta_1 = \theta_{1c}$ and $k_{2x} = 0$ the normal component of the wave vector of the second medium k_{2x} becomes imaginary for angles $\theta_1 < \theta_{1c}$. Because k_{1x} is real and k_{2x} is negative imaginary, the reflection coefficient will have an amplitude equal to that one for $\theta_1 = \theta_{1c}$ and will be imaginary with phase angles

$$\Phi_E = 2 \arctan \left(j \frac{k_{2x}}{k_{1x}} \right), \quad \Phi_M = 2 \arctan \left(j \frac{n_1^2 k_{2x}}{n_2^2 k_{1x}} \right). \quad (9.8)$$

Such a total reflection takes place for all $0 < \theta_1 < \theta_{1c}$. Reflected wave has the same amplitude as incident wave, but it also has a phase shift Φ_M and Φ_E .

Superposition of incident and reflected waves with equal amplitudes forms a standing wave in x -direction in the medium 1 with corresponding transversal wave number k_{1x} . The wave vector has real component in medium 2 $k_{2z} = \beta = k_1 \cos \theta_1$ and imaginary x -component $k_{2x} = -j\alpha_x$. Therefore,

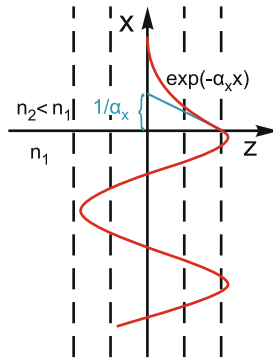


Fig. 9.2. The wave amplitude (*solid line*) distribution and phase planes (*dashed lines*) on the border between two media in case of total reflection of the incident wave

nonuniform plane wave propagates in z -direction and has a plane phase front transversal to that direction. The field decays exponentially in transversal direction with attenuation constant α_x . Such a transversally attenuated wave carries the optical power only in longitudinal direction z . The wave amplitude distribution and phase planes are shown in Fig. 9.2.

9.1.2 Characteristic Equations

Solution for TE mode can be found by substituting the phase shift Φ_E from (9.8) into (9.1). It give us the following equation:

$$\arctan\left(j\frac{k_{0x}}{k_{1x}}\right) + \arctan\left(j\frac{k_{2x}}{k_{1x}}\right) = dk_1 \sin \theta_1 - m\pi.$$

To simplify (9.1), let us introduce new variables for transversal components of the wave vector inside the slab $u = k_{1x}d = dk_1 \sin \theta_1$. For decaying field outside the slab the wave vector is complex and transversal component must be imaginary. Therefore, we introduce $v = jk_{2x}d$ for substrate (medium 2) and $w = jk_{0x}d$ for upper area (medium 0). After that we obtain simple characteristic equation also known as dispersion equation

$$\arctan\left(\frac{v}{u}\right) + \arctan\left(\frac{w}{u}\right) = u - m\pi \quad \text{or} \quad \tan(u) = \frac{u(v+w)}{u^2 - vw}. \quad (9.9)$$

Last equation has no $m\pi$.

Dispersion equation for TM mode is very similar:

$$\tan(u) = \frac{n_1^2 u (n_0^2 v + n_2^2 w)}{n_0^2 n_2^2 u^2 - n_1^4 vw}. \quad (9.10)$$

New parameters u, v, w describe transversal phase and attenuation constants inside the slab, substrate, and the space above the slab, respectively. They are limited by longitudinal components of the wave vector $k_z = \beta$ which describes field dependence along the propagation direction, and by the wave number in each medium $k_{0,1,2}$ ($k_0 = 2\pi/\lambda_0$ in air and $k_{1,2} = n_{1,2}k$ in media). The real values of β obtained from eigenvalue equations represent phase constants of propagating slab modes and describes mode propagation along the waveguide.

Taking into account the connection between components of the wave vector $k_1^2 = k_{1x}^2 + k_{1z}^2$ (see Fig. 9.1) we can write $k_{1x} = (k_1^2 - k_{1z}^2)^{1/2} = (k_1^2 - \beta^2)^{1/2}$, where β represents phase constant of the slab mode (medium 1). In the same way transversal components can be written for other areas $k_{2x} = (k_2^2 - k_{2z}^2)^{1/2} = (k_2^2 - \beta^2)^{1/2}$, and then combine it with formulae for new variables $u = k_{1x}d$, $v = jk_{2x}d$, $w = jk_{0x}d$ to obtain a set of equations for new variables u, v, w

$$\begin{aligned}
\frac{u}{d} &= k_{1x} = (k_1^2 - \beta^2)^{1/2}, \\
\frac{v}{d} &= jk_{2x} = (\beta^2 - k_2^2)^{1/2}, \\
\frac{w}{d} &= jk_{0x} = (\beta^2 - k_0^2)^{1/2}.
\end{aligned} \tag{9.11}$$

Shown characteristic equation (9.9) or (9.10) together with (9.11) form solution for the slab mode. This solution corresponds to m values which satisfy (9.1), which may have therefore different solutions depending on m . Depending on index m and polarization (H or E) we obtain H_m or E_m modes as a solution. The set of these equations are transcendental eigenvalue equations, which may be solved numerically.

9.2 Weakly Guiding Slabs

9.2.1 Graphical Solution of Characteristic Equation

For most of practical cases even a little difference between n_1 and n_2 is enough to achieve the waveguiding effect. This is case of so-called weakly guiding slabs. The critical angle for them is given by the formula:

$$\sin \theta_{2c} = \frac{(n_1^2 - n_2^2)^{1/2}}{n_1}. \tag{9.12}$$

The effect of total internal reflection in those slabs is observed in the narrow range of angles only. Due to small optical contrast, the characteristic equations can be simplified by neglecting the variable w in (9.9) and (9.10). After this simplification ($uv \gg w$) we have a common equation for both H_m and E_m waves:

$$v = -u \cdot \cot(u). \tag{9.13}$$

Equation (9.13) has neither w parameter nor refractive index n , and gives two solutions for each value of index m . This situation is known as degeneracy. Each solution in such waveguide corresponds to both H_m and E_m waves.

The characteristic equation for weakly guiding slabs can be solved graphically as shown in Fig. 9.3. In this case only the first quadrant should be taken into account, since only positive solutions have a physical meaning. One series of curves is given by (9.13).

Using formulas $u = k_{1x}d = dk_1 \sin \theta_1$ and $v = jk_{2x}d$, where $k_1 = n_1k_0$, $k_2 = n_2k_0$, $k_0 = 2\pi/\lambda_0$, and taking into account (9.11) the second relation for $v(u)$ can be written as follows:

$$u^2 + v^2 = (k_{1x}d)^2 + (jk_{2x}d)^2 = d^2 (k_1^2 - k_2^2),$$

which represent a circle $u^2 + v^2 = d^2 (k_1^2 - k_2^2)$ with a radius V

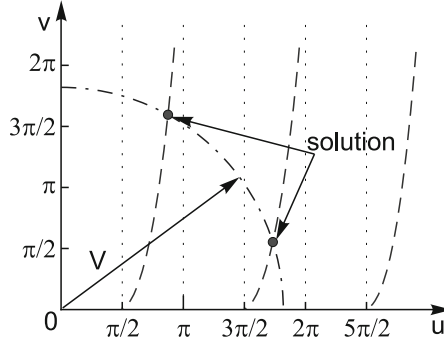


Fig. 9.3. The variation of V (dash-dotted curve) and cotangent (dashed curve) as function of u . A circle of radius V determines the propagation constants of the optical waveguide

$$V = \frac{2\pi d}{\lambda} \sqrt{n_1^2 - n_2^2}. \quad (9.14)$$

Intersection points represent solutions of the eigenvalue problem. Each of them corresponds to two slab modes. Transversal parameters u, v describe the transversal mode distribution (u is the phase parameter, and v is the transversal attenuation parameter) and are dependent on V only.

9.2.2 bV Diagram: Modal Field Distribution in a Slab Waveguide

The main practical interest receives not the transversal parameters of the wave, but the phase constant β which describes longitudinal mode distribution. To include many wave and slab parameters into analysis of the longitudinal wave behavior, the dimensionless propagation constant is introduced:

$$b = \frac{\beta^2 - n_2^2 k^2}{(n_1^2 - n_2^2) k^2}, \quad (9.15)$$

where $\beta = \frac{v^2}{V^2}$ is a longitudinal phase parameter, also known as V -dependent phase by the analogy with fibers considered above. Using these parameters it is convenient to represent mode characteristics in form of bV diagram shown in Fig. 9.4. Mode propagation is prohibited at $V < \frac{\pi}{2}$ in weakly guided slabs. This value of V is known as mode cutoff. Therefore, when we have the cutoff $V = \frac{\pi}{2}$, $b = 0$, $\beta = n_2^2 k$, the physical meaning of these expressions is the following. In case of cutoff, a mode will propagate not as guided mode but as substrate mode with substrate phase constant. Parameter $v = V\sqrt{b}$ will be equal to zero, because transversal phase parameters u, v are equal to $\frac{\pi}{2}$. Thus, exciting such a mode leads to homogenous field distribution inside the substrate since $v = 0$.

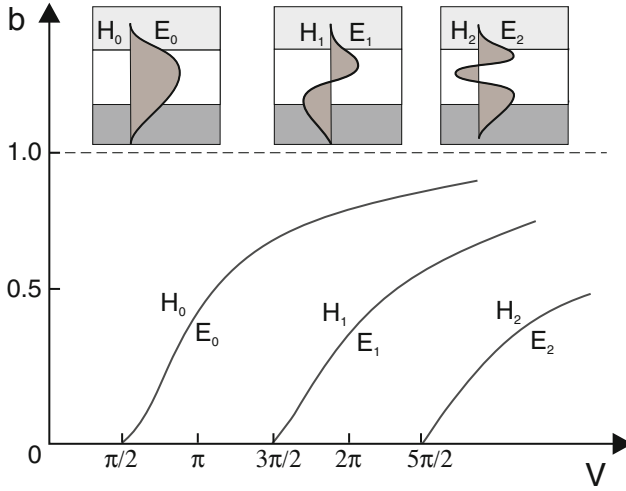


Fig. 9.4. bV diagram. The variation of the normalized constant b as a function of V

Since V increases from $V = \frac{\pi}{2}$, the cross-point in Fig. 9.4 corresponds to the situation when lower solution of the characteristic equation will be moved along the first curve starting from $\frac{\pi}{2}$. Constant v will increase as well, and converges asymptotically towards V . Simultaneously $u \rightarrow \pi, b \rightarrow 0$. This means, that slab modes will propagate far from cutoff with wave number corresponding to slab one $n_1 k$. Increasing of v denotes case when the field has less penetration into the substrate. The closer the u to π , the more field concentrates inside the slab. Since $w > v$, a mode field decays stronger within the area above the slab than within the substrate. As V increases, we obtain a new pair of modes. The mode order m shows a number of zero points within the mode distribution inside the slab.

Modal field distribution in slab waveguide is demonstrated in on insertions in Fig. 9.4, where three first guided modes are shown for the same slab. It is evident that all those modes have different values of the normalized frequency V . Guiding process and existing of modes with different order can be illustrated by the example [245], when the standing wave exists in the slab and periodically changes its order depending on different order of phase coincidence on the slab interfaces or on slab thickness. The modes depicted in Fig. 9.4 are called guided modes of the slab waveguide. They are propagating without losses along the z -axis.

For each slab waveguide there may exist a limited number of slab modes at the specific wavelength λ (solutions of (9.1)). If $V = \frac{(2m+1)\pi}{2}$, then a slab will guide $M = (2m + 2)$ modes (E_m, H_m) with order of $m = \left(\frac{V}{\pi}\right) - \frac{1}{2}$. The total number of modes in the slab is a maximum integer number, which is less than $M = \frac{V}{\pi} + 1$ for $V > \frac{\pi}{2}$.

9.3 Kinds of PhC Waveguides

Now, when description of conventional planar waveguides is given, we can start describing the PhC waveguides to have an ability to compare their properties and select between waveguides of two types.

In contrast to conventional planar waveguides, where the waveguiding effect is achieved due to the total internal reflection, the PhC waveguides are represented by a set of optically connected defects. As it was shown in Chaps. 4 and 5, one of main properties of the PhC is the possibility of light localization inside the defects of the periodic structure, so forming the row of defects in the PhC provides waveguiding effect.

The waveguide may be formed in both 2D and 3D PhCs by removing, for instance, one or several rows of elements, thus creating the waveguide area. In case of 2D PhC there is a designation which allows to determine the number of elements' rows removed from the structure. The designation Wn or WGn says that n rows were removed to form the waveguide. For example, designations $W1/WG1$, $W2/WG2$, and $W3/WG3$ tell that 1, 2, or 3 rows of elements are removed. Those examples are shown in Fig. 9.5. 3D PhC waveguides, however, do not have such a characterization, because the cross section of such waveguides may vary in wide range depending on PhC lattice type, the number of rows removed in each direction, etc. The 3D PhC waveguide may even have asymmetrical cross section allowing light flow within waveguide cross-section direction. The examples of cross sections of 3D PhC waveguides are depicted in Fig. 9.6. Possible applications for the waveguides with such cross sections are the following: simple 3D waveguide (Fig. 9.6a), polarization-maintained waveguides (Fig. 9.6b), waveguides with special profile providing peculiar interaction between radiation and embedded elements (Fig. 9.6c,d).

Here we will concentrate the attention mostly on 2D PhC waveguides. The reason is simplicity of models which are easier to understand and current technological level which does not allow effective production of 3D PhCs with embedded defects.

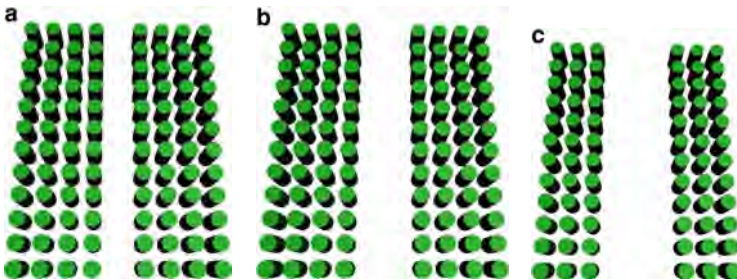


Fig. 9.5. 2D PhC waveguides with different width of waveguiding area: (a) $W1$, (b) $W2$, (c) $W3$

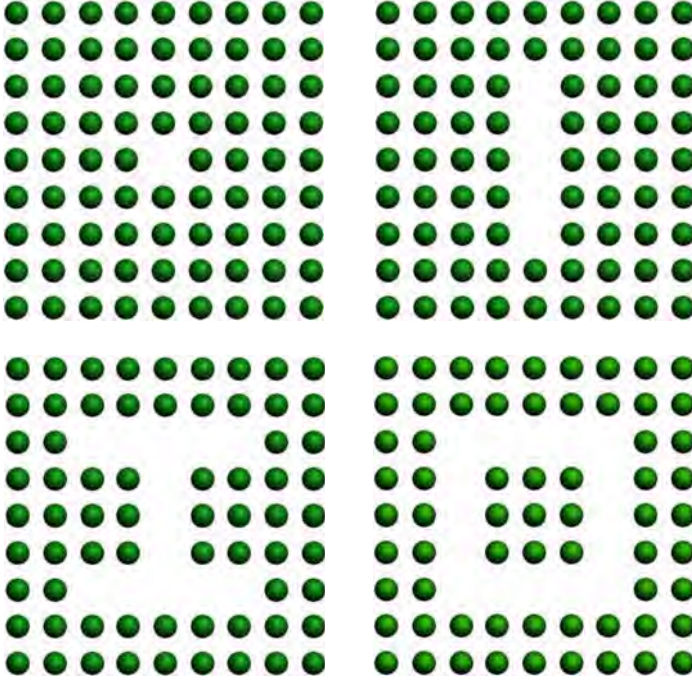


Fig. 9.6. Examples of 3D PhC waveguides cross sections

9.4 PWE Method for PhC Waveguides

In spite of apparent simplicity of the PhC waveguides, they actually possess many peculiarities to be taken into account at the design stage such as mode structure, dispersion, etc. Therefore, the design of the PhC waveguides starts from the investigation of their characteristics.

The most important characteristic of the PhC waveguide is its dispersion diagram. It allows to determine the waveguide modal properties, mode group velocities as well as group velocity dispersion. The most popular method for computation of such a characteristic is the PWE method. The method itself does not differ from that used for band structure computation of the strictly periodic PhC. However, the set of reciprocal lattice vectors the computation is carried out for is selected in different way and some terminology is changed. The PWE technique applied to PhC waveguides was briefly discussed in [205] and [209].

Let us consider the computation of dispersion diagram. First, we consider the case of 2D PhC waveguide. It is necessary to note that the 2D PhC waveguide is not perfectly periodic structure in two directions since we introduced the row of defects to form the waveguiding area. However, the waveguide is still periodic along the row defect (see Fig. 9.7). If we draw a straight line directed parallel to row of defects, the refractive index profile will be an infinite

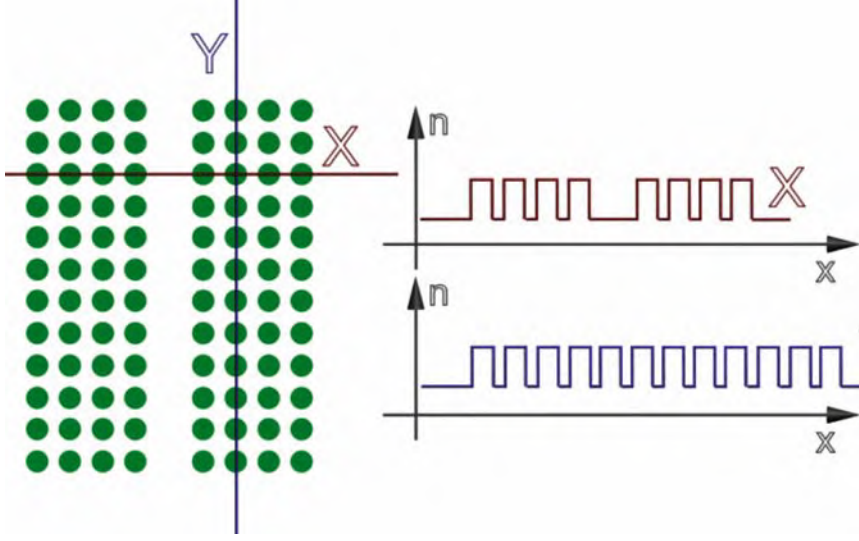


Fig. 9.7. Partial periodicity of PhC waveguide

periodic function. However, if we consider the transversal refractive index profile, the index distribution will be represented by the periodic structure with a defect. All these considerations should be taken into account when computing the waveguide dispersion diagram.

Earlier, we considered separately the band structure computation of the PhC and the PhC with defect. The unit cell of the perfectly periodic PhC contains one period of the PhC only. On the other hand, the computation technique for the defect assumes an infinite translation of the part of the PhC containing the defect. In this case, the unit cell will be larger and will contain several periods of the PhC. Now, when we have the waveguide, we should combine these two cases to obtain a new unit cell. Such a cell will be nonsquare as it is shown in Fig. 9.8. We now define the lattice vectors as follows:

$$\begin{aligned}\mathbf{R} &= \mathbf{a}_1 + \mathbf{a}_2, \\ \mathbf{a}_1 &= a \cdot \mathbf{x}, \\ \mathbf{a}_2 &= 7 \cdot a \cdot \mathbf{y},\end{aligned}\tag{9.16}$$

where a is the period of the 2D PhC, \mathbf{x} and \mathbf{y} are unit vectors in x and y directions, respectively.

Now, using (4.17), we obtain primitive reciprocal lattice vectors which finally has following form:

$$\begin{aligned}\mathbf{G} &= \mathbf{b}_1 + \mathbf{b}_2, \\ \mathbf{b}_1 &= 2\pi \frac{1}{a} \cdot \mathbf{x}, \\ \mathbf{b}_2 &= 2\pi \frac{1}{7 \cdot a} \cdot \mathbf{y}.\end{aligned}\tag{9.17}$$

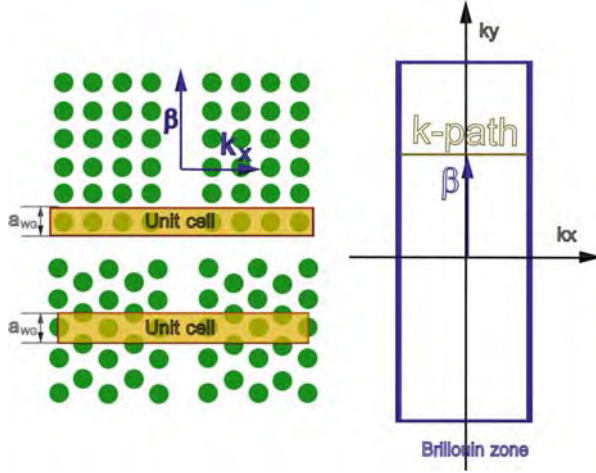


Fig. 9.8. Unit cell and Brillouin zone illustration

The reciprocal lattice vector gives us the shape of the Brillouin zone which is also depicted in Fig. 9.8. As we can see, the Brillouin zone is also nonsquare and is rotated by 90° as related to the unit cell.

Main difference in computation technique as compared to perfectly periodic PhC consists in understanding of the meaning of wave vector components. Since radiation propagate within the waveguide direction while the radiation confinement occurs in transversal direction, the wave vector is separated into two independent components. The first vector which is perpendicular to the wave propagation direction is connected with the waveguide dispersion relation. The absolute value of the wave vector component along that direction is usually referred to as propagation constant and is usually designated as β . Therefore, the computation should be carried out separately for the propagation constant and for the transversal components of the wave vector. At that, the computation process remains the same as for the microstructured fibers. The basic illustration of that redesignation of the wave vector is shown in Fig. 9.8.

Now let us consider the variation limits for both components of the wave vector. Since the structure is periodic and we have strictly defined Brillouin zone, the wave vector should vary within its limits. If the wave vector exceeds these limits, the solution repetition will take place so that it leads to increase of computation time. This concerns both the longitudinal and transversal wave vector components which also gives limitations for the set of propagation constants considered.

Taking all these considerations into account we can start with computation of the dispersion diagrams of the waveguide. Here, the computation is carried out in two stages.

The first stage is computation for transverse component of the wave vector. Within this stage, the propagation constant stays unchanged. The computation process at this stage is very similar to that one for a simple periodic PhC as shown in Chap. 5. There are, however, two differences; the first one is the set of wave vectors the computation is carried out for. Here, the set is represented by a single line which is perpendicular to the propagation direction and shifted in this direction by the value of the propagation constant as shown in Fig. 9.8. The second difference is the set of reciprocal lattice vectors. Earlier, we considered the band structure computation for structures which dimensions in all directions were equal. The reciprocal lattice vectors in this case had also an equal number of elements in all directions. However, since the waveguide's unit cell has lattice vectors like (9.16), definition of the set of reciprocal lattice vectors as previously is not allowed. We can simply validate this. For this, we synthesize the PhC waveguide from plane waves with coefficients obtained in Chap. 5. As shown in Fig. 9.9 the synthesis from the set with equal dimensions gives very draft image, so a very large number of plane waves is required to achieve satisfactory quality. On the other hand, the synthesis from the set, the dimensions of which relate to dimensions of the unit cell, gives good results even in case of low number of plane waves.

There is one more peculiarity when computation is carried out for the waveguide on the basis of hexagonal PhC. The unit cell of such a waveguide is no longer hexagonal as it was used in the case of perfectly periodic structure. Since we separated the wave vector by transversal and longitudinal components, the unit cell should be rectangular. This may be done by definition of the unit cell as shown in Fig. 9.8.

As a result of the first computation step, we have the eigen-states of the waveguide at some specific value of the propagation constant (see Fig. 9.10a). We can see several “plane” bands which correspond to the defect eigen-states and marked as bold in the figure.

At the second stage, we vary the propagation constant within the limits of the Brillouin zone which highest boundary is determined from the size of the unit cell along the waveguide direction using the relation π/a_{WG} . We carry out the computation of the eigen-states for each propagation constant in the range as shown in the first stage.

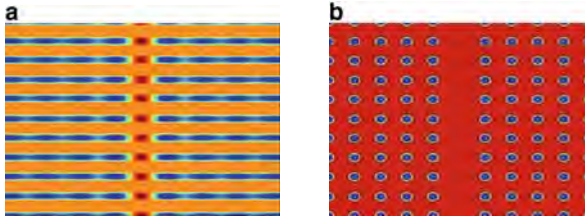


Fig. 9.9. Fourier-synthesis of the PhC waveguide using square (a) and non-square (b) set of reciprocal lattice vectors

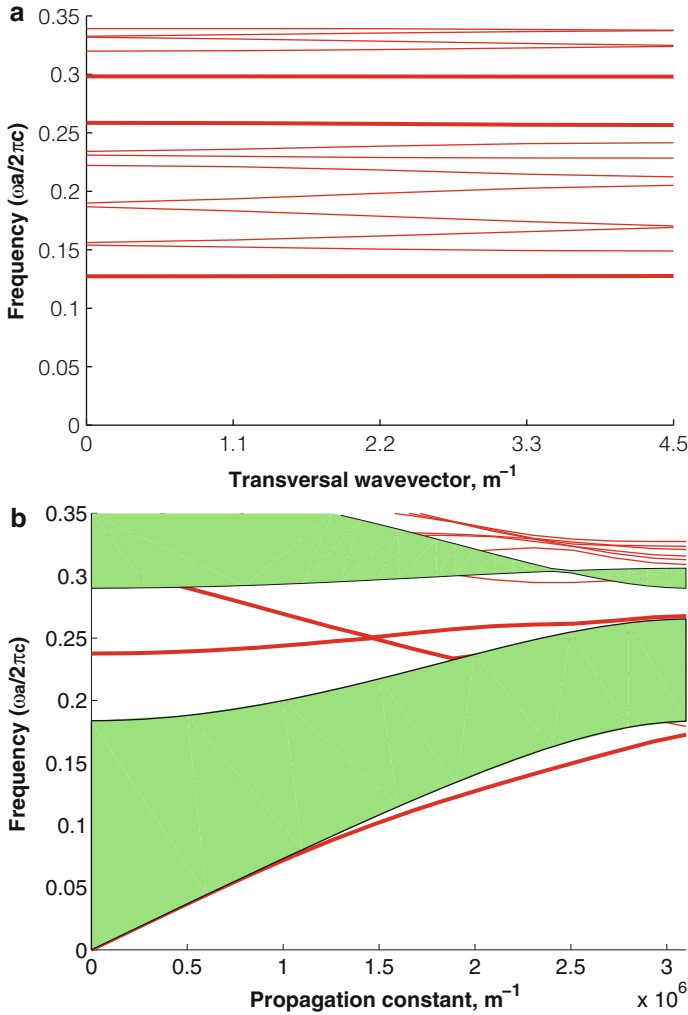


Fig. 9.10. Band structure (a) and dispersion diagram (b) of the PhC waveguide

After the computation is completed, we analyze the band structures obtained at each propagation constant. The most time-effective way of such a characteristic computation is finding the eigen-states at single point of the Brillouin zone. Since the defect eigen-frequency does not depend on the transversal component of the wave vector, the result will have satisfactory precision. Plotting the eigen-frequencies areas as a dependence of the wave vector gives the dispersion diagram of the waveguide.

Thus, we have obtained the dispersion diagram of the waveguiding structure. However, the analysis of such a characteristic is quite complicated since we do not know which frequencies will be localized inside the waveguide and which will flow out. An additional computation is usually required to complete

the analysis, namely, computation of the dispersion diagram of the defectless PhC. This characteristic gives the information about the continuum of states of the PhC surrounding the waveguide. The computation may be performed by the means of the method used for reduced band structure computation. Namely, the band structure computation is carried out at each value of propagation constant. Then, the information about forbidden and allowed frequencies is plotted as a dependence of the propagation constant. The typical result of such a computation is shown by filled areas in Fig. 9.10b.

9.5 Analysis of the Dispersion Diagram

Now, when dispersion diagram is obtained, its detailed analysis should be made to uncover all physical meanings of the waveguide eigen-states. First, the attention should be paid to the filled areas in Fig. 9.10b the continuum of states of the perfectly periodic waveguide. All the radiation i.e., the frequency and wave vector of which hit these areas will be able to propagate inside the PhC surrounding the waveguide. Therefore, such radiation will not be localized inside the waveguiding area.

The second conclusion which can be made from the dispersion diagram is the presence of the eigen-states inside the bandgap of the PhC. As we know, these eigen-states appear due to the introduction of the defect into the periodic structure. However, the eigen-frequency of the defect levels strongly depends on the propagation constant. This causes group velocity dispersion effects when radiation propagates over the waveguiding area. The dispersion diagram allows to obtain both group velocity and group velocity dispersion. The group velocity of the mode is determined as first derivative of the dispersion curve over the wave vector

$$v_g = \frac{d\omega(k)}{dk}. \quad (9.18)$$

The group velocity dispersion is determined as the second derivative of the dispersion relation over the wave vector.

$$\sigma_g = \frac{d^2\omega(k)}{dk^2}. \quad (9.19)$$

Special case should also be considered, when we have the eigen-state which is not a defect state but it allows the radiation to be localized within the waveguiding area at some specific value of the wave vector. This case is also known as total internal reflection guiding in the PhC waveguide and it is similar to that one described in Chap. 7 for microstructured fibers. As an example, we consider the first waveguide eigen-state in Fig. 9.10b. It is seen that this eigen-state lies outside the continuum of states so that the radiation with such a frequency and wave vector will not propagate inside the cladding PhC while the radiation with the same frequency but lower wave vector will flow out of the waveguide.

Now we can analyze the field distribution inside the waveguide to illustrate the light localization inside the waveguiding region and investigate the field configuration.

As we have found earlier, the mode field of the defect eigen-states is concentrated inside the waveguiding area unless its frequency falls at continuum of states. We can validate this statement by computation of the mode field distribution by means of method used for microstructured fibers. Using (7.33) we can obtain the field distribution within the period of the waveguide (here period refers to that one along the propagation direction). Translating the field distribution gives the picture over several periods. The field distribution examples are shown in Fig. 9.11 in accordance to the specific wave vectors and the numbers of the eigen-states. As an example, the picture gives the field distribution of the mode falling at the continuum of states (Fig. 9.11f); we can see the field propagated through the PhC cladding so no localization appears. Figure 9.11b–e depict the modes field distributions at propagation constant values $k_y = 1/a$ and $k_y = 1.7/a$. Investigating the field distribution, we can classify the modes of the PhC waveguides as even and odd modes. The even mode has even number of equal magnitude field distribution maxima in transverse direction (Fig. 9.11c,d). The odd mode, respectively, has odd number of maxima (Fig. 9.11b,e). Field distribution computation at different propagation constants indicates the fact that we have two different eigen-states which cross at wave vector $k_y = 1.5/a$. After crossing, the eigen-states are separated by frequency again. It should also be noted that even modes have lower group velocity than odd modes. This may be proved by using (9.18).

Now let us consider the field distribution of the mode propagating due to the total internal reflection effect. We earlier found out that the first eigen-state satisfies this condition. The field distribution of such a mode is shown in Fig. 9.11g. It is obvious that the field of the mode with the same frequency but lower wave vector will penetrate inside the PhC cladding since it falls at continuum of states. This means that the mode will not be localized.

The influence of the waveguide width on its modal properties should also be considered. The larger the waveguide width is, the larger the number of modes allowed for propagation inside the waveguide is. This is very similar to the situation with ordinary planar waveguides. The dispersion diagrams of the waveguides with different width of the guiding area, namely, W1, W2, and W3 are depicted in Figs. 9.10b and 9.12a b, respectively. It is seen that even in the simplest case of the W1 waveguide, there are two defect eigen-states possessing similar frequency, but different wave vectors. In case of larger waveguides, the number of modes propagating at similar frequency is growing. Since we determine the group velocity from the (9.18) we can see that all these modes propagate with different velocities so that the intermodal dispersion grows with waveguide width.

Concluding this section, we can mention that the PhC waveguide design problem is very complex and it includes a number of different characteristics

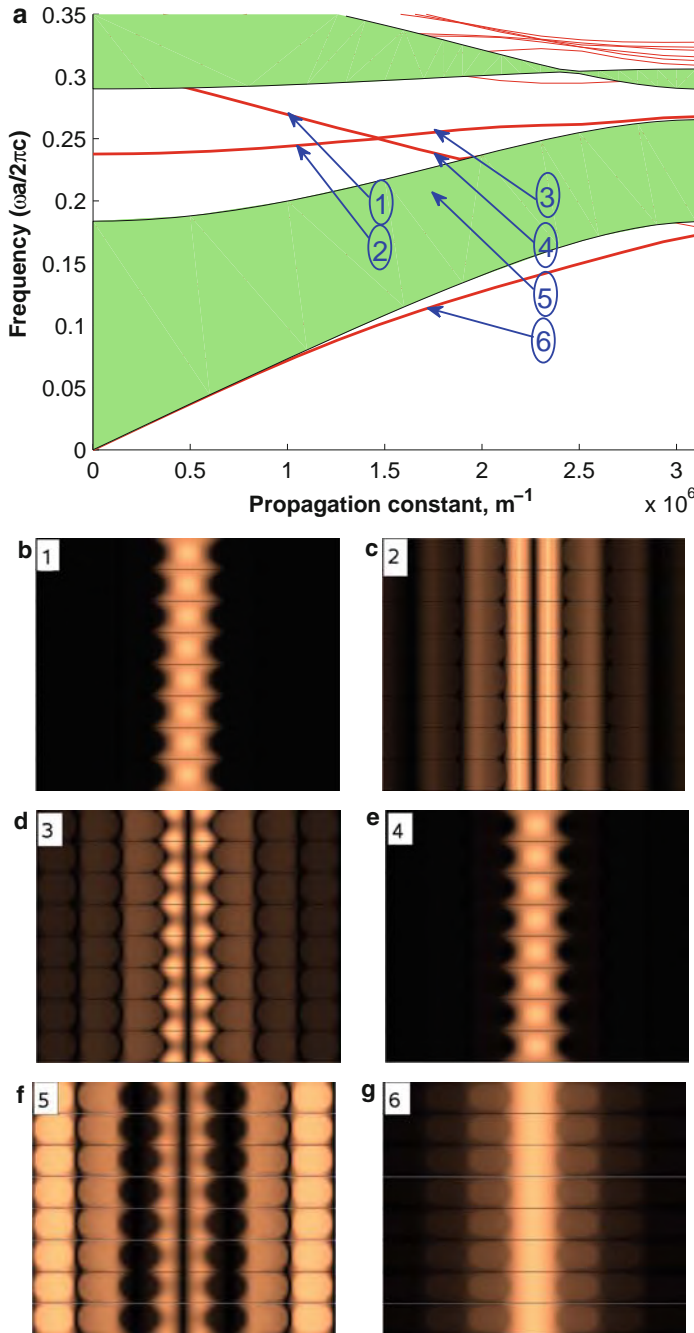


Fig. 9.11. Modes field distribution of the PhC waveguide at different propagation constants and eigen-frequencies

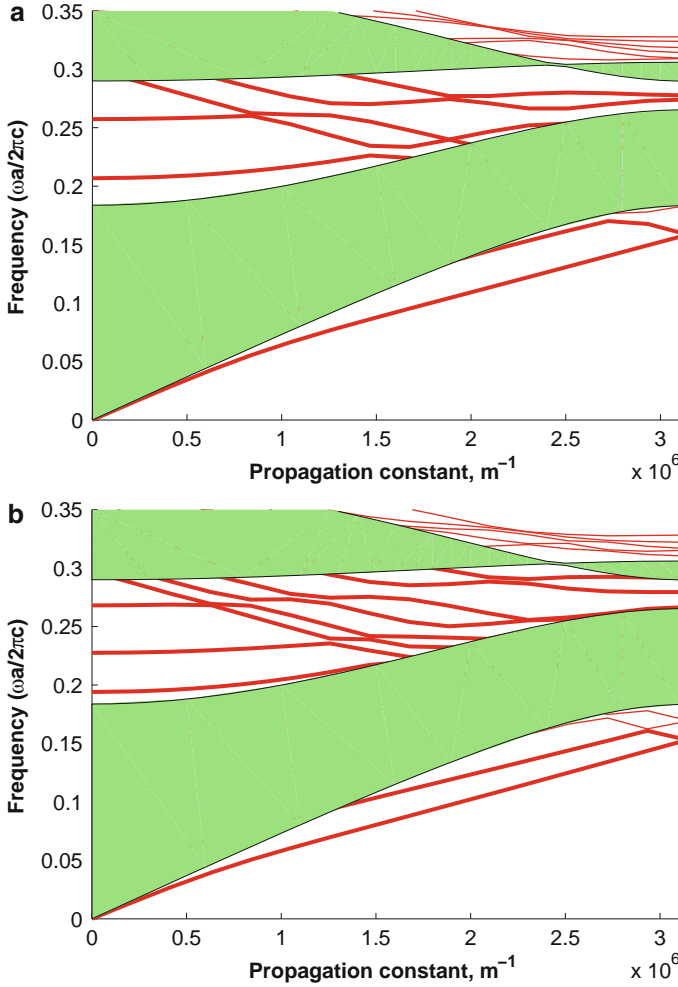


Fig. 9.12. Dispersion diagrams of W2 (a) and W3 (b) waveguides

to be taken into account which, in turn, depend on different PhC waveguide parameters. However, when all of them are considered, the waveguide can be configured with high accuracy.

9.6 FDTD Modeling of the PhC Waveguides

In all the chapters we computed characteristics of the PhC waveguides by means of the PWE method. This method allows computation of dispersion characteristics and gives us an idea of modes of field distribution. However, final stage of a device design requires field distribution and spectrum

computation within specific conditions to approve the correctness of selected parameters of the structure. The best choice in this case will be FDTD modeling which was validated in Chap. 6 by comparing with experimental results.

Now we proceed with computation of the transmittance spectra of three PhC waveguides with different lengths. All the waveguides in which the computation is carried out for have the following parameters: the lattice type is hexagonal; the cladding PhC period $a = 0.37\mu\text{m}$; the holes radius $r = 0.12\mu\text{m}$; the refractive index of the background material $n = 3.47$; and the guiding area is formed by one missing row of holes which gives us W1 waveguide.

The transmittance spectrum is computed by launching wide-spectrum pulse to the waveguide and measuring the structure response. Detailed explanation of this method of spectrum computation is given in, Sect. 6.6 and, therefore, it is not discussed here.

Here we computed the spectra for the PhC waveguides the length of which varies from 11 periods to 44 periods. The computation results are presented in Fig. 9.13b–d. Corresponding dispersion diagram of the waveguide is shown in Fig. 9.13a. In this figure we have normalized both the frequency and the propagation constant axes which makes results scalable and applicable to the waveguides design problems.

Let us analyze the transmittance spectra. We may first pay attention to the agreement between the waveguide eigen-states and the transmittance. As follows from our earlier discussion, the radiation localization inside the guiding area appears when the radiation frequency corresponds to the waveguide eigen-state. Due to this, the radiation with frequency inside the continuum of states penetrates to the cladding and form leaky mode. On the other hand, the radiation with frequency within the PhC bandgap, takes the wave vector of corresponding eigen-state and is guided by the structure. Particularly, we

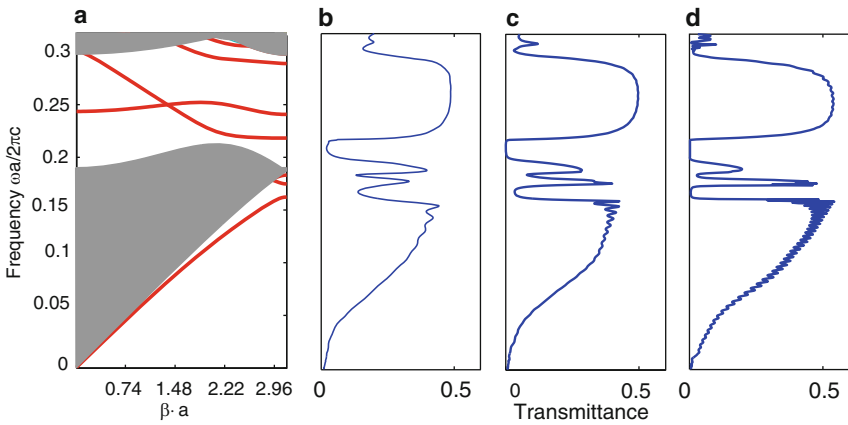


Fig. 9.13. Dispersion diagram of W1 waveguide (a) and transmittance spectra of the W1 waveguide of different length (b)–(d)

can mention two large guided frequency range, namely, from approximately 0.02 to 0.16 and from 0.21 to 0.29. The first range corresponds to TIR-guiding principle since the the first eigen-state does not lie inside the PBG. The radiation which corresponds to the second wide transmittance range is localized due to the defect eigen-state inside the PBG. As we can see, we have two eigen-states inside the PBG and, as follows from earlier analysis these eigen-states correspond to the even and odd modes.

The transmittance spectrum also has two narrow peaks which actually appear for different reasons. These peaks cover ranges from 0.173 to 0.182 and from 0.185 to 0.195. As we can see, the first one appears due to presence of two eigen-states which partially lie outside the continuum of states (within the range of $\beta \cdot a$ from 3 to 3.14). The second peak appears due to leaky modes and does not correspond to any of eigen-states outside the continuum of states.

The guided modes may easily be separated from the leaky ones by investigating the waveguides of different lengths. As we can see from Fig. 9.13b to d, the modes which were previously identified as guided modes become more clear when the length increases. On the other hand, the peak corresponding to the leaky modes which may actually be transmitted by the waveguide to a short distance (about tens of microns), becomes lower with the waveguide length.

Thus, we have have compared two characteristics of the PhC waveguides which were obtained by the means of different methods. These characteristics appeared to be in full correspondence with each other which proved the possibility to use the dispersion characteristics for the analysis and design of the PhC waveguides and devices on their basis.

9.7 Summary

1. The slab waveguide is represented by the uniform optical medium the refractive index of which is lower than the one of surrounding medium. The waveguiding effect is possible due to total internal reflection.
2. Modal properties of the slab waveguide may be determined by the solution of eigenvalue problem.
3. The PhC waveguide is represented by the set of optically connected defects. Due to peculiar properties of photonic crystals, the light within specific frequency range will be localized inside the waveguide.
4. The dispersion diagram is the most important one for determination of modal and dispersion properties of the PhC waveguide.
5. The dispersion diagram can be computed by the means of PWE method.
6. The guiding modes are subdivided by two categories, namely, even and odd modes. The kind of mode depends on what number of maxima, namely, even or odd, transversal field distribution of the mode possesses.

9.8 MATLAB Program for Computation of Dispersion Diagrams of 2D PhC Waveguide

```

function PhC_waveguide
%The program for the computation of the dispersion
%characteristic of the PhC waveguide based upon 2D
%PhC with square lattice. Parameters of the structure
%are defined by the PhC period, elements radius, and
%by the permittivities of elements and background
%material. In contrast to pure PhC, the waveguide is
%also defined by the number or the elements in
%direction transversal to radiation propagation as
%well as by the number of elements missed to form
%the defect.

%Main part of the program is implemented as a
%function because it should be run two times, namely,
%for the structure with and without defect. At first
%run, the function computes the defect eigen-states
%and at the first run it compute the continuum of
%states of the PhC.

%Input parameters: PhC period, radius of an
%element, permittivities, number of elements in
%transversal direction, defect size

%Output data: The dispersion diagram of the
%2D PhC waveguide.

clear all;

%The variable a defines the period of the structure.
%It influences on results in case of the frequency
%normalization.
a=1e-6;

%The variable r contains elements radius. Here it is
%defined as a part of the period.
r=0.4*a;

%The variable eps1 contains the information about
%the relative background material permittivity.
eps1=9;

```

```

%The variable eps2 contains the information about
%permittivity of the elements composing PhC. In our
%case permittivities are set to form the structure
%perforated membrane
eps2=1;

%Variable numElem defines the number of PhC elements
%in direction transversal to radiation propagation
numElem=7

%Number of holes missed
numDef=1

%Setting transversal wave vector to a single value
kx=0;

%Callint the function to compute the defect
%eigen-states. With this, we obtain the eigen-states
%of the linear defect
PWE(a, r, eps1, eps2, numElem, numDef, kx, 'b', 1);

numElem=1;
numDef=0;
%Setting transversal wave vector to a range of
%values within Brillouin zone
kx=0:(pi/a)/200:pi/a;

%Callint the function to compute the eigen-states
%of bulk PhC. This action fills the area of the
%continuum of states giving the possibility to
%analyze the dispersion diagram
PWE(a, r, eps1, eps2, numElem, numDef, kx, 'r', 3);

function PWE(a, r, eps1, eps2, numElem,...
            numDefect, kx_param, color, linewidth)

%The function implements the PWE method for 2D PhC
%The inputs are structure geometry and parameters,
%the number of transversal elements of the waveguide,
%the number of holes missed to form the defect and
%the transversal wave vectors set

%Computation precision parameters are set inside the
%function

```

```

%The variable precis defines the number of k-vector
%points between high symmetry points
precis=15;

%The variable nG defines the number of plane waves.
%Since the number of plane waves cannot be
%arbitrary value and should be zero-symmetric, the
%total number of plane waves may be determined
%as  $(nG*2-1)^2$ 
nG=2;

%The variable precisStruct defines contains the
%number of nodes of discretization mesh inside in
%unit cell
%discretization mesh elements.
precisStruct=30;

%The following loop carries out the definition
%of the unit cell. The definition is being
%made in discret form by setting values of inversed
%dielectric function to mesh nodes.
for n=0:numElem-1
    nx=1;
    for countX=-a/2:a/precisStruct:a/2
        ny=1;
        for countY=-a/2:a/precisStruct:a/2
            %Following condition allows to define the circle
            %with of radius r
            if((sqrt(countX^2+countY^2)<r)&&(n>=numDefect))
                %Setting the value of the inversed dielectric
                %function to the mesh node
                struct(nx+precisStruct*n,ny)=1/eps2;
            %Saving the node coordinate
                xSet(nx+precisStruct*n)=countX+a*n;
                ySet(ny)=countY;
            else
                struct(nx+precisStruct*n,ny)=1/eps1;
                xSet(nx+precisStruct*n)=countX+a*n;
                ySet(ny)=countY;
            end
            ny=ny+1;
        end
        nx=nx+1;
    end
end
end

```

```

%The computation of the area of the mesh cell. It is
%necessary for further computation of the Fourier
%expansion coefficients.
dS=(a/precisStruct)^2;

%Forming 2D arrays of nodes coordinates
[xMesh yMesh]=meshgrid(xSet(1:length(xSet)),...
                        ySet(1:length(ySet)));

%Transforming values of inversed dielectric function
%for the convenience of further computation
structMesh=(struct(1:length(xSet),1:length(ySet))*...
             dS/((max(xSet)-min(xSet))*(max(ySet)-min(ySet))))';

b1=[2*pi/a 0]./numElem;
b2=[0 2*pi/a];

%Defining the k-path within the Brilluoin zone. The
%k-path includes all high symmetry points and precis
%points between them

kx0(1:precis+1)=zeros(1,precis+1);
ky(1:precis+1)=0:b2(2)/2/precis:b2(2)/2;

%After the following loop, the variable numG will
%contain real number of plane waves used in the
%Fourier expansion
numG=1;

for Gx=-nG*numElem:nG*numElem
    for Gy=-nG:nG
        G(numG,1)=Gx*b1(1)+Gy*b2(1);
        G(numG,2)=Gx*b1(2)+Gy*b2(2);
        numG=numG+1;
    end
end
%The next loop computes the Fourier expansion
%coefficients which will be used for matrix
%differential operator computation.
for countG=1:numG-1
    for countG1=1:numG-1
        CN2D_N(countG,countG1)=sum(sum(structMesh.*...
            exp(1i*((G(countG,1)-G(countG1,1))*xMesh+...
                (G(countG,2)-G(countG1,2))*yMesh))));
    end
end
end

```

```

%The next loop computes matrix differential
%operator in case of TE mode. The computation
%is carried out for each of earlier defined
%wave vectors.
for kx_count=1:length(kx_param)
kx=kx0+kx_param(kx_count);

for countG=1:numG-1
    for countG1=1:numG-1
        for countK=1:length(kx)
            M(countK,countG,countG1)=...
                CN2D_N(countG,countG1)*...
                ((kx(countK)+G(countG,1))*...
                (kx(countK)+G(countG1,1))+...
                (ky(countK)+G(countG,2))*...
                (ky(countK)+G(countG1,2)));
        end
    end
end

%The computation of eigen-states is also carried
%out for all wave vectors in the k-path.
for countK=1:length(kx)
%Taking the matrix differential operator for
%current wave vector.
    MM(:,:)=M(countK,:,:);
%Computing the eigen-vectors and eigen-states of
%the matrix
    [D V]=eig(MM);
%Transforming matrix eigen-states to the form of
%normalized frequency.
    dispe(:,countK)=sort((sqrt(V*...
                                ones(length(V),1)))*a/2/pi);
end

figure(1);
hold on;
for u=1:15
    plot(ky,abs(dispe(u,:)),color,...
         'LineWidth',linewidth);

```

```

end
ylabel('Frequency \omega a/2\pi', 'FontSize', 20);
xlabel('Propagation constant \beta, m^{-1}', ...
      'FontSize', 20);

drawnow;
end

```

The computation technique used for implementation of the PWE method for the PhC waveguide is very similar to the one used for the computation of the band structure of strictly periodic PhC. There are, however, some essential differences in the structure parameters definitions. First, here the unit cell consists of several PhC elements rather than one. The defect of the periodic structure is also introduced to form the waveguiding area.

Another difference appears when we are defining the k -path. In case of 2D PhC band structure computation, we set the k -path to pass through all high symmetry points of the Brillouin zone. However, as we have considered in this chapter, computation of the PhC waveguide eigen-states requires transversal wave vector consideration only. The longitudinal component stays in this case for the propagation constant. In present the program, however, we consider the defect eigen-states computation. As we have seen in Chap. 5, the defect eigen-frequency does not depend on the wave vector so we can limit the consideration by a single value of the wave vector. Here we selected the point $k = 0$. However, the propagation constant here is limited by the boundaries of the Brillouin zone.

One more difference from strictly periodic PhC is the definition of the reciprocal lattice vectors set. In Sect. 9.4 we considered this step in detail. As we have seen, we cannot select the set of the reciprocal lattice vectors in which dimensions are equal. Therefore, here the size of the set in propagation direction is *numElem* times smaller than that in transversal direction. However, the set still remains zero-symmetric.

The rest of computation process is similar to one of the strictly periodic PhC. As a result of computation, we obtain the set of bands (blue lines in Fig. 9.14). Several of them are in the defect states. However, to separate the defect states from the continuum of states, it is necessary to carry out the same computation for the defectless PhC and plot the results over the defect eigen-states (red areas in Fig. 9.14). That is why the function PWE is running twice. First time it is for the structure with defect but for single value of the transversal wave vector. The second time, the function is running for defectless structure and scans over all transversal wave vectors within Brillouin zone.

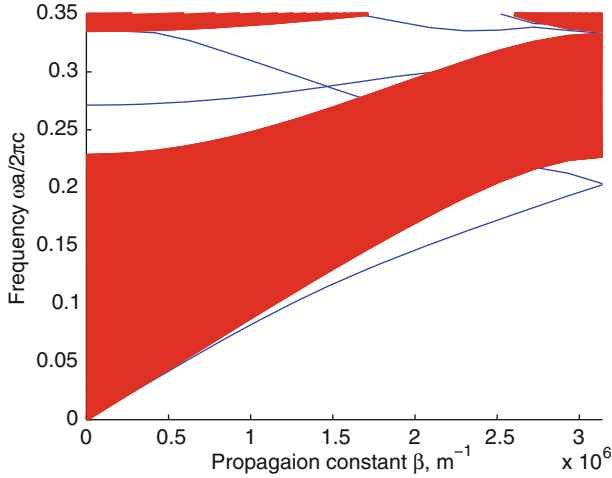


Fig. 9.14. Results of the program. The dispersion diagram of the W1 PhC waveguide

9.9 Problems and Questions

Problem 9.1. Formulate the phase conditions for guided mode in slab waveguide from the point of view of geometry optics.

Problem 9.2. Which waveguides are referred to as weakly guided?

Problem 9.3. What is the critical angle? Write down the formula for the critical angle for weakly guiding waveguide.

Problem 9.4. What the designation “W3” means for PhC waveguide?

Problem 9.5. Write down primitive lattice vectors for the W1 PhC waveguide with PhC hexagonal lattice and period $a = 0.5 \mu\text{m}$.

Problem 9.6. Calculate the reciprocal lattice primitive vectors for the W1 PhC waveguide with PhC hexagonal lattice and period $a = 0.5 \mu\text{m}$.

Problem 9.7. Modify the program to compute the continuum of states of the PhC waveguide cladding.

Problem 9.8. Modify the program to compute the eigen-states of the PhC waveguide on the basis of hexagonal lattice.

Application for Design and Simulation of Optical WDM Demultiplexer

Summary. The last chapter is intended to demonstrate a simple example of the PhC device which would include the knowledge and skills obtained in the earlier chapters. The example of the design and simulation of optical WDM demultiplexer is given in this chapter, which is one of the crucial elements of fiber-optical communication systems used for spatial separation of optical channels. We show the design of 2D PhC DEMUX presented by 2D waveguide splitter with introduced wideband filters. Design was carried out by PWE method which provided computation of PBG maps and PhDOS maps. As a result, the values of DEMUX parameters were obtained. The design results were approved by the FDTD simulation of optical field distribution inside the device as well as temporal response. Finally the original Matlab-code for computation of PBG maps of the PhC is presented at the end of the chapter, along with problems and questions for self-training.

10.1 Problem Formulation

One of the most known techniques for data compression when dealing with the optical information carrier is wavelength division multiplexing (WDM). In this technique the information transmitting over the fiber or waveguide is separated over several information channels. Each channel is presented by modulated laser beam with a specific wavelength. All the channels are gathered to a single guiding media and transmitted to the destination point. At the end of transmission line channels are separated by the wavelength and processed in some way.

Main device in WDM system is multiplexer/demultiplexer (MUX/DEMUX) which is usually used both for gathering and separation of channels. Typical DEMUXes used in WDM systems employ Mach-Zender interferometers, fiber arrays, and so on. All these devices are quite large so that their inclusion to PhC-based integrated optical circuits is complicated. Therefore, the very important problem is to design the DEMUX on the basis of 2D PhC.

In this chapter, we give an example of simple solution to the problem of WDM DEMUX design on the basis of 2D PhC [246]. DEMUX is presented

by the optical waveguide channel created by introducing a line defect into the periodic structure of the 2D PC. The splitter is formed at the output of the channel in the same structure. At the input of each port of the splitter, the wide band optical filter, formed by variation of geometrical parameters of the PC are placed. Each filter has precisely calculated band gap to provide the most efficient wavelength channel splitting.

First, we describe and compare two techniques for PhC filters design employing the PWE method. Then, the analysis of the whole device and its testing will be performed employing the FDTD method.

10.2 Band Structure Analysis

At the first stage of the PhC-DEMUX design, it is important to determine geometric and material parameters of the PhC to be used. We will start with the scheme of the PhC-DEMUX which is given in Fig. 10.1. Basic parts of the DEMUX are shown. They are the waveguide splitter with two arms and two wavelength filters embedded in those arms. For technological reasons, all these parts should be preferably made of the same material.

To determine PhC parameters required, we need to specify wavelength range within which DEMUX will be working. In this example we take two incident wavelengths $\lambda_1 = 1.31 \mu\text{m}$ and $\lambda_2 = 1.55 \mu\text{m}$ since these wavelengths are widely used in telecommunications.

Now when we have determined the wavelength to be used, there are two different techniques to determine the PhC parameters. They are the PBG analysis and photonic density of states (PhDOS) analysis which will be described in detail.

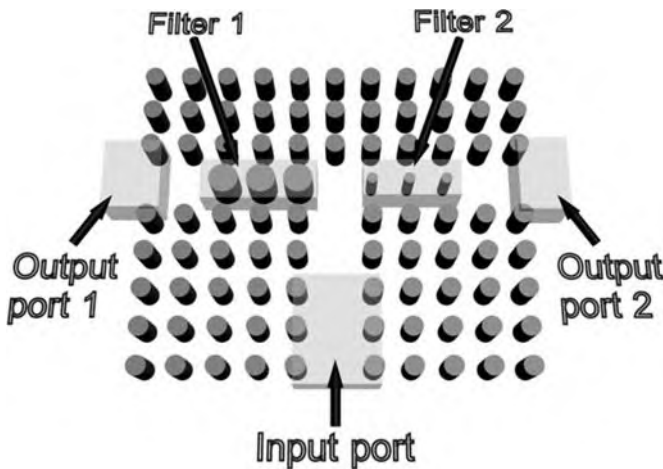


Fig. 10.1. Schematic sketch of the PhC-based DEMUX

10.2.1 Waveguide Design

Before we proceed with analysis of PhC transmittance characteristics, selection of the waveguide width should be made. Actually, it is possible to design the DEMUX on the basis of W1 waveguide. However, characteristics of filters based on such waveguides cannot be described either by PBG maps or by PhDOS maps. The reason is that these characteristics do not take into account direction of radiation propagation but give the transmittance over all possible direction.

However, if we take the filter inside W1 waveguide, we limit the propagation by one direction as we can see from Fig. 10.2. To provide all possible propagation direction we must use at least waveguide W2 with filters inside. The Fig. 10.3 illustrates transmittance spectra of the filters embedded into

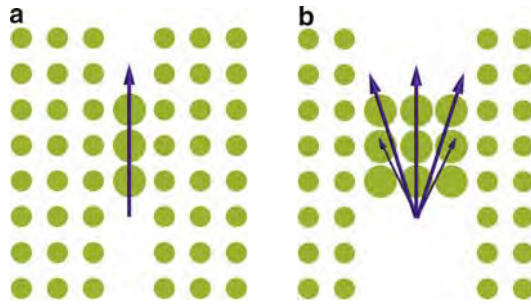


Fig. 10.2. The PhC filter inside W1 waveguide (a) and W3 waveguide (b) as well as possible directions of radiation propagation inside such filters

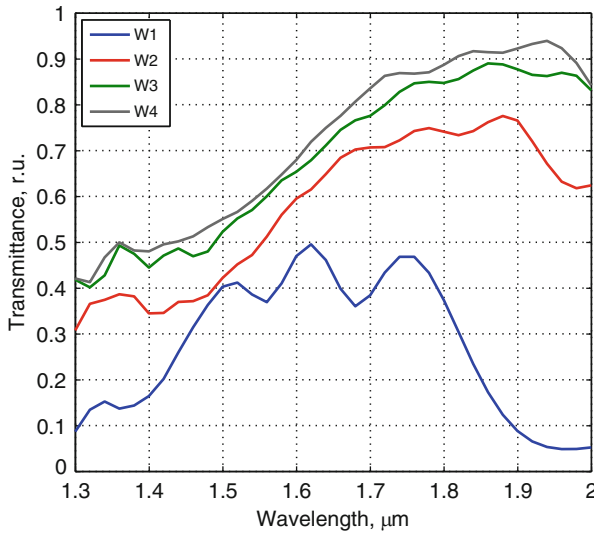


Fig. 10.3. Transmittance spectra of the PhC waveguides of different width

W1, W2, W3, and W4 waveguides. As we can see, there are essential differences between W1 and other filters. However, in Chap. 9 we have seen that number of modes of a waveguide increases with the waveguide width. Taking this into account, we restrict consideration by the waveguide W2.

10.2.2 PBG Maps Design

Let us first consider the waveguide channel. As we know, the radiation will only be guided when its wavelength lies outside the PhC continuum of states. As we have found in an earlier chapter there are two opportunities to do this, namely, to work within TIR guiding or PBG guiding. However, since we have PhC splitter here and direction of longitudinal component of the wave vector is changed at the waveguide bend, the TIR guiding will not work properly and radiation will flow outside the device. Therefore, we pay attention to the wavelength situated inside the PBG only.

Next, we pay attention at the PhC filters. The filter's function is to separate one wavelength from the other. It may be done when one filter completely reflects one wavelength while transmitting another one and the second filter acts vice versa. As we also know, the complete radiation reflectance is achieved when its wavelength lies inside the PBG.

Thus, we have the problem of PhC parameters agreement for main waveguide and both filters. The problem may be solved by considering PBG maps described in Chap. 5. General schemes for possible band structures design are shown in Fig. 10.4. In the figure, the horizontal solid lines correspond to information carrier frequencies (ω_1 and ω_2). Vertical lines designate the values of r/a for the first filter (r_1), main waveguide and splitter (r_2), and the second filter (r_3). Here we can see that central vertical line r_2 corresponds to elements

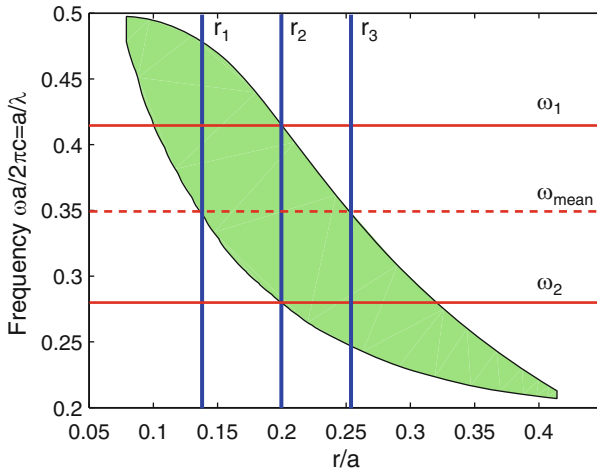


Fig. 10.4. Scheme for parameters selection of PhC-DEMUX

radius which allows both frequencies to be inside the PBG. That means that PhC with these parameters can be used as waveguide for both operating frequencies. Other two lines indicate that radiation with one wavelength only passes through the PhC. This condition corresponds to wavelength filters.

Procedure for parameters' selection consists of several steps. Since we do not have additional information about the transmittance spectrum, we assume complete reflection within the PBG range and complete radiation transmission outside the PBG. Taking this into account, we can proceed as follows:

1. Determine the r/a value for background PhC which forms waveguide and splitter. To do that we find the widest PBG and set the first vertical line.
2. The second step is to determine lattice constant of PhC. To do that we draw the straight line perpendicular to the first vertical line. The horizontal line should cross the vertical line in the middle of the PBG. Then, we take its relative frequency and find the lattice constant a by means of the formula $a = 2 \cdot \pi c \cdot \omega_r / \omega$, where ω is taken as the mean value of two operating frequencies.
3. Third, we are searching for relative frequencies corresponding to operating wavelengths. To do that we use above-mentioned formula with ω being exactly the operating frequency and a determined from the earlier step. When values are found, corresponding horizontal lines are drawn.
4. At the last step, we are searching for values of r/a where the distances from operating frequencies to the edge of the PBG are equal. At that, one of frequencies lies inside and another one outside the PBG.

The scheme gives exact values of parameters, so the design procedure of the DEMUX is now completed. The procedure may be quite simplified if the problem is solved graphically first.

Now, we discuss some examples. Consider PBG maps (see Fig. 10.5) computed for the PhCs made of silica and represented by rods or holes arranged to a square or a hexagonal lattice. With this, we take into account many possible PhC configurations which are made of pure silica.

If we then try to find the PhC parameters which satisfy above-mentioned conditions, we will see that only three of considered PhC configurations provide the opportunity for demultiplexing. The perforated membrane with holes in square lattice has very narrow band gaps so that it cannot be used for DEMUX design. For other kind of PhC, we have the following parameters. For rods arranged to square lattice, $a = 0.532 \mu\text{m}$, $r_1/a = 0.12$, $r_2/a = 0.172$, $r_3/a = 0.23$ which corresponds to relative frequencies $\omega_1 = 0.4$ and $\omega_2 = 0.34$. For rods arranged to hexagonal lattice, $a = 0.61 \mu\text{m}$, $r_1/a = 0.09$, $r_2/a = 0.14$, $r_3/a = 0.207$ which corresponds to relative frequencies $\omega_1 = 0.46$ and $\omega_2 = 0.39$. For holes arranged to hexagonal lattice, $a = 0.54 \mu\text{m}$, $r_1/a = 0.388$, $r_2/a = 0.446$, $r_3/a = 0.478$ which corresponds to relative frequencies $\omega_1 = 0.41$ and $\omega_2 = 0.35$. Let us examine the field distributions for all these cases. As we can see from Figs. 10.6 to 10.8, the DEMUX based on different PhC kinds have different efficiency of spatial separation of wavelength

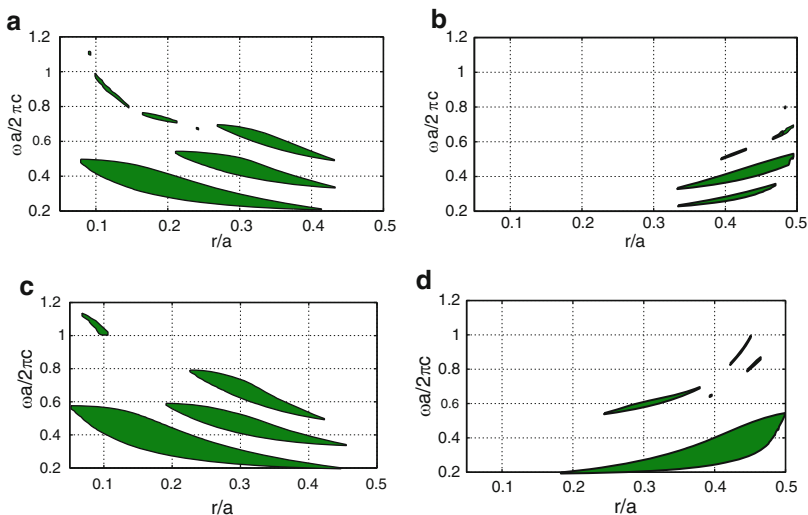


Fig. 10.5. PBG maps of the PhC represented by rods in square lattice (a), holes in square lattice (b), rods in hexagonal lattice (c) and holes in hexagonal lattice (d)

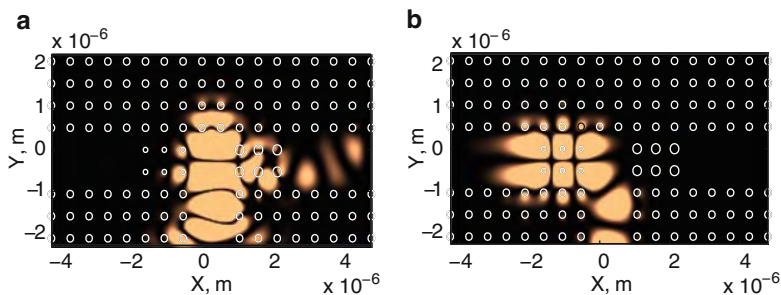


Fig. 10.6. Field distribution inside the DEMUX based upon rods in square lattice: (a) is for $\lambda = 1.31 \mu\text{m}$, (b) is for $\lambda = 1.55 \mu\text{m}$

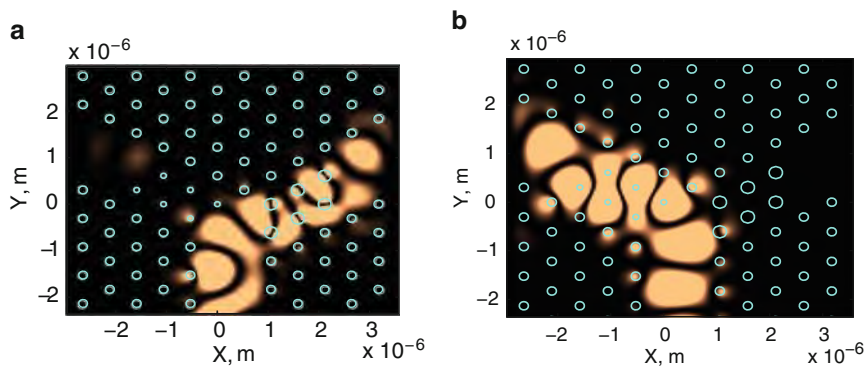


Fig. 10.7. Field distribution inside the DEMUX based upon rods in hexagonal lattice: (a) is for $\lambda = 1.31 \mu\text{m}$, (b) is for $\lambda = 1.55 \mu\text{m}$

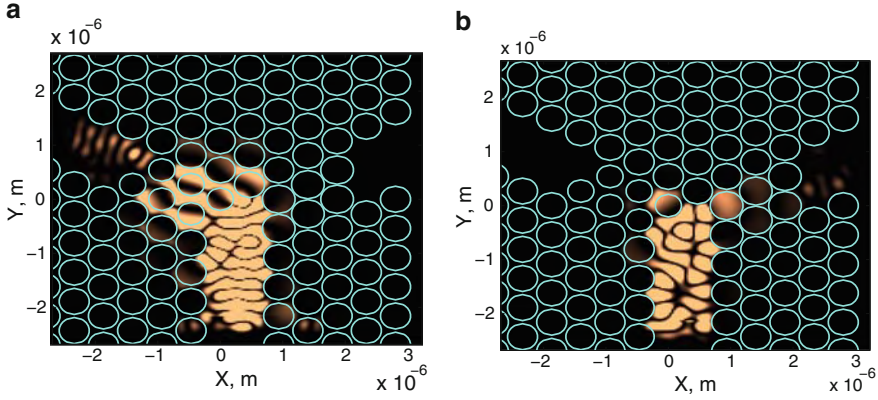


Fig. 10.8. Field distribution inside the DEMUX based upon holes in hexagonal lattice: (a) is for $\lambda = 1.31 \mu\text{m}$, (b) is for $\lambda = 1.55 \mu\text{m}$

channels. For instance, the most efficient is the PhC with rods arranged to hexagonal lattice. The device with square lattice has low transmittance at the wavelength $1.55 \mu\text{m}$ and the device on the basis of perforated membrane is inefficient at all. This is typical situation for the method of PBG maps analysis since, as we mentioned earlier, it does not provide the information about the transmittance outside the band gaps.

If we consider the design based on perforated membrane, we have to take into account technological inconvenience of the device production as well. The above-mentioned parameters selection scheme gives parameters of the PhC at which elements are almost overlap. This causes additional problems while producing such a device.

10.2.3 Photonic DOS Maps Design

The PBG maps analysis provides easy and quick design of PhC-based DEMUX. However, assumption of the transmittance homogeneity outside the PBG may cause an error in device parameters determination as we have seen from the field distributions.

Another technique to design the PhC-based DEMUX is analysis of photonic density of states (PhDOS) maps [247–249]. This technique allows to take into account transmittance characteristic of the structure so we are able to carry out more precise design of the device.

Computation of the PhDOS maps is very similar to one based on PBG maps. However, instead of taking the information of allowed and forbidden zones, we compute the PhDOS plotting it as a dependence on PhC parameters. Similar to PBG maps value of r/a is also taken here as a parameter. The PhDOS is computed by (5.27). Example of PhDOS map is given in Fig. 10.9a.

To understand the connection between the PhDOS and transmittance, we are now computing the transmittance map of the same PhC where the

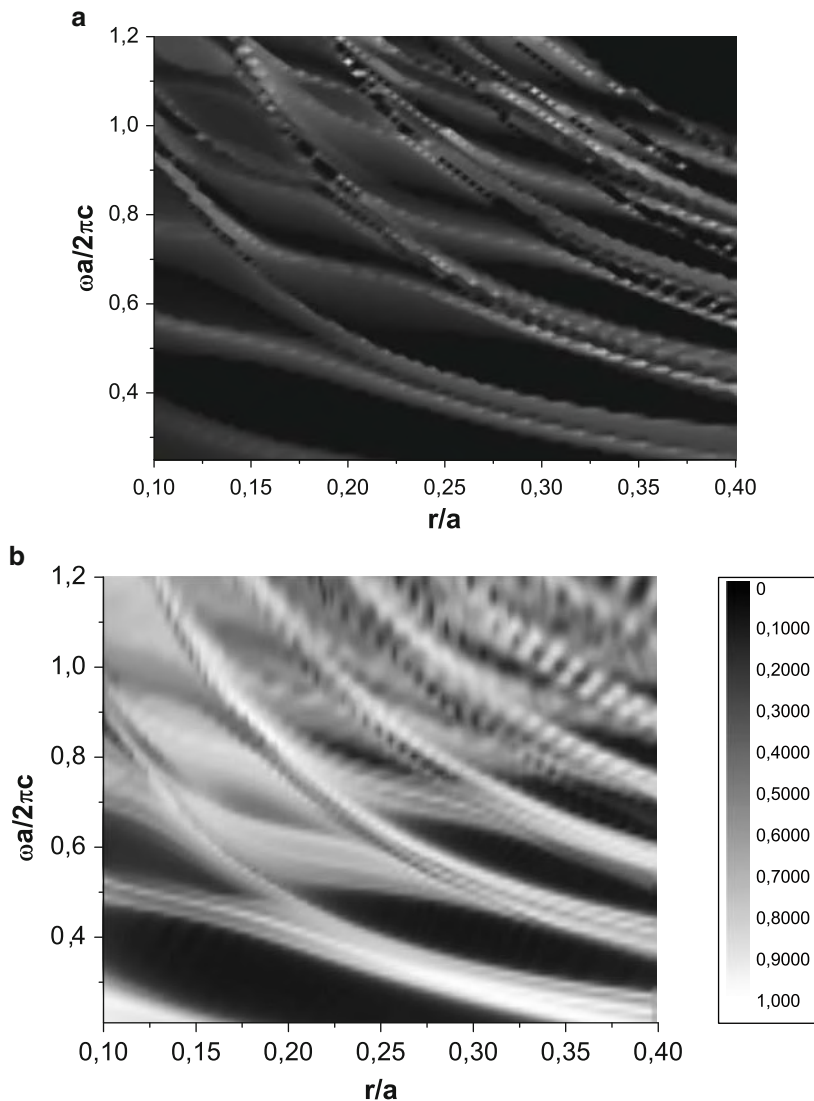


Fig. 10.9. PhDOS map (a) and corresponding transmittance map (b) of the PhC represented by rods arranged to square lattice

transmittance spectra are plotted instead of the PhDOS (see Fig. 10.9b). If we compare the PhDOS and transmittance maps, we can see that maxima of the transmittance coincide with maxima of the PhDOS. Minima coincide as well. Such a dependence may easily be understood by simple consideration. If the PhDOS at the specific frequency is high, this means that there are many ways for radiation to pass through the structure. Consequently, it has high transmittance. On the other hand, if the PhDOS is low, the number of allowed “routes” for radiation is low as well and, therefore, the transmittance is low.

Thus, we can see correspondence between the PhDOS and transmittance of the structure. Black areas in PhDOS maps correspond to complete PBG and coincide with those marked in PBG maps (see, for example, Fig. 10.5a). Consequently, we can use the PhDOS maps for the DEMUX design to have the possibility of taking into account the transmittance outside the PBGs without direct transmittance computation. On the other hand, PhDOS maps are more convenient than transmittance maps since the computation time for transmittance maps by means of FDTD technique is several times larger than that for PhDOS maps.

We will consider the same example as in Sect. 10.2.2. However, scheme for parameters selection will be changed since we are able to carry out more precise analysis. The scheme itself consists of four steps:

1. Determine the r/a value for background PhC which forms waveguide and arms of the splitter. To do that we find the widest PBG and set the first vertical line.
2. Determine the PhC lattice constant. To do that we draw straight line perpendicular to the first vertical line. The horizontal line should cross the vertical line in the middle of the PBG. Then, we take its relative frequency and find the lattice constant a by the formula $a = 2 \cdot \pi c \cdot \omega_r / \omega$, where ω is taken as mean value of two operating frequencies.
3. Then, we are searching for relative frequencies corresponding to operating wavelengths. To do that we use above-mentioned formula with ω being exactly the operating frequency and a determined from the previous step. When the values are found, corresponding horizontal lines are drawn.
4. The last step is different from that one in PBG analysis method. At this step we determine the values of r/a for the output filters. Unlike the above-described method, the PhDOS analysis considers the transmission properties outside the PBG. Therefore, we pay attention to the PhDOS value rather than the distance from the edge of the PBG. We select the value of r/a which corresponds to high PhDOS which leads to high transmittance of the filter at the operating wavelength.

Results of such a design significantly differ from the ones obtained with PBG maps analysis. Let us consider the situation of the PBG analysis technique for rods arranged to square lattice. In this case, we have the values of r/a obtained from the PBG map (Fig. 10.5a). If we now draw corresponding lines at the PhDOS map (see Fig. 10.10), we will see the reason of low transmittance at the wavelength $1.55 \mu\text{m}$ (see Fig. 10.6b). The point with $r/a = 0.12$ and $\omega = 0.34$ lies at low value of the PhDOS and, consequently, the transmittance here is low. Let us now shift the vertical line to the point of approximately maximum value of the PhDOS ($r/a = 0.105$). If we now compute the field distribution in this case, we will see in Fig. 10.11 that the field penetration through the PhC filter and, consequently, transmittance is much higher than that one shown in Fig. 10.6b.

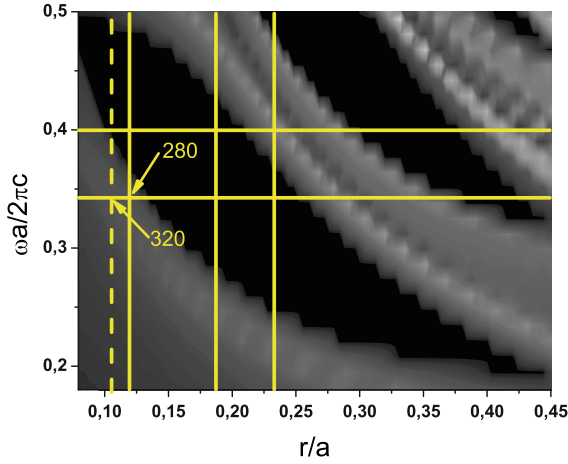


Fig. 10.10. Parameters selection scheme by means of PhDOS map

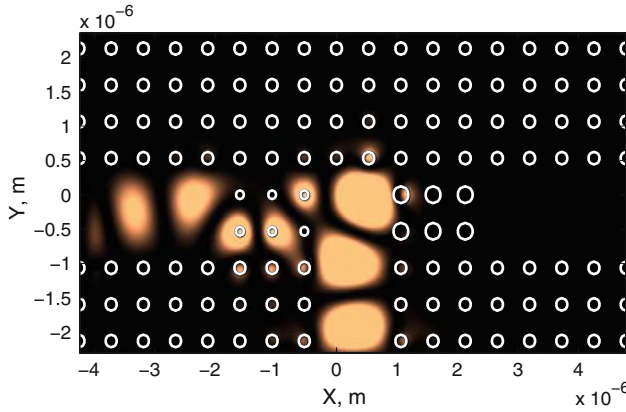


Fig. 10.11. Field distribution inside the DEMUX with parameters optimized by PhDOS map analysis

10.3 Temporal Response of DEMUX

We can now examine temporal response of the structure to the series of pulses. With this we obtain the maximum operating rate allowed for the DEMUX. To do that we launch the series of three pulses having two different wavelengths to the structure and measure the power at the outputs. Responses to the excitations with $\lambda_{\text{launch}} = 1.31 \mu\text{m}$ and $\lambda_{\text{launch}} = 1.55 \mu\text{m}$ are shown in Figs. 10.12a, b, respectively. The structure under investigation is the DEMUX based upon the structure of rods in square lattice.

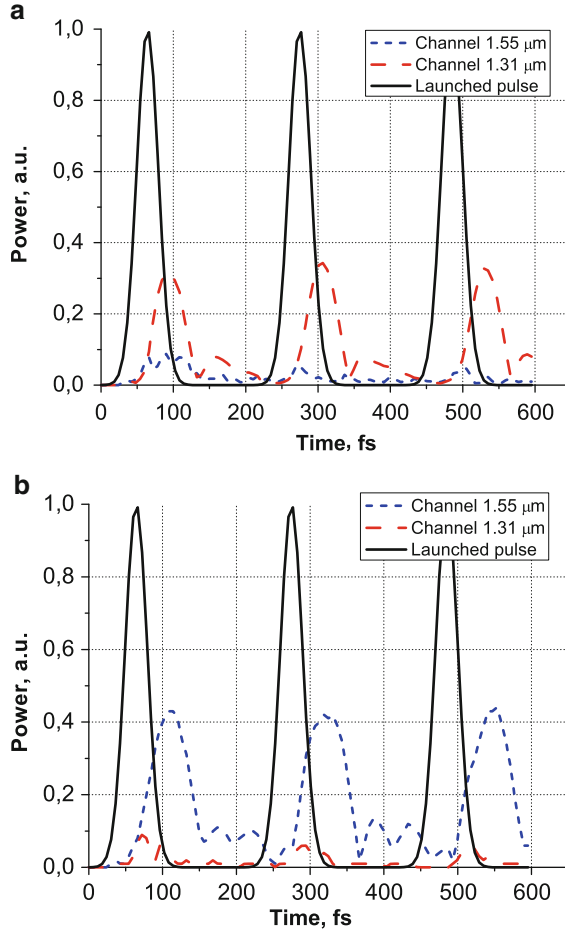


Fig. 10.12. Temporal response of the structure to the pulse with duration $\tau = 50$ fs at the wavelength $\lambda = 1.31 \mu\text{m}$ (a) and $\lambda = 1.55 \mu\text{m}$ (b)

We can see from the figure that in spite of attenuation and distortions introduced by the filters, the pulses width is almost unchanged and peak-to-valley is still big to easily distinguish the pulses. It indicates effectiveness of the device at the pulses duration of order of $\tau = 50$ fs.

10.4 Summary

Thus, in the final chapter, we have considered example of the WDM demultiplexer design and examination. The design was carried out by the PWE method which provided the computation of PBG maps and PhDOS maps.

The field distribution as well as temporal response of the device was computed by means of the FDTD method.

10.5 MATLAB Program for the Computation of the PBG Map of PhC by Means of PWE Method

```
function PBGmap

%The program for the computation of PBG map of
%2D PhC by means of PWE method.
%Parameters of the structure are defined by the PhC
%period, elements radius, and by the permittivities
%of elements and background material.
%The PBG map is computed here as a function of
%the value of elements radius
%The PWE method itself is implemented here as a
%function since it should be called for each value
%of radius within selected range

%Input parameters: PhC period, radius of an
%element, permittivities, parameter scanning range

%Output data: The PBG map of the 2D PhC.

%Variable a defines the PhC lattice constant
a=1e-6;

%Variable deltaR is the scanning step
deltaR=0.001*a;

%The loop for PBG computation at different r
%values within the range from 0 to 0.5*a
counter=1;
for r=0:deltaR:0.5*a
    clear bandgap;
%Call the function getBandgap which returns
%the band gaps lower and higher relative
%frequencies if they present or value "-1"
%otherwise
%The band gaps information is stored to the array
%gapUnsorted
    bandgap=getBandgap(a,r,1,9);
    s=size(bandgap);
    for numPBG=1:s(1)
```

```

if bandgap(1,1)>-1
    gapUnsorted(counter,1)=r;
    gapUnsorted(counter,2)=bandgap(numPBG,1);
    gapUnsorted(counter,3)=bandgap(numPBG,2);
    counter=counter+1;
end
end
display(strcat(num2str(r/(0.5*a)*100),...
               '% Completed')));
end

%Starting to sort the bandgaps to form solid
%areas. First, initialize the first array element
%with first band gap found.
gapSorted(1,1,1)=gapUnsorted(1,1);
gapSorted(1,1,2)=gapUnsorted(1,2);
gapSorted(1,1,3)=gapUnsorted(1,3);

%Following loop forms array of sorted band gaps
gapsCount(1)=2;
i=2;
numGaps=1;
for i=2:length(gapUnsorted)
    newgap=1;
    for j=1:numGaps
%The following conditions allows to separate one
%band gap from another. The condition tests if the
%band gaps are overlapped in frequency and
%are situated next to each in radius
        if((gapUnsorted(i,2)<...
            gapSorted(j,gapsCount(j)-1,3))&&...
            (gapUnsorted(i,3)>...
            gapSorted(j,gapsCount(j)-1,2))&&...
            (gapUnsorted(i,1)-...
            gapSorted(j,gapsCount(j)-1,1)<deltaR*2))

            gapSorted(j,gapsCount(j),1)=gapUnsorted(i,1);
            gapSorted(j,gapsCount(j),2)=gapUnsorted(i,2);
            gapSorted(j,gapsCount(j),3)=gapUnsorted(i,3);
            gapsCount(j)=gapsCount(j)+1;
            newgap=0;
        end
    end
end;

```

```

%If there are no previously formed band gaps, form
%new band gap
    if newgap
        numGaps=numGaps+1;
        gapsCount(numGaps)=2;
        gapSorted(numGaps,1,1)=gapUnsorted(i,1);
        gapSorted(numGaps,1,2)=gapUnsorted(i,2);
        gapSorted(numGaps,1,3)=gapUnsorted(i,3);
    end;
end;

%Plotting the solution
%Creating figure and signing the axes
figure;
axes('FontSize',16);
xlabel('Radius r, m','FontSize',20);
ylabel('Frequency \omega a/2\pi','FontSize',20);
hold on;

%Each band gap is represented in form compatible
%with function "patch"
for i=1:numGaps
    for j=1:gapsCount(i)-1
        gapForPatch(i,j,1)=gapSorted(i,j,1);
        gapForPatch(i,j,2)=gapSorted(i,j,2);
        gapForPatch(i,2*gapsCount(i)-1-j,1)=...
            gapSorted(i,j,1);
        gapForPatch(i,2*gapsCount(i)-1-j,2)=...
            gapSorted(i,j,3);
    end;

    gapForPatch(i,2*gapsCount(i),1)=gapSorted(i,1,1);
    gapForPatch(i,2*gapsCount(i),2)=gapSorted(i,1,2);

end;

siz=size(gapForPatch);
for i=1:numGaps
    %Removing zeros from arrays replacing them with
    %values from bound. Otherwise, every patch will
    %start from point (0, 0)
    for j=1:siz(2)
        if(gapForPatch(i,j,1)==0)
            gapForPatch(i,j,1)=gapForPatch(i,1,1);
            gapForPatch(i,j,2)=gapForPatch(i,1,2);

```

```

        end;
        colormap(j)=0.4;
    end;
%In the final step, the band gaps are plotted
%in figure
patch(gapForPatch(i,:,1)',gapForPatch(i,:,2)',...
      colormap,'LineWidth',2);

hold on;
end;

%The function getBandgap implements the PWE method.
%As a result of the function, we have the set of
%PBGs, namely, their lower and higher frequencies.
%All parameters determining computation precision
%are defined inside the function
function pbgSet=getBandgap(a,r,eps1,eps2)
%The variable precis defines the number of k-vector
%points between high symmetry points
precis=5;

%The variable nG defines the number of plane waves.
%Since the number of plane waves cannot be
%arbitrary value and should be zero-symmetric, the
%total number of plane waves may be determined
%as (nG*2-1)^2
%Since the function is called multiple times, high
%number of plane waves dramatically increases
%total computation time. That is why we set low
%value of nG.
nG=5;

%The variable precisStruct defines contains the
%number of nodes of discretization mesh inside in
%unit cell discretization mesh elements.
%Since the PBG map is computed as a function of
%geometric parameter, the structure should be
%defined more precisely as compared to previous
%times.
precisStruct=64;

%The following cycle loop carries out the definition
%of the unit cell. The definition is being
%made in discreet form by setting values of inversed
%dielectric function to mesh nodes.
%For the reason of high precision of the geometry

```

```

%definition, we use interpolation here as described
%in chapter 6
dr=a/precisStruct;
nx=1;
for countX=-a/2:a/precisStruct:a/2
    ny=1;
    for countY=-a/2:a/precisStruct:a/2
        %The following condition allows to define the circle
        %with of radius r
        if(sqrt(countX^2+countY^2)<r)
            %Setting the value of the inversed dielectric
            %function to the mesh node
            struct(nx,ny)=1/eps2;
        %Saving the node coordinate
        xSet(nx)=countX;
        ySet(ny)=countY;
        elseif sqrt(countX^2+countY^2)<r+dr
            %Processing the element's boundary
            struct(nx,ny)=1/(eps1+(eps2-eps1)*...
                (1-(sqrt(countX^2+countY^2)-r)/dr));
            xSet(nx)=countX;
            ySet(ny)=countY;
        else
            struct(nx,ny)=1/eps1;
            xSet(nx)=countX;
            ySet(ny)=countY;
        end
        ny=ny+1;
    end
    nx=nx+1;
end

%The computation of the area of the mesh cell. It is
%necessary for further computation of the Fourier
%expansion coefficients.
dS=(a/precisStruct)^2;

%Forming 2D arrays of nodes coordinates
xMesh=meshgrid(xSet(1:length(xSet)-1));
yMesh=meshgrid(ySet(1:length(ySet)-1))';

%Transforming values of inversed dielectric function
%for the convenience of further computation
structMesh=struct(1:length(xSet)-1,...
    1:length(ySet)-1)*dS/(max(xSet)-min(xSet))^2;

```

```

%Defining the k-path within the Brilluoin zone. The
%k-path includes all high symmetry points and precis
%points between them
kx(1:precis+1)=0:pi/a/precis:pi/a;
ky(1:precis+1)=zeros(1,precis+1);

kx(precis+2:precis+precis+1)=pi/a;
ky(precis+2:precis+precis+1)=...
    pi/a/precis:pi/a/precis:pi/a;

kx(precis+2+precis:precis+precis+1+precis)=...
    pi/a-pi/a/precis:-pi/a/precis:0;
ky(precis+2+precis:precis+precis+1+precis)=...
    pi/a-pi/a/precis:-pi/a/precis:0;

%After the following loop, the variable numG will
%contain real number of plane waves used in the
%Fourier expansion
numG=1;

%The following cycle forms the set of reciprocal
%lattice vectors.
for Gx=-nG*2*pi/a:2*pi/a:nG*2*pi/a
    for Gy=-nG*2*pi/a:2*pi/a:nG*2*pi/a
        G(numG,1)=Gx;
        G(numG,2)=Gy;
        numG=numG+1;
    end
end

%The next cycle loop computes the Fourier expansion
%coefficients which will be used for matrix
%differential operator computation.
for countG=1:numG-1
    for countG1=1:numG-1
        CN2D_N(countG,countG1)=sum(sum(structMesh.*...
            exp(1i*((G(countG,1)-G(countG1,1))*...
            xMesh+(G(countG,2)-G(countG1,2))*yMesh)))));
    end
end

%The next cycle loop computes matrix differential
%operator in case of TM. The computation
%is carried out for each of earlier defined

```



```

%wave vectors.
for countG=1:numG-1
    for countG1=1:numG-1
        for countK=1:length(kx)
            M(countK,countG,countG1)=...
                CN2D_N(countG,countG1)*...
                (sqrt((kx(countK)+G(countG,1))^2+...
                    (ky(countK)+G(countG,2))^2)*...
                sqrt((kx(countK)+G(countG1,1))^2+...
                    (ky(countK)+G(countG1,2))^2));
        end
    end
end

%The computation of eigen-states is also carried
%out for all wave vectors in the k-path.
for countK=1:length(kx)
    %Taking the matrix differential operator for current
    %wave vector.
    MM(:,:)=M(countK, :, :);
    %Computing the eigen-vectors and eigen-states of
    %the matrix
    [D V]=eig(MM);
    %Transforming matrix eigen-states to the form of
    %normalized frequency.
    dispe(:,countK)=sqrt(V*ones(length(V),1))*a/2/pi;
end

%Storing the PBGs parameters
%Setting counter of PBG to 1
PBGcounter=1;
pbgSet(1,1)=-1;
%Analyzing the first 8 bands
for u=1:8
    %In case of PBG presence, storing it into the
    %variable pbgSet which will be returned by the
    %function
    if(min(dispe(u+1,:))>max(dispe(u,:)))
        pbgSet(PBGcounter,1)=max(dispe(u,:));
        pbgSet(PBGcounter,2)=min(dispe(u+1,:));
        PBGcounter=PBGcounter+1;
    end
end
end

```

The program listed applies the PWE method to computation of PBG map. Implementation of the PWE method is similar to the one used in Chap. 5 for 2D PhC. However, here the example computes for TM polarization eigenmodes rather than TE.

Main difference here consists in analysis of results obtained with PWE method. The function `pbgSet` returns just a set of PBGs. Their sorting and organization gives possibility to obtain the PBG map. The first part of the program sorts the PBGs and plots them as patches in a single figure. Main criteria for joining the PBG to one PBG spot is its frequency overlap with the frequency of the neighbor PBG.

Some peculiarities of the program should also be mentioned here. Between them, the high precision of the unit cell geometry definition and low number of plane waves used for Fourier expansion. The reason for high precision geometry is that we compute the PBG map as a dependence of the radius. If the geometry is defined with low precision, low variation of the value of radius will cause inessential variation of the geometry during one step while during another step the geometry may vary very fast. With this, the PBG map will have steps and will not be precise. On the other hand, high accuracy in geometry definition gives high correspondence between variation of variables and actual geometry and, therefore, the PBG map will be smooth.

Let us now examine the program results. The program computes the PBG map of the dielectric rods arranged to square lattice. However, we can see some differences between the program results (see Fig. 10.13) and the results given in Fig. 10.5a. This difference is in presence of some extra PBGs in Fig. 10.13. This happens because of low number of plane waves used in the program. Due to this fact, some bands appear to be nondegenerated within some k -points which causes appearance of additional band gaps. However, if we are interested in largest PBGs only as we were in this chapter, such inaccuracy is not essential.

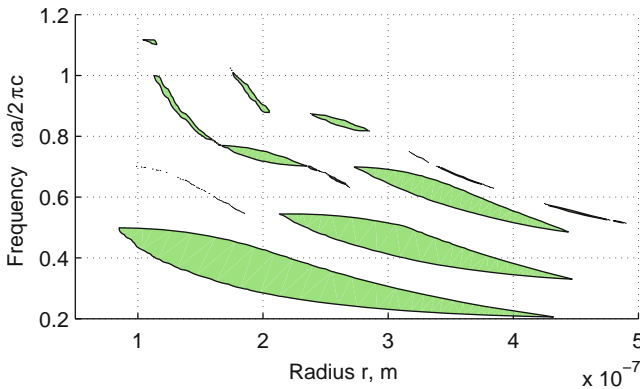


Fig. 10.13. Results of the program. The PBG map of 2D PhC with square lattice

10.6 Problems and Questions

Problem 10.1. What is the photonic band gap map?

Problem 10.2. Why the PBG filter should contain at least two elements in transversal direction?

Problem 10.3. Give the scheme for DEMUX parameters selection using PBG map.

Problem 10.4. What is the photonic density of states map?

Problem 10.5. Give the scheme for DEMUX parameters selection using PhDOS map.

Problem 10.6. Modify the program to compute the PBG map of 1D PhC.

Problem 10.7. Modify the program to compute the PBG map of 2D PhC presented by rods arranged in hexagonal lattice.

Problem 10.8. Modify the program to compute the PBG map of 2D PhC presented by rods arranged in square lattice as a dependence on the refractive index difference between rods and background material.

References

1. L. Rayleigh, On the maintenance of vibrations by forces of double frequency, and on the propagation of waves through a medium endowed with a periodic structure. *Philosophical Magazine* **24**, 145–159 (1887)
2. V.P. Bykov, Spontaneous emission in a periodic structure. *J. Exp. Theor. Phys.* **35**, 269 (1972)
3. E. Yablonovitch, Inhibited spontaneous emission in solid-state physics and electronics. *Phys. Rev. Lett.* **58**, 2059–2062 (1987)
4. S. John, Strong localization of photons in certain disordered dielectric superlattices. *Phys. Rev. Lett.* **58**, 2486–2489 (1987)
5. K.M. Ho, C.T. Chan, C.M. Soukoulis, Existence of a photonic gap in periodic dielectric structures. *Phys. Rev. Lett.* **65**, 3152–3155 (1990)
6. H.S. Sozuer, J.W. Haus, R. Inguva, Photonic bands: Convergence problems with the plane-wave method. *Phys. Rev. B* **45**, 13962–13972 (1992)
7. J.E.G.J. Wijnhoven, L.V. Willem, Preparation of photonic crystals made of air spheres in Titania. *Science* **281**, 802–804 (1998)
8. A. Blanco, E. Chomski, S. Grabtchak, et al., Large-scale synthesis of a silicon photonic crystal with a complete three-dimensional bandgap near 1.5 micrometres. *Nature* **405**, 437–440 (2000)
9. D. Englund, D. Fattal, E. Waks, et al., Controlling the spontaneous emission rate of single quantum dots in a two-dimensional photonic crystal. *Phys. Rev. Lett.* **95**, 013904, 3 p. (2005)
10. M. Mueller, A. Bauer, Th. Lehnhardt, et al., Widely tunable photonic crystal coupled cavity lasers on GaSb. *IEEE Photon. Technol. Lett.* **20**(13), 1100–1102 (2008)
11. A. Larrue, O. Bouchard, A. Monmayrant, et al., Precise frequency spacing in photonic crystal DFB laser arrays. *IEEE Photon. Technol. Lett.* **20**(24), 2120–2122 (2008)
12. L. Yu, J. Yu, Zh. Fan, et al., Realization of an ultracompact low-loss photonic crystal corner mirror. *IEEE Photon. Technol. Lett.* **19**(14), 1042–1044 (2007)
13. L. Yu, J. Yu, Y. Yu, et al., Design, fabrication and characterization of an ultracompact low-loss photonic crystal corner mirror. *IEEE J. Quant. Electron.* **43**(10), 876–883 (2007)
14. J. Heinrich, R. Langhans, J. Seufert, et al., Quantum cascade microlasers with two-dimensional photonic crystal reflectors. *IEEE Photon. Technol. Lett.* **19**(23), 1937–1939 (2007)

15. X. Checoury, Ph. Boucaud, J.-M. Lourtioz, et al., Distributed feedback-like laser emission in photonic crystal waveguides on InP substrate. *IEEE J. Select. Top. Quant. Electron.* **11**(5), 1180–1186 (2005)
16. M. Fujita, Y. Tanaka, S. Noda, Light emission from silicon in photonic crystal nanocavity. *IEEE J. Select. Top. Quant. Electron.* **14**(4), 1090–1097 (2008)
17. C. Karnutsch, M. Stroisch, M. Punke, et al., Laser diode-pumped organic semiconductor lasers utilizing two-dimensional photonic crystal resonators. *IEEE Photon. Technol. Lett.* **19**(10), 741–743 (2007)
18. S. Boutami, B.B. Bakir, J.-L. Leclercq, et al., Photonic crystal-based MOEMS devices. *IEEE J. Select. Top. Quant. Electron.* **13**(2), 244–252 (2007)
19. K. Yoshino, Y. Ohmori, A. Fujii, et al., Organic electronic devices based on polymeric material and tunable photonic crystal. *Jpn. J. Appl. Phys.* **46**(9A), 5655–5673 (2007)
20. A.M. Kasten, M.P. Tan, J.D. Sulkin, et al., Photonic crystal vertical cavity lasers with wavelength-independent single-mode behavior. *IEEE photon. Technol. Lett.* **20**(23), 2010–2012 (2005)
21. A.M. Kasten, J.D. Sulkin, P.O. Leisher, et al., Manufacturable photonic crystal single-mode and fluidic vertical-cavity surface-emitting lasers. *IEEE J. Select. Top. Quant. Electron.* **14**(4), 1123–1131 (2008)
22. M.V. Maximov, Yu.M. Shernyakov, I.I. Novikov, et al., High-power low-beam divergence edge-emitting semiconductor lasers with 1- and 2-D photonic bandgap crystal waveguide. *IEEE J. Select. Top. Quant. Electron.* **14**(4), 1113–1122 (2008)
23. P.O. Leisher, C. Chen, J.D. Sulkin, et al., High modulation bandwidth implant-confined photonic crystal vertical-cavity surface-emitting lasers. *IEEE Photon. Technol. Lett.* **19**(19), 1541–1543 (2007)
24. M. Makarova, J. Vuckovic, H. Sanda, et al., Silicon-based photonic crystal nanocavity light emitters. *Appl. Phys. Lett.* **89**, 221101, 3p (2006)
25. H. Altug, D. Englund, J. Vucovic, Ultrafast photonic crystal nanocavity laser. *Nat. Phys.* **2**(6), 484–488 (2006)
26. F.-F. Ren, M.B. Yu, J.D. Ye, et al., Enhanced vertical light extraction from ultrathin amorphous SiSi₃N₄ multilayers with photonic crystal patterns. *IEEE Photon. Technol. Lett.* **21**(2), 91–93 (2009)
27. C.M. Long, A.V. Giannopoulos, K.D. Choquette, Lateral current injection photonic crystal emitters. *IEEE/LEOS Winter Topicals Meeting Series*, (Innsbruck, Austria, 12–14 January 2009), pp.62–63
28. J. Park, J.-K. Oh, K.-W. Kwon, et al., Improved light output of photonic crystal light-emitting diode fabricated by anodized aluminum oxide nano-patterns. *IEEE Photon. Technol. Lett.* **20**(4), 321–323 (2008)
29. J. Park, J.-K. Oh, K.-W. Kwon, et al., Integration of photonic crystals on GaN-based blue LEDs using silicon mold substrates. *IEEE J. Quant. Electron.* **44**(10), 984–989 (2008)
30. C.H. Lin, H.H. Yen, C.F. Lai, et al., Enhanced vertical extraction efficiency from a thin-film InGaNGaN light-emitting diode using a 2-D photonic crystal and an omnidirectional reflector. *IEEE Photon. Technol. Lett.* **20**(10), 836–838 (2008)
31. M.-L. Hsieh, K.-C. Lo, Y.-S. Lan, et al., One-shot exposure for patterning two-dimensional photonic crystals to enhance light extraction of InGaNGaN-based green LEDs. *IEEE Photon. Technol. Lett.*, **20**(10), 141–143 (2008)

32. A.J. Danner, B. Wang, S.J. Chua, et al., Fabrication of efficient light-emitting diodes with a self-assembled photonic crystal array of polystyrene nanoparticles. *IEEE Photon. Technol. Lett.* **20**(1), 48–50 (2008)
33. H.K. Cho, S.-K. Kim, D.K. Bae, et al., Laser liftoff GaN thin-film photonic crystal GaN-based light-emitting diodes. *IEEE Photon. Technol. Lett.* **20**(24), 2096–2098 (2008)
34. H. Benisty, J. Danglot, A. Talneau, et al., Investigation of extracting photonic crystal lattices for guided modes of GaAs-based heterostructures. *IEEE J. Quant. Electron.* **44**(8), 777–789 (2008)
35. L.B. Chang, Y.-H. Chang, M.-J. Jeng, Light output improvement of InGaN-based light-emitting diodes by microchannel structure. *IEEE Photon. Technol. Lett.* **19**(15), 1175–1177 (2007)
36. S. Noda, Recent progresses and future prospects of two- and three-dimensional photonic crystals. *IEEE J. Lightwave Technol.* **24**(12), 4554–4567 (2006)
37. J. Wang, M. Qiu, High-Q optical filter based on photonic crystal surface-mode microcavity. *IEEE/LEOS Winter Topicals Meeting Series* (Innsbruck, Austria, 2009), pp.22–23
38. A. Khorshidahmad, A.G. Kirk, Nested photonic crystal cavity for on-chip wavelength conversion. *IEEE/LEOS Winter Topicals Meeting Series*, (Innsbruck, Austria, 2009), pp.60–61
39. Q. Chen, M.D. Archbold, D.W.E. Allsopp, Design of ultrahigh-Q 1-D photonic crystal microcavities. *IEEE J. Quant. Electron.* **45**(3), 233–239 (2009)
40. Y. Tanaka, T. Asano, S. Noda, Design of photonic crystal nanocavity with Q-Factor of 10^9 . *IEEE J. Lightwave. Technol.* **26**(11), 1532–1539 (2008)
41. I.-K. Hwang, M.-K. Kim, Y.-H. Lee, All-optical switching in InGaAsP-InP photonic crystal resonator copled with microfiber. *IEEE Photon. Technol. Lett.* **19**(19), 1535–1537 (2007)
42. I. Fushman, E. Waks, D. Englund, et al., Ultrafast nonlinear optical tuning of photonic crystal cavities. *Appl. Phys. Lett.* **90**, id. 091118, 3p (2007)
43. C.-H. Chen, Y. Fainman, Photonic bandgap microcavities with flat-top response. *IEEE J. Select. Top. Quantum. Electron.* **13**(2), 262–269 (2007)
44. K. Staliunas, Spatial filtering of light beams in chirped photonic crystals. *IEEE/LEOS Winter Topicals Meeting Series* (Innsbruck, Austria, 2009), pp. 176–177
45. T.-T. Shih, Y.-D. Wu, J.-J. Lee, Proposal for compact optical triplexer filter using 2-D photonic crystals. *IEEE Photon. Technol. Lett.* **21**(1), 18–20 (2009)
46. S.S. Oh, C.-G. Choi, Photonic-crystal-slab-type guided mode resonance filters in infrared range. *IEEE Photon. Technol. Lett.* **21**(5), 316–318 (2009)
47. D.M. Beggs, T.P. White, L. Cairns, et al., Ultrashort photonic crystal optical switch actuated by a microheater. *IEEE Photon. Technol. Lett.* **21**(1), 24–26 (2009)
48. J. Ma, C. Jiang, Demonstration of ultraslow modes in asymmetric line-defect photonic crystal waveguides. *IEEE Photon. Technol. Lett.* **20**(14), 1237–1239 (2008)
49. C. Lee, R. Radhakrishnan, C.-C. Chen, et al., Design and modeling of a nanomechanical sensor using silicon photonic crystals. *IEEE J. Lightwave. Technol.* **26**(7), 839–846 (2008)
50. Y. Kawaguchi, N. Kono, K. Saitoh, et al., Loss reduction mechanism for coupled cavity waveguides in one-dimensional photonic crystals. *IEEE Journ. Lightwave. Technol.*, **26**(20), 3461–3467 (2008)

51. L. Gu, W. Jiang, X. Chen, et al., Physical mechanism of p-i-n-diode-based photonic crystal silicon electrooptic modulators for gigahertz operation. *IEEE J. Select. Top. Quantum. Electron.* **14**(4), 1132–1139 (2008)
52. Y. Cui, Q. Wu, E. Schonbrun, et al., Silicon-based 2-D slab photonic crystal TM polarizer at telecommunication wavelength. *IEEE Photon. Technol. Lett.* **20**(8), 641–643 (2008); Corrections in *IEEE Photon. Technol. Lett.* **20**(14), 1276 (2008)
53. L. Martinelli, H. Benisty, O. Drisse, et al., Impact of lithographic grid irregularity assessed on photonic crystal device selectivity. *IEEE Photon. Technol. Lett.* **19**(5), 282–284 (2007)
54. N. Kono, M. Koshiba, Magneto-photonic crystal slab waveguides with lower-refractive-index-silica claddings. *IEEE Photon. Technol. Lett.* **19**(5), 258–260 (2007)
55. L. Gu, W. Jiang, X. Chen, et al., Thermooptically tuned photonic crystal waveguide silicon-on-insulator MachZehnder interferometers. *IEEE Photon. Technol. Lett.* **19**(5), 342–344 (2007)
56. S. Assefa, S.J. McNab, Y.A. Vlasov, Transmission of slow light through photonic crystal waveguide bends. *Opt. Lett.* **31**(6), 745–747 (2006)
57. P. Strasser, G. Stark, F. Robin, et al., Optimization of a 60° waveguide bend in InP-based 2D planar photonic crystals. *J. Opt. Soc. Am. B* **25**(1), 67–73 (2008)
58. F. Monifi, M. Djavid, A. Ghaffari, et al., Design of efficient photonic crystal bend and power splitter using super defects. *J. Opt. Soc. Am. B* **25**(11), 1805–1810 (2008)
59. H. Kurt, D.S. Citrin, Reconfigurable multimode photonic-crystal waveguides. *Opt. Express* **16**(16), 11995–12001 (2008)
60. D. Gao, Z. Zhou, D.S. Citrin, Self-collimated waveguide bends and partial bandgap reflection of photonic crystals with parallelogram lattice. *J. Opt. Soc. A* **25**(3), 791–795 (2008)
61. G.Y. Dong, X.L. Yang, L.Z. Cai, et al., Improvement of transmission properties through two-bend resonance by holographic design for a two-dimensional photonic crystal waveguide. *Opt. Express* **16**(20), 15375–15381 (2007)
62. C. Xudong, C. Hafner, R. Vahldieck, et al., Sharp trench waveguide bends in dual mode operation with ultra-small photonic crystals for suppressing radiation. *Opt. Express* **14**(10), 4351–4356 (2006)
63. R.-J. Liu, Z.-Y. Li, F. Zhou, et al., Near-field studies of microwave three-dimensional photonic crystals with waveguides. *Opt. Express* **15**(23), 15531–15538 (2007)
64. S.-H. Jeong, N. Yamamoto, J.-I. Sugisaka, et al., GaAs-based two-dimensional photonic crystal slab ring resonator consisting of a directional coupler and bent waveguides. *J. Opt. Soc. Am B* **24**(8), 1951–1959 (2007)
65. C. Hafner, C. Xudong, J. Smajic, et al., Efficient procedures for the optimization of defects in photonic crystal structures. *J. Opt. Soc. Am A* **24**(4), 1177–1188 (2007)
66. Y. Morita, Y. Tsuji, K. Hirayama, Proposal for a compact resonant-coupling-type polarization splitter based on photonic crystal waveguide with absolute photonic bandgap. *IEEE Photon. Technol. Lett.* **20**(2), 93–95 (2008)
67. A.A.M. Kok, E.J. Geluk, F. Karouta, et al., Short polarization filter in pillar-based photonic crystals. *IEEE Photon. Technol. Lett.* **20**(16), 1369–1371 (2008)

68. Y. Shi, D. Dai S. He, Proposal for an ultracompact polarization-beam splitter based on a photonic-crystal-assisted multimode interference coupler. *IEEE Photon. Technol. Lett.* **19**(11), 825–827 (2007)
69. A. Ghaffari, M. Djavid, M.S. Abrishamian, Power splitters with different output power levels based on directional coupling. *Appl. Optics* **48**(8), 1606–1609 (2009)
70. O. Kilic, S. Fan, O. Solgaard, Analysis of guided-resonance-based polarization beam splitting in photonic crystal slabs. *J. Opt. Soc. Am. A* **25**(11), 2680–2692 (2008)
71. M. Djavid, A. Ghaffari, F. Monifi, et al., Photonic crystal power dividers using L-shaped bend based on ring resonators. *J. Opt. Soc. Am. B* **25**(8), 1231–1235 (2008)
72. Y.-D. Wu, M.-L. Huang, T.-T. Shih, Optical interleavers based on two-dimensional photonic. *Appl. Optics* **46**(29), 7212–7217 (2007)
73. E. Schonbrun, Q. Wu, W. Park, et al., Polarization beam splitter based on a photonic crystal heterostructure. *Opt. Lett.* **31**(21), 3104–3106 (2006)
74. H. Kurt, D.S. Citrin, A novel optical coupler design with graded-index photonic crystals. *IEEE Photon. Technol. Lett.* **19**(19), 1532–1534 (2007)
75. F. AbdelMalek, W. Belhadj, S. Haxha, et al., Realization of a high coupling efficiency by employing a concave lens based on two-dimensional photonic crystals with a negative refractive Index. *IEEE J. Lightwave. Technol.* **29**(10), 1368–1374 (2007)
76. H. Kurt, D.S. Citrin, Graded index photonic crystals, *Opt. Express* **15**(3), 1240–1253 (2007)
77. W. Bogaerts, D. Taillaert, B. Luyssaert, P. Dumon, Basic structures for photonic integrated circuits in Silicon-on-insulator. *Opt. Express* **12**(8), 1583–1591 (2004)
78. P. Sanchis, J. Garcia, A. Martinez, et al., Analysis of adiabatic coupling between photonic crystal single-line-defect and coupled-resonator optical waveguides. *Opt. Lett.* **28**(20), 1903–1905 (2003)
79. S.J. McNab, N. Moll, Y.A. Vlasov, Ultra-low loss photonic integrated circuit with membrane-type photonic crystal waveguides. *Opt. Express* **11**(22), 2927–2939 (2003)
80. P. Pottier, De. GnanM, R.M. La Rue, Efficient coupling into slow-light photonic crystal channel guides using photonic crystal tapers. *Opt. Express* **15**(11), 6569–6575 (2007)
81. P. Bienstman, S. Assefa, S.G. Johnson, et al., Taper structures for coupling into photonic crystal slab waveguides. *J. Opt. Soc. Am. B* **20**(9), 1817–1821 (2003)
82. A. Talneau, Ph. Lalanne, M. Agio, et al., Low-reflection photonic-crystal taper for efficient coupling between guide sections of arbitrary widths. *J. Opt. Soc. Am. B* **20**(9), 1817–1821 (2003)
83. P.-G. Luan, K.-D., Chang, Periodic dielectric waveguide beam splitter based on co-directional coupling. *Opt. Express* **15**(8), 4536–4545 (2007)
84. S. Kim, I. Park, H. Lim, Proposal for ideal 3-dB splitters/combiners in photonic crystals. *Opt. Lett.* **30**(3), 257–259 (2005)
85. L.H. Frandsen, P.I. Borel, X.Y. Zhuang, et al., Ultralow-loss 3-dB photonic crystal waveguide splitter. *Opt. Lett.* **29**(14), 1623–1625 (2004)

86. P. Strasser, R. Flueckiger, R. Wueest, et al., InP-based compact photonic crystal directional coupler with large operation range. *Opt. Express* **15**(13), 8472–8478 (2007)
87. A. Talneau, M. Mulot, S. Anandb, et al., Modal behavior of single-line photonic crystal guiding structures on InP substrate. *Photon. Nanostruct.* **2** 1–10 (2004)
88. S. Kim, I. Park, H. Lim, Design of photonic crystal splitters/combiners. *Proc. Soc. Photo. Opt. Instrum. Eng.* **5597**, 129–135 (2004)
89. H. Scherer, K. Namje, S. Deubert, et al., Integrated four-channel GaAs-based quantum dot laser module with photonic crystals. *J. Vac. Sci. Technol. B* **23**(6), 3193–3196 (2005)
90. S. Asefa, S.J. McNab, Y.A. Vlasov, Transmission of slow light through photonic crystal waveguide bends. *Opt. Lett.* **31**(6), 745–747 (2006)
91. N. Horiuchi, Y. Segawa, T. Nozokido, et al., High-transmission waveguide with a small radius of curvature at a bend fabricated by use of a circular photonic crystal. *Opt. Lett.* **30**(9), 973–975 (2005)
92. J. Smajic, C. Hafner, D. Erni, Design and optimization of an achromatic photonic crystal bend. *Opt. Express* **11**(12), 1378–1384 (2003)
93. A. Sharkawy, D. Pustai, S. Shi, et al., High transmission through waveguide bends by use of polycrystalline photonic-crystal structures. *Opt. Lett.* **28**(14), 1197–1199 (2003)
94. K. Miura, Y. Ohtera, N. Akutsu, et al., Reduction of propagation and bending losses of heterostructured photonic crystal waveguides by use of a high- Δ structure. *Opt. Lett.* **28**(9), 734–736 (2003)
95. M. Augustin, H.-J. Fuchs, D. Schelle, et al., Highly efficient waveguide bends in photonic crystal with a low in-plane index contrast. *Opt. Express* **11**(24), 3284–3289 (2003)
96. G.P. Nordin, S. Kim, J. Cai, et al., Hybrid integration of conventional waveguide and photonic crystal structures. *Opt. Express* **10**(23), 1334–1341 (2002)
97. A. Talneau, L. Le Gouezigou, N. Bouadma, et al., Photonic-crystal ultrashort bends with improved transmission and low reflection at $1.55\mu\text{m}$. *Appl. Phys. Lett.* **80**(4), 547–549 (2002)
98. N. Fukaya, D. Ohsaki, T. Baba, Two-dimensional photonic crystal waveguides with 60° bends in a thin slab structure. *Jpn. J. Appl. Phys.* **39**(5A), 2619–2623 (2000)
99. Y. Zhang, B. Li, Photonic crystal-based bending waveguides for optical interconnections. *Opt. Express* **14**(12), 5723–5732 (2006)
100. Y. Zhang, B. Li, Ultracompact waveguide bends with simple topology in two-dimensional photonic crystal slabs for optical communication wavelengths. *Opt. Lett.* **32**(7), 787–789 (2007)
101. B. Chen, T. Tang, H. Chen, Study on a compact flexible photonic crystal waveguide and its bends. *Opt. Express* **17**(7), 5033–5038 (2009)
102. A. Tetu, M. Kristensen, L.H. Frandsen, et al., Broadband topology-optimized photonic crystal components for both TE and TM polarizations. *Opt. Express* **13**(21), 8606–8611 (2005)
103. P.I. Borel, A. Harpoth, L.H. Frandsen, et al., Topology optimization and fabrication of photonic crystal structures. *Opt. Express* **12**(9), 1996–2001 (2004)
104. M. Tokushima, H. Kosaka, A. Tomita, et al., Triple-exposure method for fabricating triangular-lattice photonic crystals. *Jpn. J. Appl. Phys.* **39**(7A), 4236–4240 (2000)

105. M.H. Shih, W.J. Kim, W. Kuang, et al., Experimental characterization of the reflectance of 60° waveguide bends in photonic crystal waveguides. *Appl. Phys. Lett.* **86**, 191104 (2005)
106. P. Bettini, S. Boscolo, M. Midrio, Design optimization of waveguide bends in photonic crystals. *IEEE Trans. Magn.* **45**(3), 1630–1633 (2009)
107. L. Wu, M. Mazilu, J.-F. Gallet, et al., Planar photonic crystal polarization splitter. *Opt. Lett.* **29**(14), 1620–1622 (2004)
108. S. Shi, A. Sharkawy, C. Chen, et al., Dispersion-based beam splitter in photonic crystals. *Opt. Lett.* **29**(6), 617–619 (2004)
109. C.-C. Chen, H.-D. Chien, P.-G. Luan, Photonic crystal beam splitters. *Appl. Optics.* **43**(33), 6187–6190 (2004)
110. S. Kim, G.P. Nordin, J. Cai, et al., Ultracompact high-efficiency polarizing beam splitter with a hybrid photonic crystal and conventional waveguide structure. *Opt. Lett.* **28**(23), 2384–2386 (2003)
111. Z. Xu, J. Wang, Q. He, et al., Optical filter based on contra-directional waveguide coupling in a 2D photonic crystal with square lattice of dielectric rods. *Opt. Express* **13**(15), 5608–5613 (2005)
112. I. Park, H.-S. Lee, H.-J. Kim, et al., Photonic crystal power-splitter based on directional coupling. *Opt. Express* **12**(15), 3599–3604 (2004)
113. C.-C. Chen, C.-Y. Chen, W.-K. Wang, et al., Photonic crystal directional couplers formed by InAlGaAs nano-rods. *Opt. Express* **13**(1), 38–43 (2005)
114. B. Momeni, M. Chamanzar, E.S. Hosseini, et al., Strong angular dispersion using higher bands of planar silicon photonic crystals. *Opt. Express* **16**(18), 14213–14220 (2008)
115. F. Cuesta-Soto, B. Garcia-Banos, J. Marti, Compensating intermodal dispersion in photonic crystal directional couplers. *Opt. Lett.* **30**(23), 3156–3158 (2005)
116. A. Bakhtazad, A.G. Kirk, First-band S-vector photonic-crystal superprism demultiplexer design and optimization. *J. Lightwave. Technol.* **25**(5), 1322–1333 (2007)
117. X. Liu, X. Sun, P. Gu, Enhanced superprism effect based on positive/negative lateral shift of reflective beam in a FabryPerot filter. *Opt. Lett.* **32**(16), 2321–2323 (2007)
118. T. Prasad, V.L. Colvin, Z. Jian, et al., Superprism effect in a metal-clad terahertz photonic crystal slab. *Opt. Lett.* **32**(6), 683–685 (2007)
119. D. Bernier, X. Le Roux, A. Lupu, et al., Compact, low cross-talk CWDM demultiplexer using photonic crystal superprism. *Opt. Express* **16**(22), 17209–17214 (2008)
120. Y. Wang, Zh. Cao, T. Yu, et al., Enhancement of the superprism effect based on the strong dispersion effect of ultrahigh-order modes. *Opt. Lett.* **33**(11), 1276–1278 (2008)
121. Zh. Liu, S. Durant, H. Lee, et al., Experimental studies of far-field superlens for sub-diffractive optical imaging. *Opt. Express* **15**(11), 6947–6954 (2007)
122. Y. Xiong, Zh. Liu, S. Durant, Tuning the far-field superlens: from UV to visible. *Opt. Express* **15**(12), 7095–7102 (2007)
123. X.H. Sun, X.M. Tao, K.Ch. Kwan, Effects of material composition on the superlens frequency of photonic crystals. *J. Opt. Soc. Am. B* **25**(4), 571–575 (2008)
124. B. Wang, L. Shen, S. He, Superlens formed by a one-dimensional dielectric photonic crystal. *J. Opt. Soc. Am. B* **25**(3), 391–395 (2008)

125. X. Yang, Y. Liu, J. Ma, et al., Broadband super-resolution imaging by a superlens with unmatched dielectric medium. *Opt. Express*, **16**(24), 19686–19694 (2008)
126. A. Hakansson, J. Sanchez-Dehesa, Inverse designed photonic crystal demultiplex waveguide coupler. *Opt. Express*, **13**(14), 5440–5449 (2005)
127. L. Martinelli, H. Benisty, O. Khayam, et al., Analysis and optimization of compact demultiplexer monitor based on photonic-crystal waveguide. *J. Lightwave Technol.* **25**(9), 2385–2394 (2007)
128. T. Stomeo, F. Van Laere, M. Ayre, et al., Integration of grating couplers with a compact photonic crystal demultiplexer on an InP membrane. *Opt. Lett.* **33**(8), 884–886 (2008)
129. F. Van Laere, T. Stomeo, C. Cambournac, et al., Nanophotonic polarization diversity demultiplexer chip. *J. Lightwave Technol.* **27**(4), 417–425 (2009)
130. Y.-D. Wu, K.-W. Hsu, T.-T. Shih, et al., New design of four-channel add-drop filters based on double-resonant cavity photonic crystals. *J. Opt. Soc. Am. B.* **26**(4), 640–644 (2009)
131. C.M. Soukoulis, M. Kafesaki, E.N. Economou, Negative-index materials: New frontiers in optics. *Adv. Mater.* **18**, 1941–1952 (2006)
132. T. Baba, T. Matsumoto, T. Asatsuma, Negative refraction in photonic crystals, *Adv. Sci. Technol.* **55**, 91–100 (2008)
133. C.M. Zhou, J. T. Koschny, et al., The science of negative index materials. *J. Phys. Condens. Matter.* **20**, 1–7 (2008)
134. J.A. Ferrari, C.D. Perciante, Superlenses, metamaterials, and negative refraction. *J. Opt. Soc. Am. A* **26**(1), 78–84 (2009)
135. M.S. Rill, C.E. Kriegler, M. Thiel, et al., Negative-index bianisotropic photonic metamaterial fabricated by direct laser writing and silver shadow evaporation. *Opt. Lett.* **34**(1), 19–21 (2009)
136. E. Waks, J. Vuckovic, Dispersive properties and large Kerr nonlinearities using dipole-induced transparency in a single-sided cavity. *Phys. Rev. A* **73**, 041803-1–041803-4 (2006)
137. T. Ahmadi Tameh, B. Memarzadeh Isfahani, A.R. Maleki Javan, et al., Enhancement of nonlinearity in nonlinear photonic crystal ring resonators for all-optical switching. *IEEE/LEOS Winter Topicals Meeting Series*, 26–27 (2009)
138. I.V. Guryev, O. V. Shulika, I.A. Sukhoivanov, et al., Improvement of characterization accuracy of the nonlinear photonic crystals using finite elements-iterative method. *Appl. Phys. B - Lasers and Optics* **84**(1-2), 83–87 (2006)
139. I.V. Guryev, I.A. Suhoivanov, E. Alvarado Mendez, et al., Theoretical study of optical processes in nonlinear photonic crystals devices, *The International Workshop on Optoelectronic Physics and Technology*, Kharkov, Ukraine, 25–28 (2007)
140. E. Alvarado-Mendez, J.A. Andrade Lucio, M. Trejo-Duran, et al., Experimental evidence of dark lattices in nonlinear liquid medium. *Mol. Cryst. Liq. Cryst.* **488**, 127–134 (2008)
141. P. Tran, Optical limiting and switching of short pulses by use of a nonlinear photonic bandgap structure with a defect, *J. Opt. Soc. Am. B.* **14**(10), 2589–2595 (1997)
142. J. Zhou, H. Shao, J. Zhao, et al., Storage and release of femtosecond laser pulses in a resonant photonic crystal. *Opt. Lett.* **30**(12), 1560–1562 (2005)

143. B.Z. Steinberg, A. Boag, Propagation in photonic crystal coupled-cavity waveguides with discontinuities in their optical properties. *J. Opt. Soc. Am. B* **23**(7), 1442–1450 (2006)
144. Y. Cao, P. Lu, Zg. Yang, et al., An efficient method of all-optical buffering with ultra-small core photonic crystal fibers. *Opt. Express* **16**(18), 14142–14150 (2008)
145. C. Li, H. Tian, Y. Ji, Investigation of slow light utilized as optical storage in photonic crystal coupled resonator optical waveguide. *Proc. SPIE* **7279**, 727914 (2008)
146. S. Sandhu, M.L. Povinelli, S. Fan, Stopping and time reversing a light pulse using dynamic loss tuning of coupled-resonator delay lines. *Opt. Lett.* **32**(22), 3333–3335 (2007)
147. D.G. Angelakis, M.F. Santos, V. Yannopapas, et al., A proposal for the implementation of quantum gates with photonic-crystal waveguides. *Phys. Lett. A* **362**(5-6), 377–380 (2007)
148. Zh.-H. Zhu, W.-M. Ye, J.-R. Ji, et al., High-contrast light-by-light switching and AND gate based on nonlinear photonic crystals. *Opt. Express* **14**(5), 1783–1788 (2006)
149. A. Shinya, S. Matsuo, Yosia, et al., All-optical on-chip bit memory based on ultra high Q InGaAsP photonic crystal. *Opt. Express* **16**(23), 19382–19387 (2008)
150. P. Andalib, N. Granpayeh, All-optical ultracompact photonic crystal AND gate based on nonlinear ring resonators. *J. Opt. Soc. Am. B* **26**(1), 10–16 (2009)
151. I.V. Guryev, J.A.A. Lucio, O.G.I. Manzano, et al., Optical power limiter on the basis of 2D photonic crystal. *Int. Conf. Advanced Optoelectronics and Lasers, CAOL 2008, Crimea, Ukraine*, 180–182 (2008)
152. H. Xiao, D. Yao, Optical limitation in two-dimensional nonlinear photonic crystal with triangular lattice. *Phys. Lett. A* **359**(6), 723–727 (2006)
153. C.R. Rosberg, F.H. Bennet, D.N. Neshev, et al., Tunable diffraction and self-defocusing in liquid-filled photonic crystal fibers. *Opt. Express*, **15**(19), 12145–12150 (2007)
154. D.N. Christodoulides, N.K. Efremidis, Discrete temporal solitons along a chain of nonlinear coupled microcavities embedded in photonic crystals. *Opt. Lett.* **27**(8), 568–570 (2002)
155. K. Gallo, G. Assanto, Spatial solitons in $\chi^{(2)}$ planar photonic crystals. *Opt. Lett.* **32**(21), 3149–3151 (2007)
156. B. Maes, P. Bienstman, R. Baets, Bloch modes and self-localized waveguides in nonlinear photonic crystals. *JOSA B* **22**(3), 613–619 (2005)
157. F. Poli, A. Cucinotta, D. Passaro, et al., Single-mode regime in large-mode-area rare-earth-doped rod-type PCFs. *IEEE J. Select. Top. Quant. Electron.* **15**(1), 54–60 (2009)
158. J.M. Dudley, 10 years of nonlinear optics in photonic crystal fiber: Progress and perspectives. *IEEE/LEOS Winter Topicals Meeting Series (Innsbruck, Austria, 2009)*, p. 182
159. L. Dong, T.-W. Wu, H.A. McKay, et al., All-glass large-core leakage channel fibers. *IEEE J. Select. Top. Quant. Electron.* **15**(1), 47–53 (2009)
160. C.J.S de Matos, Modeling long-pass filters based on fundamental-mode cutoff in photonic crystal fibers. *IEEE Photon. Technol. Lett.* **21**(2), 112–114 (2009)
161. X. Zhao, G. Zhou, S. Li, et al., Photonic crystal fiber for dispersion compensation. *Appl. Opt.* **47**(28), 5190–5196 (2008)

162. Y. Tsuchida, K. Saitoh, M. Koshiba, A design method for single-polarization holey fibers with improved beam quality factor. *IEEE Photon. Technol. Lett.* **26**(14), 2162–2164 (2008)
163. G. Ren, P. Shum, J. Hu, et al., Study of polarization-dependent bandgap formation in liquid crystal filled photonic crystal fibers. *IEEE Photon. Technol. Lett.* **20**(15), 602–604 (2008)
164. S.M. Abdur Razzak, Y. Namihiro, Proposal for highly nonlinear dispersion-flattened octagonal photonic crystal fibers. *IEEE Photon. Technol. Lett.* **20**(4), 249–251 (2008)
165. S.M. Abdur Razzak, Y. Namihiro, Tailoring dispersion and confinement losses of photonic crystal fibers using hybrid cladding. *IEEE J. Lightwave. Technol.*, **26**(13), 1909–1914 (2008)
166. A. Millo, L. Lobachinsky, A. Katzir, Single-mode index-guiding photonic crystal fibers for the middle infrared. *IEEE Photon. Technol. Lett.* **20**(10), 869–871 (2008)
167. F. Zhang, M. Zhang, X. Liu, et al., Design of wideband single-polarization single-mode photonic crystal fiber. *IEEE J. Lightwave. Technol.* **25**(5) 1184–1189 (2007)
168. S. Yang, Y. Zhang, J. Li, et al., Experimental study of mode field evolution of dual-core photonic crystal fiber. *IEEE Photon. Technol. Lett.* **19**(19), 1523–1525 (2007)
169. G. Ren, P. Shum, L. Zhang, et al., Low-loss all-solid photonic bandgap fiber. *Opt. Lett.* **32**(9), 1023–1025 (2007)
170. M. Delgado-Pinar, A. Diez, J.L. Cruz, et al., High extinction-ratio polarizing endlessly single-mode photonic crystal fiber. *IEEE Photon. Technol. Lett.* **19**(8), 562–564 (2007)
171. D. Chen, L. Shen, Ultrahigh birefringent photonic crystal fiber with ultralow confinement loss. *IEEE Photon. Technol. Lett.* **19**(4), 185–187 (2007)
172. S. Yang, Y. Zhang, L. He, et al., Broadband dispersion-compensating photonic crystal fiber. *Opt. Lett.* **31**(19), 2830–2832 (2006)
173. Symposium on Microstructured and Nanostructured Optical Fibers in ICMAT 2007. *Opt. Quantum. Electron.* **39**, 12–13 (2007)
174. J.S. Sanghera, L.B. Shaw, I. D. Aggarwal, Chalcogenide glass-fiber-based Mid-IR sources and applications. *IEEE J. Select. Top. Quantum. Electron.* **15**(1), 114–119 (2009)
175. A.V. Dyogtyev, R. DeLaRue, I.A. Sukhoivanov, Passive fiber-optical components based on the photonic crystals, The International Workshop on Optoelectronic Physics and Technology, Kharkov, Ukraine, 40–41 (2007)
176. I.A. Sukhoivanov, J.A. Andrade-Lucio, R. Rojas-Laguna: Tapered photonic crystal fiber couplers for optical in-tegration RIAO/OPTILAS 2004. *Proc. Soc. Photo. Opt. Instrum. Eng.* 5622, 967–971 (2004)
177. I.A. Sukhoivanov, R. Rojas-Laguna, J.-A. Andrade-Lucio, et al., Waveguide couplers formed by tapered photonic crystal fiber. *Proc. Soc. Photo. Opt. Instrum. Eng.* 5450-30, 231–239 (2004)
178. J. Limpert, F. Roeser, D.D. Schimpf, et al., High repetition rate gigawatt peak power fiber laser systems: Challenges, design, and experiment. *IEEE J. Select. Top. Quantum. Electron.* **15**(1), 159–169 (2009)
179. T. Geernaert, G. Luyckx, E. Voet, et al., Transversal load sensing with fiber Bragg gratings in microstructured optical fibers. *IEEE Photon. Technol. Lett.* **21**(1), 6–8 (2009)

180. X. Yu, Y. Sun, G.B. Ren, et al., Evanescent field absorption sensor using a pure-silica defected-core photonic crystal fiber. *IEEE Photon. Technol. Lett.* **20**(5), 336–338 (2008)
181. Y.-J. Song, M.-L. Hu, C.-L. Wang, et al., Environmentally stable, high pulse energy Yb-doped large-mode-area photonic crystal fiber laser operating in the soliton-like regime. *IEEE Photon. Technol. Lett.* **20**(13), 1088–1090 (2008)
182. Q. Shi, Z. Wang, L. Jin, et al., A hollow-core photonic crystal fiber cavity based multiplexed FabryPerot interferometric strain sensor system. *IEEE Photon. Technol. Lett.* **20**(15), 1329–1331 (2008)
183. Y.S. Shinde, H.K. Gahir, Dynamic pressure sensing study using photonic crystal fiber: Application to tsunami sensing. *IEEE Photon. Technol. Lett.* **20**(4), 279–281 (2008)
184. J. E. Sharping, Microstructure fiber based optical parametric oscillators. *IEEE J. Lightwave. Technol.* **26**(14), 2184–2191 (2008)
185. J. Ju, W. Jin, H.L. Ho, Compact in-fiber interferometer formed by long-period gratings in photonic crystal fiber. *IEEE Photon. Tehcnol. Lett.* **20**(23), 1899–1901 (2008)
186. K. Igarashi, K. Kikuchi, Optical signal processing by phase modulation and subsequent spectral filtering aiming at applications to ultrafast optical communication systems. *IEEE J. Select. Top. Quantum. Electron.* **14**(3), 551–565 (2008)
187. M.Y. Chen, H. Subbaraman, R.T. Chen, Photonic crystal fiber beamformer for multiple X-band phased-array antenna transmissions. *IEEE Photon. Technol. Lett.* **20**(5), 375–377 (2008)
188. L. Orsila, R. Herda, O.G. Okhotnikov, Monolithic fiber mirror and photonic crystal technology for high repetition rate all-fiber soliton lasers. *IEEE Photon. Technol. Lett.* **19**(24), 2009–2011 (2007)
189. K. Nakajima, T. Matsui, K. Kurokawa, et al., High-speed and wideband transmission using dispersion-compensating/managing photonic crystal fiber and dispersion-shifted fiber. *IEEE J. Lightwave. Technol.* **25**(9), 2719–2726 (2007)
190. T. Matsui, K. Nakajima, I. Sankawa, Dispersion compensation over all the telecommunication bands with double-cladding photonic-crystal fiber. *IEEE J. Lightwave. Technol.* **25**(3), 757–762 (2007)
191. C.C. Lee, P.K.A. Wai, H.Y. Tam, et al., 10-Gb/s wavelength transparent optically controlled buffer using photonic-crystal-fiber-based nonlinear optical loop mirror. *IEEE Photon. Technol. Lett.* **19**(12), 898–900 (2007)
192. R. Jiang, R.E. Saperstein, N. Alic, et al., Continuous-wave band translation between the near-infrared and visible spectral ranges. *IEEE J. Lightwave. Technol.* **25**(1), 58–66 (2007)
193. H.S. Jang, K.N. Park, K.S. Lee, Characterization of tunable photonic crystal fiber directional couplers. *Appl. Opt.* **46**(18), 3688–3693 (2007)
194. S.M. Hendrickson, T.B. Pittman, J.D. Franson, Microcavities using holey fibers. *IEEE J. Lightwave. Technol.* **25**(10), 3068–3071 (2007)
195. H. Hasegawa, Y. Oikawa, M. Nakazawa, A 10-GHz optoelectronic oscillator at 850 nm using a single-mode VCSEL and a photonic crystal fiber. *IEEE Photon. Technol. Lett.* **19**(19), 1451–1453 (2007)
196. M.P. Fok, C. Shu, Multipump four-wave mixing in a photonic crystal fiber for 6×10 Gb/s wavelength multicasting of DPSK signals. *IEEE Photon. Technol. Lett.* **19**(15), 1166–1168 (2007)

197. S. Asimakis, G. Meloni, J.Y.Y. Leong, et al., Low walk-off Kerr-shutter using a dispersion-shifted lead silicate holey fiber. *IEEE Photon. Technol. Lett.* **19**(15), 1112–1114 (2007)
198. T.R. Wolinski, A. Czapla, S. Ertman, et al., Tunable highly birefringent solid-core photonic liquid crystal fibers. *Opt. Quant. Electron.* **39**, 1021–1032 (2007)
199. T.T. Alkeskjold, L. Scolari, D. Noordegraaf, et al., Integrating liquid crystal based optical devices in photonic crystal fibers. *Opt. Quant. Electron.* **39**, 1009–1019 (2007)
200. J. Limpert, F. Roeser, T. Schreiber, et al., High-power ultrafast fiber laser systems. *IEEE J. Select. Top. Quant. Electron.* **12**(2), 233–244 (2006)
201. M. Born, E. Wolf, *Principles of Optics: Electromagnetic Theory of Propagation, Interference and Diffraction of Light*, 7th Edn. (Cambridge University Press, 1999)
202. G.P. Agrawal, *Fiber Optic Communication Systems*, 3rd edn. (Wiley, NY 2002)
203. A. Jeffrey, *Advanced Engineering Mathematics, International Edition*. (Academic Press 2001)
204. C. R. Giles, Lightwave applications of fiber Bragg gratings. *J. Lightwave Technol.* **15**(8), 1391–1404 (1997)
205. J.D. Joannopoulos, R.D. Meade, J.N. Winn, *Photonic Crystals: Molding the Flow of Light (Second Edition)*. (Princeton University Press, Princeton 1995)
206. K. Sakoda, *Optical Properties of Photonic Crystals (First Edition)*. (Springer, Heidelberg, 2001)
207. W.A. Harrison, *Solid State Theory*. (Dover, NY, 1979)
208. C. Kittel, *Introduction to Solid State Physics*. (Wiley, NY, 1996)
209. J.-M. Lourtioz, H. Benisty, V. Berger, et al., *Photonic Crystals, Towards Nanoscale Photonic Devices*. (Springer, Heidelberg, 2005)
210. K. Yitzhak, *An introduction to Harmonic Analysis, 2nd corrected ed.* (Dover, NY, 1976)
211. G.H. Golub, C.F. Van Loan, *Matrix Computations (Third Edition)*. (Johns Hopkins University Press, 1996)
212. J. Koringa, On the calculation of the energy of a Bloch wave in a metal. *Physica* **13**, 392 (1947)
213. W. Kohn, N. Rostoker, Solution of Schroedinger equation in periodic lattice with an application to metallic lithium. *Phys. Rev.* **94**, 1111 (1954)
214. V. N. Astratov, D. M. Whittaker, I. S. Culshaw, et al., Photonic band-structure effects in the reflectivity of periodically patterned waveguides. *Phys. Rev. B* **60**(24), 255–258 (1999)
215. A. Taflove, S.C. Hagness, *Computational Electrodynamics: The Finite-Difference Time-Domain Method*, 3rd edn. (Artech House, Norwood, MA, 2005)
216. A. Cheng, D. T. Cheng, Heritage and early history of the boundary element method. *Eng. Anal. Bound. Elem.* **29**, 268–302 (2005)
217. K. Gustafson, Domain decomposition, operator trigonometry, robin condition. *Contemp. Math.* **218**, 432–437 (1998)
218. J. Berenger, A perfectly matched layer for the absorption of electromagnetic waves. *J. Comput. Phys.* **114**, 185–200 (1994)
219. S.D. Gedney, An anisotropic perfectly matched layer absorbing media for the truncation of FDTD lattices. *Antennas and propagation, IEEE Trans. Magn.* **44**, 1630–1639 (1996)

220. W.C. Chew, W.H. Weedon, A 3d perfectly matched medium from modified Maxwell's equations with stretched coordinates. *Microwave Opt. Tech. Lett.* **7**, 590–604 (1994)
221. F.L. Teixeira, W.C. Chew, General closed-form PML constitutive tensors to match arbitrary bianisotropic and dispersive linear media. *IEEE Microw. Guided. Wave. Lett.* **8**, 223–225 (1998)
222. D. Labilloy, H. Benisty, C. Weisbuch, et al., Finely resolved transmission spectra and band structure of two-dimensional photonic crystals using emission from InAs quantum dots. *Phys. Rev. B* **59**(3), 1649–1652 (1999)
223. H.G. Unger, *Planar Optical Waveguides and Fibres*. (Clarendon Press, Oxford, 1977)
224. D. Hondors, P. Debye, Elektromagnetische wellen an dielektrischen Draeten. *Ann. Phys.* **32**, 465–476 (1910)
225. H. Buchholz, Die quasioptik der Ultrakurzwellenleiter. *Electrische Nachrichtentechnik* **15**, 297–320 (1958)
226. N.S. Kapany, *Fiber Optics Principles and Applications*. (Academic Press, NY, 1967)
227. K.C. Kao, G.A. Hockham, Dielectric-fibre surface waveguides for optical frequencies. *Proc. I.E.E.* **113**(7), 1151–1158 (1996)
228. J. C. Knight, T. A. Birks, P. St. J. Russell, et al., All-silica single-mode optical fiber with photonic crystal cladding. *Opt. Lett.* **21**, 1547–1549 (1996)
229. D. Marcuse, *Light Transmission Optics*. (Van Nostrand, NY, 1982)
230. P. Yeh, A. Yariv, E. Marom, Theory of Bragg fiber. *J. Opt. Soc. Am.* **68**, 1196–1201 (1978)
231. C. M. Smith, N. Venkataraman, M. T. Gallagher, et al., Low-loss hollow-core silica/air photonic bandgap fibre. *Nature* **424**, 657–659 (2003)
232. J. C. Knight, J. Arriaga, T. A. Birks, et al., Anomalous dispersion in photonic crystal fiber. *IEEE Photon. Technol. Lett.* **12**, 807–809 (2000)
233. J. C. Knight, F. Gerome, W. J. Wadsworth, Hollow-core photonic crystal fibres for delivery and compression of ultrashort optical pulses. *Opt. Quant. Electron.* **39**, 1047–1056 (2007)
234. A. L. Gaeta, Supercontinuum generation in microstructured fibers. *OSA Technical Dig. Conf. Lasers and Electro-Optics*, Paper CMK3, 48 (2001)
235. J.C. Travers, A.B. Rulkov, B.A. Cumberland, et al., Non-linear applications of microstructured optical fibres. *Opt. Quant. Electron.* **39**, 963–974 (2007)
236. S. Coen, A. H. L. Chau, R. Leonhardt, et al., White light supercontinuum generation with 60-ps pump pulses in a photonic crystal fiber. *Opt. Lett.* **26**, 1356–1358 (2001)
237. T. A. Birkst, D. Mogilevtsev, J. C. Knight, The analogy between photonic crystal fibres and step index fibres. *Optical Fiber Communication Conference, 1999, and the International Conference on Integrated Optics and Optical Fiber Communication. OFC/IOOC*, **4**, 114–116 (1999)
238. N.A. Mortensen, J.R. Folken, P. M. W. Skovgaard, Numerical aperture of single-mode photonic crystal fibers. *IEEE Photon. Technol. Lett.* **14**(8), 1094–1096 (2002)
239. T. Sorensen, J. Broeng, A. Bjarklev, et al., Spectral macro-bending loss considerations for photonic crystal fibres. *IEE Proc. Optoelectron.* **149**(5/6), 206–210 (2002)
240. G. Bouwmans, V. Pureur, A. Betourne, et al., Progress in solid core photonic bandgap fibers. *Opt. Quantum Electron.* **39**, 949–961 (2007)

- 241. W. Tong, H. Wei, J. Li, et al., Investigation of all-solid photonic bandgap fiber with low losses in low-order bandgaps. *Opt. Quant. Electron.* **39**, 1071–1080 (2007)
- 242. H. Yu D. Yang, Finite difference analysis of 2-D photonic crystals. *IEEE Trans. microw. Theory Tech.* **44**(12), 2688–2695 (1996)
- 243. N. Brenner, C. Rader, A new principle for fast fourier transformation. *IEEE Trans. Acoust. Speech Signal Process* **24**, 264–266 (1976)
- 244. N. Sukumar, J. E. Pask, Classical and enriched finite element formulations for Bloch-periodic boundary conditions. In. *J. Numer. Methods Eng.* doi: 10.1002/nme.2457
- 245. G. Grau, W. Freude, *Optische Nachrichtentechnik Einr Einfuerung* (in German). (Springer, Heidelberg, 1986)
- 246. I.A. Sukhoivanov, I.V. Guryev, O.V. Shulika, et al., Design of the photonic crystal demultiplexers for ultra-short optical pulses using the gap-maps analysis. *J. Optoelectron. Adv. Materi.* **8**(4), 1622–1626 (2006)
- 247. I.V. Guryev, I.A. Sukhoivanov, E. Cabal Yopez, et al., Comparative Analysis of the PBG and PhDOS maps synthesis, 1st Multiconference of Electronics and Photonics (Conference on Advanced Optoelectronics and lazers MEP/CAOL 2006), Guanajuato, Mexico, 17–20 (2006)
- 248. I. A. Sukhoivanov, I. V. Guryev, J. A. Andrade Lucio, et al., Photonic Density of States Maps for Design of Photonic Crystal Devices LDSD 2007: The Sixth International Conference on Low Dimensional Structures and Devices, 15–20 (2007)
- 249. I. A. Sukhoivanov, I. V. Guryev, J. A. Andrade Lucio, E. Alvarado Mendez, M. Trejo-Duran, M. Torres-Cisneros. Photonic Density of States Maps for Design of Photonic Crystal Devices. *Microelect. J.* **38**(3–4), 685–689 (2008)

Index

- 1D Photonic crystal, [1](#)
- 2D Photonic crystal, [1](#)
- 3D PhC waveguides, [185](#)
- 3D Photonic crystal, [2](#)

- Absorption coefficient, [22](#), [111](#)
- Angular frequency, [18](#)

- Background PhC, [209](#), [213](#)
- Band gap diagram, [152](#)
- Band structure, [5](#), [80](#), [84](#), [168](#), [169](#)
 - analysis, [81](#), [82](#)
- Band structure computation
 - of 1D PhC, [50](#)
 - of 2D PhC, [71](#)
 - of 3D PhC, [69](#)
- Base element of the PhC, [49](#)
- Basis functions, [46](#), [47](#), [69](#), [70](#)
- Basis vectors, [48](#)
- Bessel functions, [131](#), [138](#)
- Bloch theorem, [42](#), [50](#)
- Bloch wave, [68](#), [71](#)
- Boundary conditions, [30](#), [31](#), [109](#), [179](#)
- Bragg, [1](#)
 - condition, [32](#)
 - distributed reflector, [32–35](#)
 - grating, [32](#), [33](#)
 - reflector, [9](#)
 - wavelength, [32](#), [34](#), [39](#)
- Brillouin zone, [48](#), [49](#)
 - of the 2D PhC with hexagonal lattice, [49](#)
- bV-diagram
 - of the slab waveguide, [183](#)

- Complete photonic band gap, [81](#), [82](#)
- Computation domain, [164](#)
- Computation mesh, [106](#), [108](#), [110](#), [113](#)
- Computation region, [105](#)
 - discretization, [108](#)
- Computation region definition, [164](#)
- Computation time, [167](#), [169](#)
- Continuum of states, [144](#), [145](#), [150](#), [151](#), [191](#)
- Conventional optical fibers, [129](#), [137](#)
- Cramer's method, [31](#), [39](#)

- Defect, [33](#), [35](#), [88](#)
- Defect thickness, [34](#), [35](#)
- Delta-pulse, [166](#)
- Density of modes, [84](#)
- Diamond lattice, [7](#)
- Dielectric constant, [21](#)
 - frequency-dependent, [23](#)
- Dielectric function, [42–44](#), [46](#), [47](#), [50](#), [51](#), [55](#)
 - inverted, [51](#), [55](#)
- Dielectric rods, [73](#)
- Dielectric spheres, [72](#)
- Dirichlet boundary conditions, [110](#)
- Discretization of the space, [103](#), [104](#), [108–110](#)
- Discretization of the unit cell, [75](#)
- Dispersion
 - chromatic, [22](#)
 - material, [22](#)
- Dispersion diagram, [151](#), [191](#), [192](#)
 - of the PhC waveguide, [186–188](#), [190](#)
- Dispersion relation, [42](#)

- Effective refractive index, 135, 137, 146
- Eigen-frequency, 5, 52, 89
- Eigen-function, 42
- Eigen-problem, 42, 44, 50
 - for matrix, 53
- Eigen-state, 3, 5, 7, 52
 - of 3D PhC, 69
- Eigen-value, 42, 52, 53, 57, 71, 132
- Eigen-value equation, 50
- Eigen-vector, 53, 143
- Electric susceptibility, 20, 22
- Even mode, 192

- Face-centered cubic lattice, 5, 7
- Field distribution, 103, 104, 106, 109
- Finite differences time domain method, 163
- Finite-difference time-domain method, 103
- First band structure, 7
- Fourier expansion, 72, 73
 - arbitrary dielectric function, 74
 - coefficients, 51, 52, 55, 64
 - dielectric rods, 73
 - dielectric spheres, 72
 - of the dielectric function, 55
 - validation for 1D dielectric function, 56, 57
 - validation for 2D dielectric function, 76
- Fourier transform, 47

- Gain, 22
- Gaussian-modulated high frequency signal, 166
- GLAD, 5
- Group velocity, 23, 24, 82, 135
- Group velocity dispersion, 186, 191
- Guided mode, 128, 130–132, 134

- Hankel function, 131
- Helmholtz equation, 28–30, 42, 50, 57, 58, 68, 71
- High symmetry points of the Brillouin zone, 78, 80
- History of PhC, 6
- Hybrid modes, 133, 134

- In-plane band structure, 87
- Index-guided microstructured fiber, 144, 145
- Index-guided microstructured fibers, 144
- Initial conditions, 30, 31, 109
- Initial pulse profile, 109
- Inversed dielectric function, 71, 72
- Inverted face-centered cubic lattice, 8

- k-path, 79
- Korringa-Kohn-Rostoker method, 70

- Laplace operator, 28
- Lattice vector, 45, 71, 187
 - of the PhC with defect, 88
- Layer thickness, 27
- Layered structure, 27, 29–31
- Leaky mode, 130
- Linearly polarized mode, 134, 135
- Losses, 22

- Master equation
 - for 1D PhC, 51
 - for 2D PhC, 71
 - for 3D PhC, 69
- Maxwell's equations, 14, 15, 28
 - in dielectric medium, 16
 - in vacuum, 18
- Maxwell's Equations Discretization, 104
- Medium
 - anisotropic, 17
 - dielectric, 17, 20, 21
 - lossy, 21
 - homogeneous, 14, 17
 - isotropic, 17, 20, 21
 - linear, 20, 42
 - non-dispersive, 42
 - non-magnetic, 28
 - optical, 5, 13, 14, 16
 - periodic, 43
 - uniform, 42, 43
- Meridional ray, 133
- Microstructured fiber, 129, 140
- Mixed boundary conditions, 110
- Mode, 14, 17, 23
- Mode field distribution, 142
- Mode group velocity, 186, 191

- Mode index, 135
- Multimode fiber, 138

- Neumann boundary conditions, 110
- Neumann function, 131
- Nodes-sources, 109

- Odd mode, 192
- Off-axis band structure, 58
- Off-plane band structure, 85, 87
- Off-plane Brillouin zone, 86
- Orthogonally polarized mode, 135

- Perfectly matched layer, 111, 113
- Periodic boundary conditions, 111, 165
- Periodic function, 47
- Periodic structure, 3, 5–7
- Permittivity, 13
 - relative, 21, 28
- Phase velocity, 23
- PhC filters, 206, 208
- PhC with defect, 88
- Photonic band gap, 3, 6, 54, 81, 82
- Photonic band gap fibers, 150
- Photonic band gap map, 83, 208
- Photonic band structure, 5
- Photonic crystal, 1
 - applications, 9
 - lattice, 3, 5
- Photonic crystal demultiplexer, 206, 208, 209, 211, 214
- Photonic crystal waveguide, 207
- Photonic density of states, 52, 84
- Photonic density of states map, 211–214
- Plane wave, 19, 23, 42, 47, 142
- Plane wave expansion method, 42, 88
 - advantages and disadvantages, 93
- Polar coordinate system, 74
- Poynting vector, 17
- Primitive lattice vector, 46
- Propagation constant, 131, 133, 141, 142, 150, 188
- Pulse response analysis, 167
- Pulse response spectrum, 167

- Quasi-diamond lattice, 5

- Radiation
 - propagation direction, 6

- Radiation mode, 130
- Reciprocal lattice, 49
- Reciprocal lattice vector, 47, 188
 - the set of, 79
- Reciprocal lattice vectors
 - the set of, 80
- Recurrent formula
 - for 1D problem, 107
 - for 2D problem, 106, 107
 - for 3D problem, 105
 - for 3D problem with PML, 112
- Reduced band structure, 59, 83
- Reflectance, 30
 - spectrum, 32
- Refractive index, 21, 22
- Robin boundary conditions, 111

- Similarities between PhC and solid-state, 2
- Single-mode condition
 - for conventional fiber, 138
 - for microstructured fiber, 144, 145
- Single-mode fiber, 135, 139
- Single-mode Fibers, 138
- Spherical coordinate system, 72
- Spherical wave expansion method, 70
- Spiral lattice, 5
- Square mesh, 75
- Step-index fiber, 130, 139
- Strictly periodic structure, 88

- Tangential component of the electric field, 30
- Temporal response, 168
- Temporal response of DEMUX, 214, 215
- Total internal reflection, 144, 182
- Total internal reflection guiding
 - in PhC waveguide, 191
- Translation rules, 45
- Translation symmetry, 48
- Transmittance, 30, 32, 34
 - spectrum, 32, 33
- Transmittance map, 211–213

- Unit cell, 44, 45, 75, 142, 164, 187
 - of the PhC with defect, 88

- Vertical cavity surface emitting lasers, 1, 9

- W1-waveguide, [185](#), [192](#)
- W2-waveguide, [185](#), [192](#)
- W3-waveguide, [185](#), [192](#)
- Wave
 - backward, [29–32](#)
 - forward, [29–31](#)
 - front, [19](#)
 - monochromatic, [23](#), [24](#)
 - packet, [24](#)
 - propagation direction, [17](#), [23](#)
- Wave equation, [19](#), [21](#), [27](#), [28](#)
 - in dielectric medium, [22](#)
 - in vacuum, [18](#)
- Wave function, [68](#)
 - in wave vector space, [68](#), [69](#)
- Wave vector, [5–7](#), [18](#), [19](#), [28](#)
- Wave vector representation, [47](#), [68](#), [69](#)
- Wave vectors set, [52](#), [78](#)
- Waveguide channel, [206](#), [208](#)
- Waveguide splitter, [205](#), [206](#)
- Wavelength division multiplexer, [33](#)
- Wavenumber, [19](#)
- Weakly guiding fiber, [135](#)
- Wide band optical filter, [206](#)
- Woodpile lattice, [5](#)